UNIVERSITY OF CALIFORNIA SAN DIEGO

Multiscale Modeling of General Grain Boundaries: From Computing Grain Boundary Diagrams to Machine Learning to Deciphering the Physical Mechanism of Segregation

A dissertation submitted in partial satisfaction of the
requirements for the degree Doctor of Philosophy

in

Materials Science and Engineering

by

Chongze Hu

Committee in charge:

Professor Jian Luo, Chair
Professor Vitali Nesterenko
Professor Tod Pascal
Professor Kenneth Vecchio
Professor Kesong Yang

2020

The Dissertation of Chongze Hu is approved, and it is acceptable in quality and form for publication on microfilm and electronically:

_____

_____

_____

_____

_____

Chair

University of California San Diego

2020

DEDICATION

To my parents

TABLE OF CONTENTS

LIST OF FIGURES

LIST OF TABLES

ACKNOWLEDGEMENTS

First, I would like to thank my Ph.D. advisor, Dr. Jian Luo, for his education of research fundamentals and guidance on multiple projects. He introduced me to methodologies of research and critical thinking, which I believe will benefit my life in many ways in the future. It was a great honor to learn from him in the past three years. I would also like to thank my committee members, Dr. Kenneth S. Vecchio, Dr. Tod Pascal, Dr. Vitali Nesterenko, and Dr. Kesong Yang, for their valuable suggestions and precious time.

Secondly, I would like to acknowledge my collaborators and co-authors, Dr. Zhiyang Yu, Dr. Shyue Ping Ong, Dr. Chi Chen, Dr. Wenqing Zhang, Dr. Naixie Zhou, Yunxing Zuo, Dr. Xiangguo Li, Dr. Jiuyuan Nie, Dr. Zhishan Luo, Qizhang Yan, and Yanwen Li, with whom I had many valuable discussions. Especially, I would like to appreciate Dr. Shengfeng Yang for the initial training on simulation.

I'm also grateful to my group members, Dr. Joshua Gild, Dr. Jiuyuan Nie, Andrew Wright, Qizhang Yan, Shu-Ting Ko, Mingde Qin, Dawei Zhang, Yi Liu, and Siyuan Shao, for the stimulating discussions and advices. I would also like to thank other colleagues, Sicong Jiang, Hui Zheng, and Fulong Li, for their help and friendship.

Lastly and most importantly, I would like to thank my family members, Fuqin Zhang and Xueli Hu, for their love, understanding, and encouragement.

Chapter 2, in part, is a reprint of the material "First-Order Interfacial Transition in Si-Au Binary System: Hybrid Monte Carlo and Molecular Dynamics

Simulations Verified by First-Principles Calculations", C. Hu and J. Luo, as it appears in Scripta Materialia, 2019, 158, 11-15. The dissertation author was the primary investigator and first author of this paper.

Chapter 3, in part, is a reprint of the material "Genetic Algorithm-Guided Deep Learning of Grain Boundary Diagrams: Addressing the Challenge of Five Degrees of Freedom", C. Hu, Y. Zuo, C. Chen, S. Ong, and J. Luo, as it appears in Materials Today, 2020, 38, 49-57. The deep learning models were developed by Y. Zuo, C. Chen, and S. Ong. The dissertation author was the primary investigator and first author of this paper.

Chapter 4, in part, is a reprint of the material "Deciphering the Grain-Boundary Properties in High-Entropy Alloys in a 5D Space: Coupled Segregation and Disordering", C. Hu and J. Luo, in preparation. The dissertation author was the primary investigator and first author of this paper.

Chapter 5, in part, is a reprint of the material "Grain-Boundary Diagram of Mechanical Properties for Al-Ga Binary System", C. Hu, Y. Li, Z. Yu, and J. Luo, in preparation. The electron microscopy characterization was carried out by Y. Li and Z. Yu. The dissertation author was the primary investigator to perform MD simulations and first author of this paper.

Chapter 6, in part, is a reprint of manuscript "A highly Asymmetric Interfacial Structure in WC: Expanding Classical Grain Boundary Segregation and New Complexion Theory", Z. Luo, C. Hu, L. Xie, H. Nie, C. Xiang, X. Gu, J. He, W. Zhang, Z. Yu, and J. Luo, Materials Horizon, 2020, 7, 173-180. The experiments

were carried out by Z. Luo et al. The dissertation author was the primary investigator to perform theoretical calculation and the first co-author of this paper.

Chapter 7, in part, is a reprint of manuscript “Uncovering Electrochemically Induced Grain Boundary Phase-Like Transition” J. Nie, C. Hu, Q. Yan, and J. Luo, manuscript submitted. The experiments were carried out by J. Nie with the help of Q. Yan. The dissertation author was the primary investigator to perform theoretical calculations and first co-author of this paper.

VITA

2015	Bachelor of Science	Clemson University, USA
2016	Master of Science	University of Minnesota Twin Cities, USA
2020	Doctor of Philosophy	University of California San Diego, USA

PUBLICATIONS

1. **C. Hu**, J. Luo, “First-Order Interfacial Transition in Si-Au Binary System: Hybrid Monte Carlo and Molecular Dynamics Simulations Verified by First-Principles Calculations”, Scripta Materialia, 2019, 158, 11-15.

2. **C. Hu**, Y. Zuo, C. Chen, S. Ong, J. Luo, “Genetic Algorithm-Guided Deep Learning of Grain Boundary Diagrams: Addressing the Challenge of Five Degrees of Freedom”, Materials Today, 2020.

3. **C. Hu**, J. Luo, “Decipering the Grain-Boundary Properties in High-Entropy Alloys in a 5D Space: Coupled Segregation and Disordering“, (in preparation).

4. **C. Hu**, Z. Yu, J. Luo, “Developing Grain-Boundary Mechanical Properties Diagrams in Al-Ga Binary System “, (in preparation).

5. Z. Luo, **C. Hu** (equal contribution), L. Xie, H. Nie, C. Xiang, X. Gu, J. He, W. Zhang, Z. Yu, J. Luo, “A Highly Asymmetric Interfacial Superstructure in WC: Expanding the Classic Grain Boundary Segregation and New Complexion Theories”, Materials Horizon, 2020, 7, 173-180.

6. J. Nie, **C. Hu** (equal contribution), Q. Yan, J. Luo, “Uncovering Electrochemically Induced Grain-Boundary Phase-like Transitions”, (Submitted).

ABSTRACT OF THE DISSERTATION

Multiscale Modeling of General Grain Boundaries: From Computing Grain Boundary Diagrams to Machine Learning to Deciphering the Underlying Mechanism of Segregation

by

Chongze Hu

Doctor of Philosophy in Materials Science and Engineering

University of California San Diego, 2020

Professor Jian Luo, Chair

Most natural and engineered crystalline materials are polycrystalline, and grain boundaries (GBs) are the central crystal imperfections for describing these polycrystalline materials. Solute or impurity segregation at GB is a critical interfacial phenomenon because it can induce GB structural transformation, dramatically change the microstructural evolution, and cause catastrophic GB embrittlement. In a broader context, GB segregation (*a.k.a* adsorption) can control a broad range of kinetic, electronic, thermal, magnetic, and other materials

properties. Thus, understanding the underlying physical mechanism of GB segregation is of both fundamental and practical interest to materials science community.

It has been proposed that GB can adopt thermodynamic equilibria like a three-dimensional (3D) bulk phase. Such a GB state can be considered as a 2-D stabilized interfacial phase, which also named as “complexion” to differentiate from abutting bulk phases. Since the properties of GB can be as important as those of bulk phases, it is also useful to develop GB counterparts to “bulk” phase diagrams by constructing GB “complexion” diagrams as a function of temperature and bulk composition. It is interesting to note that, in some systems such as Mo-Ni and Si-Au binary systems, the computed GB diagrams exhibit first-order transformation lines with critical points, which unequivocally suggests the phase-like GB transition behavior. Meanwhile, GB transition can be continuous in many other systems, e.g., Cu-Ag, Cu-Zn, Al-Ga, *etc*. In both cases, developing GB diagrams as a function of temperature and bulk composition is meaningful and useful.

However, constructing GB diagrams is difficult for both experiments and modeling. On one hand, the advanced electron microscopy and atom probe tomography are common experimental tools used to characterize atomic-level GB structures, but the sample preparation and experimental procedure are complicate for characterizing even one GB. On the other hands, theoretical modeling of GB diagrams were mainly based on phenomenological or Lattice-type models, but these models are too simplified and cannot reflect atomistic details of GB. First-principles calculation was used to calculate interfacial energetic diagram of WC,

but only few configurations were investigated. Later, large-scale molecular dynamic simulations were adopted to compute GB diagrams, but most of studies were limited to symmetric tilt and twist GBs. The more general (asymmetric) GBs, which are more ubiquitous in polycrystalline materials, are still scarcely studied. Thus, one motivation of this dissertation is to construct GB diagrams for “general” GBs.

Furthermore, a GB has five macroscopic degrees of freedoms (DOFs), thus developing GB diagrams as a function of five DOFs associated with temperature and bulk composition in 7-D space remains a grand challenge even for a simple binary system. Recently, a new class of high-entropy alloys (HEAs), which generally contains five or more consecutive elements, has created extensive research interests. The large compositional space of HEA also makes it impossible to develop GB diagrams as a function of four compositional DOFs and temperature in 5-D space even for one specific GB. Therefore, we applied advanced computational techniques by combining high-throughput simulations and machine learning to predict GB diagrams in high-dimensional space.

Finally, it is also interesting to decipher the fundamental mechanism of GB segregation. Notably, first-principles calculations were used to explain the formation mechanism of a highly asymmetric interfacial structure of WC. Further, *ab initio* molecular dynamic simulations were performed to verify the enhanced grain growth by electrochemical reduction in Bi_2O_3-doped ZnO. The understanding of physical mechanism of GB segregation not only broadens our knowledge of GB segregation, but also enriches the segregation theories.

Chapter 1. Introduction

1.1. Grain Boundary: Description, Partition, and Thermodynamics

1.1.1. Brief Overview

Grain boundaries (GBs) are the interfaces between pairs of contiguous grains with same crystal structure but different crystallographic orientation [1-4]. Thus, GBs can be considered as a transition region, where atoms are shifted from their regular positions as compared to the crystal interior [1-4]. Due to the different atomic configurations, the properties of GBs can differ from those of bulk phases. In polycrystalline materials, GBs are the most ubiquitous crystal imperfection, and thus their properties can strongly control a broad range of physical, chemical, mechanical, and other properties for whole materials [5-7]. For example, intergranular fracture can occur at GBs and spread in such a 3-D networks [8]. In addition, the change in chemical composition (e.g., solute or impurity segregation) at GBs can induce structural transformation, and consequently, the synergistic effect of GB structural transition and chemistry can control a variety of materials properties [9-11]. Therefore, tuning the structural and chemical states of GB can be treated as an important strategy to engineering the microstructure of polycrystalline materials.

1.1.2. Crystallographic Description of Grain Boundary

To describe a GB, several variables must be specified. Within the framework of the coincident-site lattice (CSL) description [2, 12-14], a GB can be

fully characterized by five crystallographic degrees of freedom (DOFs). Here, three of them determine the specific mutual misorientation of the adjoining grain 1 and grain 2 (Fig. 1.1). The misorientation is generally represented by a rotation with a well-defined rotation axis ***o*** (2 DOFs) and misorientation angle θ_{mis} (1 DOF). Besides, the orientation of mis-orientated (boundary) planes of grain 1 and grain 2 is generally represented by normal ***n*** (2 DOFs, see Fig. 1.1). Following the CSL description method, a GB can be further defined using a notation θ_{mis}, [u_{tlt} v_{tlt} w_{tlt}] (*h k l*), where [u_{tlt} v_{tlt} w_{tlt}] is the Miller indices of rotation axis ***o***, and (*h k l*) is the boundary plane.

Although above mentioned five DOFs can unambiguously define a GB, several drawbacks exist for CSL description [2, 15]. For example, the symmetry properties involving the interface plane are not easily to be extracted based on this method. Moreover, it is even difficult to visualize an unrelaxed GB structure with simple interface plane. For example, 70.53^{o}, [110], (111) represents a simple (111) twin GB. Thus, new GB description scheme may be considered to characterize GB structures.

Wolf and Lutsko proposed an interface-plane (IP) scheme [15] to define GB using the notation of ϕ_{twst}, ($h_1k_1l_1$), ($h_2k_2l_2$), where ϕ_{twst} is the twist rotation angle of two boundary planes, ($h_1k_1l_1$) and ($h_2k_2l_2$) are the boundary planes of grain A and B respectively. In this manner, the above mentioned (111) twin GB can be written as 60^{o}, (111), (111), which is apparently easy to understand compared to the CSL notation. However, I-P scheme also has several disadvantages. For

example, the twist component (e.g., ϕ_{twst}) of a general GB in I-P scheme is not easily to obtain by experiments [15].

It should be noted that a GB defined by CSL scheme can be completely expressed by I-P scheme [15]. Simply speaking, the single rotation in CSL misorientation scheme can be decomposed to tilt rotation plus one twist rotation (Fig. 2). Several mathematical relationships can be achieved:

$$\boldsymbol{n}_{tlt} = \boldsymbol{n}_1 \times \boldsymbol{n}_2 / |\boldsymbol{n}_1 \times \boldsymbol{n}_2| \text{ and } \sin\varphi_{\mathrm{tlt}} = |\boldsymbol{n}_1 \times \boldsymbol{n}_2| \quad (1)$$

where $\boldsymbol{n}_{tlt} = [u_{\mathrm{tlt}}\ v_{\mathrm{tlt}}\ w_{\mathrm{tlt}}]$ is the tilt rotation axis, φ_{tlt} is the tilt rotation angle, and $\boldsymbol{n}_1$ and $\boldsymbol{n}_2$ are GB normal vector of Plane 1 and Plane 2. Next, the decomposed twist-rotation axis can be fixed to $\boldsymbol{n}_2$ (Fig. 2), and associated twist angle (ϕ_{twst}) can be simply obtained by [15]:

$$1 + \cos\phi_{\mathrm{twst}} = 2(1 + \cos\theta_{\mathrm{mis}})/(1+\cos\varphi_{\mathrm{tlt}}) \quad (2)$$

Using the Eqs. (1) and (2), the CSL notation can transition to I-P notation, and vice versa. By combining these two schemes, it is more interesting to characterize GB into groups based on individual DOFs. Notably, four types of GB (i.e., symmetric tilt, twist, asymmetric tilt, and mixed tilt-twist GBs) can be categorized based on the symmetry relation of boundary planes and twist rotation angle (ϕ_{twst}), see Fig. 3. For example, the symmetric tilt GB exhibit mirror symmetry because of pure tilt GB, so it has $\{h_1k_1l_1\} = \{h_2k_2l_2\}$ and $\phi_{\mathrm{twst}} = 0$. Note that the mixed tilt-twist GB is also called “random” or “general” GB based on the various terminologies [2, 16]. However, misleading sometimes exists because they can be also used to specify the GB character in the aspect of properties. This

dissertation calls this type of GBs “mixed”. Generally, the symmetric tilt and twist GBs have relatively simple atomic configurations and thus have been extensively studied by both experiments and modeling [14, 17-21]. On the contrary, the asymmetric tilt and mixed GBs with more complex structures are seldom investigated, but they are more ubiquitous in polycrystalline materials [16, 22, 23]. Therefore, one major motivation of this dissertation is to explore the GB properties of general GBs

1.1.3. Grain Boundary Thermodynamics

Since GB is one type of interface, their thermodynamic treatment should be consistent with general thermodynamic of interfaces. The first thermodynamic description of interface is proposed by Gibbs [24], and further developed by John Cahn [25]. This dissertation adopted Cahn formalism to introduce thermodynamic state functions of GBs. Let us consider an open system composed of two *N*-component grains A and B with same phase but different orientation (Fig. 4). When the growing of this bicrystal reaches the equilibrium transport state under the constant temperature *T*, pressure *P*, and chemical potentials μ_i, the increase of the internal energy (*U*) of the system can be written as:

$$dU = TdS - PdV + \sum_{i=1}^{N} \mu_i dn_i + \sigma dA, \quad (3)$$

where S is the entropy of the system, V is the volume, n_i is the number of component *i*, σ is GB internal energy, and *A* is the GB area. Note that σ also represents the change of internal energy with the change of GB area at constant S and V,

$$\sigma = \left(\frac{\partial U}{\partial A}\right)_{S,\ V, n_i}, \tag{4}$$

Using the fundamental relationship among the thermodynamic state functions, where enthalpy $H = U + PV$, Helmholtz energy $F = U - TS$, Gibbs energy $G = U+PV-TS$, following relations can be achieved for GB energy σ:

$$\sigma = \left(\frac{\partial F}{\partial A}\right)_{T,\ V, n_i}, \tag{5}$$

$$\sigma = \left(\frac{\partial H}{\partial A}\right)_{S,\ P, n_i}, \tag{6}$$

$$\sigma = \left(\frac{\partial G}{\partial A}\right)_{T,\ P, n_i}, \tag{7}$$

Here, the Eq. (7) defines the GB energy σ as the change of Gibbs energy of the system under constant temperature and pressure in a closed system.

1.2. Grain Boundary Segregation

1.2.1. Overview

GBs can be treated as the crystal imperfection and thus their free energy will be higher than the bulk phases with the same number of atoms. To minimize the total free energy, GBs generally interact with other lattice defects such as dislocations, vacancies, solute or impurity atoms, *etc*. Notably, such interaction can cause the redistribution or enrichment of solute or impurity atoms at GBs and this phenomenon is also known as GB segregation (*a.k.a*. adsorption). Extensive studies have found that solute or impurity segregation at GB can dramatically change microstructural evolution and various materials properties [26, 27], thus

understanding GB segregation is a key avenue to deciphering the complex structure-property-processing relation.

1.2.2. Thermodynamics of GB segregation

It is interesting to review some classical thermodynamic models that were used to study GB segregation. Starting with ideal solution, the Langmuir-Mclean segregation equation was used to address relation the between of GB composition as a function of bulk composition and temperature [1]:

$$\frac{x_{\mathrm{GB}}}{1-x_{\mathrm{GB}}} = \frac{x_{\mathrm{b}}}{1-x_{\mathrm{b}}} \exp\left(-\frac{\Delta G_{\mathrm{Seg}}}{RT}\right), \tag{8}$$

where x_{GB} and x_{b} are solute composition at GB and bulk phases, ΔG_{Seg} is the standard molar Gibbs free energy of segregation, R is Boltzmann constant, and T is temperature. Historically, Langmuir-Mclean equation was the first description of segregation behavior at solid interface in terms of composition and temperature. However, there are few limitations for Langmuir-Mclean model due to simple assumptions: (*i*) GB excess adsorption is homogeneous, (*ii*) GB was treated as a separate entity that is in equilibrium with bulk phases.

Later, it is assumed that GB can be represented as a regular solution and bulk phase can be treated as ideal solution. The Fowler-Guggenheim isotherm [28], that was first proposed for surface adsorption, was later adopted for GB segregation:

$$\frac{x_{\mathrm{GB}}}{1-x_{\mathrm{GB}}} = \frac{x_{\mathrm{b}}}{1-x_{\mathrm{b}}} \exp\left(-\frac{\Delta G_{\mathrm{Seg}}^{(0)} + z\omega \cdot x_{\mathrm{GB}}}{RT}\right), \tag{9}$$

where $\Delta G_{\mathrm{Seg}}^{(0)}$ is the intrinsic Gibbs free energy of segregation, z is the coordination number, and ω is the parameter of absorbate-absorbate interaction. It was found that Fowler-Guggenheim isotherm is valid for regular substitutional solid solution even for both cases of a local miscibility gap and an ordering tendency in bulk [3]. However, Fowler-Guggenheim model also has few limitations: (*i*) homogeneous segregation, (*ii*) GB cannot be considered as separate thermodynamic entity, for example, segregation can induce more disordered GB and GB disordering can be further coupled with segregation [29-31].

Thus, more realistic models should consider the disorder effect on GB segregation. Here, the author of this dissertation aims to (*i*) decipher the coupling effect of GB segregation and disorder, and further (*ii*) develop a more realistic model to capture this complex effect.

1.3. Grain Boundary Complexion

1.3.1. Overview of Complexion

In a broader context, GB can achieve an equilibrium state for a given set of thermodynamic variables such as temperature, pressure, and chemical potentials and may transform analogous to bulk phase transitions [32-35]. Such an equilibrium GB state can be considered as interfacial phase that is thermodynamically 2D [28], which is also named “complexion”, to differentiate it from abutting 3D thin layers precipitated on GB [32-35]. Recently, the term

“complexion” has been broadly recognized and adopted to describe GB “phase-like” transition behavior.

The GB complexion transition often occur independent of bulk phase transformation, e.g., at different temperature, pressure, and chemical potentials, and it is more difficult to capture and predict GB complexion transition compared to bulk phase transition [32-34]. With the development of advance electron microscopy technique, more and more evidence have shown that GB can exhibit complexion transition [21, 26, 36, 37]. Since this behavior can have influence on a variety of materials phenomena, such as abnormal grain growth [38, 39], liquid-metal embrittlement [26, 40], solid-state activated sintering [41, 42], *etc*., understanding GB complexion transition is of fundamental interest to materials science community.

1.3.2. Grain Boundary “Complexion” Diagrams

Phase diagrams are unambiguously one of the most important materials science tools that map the 3D bulk phase as a function of temperature and composition. In polycrystalline materials, since the properties of GB can be as important as those of bulk phases [5-7], it is fairly useful to develop GB counterpart of bulk phase diagram by mapping out GB states and properties as a function temperature and composition [43]. Recently, a series of GB diagrams have been reported. For example, some computed GB diagrams, e.g., Cu-Bi [44], Mo-Ni [45], and Si-Au [46] binary systems, exhibit first-order transition with critical lines, which supports that GB can have “phase-like” behavior. Meanwhile, some GBs exhibit

continuous complexion transitions in many other materials, such as Cu-Ag [23, 47, 48], Cu-Zr [49], Al-Ga (see Chapter 5) systems, *etc*. In both cases, constructing GB properties diagrams as a function of temperature and bulk composition can be broadly useful.

However, developing GB properties diagram remain challenge for both experiments and computational simulation. On one hand, advance electron microscopy, such as aberration corrected scanning transmission electron microscopy (AC STEM) [22, 36, 37] and atom probe tomography (APT) [50-52] can be used to characterize atomic-level GB structures . However, the sample preparation and experimental procedure are highly complex and time-consuming even for study a small number of GBs at one given thermodynamic condition. On the contrary, a GB property diagram was generally interpolated from tens of GB states at different temperature and composition [45, 46]. Thus, constructing GB by using experimental tool is almost impossible.

On the other hands, computational modeling has been broadly used to develop GB property diagrams. Specifically, the classical thermodynamic and lattice-type models have been used to construct GB diagrams as a function of temperature and composition [29, 41, 43, 53]. However, these models are either phenomenological or highly simplified, meaning that they cannot capture the atomistic details of GB structures. Later, first-principle calculations combined with cluster-expansion method was adopted to develop the interfacial diagram of WC-Co system [54], but only a few atomic configurations were investigated. Recently, the large-scale molecular dynamic (MD) and hybrid Monte Carlo/molecular

dynamic (MC/MD) simulations were used to develop GB diagrams as a function of temperature and composition [45, 46], but most of studies surveyed either symmetric tilt or twist GBs. The more general GBs, which are ubiquitous in polycrystalline materials and often weak links chemically and mechanically, are hitherto scarcely studied.

Furthermore, five macroscopic DOFs of a GB associated with temperature and composition make it a mission impossible to develop GB diagrams in 7D space by using any conventional tools and thus motive us to explore more powerful method to address this challenge. Recently, some advance computational methods, such as genetic algorithm (GA) [19, 45], evolutional algorithm [55, 56], Bayesian optimization [57], and machine learning (ML) [58-62], combined with high-throughput calculations [18], data mining [63], and virtual screening [64] have been used to investigate GB properties under certain temperature or chemical potential, e.g., GB energy at 0 K [18, 62], but seldom are used to develop GB diagrams. Besides, most of these studies still focus on the special GBs such as symmetric tilt and twist GBs, but little for general GBs. Thus, this dissertation also aims to develop advanced computational techniques that can be used to predict GB property diagrams as a function of five DOFs for any type GBs.

More interestingly, a new class of materials called high-entropy alloys (HEAs) [65-69], also known as multi-principle elemental alloys (MPEAs) [70] or complex concentrated alloys (CCA) [71], have attracted worldwide interest owing to optimal mechanical and functional performances. Generally, HEAs contain five or more consecutive metallic elements [65-69] and thus four (at least) independent

compositional DOFs associate with temperature make it also impossible to map out all HEA GB states and properties in 5D space. Therefore, one motivation of this dissertation is to develop GB diagrams for HEAs.

Indeed, all abovementioned GB diagrams are mainly constructed for GB structural properties, such as GB excess of adsorption, excess of disorder, and free volume [23, 45, 46], but they are seldom developed for functional properties. In this dissertation, the author also aims to construct GB mechanical properties diagrams, such as fracture toughness and ultimate tensile strength. These novel GB diagrams based on mechanical performance are believed to be highly useful to optimize mechanical performance of polycrystalline materials.

1.4. Motivation and Overview

The motivation of this dissertation is applying multiscale modeling, e.g., hybrid MC/MD simulations, first-principles calculation, and *ab initio* MD simulation, to study the general GBs that are more ubiquitous in polycrystalline materials. First, this dissertation aims to develop GB property diagrams as the important materials science tool. Second, this dissertation aims to apply more advance computational methods to address the challenge of five DOFs of GB and large compositional space of HEAs. Finally, this dissertation aims to decipher the fundamental mechanism of GB segregation, expand our basic knowledge of segregation, and enrich segregation theories.

In **Chapter 2**, the hybrid MC/MD simulation was performed to develop GB diagrams of Si-Au binary system. Notably, the simulations revealed the occurrence

of first-order phase-like adsorption transformations in Au-doped Si twist GB at low temperature, which become continuous at high temperatures above a GB critical point. The predicted first-order GB transformations from nominally “clean” GBs to bilayer adsorption of Au are supported by a prior experiment. The hexagonal Au segregation pattern predicted by MC/MD simulations was further verified by first-principle calculations. The maps of differential charge density revealed that strong charge transfer at Au-doped Si GB.

In **Chapter 3**, by combining isobaric semi-grand canonical ensemble hybrid MC/MD simulation with genetic algorithm (GA) and deep neural networks (DNN) models, GB property diagrams can be predicted as a function of five crystallographic DOFs with temperature and bulk composition in 7D space. The DNN prediction is ~10^8 faster than atomistic simulations, thereby enabling the construction of the property diagrams for millions of distinctly different GBs of five DOFs. Notably, the excellent prediction accuracies can be achieved not only for symmetric tilt and twist GBs, but also for asymmetric tilt and mixed GBs; the latter are seldom studied but more ubiquitous in polycrystalline materials. This data-driven prediction of GB diagrams in 7D space opens new paradigm.

In **Chapter 4**, by combining high-throughput MC/MD simulations and artificial neural networks (ANN), we can predict GB properties of HEA, e.g., CrMnFeCoNi, as a function of four independent compositional DOFs and temperature in a 5D space. Furthermore, systematical MC/MD simulations reveal the GB segregation behavior in HEAs that cannot be predicted from classical models; for example, the site competition in more ordered GB leads to weak

segregation in medium-entropy alloys, while the segregation of multiple elements coupled with GB disordering can induce strong co-segregations in HEAs. Finally, a physics-informed model was developed for the GB segregation in HEA. This study not only provides a new paradigm to predict GB properties of HEAs in a 5D space, but also reveal the new coupled segregation and disordering effects in HEA.

In **Chapter 5**, using Al-Ga binary system as one model, the hybrid MC/MD simulations were used to develop GB structural properties diagrams, e.g., GB excess of adsorption, disorder, free volume, for an asymmetric GB. Furthermore, two types of GB mechanical properties diagrams, e.g., fracture toughness and ultimate tensile strength, have been constructed as a function of temperature and bulk compositions. Notably, the ductile-to-brittle transition line can be clearly identified on GB diagrams. In addition, a modified Langmuir-Mclean model was developed to predict the GB adsorption property with high accuracy.

In **Chapter 6**, we reveal a highly asymmetric interfacial superstructure at a mixed twist and tilt GB of WC that significantly broadens our understanding of GB segregation structure. Specifically, this interfacial structure is different from all prior experimentally observations for the following aspect. First, the segregation of Ti and Co are asymmetric. Second, the maxima of Ti and Co segregation occur at the off-the-center atomic planes in the opposite sides, separated by a W-rich layer. Third, solution segregation can further induce asymmetric interfacial structural transition. Notably, this unexpected GB structure may not be uncommon and we propose factors favoring their formation. Thus, this study extends our fundamental knowledge of atomic-level GB segregation structures.

In **Chapter 7**, using Bi_2O_3-doped ZnO as a model, first-principles calculations have been conducted to verify the experimentally proposed new mechanism of reduction-induced interfacial ordering. The DFT-optimized structures agree with AC STEM, including quantitative comparisons of order/disorder, interfacial width, and layered structures. Further, a generalized thermodynamic model supported by DFT calculations was proposed, which explains the physical origin of reduction-induced GB disorder-order transition. The *ab initio* MD simulations were performed and further revealed the increased GB diffusivities in the reduced and ordered GB, which explained the increased GB mobility and abnormal grain growth observed in experiment. Finally, DFT-calculated charge density difference and Bader charge analysis decipher the underlying mechanism of why reduced GB have increased kinetics.

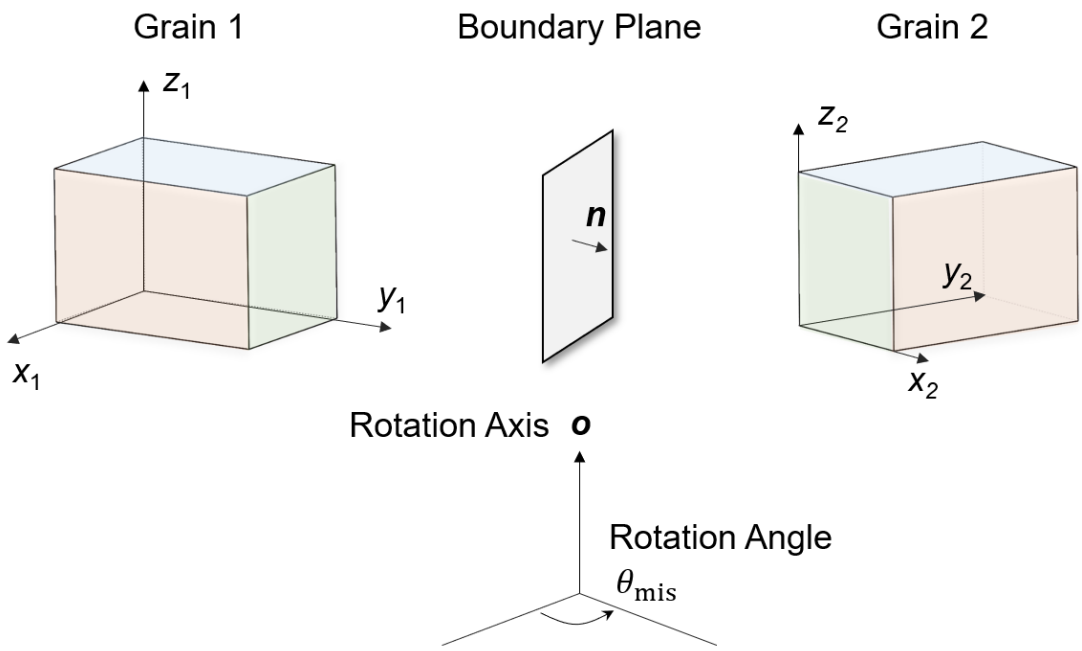

Figure 1.1 Schematic diagram of Grain boundary description. The x_1, y_1, z_1 and x_2, y_2, z_2 are the axes in the coordination of grain 1 and grain 2. ***n*** is the orientation of boundary plane of A and B. The rotation axis is ***o*** and rotation angle of misorientation is θ_{mis}.

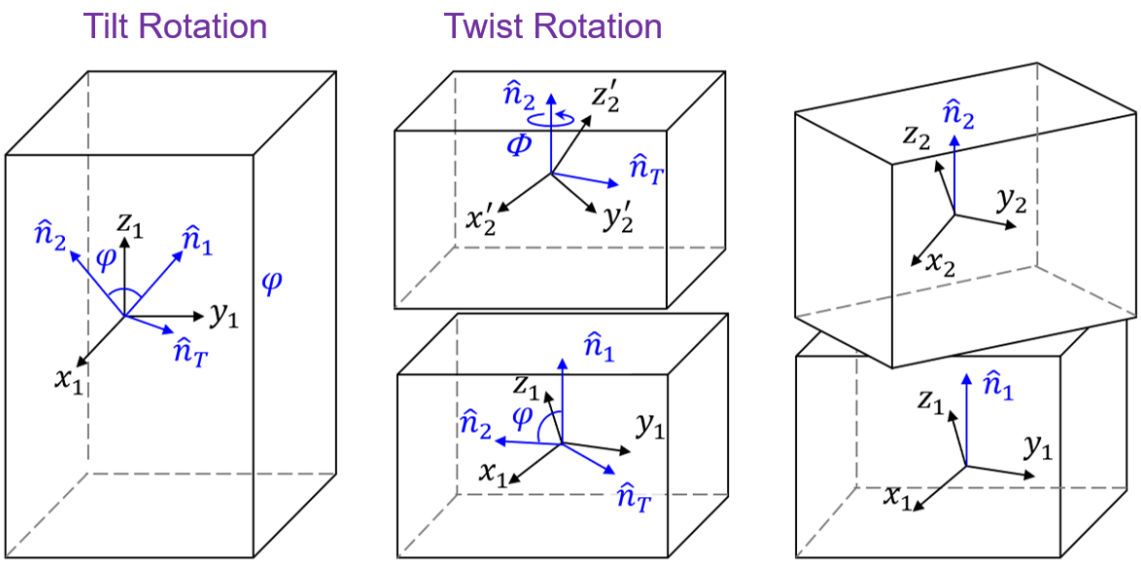

Figure 1.2 Schematic diagram showing that one coincident-site-lattice (CSL) GBs can be decomposed into one tilt rotation plus one twist rotation.

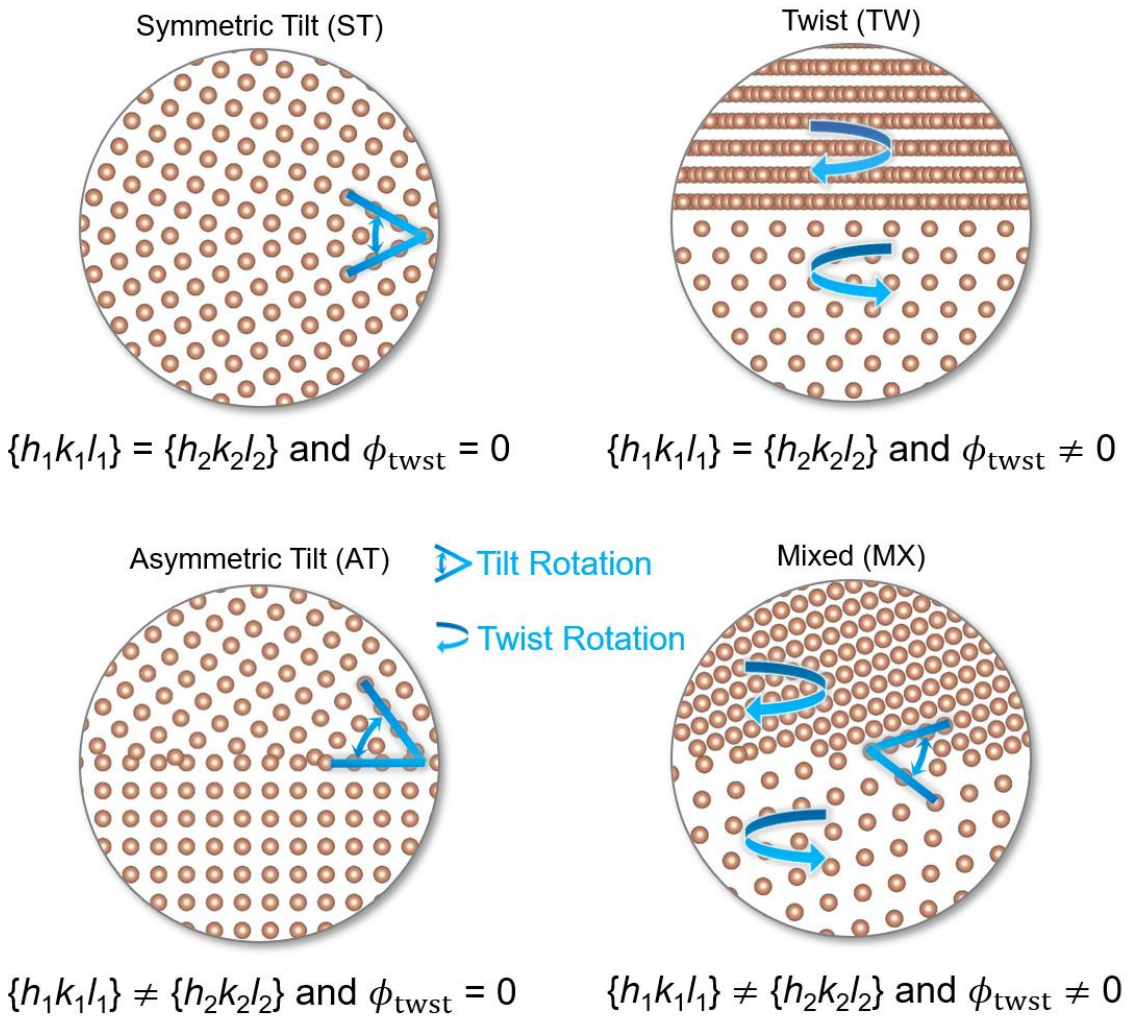

Figure 1.3 Schematic diagrams of four types GB structures: symmetric tilt, twist, asymmetric tilt, and mixed tilt-twist (random) GB.

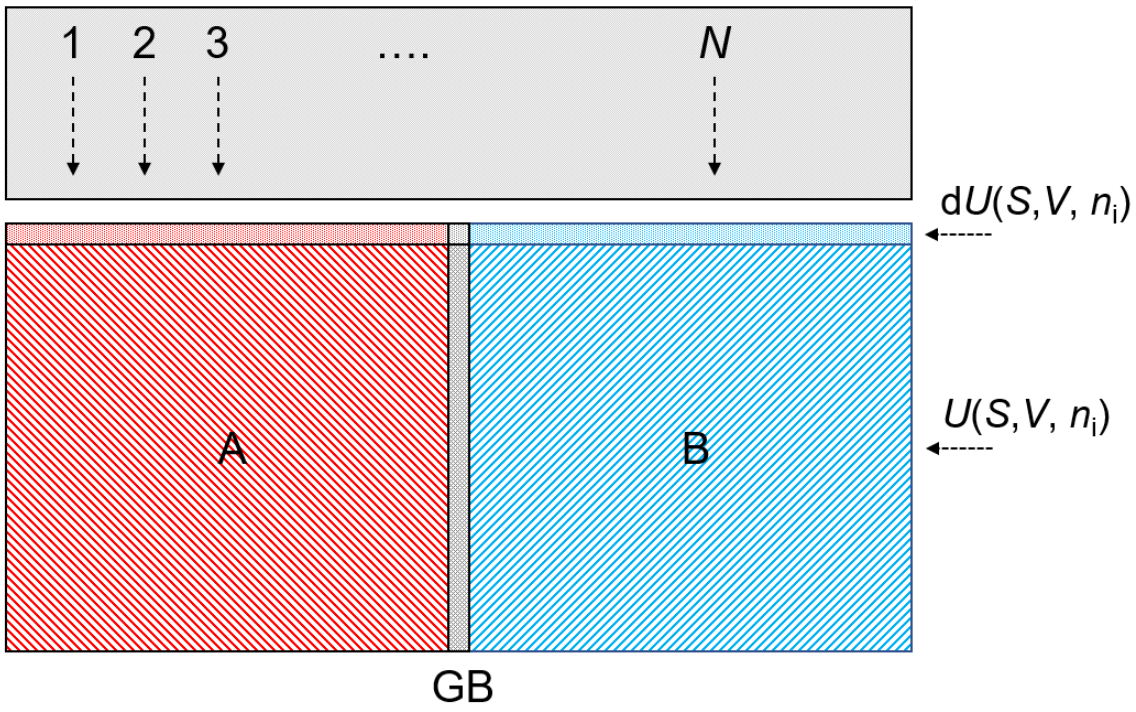

Figure 1.4 Schematic diagram of introducing the grain boundary energy based on a growing bicrystal model.

References

[1] D. McLean, Grain Boundaries in Metals, Oxford, Clarendon Press, (1957).

[2] P. Lejček, Grain Boundaries: Description, Structure and Thermodynamics, in: P. Lejcek (Ed.) Grain Boundary Segregation in Metals, Springer Berlin Heidelberg, Berlin, Heidelberg, 2010, pp. 5-24.

[3] P. Lejček, S. Hofmann, Thermodynamics and structural aspects of grain boundary segregation, Critical Reviews in Solid State and Materials Sciences, 20 (1995) 1-85.

[4] E.M. Lehockey, G. Palumbo, P. Lin, A.M. Brennenstuhl, On the relationship between grain boundary character distribution and intergranular corrosion, Scripta Materialia, 36 (1997) 1211-1218.

[5] R.Z. Valiev, V.Y. Gertsman, O.A. Kaibyshev, Grain boundary structure and properties under external influences, physica status solidi (a), 97 (1986) 11-56.

[6] P. Lejček, M. Šob, V. Paidar, Interfacial segregation and grain boundary embrittlement: An overview and critical assessment of experimental data and calculated results, Progress in Materials Science, 87 (2017) 83-139.

[7] J. Han, S.L. Thomas, D.J. Srolovitz, Grain-boundary kinetics: A unified approach, Progress in Materials Science, 98 (2018) 386-476.

[8] U. Krupp, Dynamic Embrittlement — Time–dependent Quasi–brittle Intergranular Fracture at High Temperatures, International Materials Reviews, 50 (2005) 83-97.

[9] A. Kwiatkowski da Silva, R.D. Kamachali, D. Ponge, B. Gault, J. Neugebauer, D. Raabe, Thermodynamics of grain boundary segregation, interfacial spinodal and their relevance for nucleation during solid-solid phase transitions, Acta Materialia, 168 (2019) 109-120.

[10] M. Všianská, M. Šob, The effect of segregated sp-impurities on grain-boundary and surface structure, magnetism and embrittlement in nickel, Progress in Materials Science, 56 (2011) 817-840.

[11] P. Wynblatt, Interfacial Segregation Effects in Wetting Phenomena, Annual Review of Materials Research, 38 (2008) 173-196.

[12] H. Grimmer, W. Bollmann, D.H. Warrington, Coincidence-site lattices and complete pattern-shift in cubic crystals, Acta Crystallographica Section A, 30 (1974) 197-207.

[13] H. Grimmer, The generating function for coincidence site lattices in the cubic system, Acta Crystallographica Section A, 40 (1984) 108-112.

[14] V. Paidar, A classification of symmetrical grain boundaries, Acta Metallurgica, 35 (1987) 2035-2048.

[15] D. Wolf, J.F. Lutsko, On the geometrical relationship between tilt and twist grain boundaries, Zeitschrift für Kristallographie - Crystalline Materials, 189 (1989) 239-262.

[16] A. Morawiec, K. Glowinski, On “macroscopic” characterization of mixed grain boundaries, Acta Materialia, 61 (2013) 5756-5767.

[17] D. Wolf, Structure-energy correlation for grain boundaries in F.C.C. metals—I. Boundaries on the (111) and (100) planes, Acta Metallurgica, 37 (1989) 1983-1993.

[18] H. Zheng, X.-G. Li, R. Tran, C. Chen, M. Horton, D. Winston, K.A. Persson, S.P. Ong, Grain boundary properties of elemental metals, Acta Materialia, 186 (2020) 40-49.

[19] A.L.S. Chua, N.A. Benedek, L. Chen, M.W. Finnis, A.P. Sutton, A genetic algorithm for predicting the structures of interfaces in multicomponent systems, Nature Materials, 9 (2010) 418-422.

[20] B. Feng, T. Yokoi, A. Kumamoto, M. Yoshiya, Y. Ikuhara, N. Shibata, Atomically ordered solute segregation behaviour in an oxide grain boundary, Nature Communications, 7 (2016) 11079.

[21] T. Meiners, T. Frolov, R.E. Rudd, G. Dehm, C.H. Liebscher, Observations of grain-boundary phase transformations in an elemental metal, Nature, 579 (2020) 375-378.

[22] Z. Yu, P.R. Cantwell, Q. Gao, D. Yin, Y. Zhang, N. Zhou, G.S. Rohrer, M. Widom, J. Luo, M.P. Harmer, Segregation-induced ordered superstructures at general grain boundaries in a nickel-bismuth alloy, Science, 358 (2017) 97.

[23] C. Hu, Y. Zuo, C. Chen, S. Ping Ong, J. Luo, Genetic algorithm-guided deep learning of grain boundary diagrams: Addressing the challenge of five degrees of freedom, Materials Today, (2020).

[24] T. Tadros, Gibbs Adsorption Isotherm, in: T. Tadros (Ed.) Encyclopedia of Colloid and Interface Science, Springer Berlin Heidelberg, Berlin, Heidelberg, 2013, pp. 626-626.

[25] J.W. Cahn, Thermodynamics of Solid and Fluid Surfaces, in: The Selected Works of John W. Cahn, 1998, pp. 377-378.

[26] J. Luo, H. Cheng, K.M. Asl, C.J. Kiely, M.P. Harmer, The Role of a Bilayer Interfacial Phase on Liquid Metal Embrittlement, Science, 333 (2011) 1730-1733.

[27] R.F. Klie, J.P. Buban, M. Varela, A. Franceschetti, C. Jooss, Y. Zhu, N.D. Browning, S.T. Pantelides, S.J. Pennycook, Enhanced current transport at grain boundaries in high-Tc superconductors, Nature, 435 (2005) 475-478.

[28] E.W. Hart, Two-dimensional phase transformation in grain boundaries, Scripta Metallurgica, 2 (1968) 179-182.

[29] M. Tang, W.C. Carter, R.M. Cannon, Grain Boundary Transitions in Binary Alloys, Physical Review Letters, 97 (2006) 075502.

[30] Y. Mishin, W.J. Boettinger, J.A. Warren, G.B. McFadden, Thermodynamics of grain boundary premelting in alloys. I. Phase-field modeling, Acta Materialia, 57 (2009) 3771-3785.

[31] R. Kikuchi, J.W. Cahn, Grain boundaries with impurities in a two-dimensional lattice-gas model, Physical Review B, 36 (1987) 418-428.

[32] P.R. Cantwell, M. Tang, S.J. Dillon, J. Luo, G.S. Rohrer, M.P. Harmer, Grain boundary complexions, Acta Materialia, 62 (2014) 1-48.

[33] S.J. Dillon, M. Tang, W.C. Carter, M.P. Harmer, Complexion: A new concept for kinetic engineering in materials science, Acta Materialia, 55 (2007) 6208-6218.

[34] P.R. Cantwell, T. Frolov, T.J. Rupert, A.R. Krause, C.J. Marvel, G.S. Rohrer, J.M. Rickman, M.P. Harmer, Grain Boundary Complexion Transitions, Annual Review of Materials Research, (2020).

[35] A.R. Krause, P.R. Cantwell, C.J. Marvel, C. Compson, J.M. Rickman, M.P. Harmer, Review of grain boundary complexion engineering: Know your boundaries, Journal of the American Ceramic Society, 102 (2019) 778-800.

[36] T. Hu, S. Yang, N. Zhou, Y. Zhang, J. Luo, Role of disordered bipolar complexions on the sulfur embrittlement of nickel general grain boundaries, Nature Communications, 9 (2018) 2764.

[37] S. Ma, P.R. Cantwell, T.J. Pennycook, N. Zhou, M.P. Oxley, D.N. Leonard, S.J. Pennycook, J. Luo, M.P. Harmer, Grain boundary complexion transitions in WO3- and CuO-doped TiO2 bicrystals, Acta Materialia, 61 (2013) 1691-1704.

[38] S.G. Kim, Y.B. Park, Grain boundary segregation, solute drag and abnormal grain growth, Acta Materialia, 56 (2008) 3739-3753.

[39] D. Raabe, M. Herbig, S. Sandlöbes, Y. Li, D. Tytko, M. Kuzmina, D. Ponge, P.P. Choi, Grain boundary segregation engineering in metallic alloys: A pathway to the design of interfaces, Current Opinion in Solid State and Materials Science, 18 (2014) 253-261.

[40] E. Senel, J.C. Walmsley, S. Diplas, K. Nisancioglu, Liquid metal embrittlement of aluminium by segregation of trace element gallium, Corrosion Science, 85 (2014) 167-173.

[41] P. Wynblatt, D. Chatain, Solid-state wetting transitions at grain boundaries, Materials Science and Engineering: A, 495 (2008) 119-125.

[42] J. Luo, H. Wang, Y.-M. Chiang, Origin of Solid-State Activated Sintering in Bi2O3-Doped ZnO, Journal of the American Ceramic Society, 82 (1999) 916-920.

[43] J. Luo, Developing Interfacial Phase Diagrams for Applications in Activated Sintering and Beyond: Current Status and Future Directions, Journal of the American Ceramic Society, 95 (2012) 2358-2371.

[44] L.S. Chang, E. Rabkin, B.B. Straumal, B. Baretzky, W. Gust, Thermodynamic aspects of the grain boundary segregation in Cu(Bi) alloys, Acta Materialia, 47 (1999) 4041-4046.

[45] S. Yang, N. Zhou, H. Zheng, S.P. Ong, J. Luo, First-Order Interfacial Transformations with a Critical Point: Breaking the Symmetry at a Symmetric Tilt Grain Boundary, Physical Review Letters, 120 (2018) 085702.

[46] C. Hu, J. Luo, First-order grain boundary transformations in Au-doped Si: Hybrid Monte Carlo and molecular dynamics simulations verified by first-principles calculations, Scripta Materialia, 158 (2019) 11-15.

[47] R.K. Koju, Y. Mishin, Relationship between grain boundary segregation and grain boundary diffusion in Cu-Ag alloys, Physical Review Materials, 4 (2020) 073403.

[48] P.L. Williams, Y. Mishin, Thermodynamics of grain boundary premelting in alloys. II. Atomistic simulation, Acta Materialia, 57 (2009) 3786-3794.

[49] Z. Pan, T.J. Rupert, Effect of grain boundary character on segregation-induced structural transitions, Physical Review B, 93 (2016) 134113.

[50] T. Yang, Y.L. Zhao, W.P. Li, C.Y. Yu, J.H. Luan, D.Y. Lin, L. Fan, Z.B. Jiao, W.H. Liu, X.J. Liu, J.J. Kai, J.C. Huang, C.T. Liu, Ultrahigh-strength and ductile superlattice alloys with nanoscale disordered interfaces, Science, 369 (2020) 427-432.

[51] M. Herbig, D. Raabe, Y.J. Li, P. Choi, S. Zaefferer, S. Goto, Atomic-Scale Quantification of Grain Boundary Segregation in Nanocrystalline Material, Physical Review Letters, 112 (2014) 126103.

[52] N.J. Peter, T. Frolov, M.J. Duarte, R. Hadian, C. Ophus, C. Kirchlechner, C.H. Liebscher, G. Dehm, Segregation-Induced Nanofaceting Transition at an

Asymmetric Tilt Grain Boundary in Copper, Physical Review Letters, 121 (2018) 255502.

[53] N. Zhou, Z. Yu, Y. Zhang, M.P. Harmer, J. Luo, Calculation and validation of a grain boundary complexion diagram for Bi-doped Ni, Scripta Materialia, 130 (2017) 165-169.

[54] S.A.E. Johansson, G. Wahnström, First-principles study of an interfacial phase diagram in the V-doped WC-Co system, Physical Review B, 86 (2012) 035403.

[55] Q. Zhu, A. Samanta, B. Li, R.E. Rudd, T. Frolov, Predicting phase behavior of grain boundaries with evolutionary search and machine learning, Nature Communications, 9 (2018) 467.

[56] C. Yang, M. Zhang, L. Qi, Grain boundary structure search by using an evolutionary algorithm with effective mutation methods, Computational Materials Science, 184 (2020) 109812.

[57] S. Kikuchi, H. Oda, S. Kiyohara, T. Mizoguchi, Bayesian optimization for efficient determination of metal oxide grain boundary structures, Physica B: Condensed Matter, 532 (2018) 24-28.

[58] L. Huber, R. Hadian, B. Grabowski, J. Neugebauer, A machine learning approach to model solute grain boundary segregation, npj Computational Materials, 4 (2018) 64.

[59] J.A. Gomberg, A.J. Medford, S.R. Kalidindi, Extracting knowledge from molecular mechanics simulations of grain boundaries using machine learning, Acta Materialia, 133 (2017) 100-108.

[60] E.R. Homer, D.M. Hensley, C.W. Rosenbrock, A.H. Nguyen, G.L.W. Hart, Machine-Learning Informed Representations for Grain Boundary Structures, Frontiers in Materials, 6 (2019).

[61] T.A. Sharp, S.L. Thomas, E.D. Cubuk, S.S. Schoenholz, D.J. Srolovitz, A.J. Liu, Machine learning determination of atomic dynamics at grain boundaries, Proceedings of the National Academy of Sciences, 115 (2018) 10943-10947.

[62] T. Tamura, M. Karasuyama, R. Kobayashi, R. Arakawa, Y. Shiihara, I. Takeuchi, Fast and scalable prediction of local energy at grain boundaries: machine-learning based modeling of first-principles calculations, Modelling and Simulation in Materials Science and Engineering, 25 (2017) 075003.

[63] S. Kiyohara, T. Mizoguchi, Effective search for stable segregation configurations at grain boundaries with data-mining techniques, Physica B: Condensed Matter, 532 (2018) 9-14.

[64] S. Kiyohara, H. Oda, T. Miyata, T. Mizoguchi, Prediction of interface structures and energies via virtual screening, Science Advances, 2 (2016) e1600746.

[65] Y.F. Ye, Q. Wang, J. Lu, C.T. Liu, Y. Yang, High-entropy alloy: challenges and prospects, Materials Today, 19 (2016) 349-362.

[66] E.P. George, D. Raabe, R.O. Ritchie, High-entropy alloys, Nature Reviews Materials, 4 (2019) 515-534.

[67] M.-H. Tsai, J.-W. Yeh, High-Entropy Alloys: A Critical Review, Materials Research Letters, 2 (2014) 107-123.

[68] B.S. Murty, J.W. Yeh, S. Ranganathan, Chapter 6 - High-Entropy Alloy Solid Solutions, in: B.S. Murty, J.W. Yeh, S. Ranganathan (Eds.) High Entropy Alloys, Butterworth-Heinemann, Boston, 2014, pp. 91-118.

[69] D.B. Miracle, O.N. Senkov, A critical review of high entropy alloys and related concepts, Acta Materialia, 122 (2017) 448-511.

[70] O.N. Senkov, J.D. Miller, D.B. Miracle, C. Woodward, Accelerated exploration of multi-principal element alloys with solid solution phases, Nature Communications, 6 (2015) 6529.

[71] S. Gorsse, J.-P. Couzinié, D.B. Miracle, From high-entropy alloys to complex concentrated alloys, Comptes Rendus Physique, 19 (2018) 721-736.

[72] S.-J.L. Kang, Sintering: densification, grain growth and microstructure, Elsevier, 2004.

Chapter 2. First-Order Grain Boundary Adsorption Transition in Au-Doped Si Binary System

2.1. Introduction

The physical properties of polycrystalline materials can be significantly altered by adsorption (a.k.a. segregation) of alloying elements or impurities at grain boundaries (GBs) [1-3]. Moreover, GB can exhibit phase-like behaviors [4-8]. A term “complexions” was introduced to describe the interfacial phases that are thermodynamically 2-D (despite having an effective thickness and through-thickness compositional and structural gradients), to differentiate them from thin layers of thermodynamically 3-D (bulk) Gibbs phases present at interfaces; notably, Dillon et al. catalogued six types of GB complexions [4, 5].

Similar to bulk phase diagrams, we may construct GB diagrams to represent the stability of 2-D interfacial phases (complexions) as functions of bulk composition and temperature [5, 6, 9]. Recently, bulk CALPHAD (CALculation of PHAse Diagrams) methods have been extended to GBs to construct GB λ diagrams [10-13], which have been successfully used to predict high-temperature GB disordering and related GB-controlled sintering behaviors [10, 11, 13-16]. Furthermore, diffuse-interface [9, 17, 18] and lattice-type [19-22] models have been used to compute more rigorous GB phase/complexion diagrams with first-order transition lines and critical points.

To further reveal atomic-level structural details underlying interfacial transformations, molecular dynamics (MD) simulations and density functional theory (DFT) calculations have been used. Notably, Frolov et al. applied MD and semi-grand canonical Monte Carlo (MC) simulations to investigate GB structural transformations in pure and Ag-doped Cu [23-25]. Pan et al. carried out hybrid MC/MD simulations to study segregation-induced structural transformation in Zr-doped Cu [26]. Johansson et al. also used a DFT based cluster-expansion method to construct interfacial phase diagram for V-doped WC-Co hetero-phase interface [27]. In one recent study, Yang et al. combined genetic algorithm (GA) with hybrid MC/MD simulations in semi-grand canonical ensembles to construct a GB phase (complexion) diagram for the Σ5 (210) tilt GB in Ni-doped Mo, with a first-order transition line ending at a GB critical point [28]. Moreover, the semi-grand-canonical-ensemble simulations also reveal that the first-order GB transitions break the mirror symmetry of the title GB, representing a new interfacial phenomenon discovered by atomistic simulations.

Yet, most previous studies investigated GB structures with relatively small Σ values, whereas more general GBs are prevailing in real polycrystals and can often be weak mechanically and chemically. In a prior experiment study [29], Ma et al. revealed that twist Au-doped Si Σ43 GB exhibited an abrupt transition from “clean” GB to a bilayer adsorption of Au. However, the atomic-level details of this Au-based bilayer and its stability as a function of temperature and bulk composition have not been revealed. Motivated by this experimental observation [29], herein

we combined hybrid MC/MD simulations and first-principles DFT calculations to characterize Au-doped Si Σ43 and Σ21 twist GBs, and subsequently construct a GB phase diagram with a first-order transformation line and a GB critical point.

2.2. Computational Methods

2.2.1. Hybrid MC/MD Simulation

The initial undoped Σ43 GB containing 41264 atoms with a twist angle 15^{o} (matching that adopted in a prior experiment [29]) was constructed by using GBstudio [30]. An angular-dependent potential (ADP) recently developed from ab initio calculations by Starikov et al. was adopted for simulating the Si-Au binary system [31]. To test this ADP, we first calculated the Si melting temperature (T_m) and the Si-Au bulk phase diagram. The calculated T_m of the pure Si is around 1325 K, which is consistent with the value obtained by Starikov et al. (~1390 K), but smaller than experimental value of 1689 K [32]. Yet, Starikov et al. showed that this potential is precise enough to predict the interatomic behaviors of the Si-Au binary system in liquid, amorphous, and solid phases. Consistently, the liquidus line in our calculated phase diagram match well with experiment, though the solid solubilities of Au in Si obtained are higher. For convenience, we normalize temperature to the calculated T_m of Si and bulk composition (X_{Au}) to the maximum solid solubility from the simulation ($X_{\text{Max Solubility}}$) for the calculations.

2.2.2. First-Principles Calculations

The DFT calculations were performed using the Vienna ab initio simulation package (VASP) [33, 34]. The Kohn-Sham equations were solved with the projector-augmented wave (PAW) method [35]. The semi-local Perdew-Burke-Ernzerhof (PBE) exchange-correlation functional [36, 37] was adopted for structural optimization until the Hellmann-Feynman forces were smaller than 10^{-2} eV/Å. Both lattice parameters and atomic positions were allowable to relax for the undoped Si Σ21 GB; but we fixed these optimized lattice parameters and only optimized atomic positions for Au substitutions for Au-doped Si. The Brillouin-zone integrations were performed on Γ-centered 1×1×1 *k*-point grid due to the large crystal structures. The kinetic energy cutoff was set to 400 eV, and the "accurate" precision settings was adopted to avoid wrap-around errors. The spin polarization was considered for all calculations.

2.3. Results and Discussion

2.3.1. Hybrid MC/MD Simulation on Au-Doped Si Twist GB

Fig. 2.1(a) shows a simulated atomic structure of an undoped Si twist Σ43 GB relaxed by MD at 0.75 Tm. An associated simulated STEM high-angle annual dark-field (HAADF) micrograph is displayed in Fig. 2.1(b), which agree well with experimental STEM HAADF image shown in Fig. 2.1(c) from Ref. [29]. The atomic structure of an Au-doped Si Σ43 GB obtained via hybrid MC/MD simulation (at T = 0.60 T_m and $\Delta\mu = -0.3\ eV$) is displayed in Fig. 2.1(d). The Au atomic distribution

along z direction (c.f. inset in Fig. 2.1(d)) shows that most Au atoms (represented by red dots in Fig. 2.1(d)) segregate at the GB with a bilayer-like distribution, which matches two bright fringes in the simulated (Fig. 2.1(e)) and experimental (Fig. 2.1(f)) STEM HAADF images. The different contrasts in simulated and experimental HAADF images may be due to the different specimen thickness and STEM conditions; nonetheless, both of them exhibit two bright fringes as signatures of the Au-based bilayers (indicated by red arrows in Fig. 2.1).

2.3.2. First-Order Grain Boundary Adsorption Transition

To quantitively investigate possible adsorption transitions, we calculated GB excess of Au solute (i.e., the amount of adsorption, Γ_{Au}) as a function of normalized temperature and composition. Fig. 2.2(a) shows a GB adsorption map at the high temperature range from 0.53-0.83 T_m. Fig. 2.2(b) further shows a close-up of the low-temperature, low-Au-content region of the adsorption map, with a first-order line that ends at a GB critical point at ~0.33 T_m. The occurrence of first-order adsorption transitions can be clearly evident in the Γ_{Au} vs. normalized X_{Au} curves at T = 0.23 T_m and 0.30 T_m, respectively (Fig. 2.2(c)). The transition becomes continuous at high temperatures (above the GB critical point), as illustrated, e.g., in the adsorption isotherms at T = 0.53 T_m and 0.60 T_m (Fig. 2.2(c)). Indeed, this predicted first-order adsorption transition is supported by prior experimental observation; specifically, the inset in Fig. 2.2(c) is a STEM HAADF image showing an abrupt transition from Au bilayer adsorption to “clean” GB evident in a prior experimental study.

2.3.3. Common Neighbor Analysis for Au Segregation Structure

To further explore structural details on the Au bilayer adsorption, we performed common neighbor analysis (CNA) to investigate Si cubic diamond (CD) structures by using the OVITO software [38]. The simulated atomic structure by hybrid MC/MD simulation at T = 0.60 T_{m} and $\Delta\mu = -0.3\ e\mathrm{V}$ and the associated simulated STEM HAADF image of a Au-doped Si Σ43 GB are shown in Fig. 2.3(a) and 3(b), respectively. The CNA results displayed in Fig. 2.3(c) show that the atoms in simulated Σ43 GB structure mainly follow one of the three different types of structural orders: (*i*) the bulk-like CD order, (*ii*) the CD^{1st} structural order, which is defined as the atoms that preserve all the 1st nearest neighbors atoms but at least one of 2nd nearest neighbors does not follow the bulk structure), and (*iii*) the CD^{2nd} structural order, which is defined as the atoms with at least one of (1st) neighbors atoms is missing or does not the CD structure. By plotting the relative fractions of the CD^{1st} and CD^{2nd} type atoms along z-direction, Fig. 2.3(c) shows that these two types of boundary structural orders mainly exist in the two atom planes at the twist GB core, coincident the spatial distribution of the adsorbed Au bilayers. This can be further illustrated by plotting the decomposed Au adsorption maps according to these two type of boundary structural orders (Fig. 2.4), where the number of the CD^{2nd} type adsorbed Au atoms are much greater than that of the CD^{1st} type. In other words, most adsorbed Au atoms have the CD^{2nd} type structural order.

2.3.4. First-Principles Calculations on Au Hexagonal Segregation Pattern

Furthermore, we performed first-principles density functional theory (DFT) calculations to validate the hybrid MC/MD simulation results. Unfortunately, the minimal cell to simulate Si Σ43 GB structure has ~4000 atoms, which is infeasible for DFT calculations. Thus, we examine a Si Σ21 GB with a twist angle 21.8^{o}, which can reduce to 336 atoms in the minimal (irreducible) cell, enabling affordable DFT calculations. Before conducting DFT calculations, we first applied hybrid MC/MD simulations for a large cell of Si Σ21 GB containing 32256 atoms (containing many irreducible cells for statistic accuracies), to compare with the Σ43 GB, at the identical conditions of T = 0.60 T_m and $\Delta\mu = -0.3\ eV$. The calculated Γ_{Au} is about 2.71 nm^{-2} for the Σ21 GB, on a par with the simulated Γ_{Au} of ~2.36 nm^{-2} of the Σ43 GB at this condition (T = 0.60 T_m and $\Delta\mu = -0.3\ eV$). Moreover, the simulated atomic structures of Σ43 vs. Σ21 GBs show comparable profiles of adsorbed Au atoms as well as the CD^{1st} and the CD^{2nd} types of atoms distributions (Figs. 2.3(c) vs. 3(f)), and simulated STEM HAADF images (Fig. 3(b) vs. Fig. 3(e)) also show similar signature bilayer-like bright fringes. Thus, we conclude the adsorption behaviors at these two GBs are similar and we conduct DFT calculations on the Σ21 GB with a smaller cell.

To construct the initial Au-doped structure for DFT calculations, we first examined the Au segregation (adsorption) structures obtained by the hybrid MC/MD simulation at T = 0.23 T_m and $\Delta\mu = -0.56\ eV$ (near the first-order transformation at 0.23 T_m). Interestingly, both Σ43 and Σ21 GBs exhibit hexagon-

shape Au segregation patterns, as shown the purple hexagons in Figs. 4(a) and 4(b), respectively. By carefully analyzing these adsorbed Au atoms via CNA, we found that around 85~90% Au atoms belong to the CD^{2nd} type. To obtain similar Γ_{Au} values as Σ43 and Σ21 GBs, which are 5.13 nm^{-2} and 5.98 nm^{-2} (Figs. 2.5(a) and 2.5(b)) , respectively, at T = 0.23 T_m and $\Delta\mu = -0.56\ eV$ (that represents the low-temperature bilayer structure, just above the 1st-order adsorption transition), from hybrid MC/MD simulations, we substituted 19 Si atoms by Au at the GB region to obtain a Γ_{Au} value of 5.31 nm^{-2} for DFT calculations (represented by the grey diamond cell in Fig. 2.5(c)). After structural optimization, the hexagon-shape Au segregation pattern survived as the stable structure (Fig. 2.5(c)), matching well with the hybrid MC/MD simulation results (Fig. 2.5(b)). To verify the energetic stability of this structure, we randomly generated 45 different configurations by gradually shifting these 19 Au atoms from CD^{1st} layers to CD^{2nd} layer (see definitions of CD^{1st} and CD^{2nd} layers in Fig. 2.6); the CNA results of DFT optimized GB structure are shown in Figs. 2.5(d) and 2.5(e). The total energies of these configurations as a function of the Au fracture in the CD^{2nd} type (X'_{Au}) are plotted in Fig. 2.5(f); indeed, DFT calculations verified that the Au segregation pattern (Figs. 2.5(b) and 2.5(c)) obtained by the hybrid MC/MD has the lowest energies (represented by the blue dot in Fig. 2.5(f)). It is also worth noting that two Au (out of 19) atoms, initially placed on the CD^{1st} layers, moved to CD^{2nd} layers after structural optimization; hence, we plotted this configuration (blue dot) at X'_{Au} = 1. In addition, Fig. 2.5(f) indicates that total energy tends to decrease by shifting Au

atoms from CD^{1st} to CD^{2nd} layers, indicating that Au atoms more favorably segregate at the CD^{2nd} layers (or with the CD^{2nd}-type structural order).

2.3.5. Differential Charge Density between Au and GBs

By examining the bonding environments at GBs, we found that Au atoms on the CD^{2nd} layers form bonds directly with Si atoms instead of Au atoms on the opposite side of the CD^{2nd} layer. This supports prior simple regular-solution model that stability of Au bilayer can be attributed to strong Si-Au bonding. To gain more insights on interfacial charge transfer, we calculated differential charge density (DCD) by using $\Delta\rho = \rho_{Au@\Sigma21} - \rho_{\Sigma21} - \rho_{Au}$, where $\rho_{Au@\Sigma21}$ is the charge density of the Au-doped Si $\Sigma21$ GB, $\rho_{\Sigma21}$ is the charge density of Si $\Sigma21$, and ρ_{Au} is the charge density of Au. Fig. 2.5(g) is the DCD map for the 19 Au atoms absorbed at the CD1st layers at X'_{Au} = 0 (indicated by the orange arrow in Fig. 2.5(f)); Fig. 2.5(h) is the DCD map the 19 Au atoms absorbed at the CD2nd layers at X'_{Au} = 1 (indicated by the blue arrow in Fig. 2.5(f)). It shows that latter configuration has stronger charge transfer at the GB region compared to the Au substitution at CD^{1st} layers. Hence, it is hypothesized that the strong interfacial charge transfer can enhance the Si-Au bonding to promote Au segregation at Si GBs.

2.4. Conclusions

In conclusion, we applied hybrid MC/MD simulations in semi-grand canonical ensembles to investigate the Au adsorption configuration and associated first-order transformation at twist Si GBs, and further verified them with

first-principles DFT calculations. A first-order (phase-like) adsorption transition was revealed by hybrid MC/MD simulations at low temperatures, which vanishes at a GB critical point and becomes continuous at high temperatures. The DFT calculations have verified that the hexagon-shape Au segregation/adsorption pattern obtained by hybrid MC/MD simulation has the lowest energy. The formation of bilayer adsorption of Au at Si twist GB and the occurrence of first-order GB adsorption transformations are consistent with the prior experimental observation. Additional structural and charge transfer details of Au segregation structure have been revealed by hybrid MC/MD simulations and first-principles DFT calculations.

A GB adsorption diagram has been constructed with a well-defined first-order GB phase-like (complexion) transition line that ends at a GB critical point, extending a recent success of computing GB “phase” (complexion) diagrams with atomistic simulations to another system. This work also represents the first case where the a thermodynamically 2-D interfacial phase or complexion and the associated first-order GB transformations suggested by a prior experiment have been successfully reproduced by semi-grand-canonical-ensemble hybrid MC/MD atomistic simulations, and further verified by first-principles DFT calculations.

Chapter 2, in part, is a reprint of the material “First-Order Interfacial Transition in Si-Au Binary System: Hybrid Monte Carlo and Molecular Dynamics Simulations Verified by First-Principles Calculations”, C. Hu and J. Luo, as it appears in Scripta Materialia, 2019, 158, 11-15. The dissertation author was the primary investigator and first author of this paper.

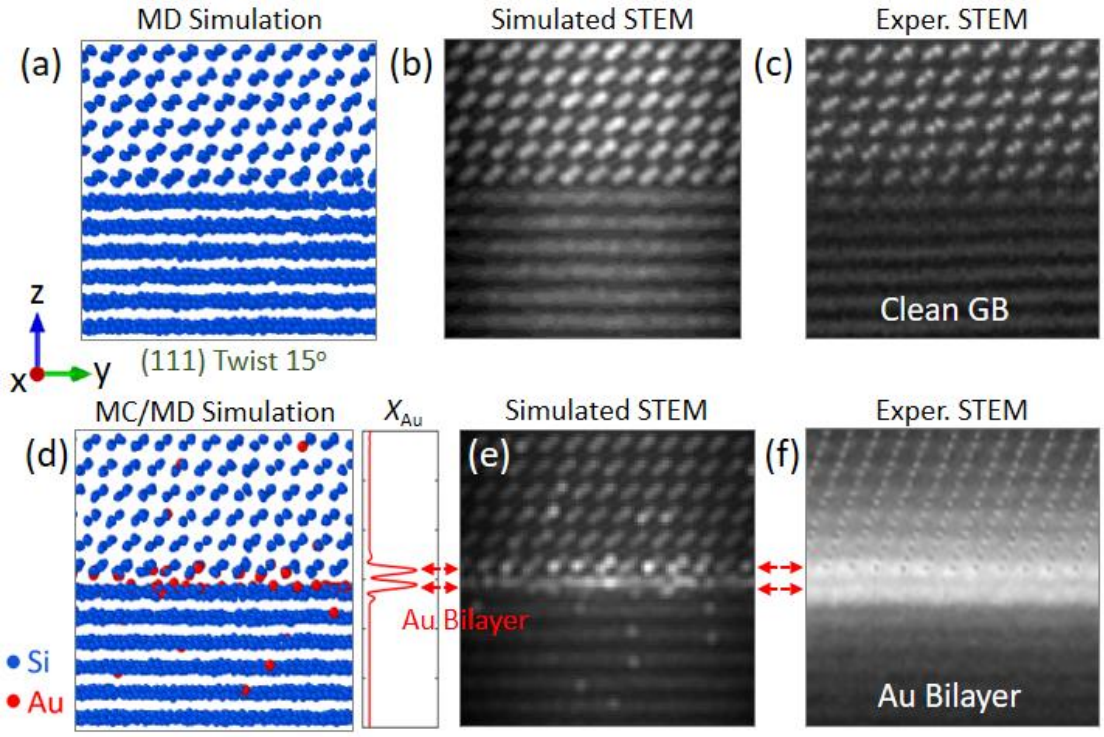

Figure 2.1 (a) The atomic structure of the undoped Si Σ43 GB obtained by MD simulations at $T = 0.75\ T_m$ and (b) associated simulated STEM HAADF micrograph, along with (c) an experimental STEM HAADF micrograph. (d) The atomic structure of the Au-doped Si Σ43 GB obtained by hybrid MC/MD simulation at $T = 0.60\ T_m$ and $\Delta\mu = -0.3\ eV$. The inset is the Au atomic fraction (X_{Au}) averaged along the z direction. (e) A simulated STEM HAADF micrograph from the hybrid MC/MD simulated interfacial structure, and (f) an experimental STEM HAADF micrograph. The brightness and contrast of the experimental micrographs are adjusted to roughly match those of simulated images.

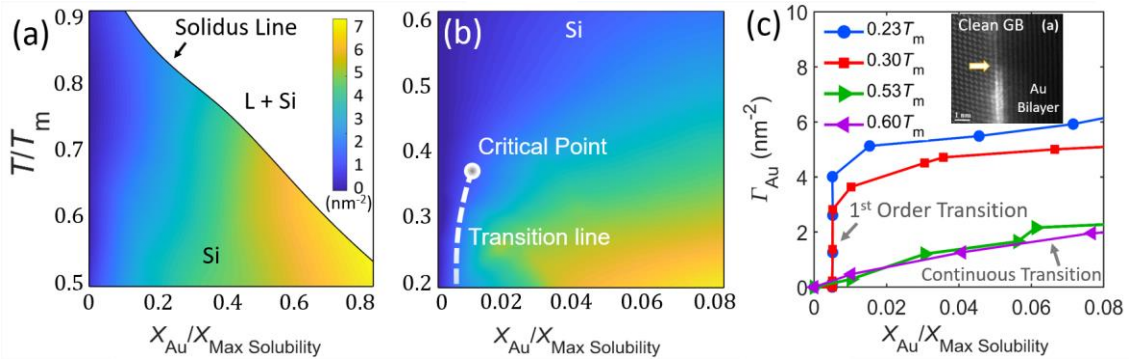

Figure 2.2 The computed maps of GB solute excess (or adsorption) of Au per unit area, Γ_{Au}, in (a) the high-temperature range and (b) the low-temperature range, respectively. The white dashed line in panel (b) indicates first-order phase-like transformations and it ends at a GB critical point. (c) Computed Γ_{Au} *vs*. normalized bulk composition ($X_{\mathrm{Au}}/X_{\mathrm{Max\ Solubility}}$) curves at T = 0.23 T_{m}, 0.30 T_{m}, 0.53 T_{m}, and 0.60 T_{m}., respectively. First-order GB transformations correspond to abrupt jumps in Γ_{Au} at T = 0.23 T_{m} and 0.30 T_{m}. The inset is a STEM HAADF, showing an abrupt transition from an intrinsic (nominally “clean”) GB to bilayer adsorption of Au.

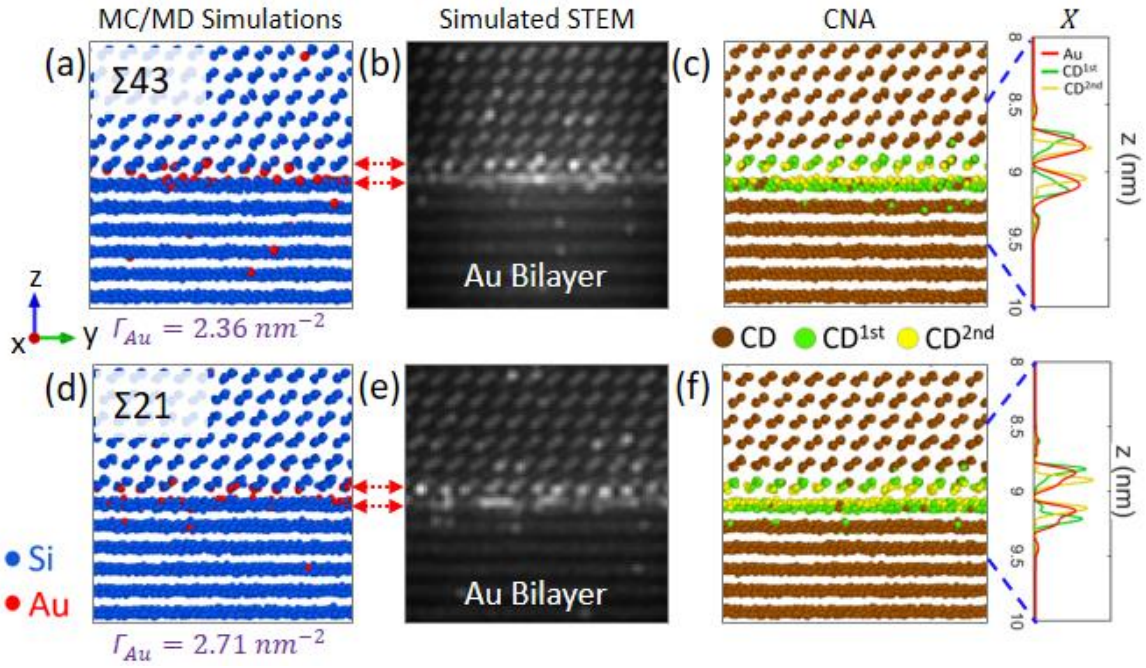

Figure 2.3 Hybrid MC/MD simulations at T = 0.60 T_m and $\Delta\mu = -0.3\ eV$ for (a) a Σ43 GB and (d) a Σ21 GB, simulated STEM HAADF micrographs for the (b) Σ43 and (e) Σ21 GBs, and common neighbor analysis (CNA) results of the (c) Σ43 and (f) Σ21 GBs. The insets are the expanded views of Au atomic fraction profiles, as well as the decomposed compositional profiles for the CD^{1st} and CD^{2nd} type atoms, along the z direction.

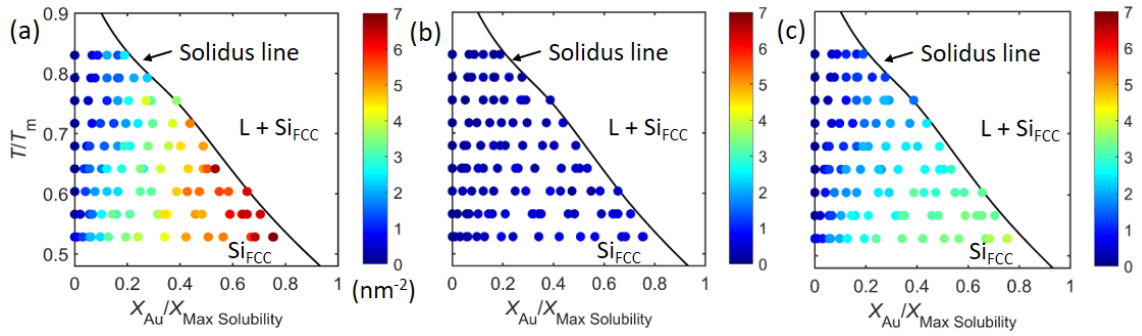

Figure 2.4 (a) A computed GB adsorption diagram representing the total GB excess of Au atoms at the Si Σ43 twist GB as a function of normalized temperature and bulk composition, which are subsequently decomposed into two diagrams to show the adsorption amounts of the Au atoms in (b) the CD^{1st} layer and (c) the CD^{2nd} layer, respectively.

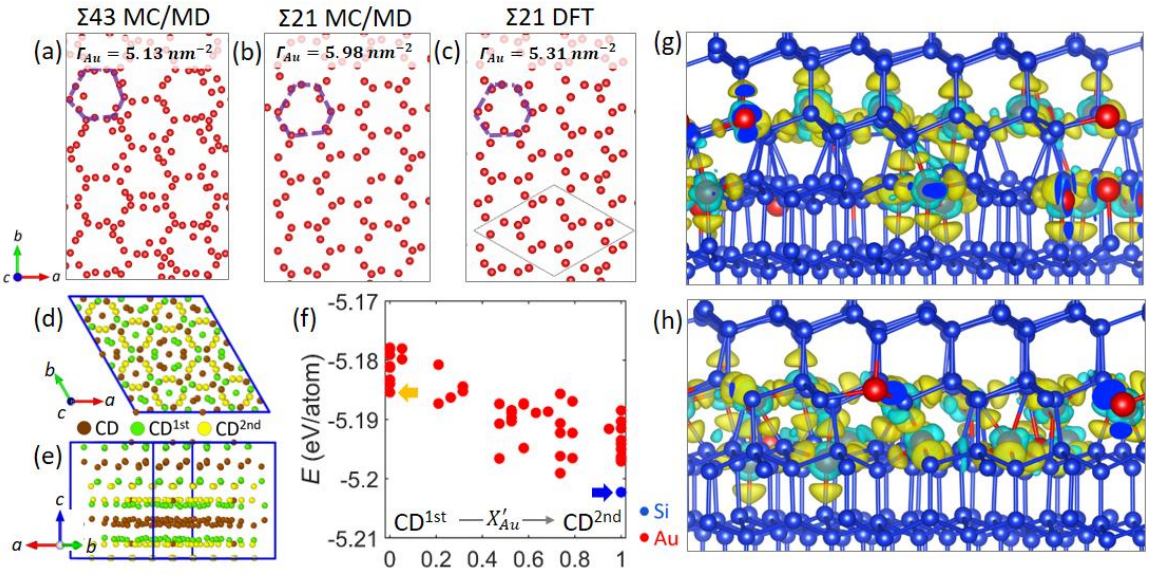

Figure 2.5 Segregation patterns of Au atoms at the Si (a) Σ43 and (b) Σ21 GBs simulated by hybrid MC/MD simulations at T = 0.60 T_m and $\Delta\mu = -0.3\ eV$. (c) DFT optimized Au segregation pattern at the Si Σ21 GB. The purple dashed hexagons indicate periodic Au segregation patterns and the grey diamond cell represents an irreducible unit of the Σ21 GB. (d) and (e) are the common neighbor analysis (CNA) results of the DFT-optimized Σ21 GB structure without Au doping. (f) Ground state energies as a function of Au substitution composition shifting from the CD^{1st} to the CD^{2nd} layer. The orange arrow represents the grand state configuration with the lowest energy when all Au atoms substitute Si in the CD^{1st} layer, and blue arrow points to the hybrid MC/MD simulated structure. The differential charge density maps of two structures indicated by the orange and blue arrows are shown in (g) and (h), respectively. The yellow iso-surfaces indicate electron accumulation and cyan iso-surfaces show electron depletion.

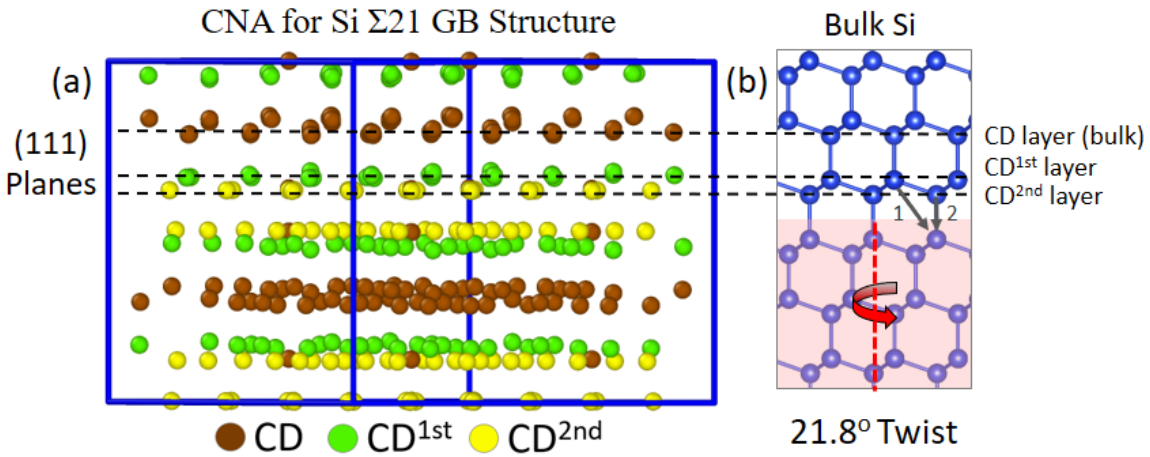

Figure 2.6 (a) Common neighbor analysis (CNA) of the DFT-optimized Si Σ21 undoped grain boundary (GB) structure. (b) Bulk Si cubic diamond (CD) crystal structure. When the bottom shaded part twists around red dashed axis (to for the twist GB), the CD-type atoms can always maintain perfect bulk structure. The CD^{1st}-type atoms preserve all their first-nearest neighbor atoms, while at least one of their second-nearest neighbor atoms is missing or off the lattice (as indicated by Arrow 1). The CD^{2nd}-type atoms have at least one of their first-nearest neighbor atoms missing or off the lattice (as indicated by Arrow 2). Noting that CD, CD^{1st} and CD^{2nd} type atoms sit in parallel atomic planes of the (111) orientation in the ideal twist GB structure shown here, indicated by the parallel dashed lines. Thus, "CD^{1st} layer" and "CD^{2nd} layer" are used in the discussion of 0K DFT simulated results.

References

[1] Z. Yu, P.R. Cantwell, Q. Gao, D. Yin, Y. Zhang, N. Zhou, G.S. Rohrer, M. Widom, J. Luo, M.P. Harmer, Segregation-induced ordered superstructures at general grain boundaries in a nickel-bismuth alloy, Science, 358 (2017) 97.

[2] M. Yamaguchi, M. Shiga, H. Kaburaki, Grain Boundary Decohesion by Impurity Segregation in a Nickel-Sulfur System, Science, 307 (2005) 393-397.

[3] G. Duscher, M.F. Chisholm, U. Alber, M. Rühle, Bismuth-induced embrittlement of copper grain boundaries, Nature Materials, 3 (2004) 621-626.

[4] S.J. Dillon, M. Tang, W.C. Carter, M.P. Harmer, Complexion: A new concept for kinetic engineering in materials science, Acta Materialia, 55 (2007) 6208-6218.

[5] P.R. Cantwell, M. Tang, S.J. Dillon, J. Luo, G.S. Rohrer, M.P. Harmer, Grain boundary complexions, Acta Materialia, 62 (2014) 1-48.

[6] W.D. Kaplan, D. Chatain, P. Wynblatt, W.C. Carter, A review of wetting versus adsorption, complexions, and related phenomena: the rosetta stone of wetting, Journal of Materials Science, 48 (2013) 5681-5717.

[7] M.P. Harmer, The Phase Behavior of Interfaces, Science, 332 (2011) 182-183.

[8] T. Watanabe, Grain boundary engineering: historical perspective and future prospects, Journal of Materials Science, 46 (2011) 4095-4115.

[9] M. Tang, W.C. Carter, R.M. Cannon, Grain Boundary Transitions in Binary Alloys, Physical Review Letters, 97 (2006) 075502.

[10] J. Luo, Developing Interfacial Phase Diagrams for Applications in Activated Sintering and Beyond: Current Status and Future Directions, Journal of the American Ceramic Society, 95 (2012) 2358-2371.

[11] X. Shi, J. Luo, Developing grain boundary diagrams as a materials science tool: A case study of nickel-doped molybdenum, Physical Review B, 84 (2011) 014105.

[12] X. Shi, J. Luo, Grain boundary wetting and prewetting in Ni-doped Mo, Applied Physics Letters, 94 (2009) 251908.

[13] X. Shi, J. Luo, Decreasing the Grain Boundary Diffusivity in Binary Alloys with Increasing Temperature, Physical Review Letters, 105 (2010) 236102.

[14] N. Zhou, J. Luo, Developing grain boundary diagrams for multicomponent alloys, Acta Materialia, 91 (2015) 202-216.

[15] J. Luo, Liquid-like interface complexion: From activated sintering to grain boundary diagrams, Current Opinion in Solid State and Materials Science, 12 (2008) 81-88.

[16] N. Zhou, T. Hu, J. Luo, Grain boundary complexions in multicomponent alloys: Challenges and opportunities, Current Opinion in Solid State and Materials Science, 20 (2016) 268-277.

[17] Y. Mishin, W.J. Boettinger, J.A. Warren, G.B. McFadden, Thermodynamics of grain boundary premelting in alloys. I. Phase-field modeling, Acta Materialia, 57 (2009) 3771-3785.

[18] M. Tang, W.C. Carter, R.M. Cannon, Diffuse interface model for structural transitions of grain boundaries, Physical Review B, 73 (2006) 024102.

[19] P. Wynblatt, D. Chatain, Solid-state wetting transitions at grain boundaries, Materials Science and Engineering: A, 495 (2008) 119-125.

[20] J. Luo, Grain boundary complexions: The interplay of premelting, prewetting, and multilayer adsorption, Applied Physics Letters, 95 (2009) 071911.

[21] J.M. Rickman, H.M. Chan, M.P. Harmer, J. Luo, Grain-boundary layering transitions in a model bicrystal, Surface Science, 618 (2013) 88-93.

[22] J.M. Rickman, J. Luo, Layering transitions at grain boundaries, Current Opinion in Solid State and Materials Science, 20 (2016) 225-230.

[23] T. Frolov, D.L. Olmsted, M. Asta, Y. Mishin, Structural phase transformations in metallic grain boundaries, Nature Communications, 4 (2013) 1899.

[24] T. Frolov, S.V. Divinski, M. Asta, Y. Mishin, Effect of Interface Phase Transformations on Diffusion and Segregation in High-Angle Grain Boundaries, Physical Review Letters, 110 (2013) 255502.

[25] T. Frolov, M. Asta, Y. Mishin, Segregation-induced phase transformations in grain boundaries, Physical Review B, 92 (2015) 020103.

[26] Z. Pan, T.J. Rupert, Effect of grain boundary character on segregation-induced structural transitions, Physical Review B, 93 (2016) 134113.

[27] S.A.E. Johansson, G. Wahnström, First-principles study of an interfacial phase diagram in the V-doped WC-Co system, Physical Review B, 86 (2012) 035403.

[28] S. Yang, N. Zhou, H. Zheng, S.P. Ong, J. Luo, First-Order Interfacial Transformations with a Critical Point: Breaking the Symmetry at a Symmetric Tilt Grain Boundary, Physical Review Letters, 120 (2018) 085702.

[29] S. Ma, K. Meshinchi Asl, C. Tansarawiput, P.R. Cantwell, M. Qi, M.P. Harmer, J. Luo, A grain boundary phase transition in Si–Au, Scripta Materialia, 66 (2012) 203-206.

[30] H. Ogawa, GBstudio: A Builder Software on Periodic Models of CSL Boundaries for Molecular Simulation, MATERIALS TRANSACTIONS, 47 (2006) 2706-2710.

[31] S.V. Starikov, N.Y. Lopanitsyna, D.E. Smirnova, S.V. Makarov, Atomistic simulation of Si-Au melt crystallization with novel interatomic potential, Computational Materials Science, 142 (2018) 303-311.

[32] B. Ressel, K.C. Prince, S. Heun, Y. Homma, Wetting of Si surfaces by Au–Si liquid alloys, Journal of Applied Physics, 93 (2003) 3886-3892.

[33] G. Kresse, J. Hafner, Ab initio molecular dynamics for liquid metals, Physical Review B, 47 (1993) 558-561.

[34] G. Kresse, J. Furthmüller, Efficient iterative schemes for ab initio total-energy calculations using a plane-wave basis set, Physical Review B, 54 (1996) 11169-11186.

[35] P.E. Blöchl, Projector augmented-wave method, Physical Review B, 50 (1994) 17953-17979.

[36] J.P. Perdew, K. Burke, M. Ernzerhof, Generalized Gradient Approximation Made Simple, Physical Review Letters, 77 (1996) 3865-3868.

[37] G. Kresse, D. Joubert, From ultrasoft pseudopotentials to the projector augmented-wave method, Physical Review B, 59 (1999) 1758-1775.

[38] A. Stukowski, Visualization and analysis of atomistic simulation data with OVITO–the Open Visualization Tool, Modelling and Simulation in Materials Science and Engineering, 18 (2009) 015012.

Chapter 3. Genetic Algorithm-Guided Deep Learning of Grain Boundary Diagrams: Addressing the Challenge of Five Degrees of Freedom

3.1. Introduction

Most engineered and natural materials are polycrystalline, where grain boundaries (GBs) can often control a variety of properties. Like a three-dimensional (3D) bulk phase, a GB can adopt an equilibrium state for a given set of thermodynamic variables such as temperature, pressure, and chemical potential [1-3]. Such a GB equilibrium state can be treated as an interfacial phase that is thermodynamically 2D, which is also named as “complexion” to differentiate it from a thin layer of 3D phase precipitated at the GB [1-3]. Impurities or solutes adsorption (*a.k.a.* segregation) at GBs, which can occur along with GB structural transformations [1, 2], can drastically change microstructural evolution [1, 2] or cause catastrophic embrittlement [4, 5]. More generally, GB adsorption and structures can affect a broad range of kinetic, mechanical, electronic/ionic, magnetic, thermal, and other properties [1, 2, 6]. Thus, understanding the GB composition-structure-property relation is of both fundamental and practical interest.

Phase diagrams, maps of thermodynamically stable (3D bulk) phases as functions of temperature and composition, are one of the most important materials science tools. Since the properties of GBs can be as important as those of the bulk phases in polycrystalline materials, it can be broadly useful to map out the GB states and properties as functions of temperature and bulk composition, thereby

constructing the GB counterparts to bulk phase diagrams [7-12]. Some computed GB diagrams include first-order transformation lines [3, 7, 8, 10], while GB transformations are continuous in many other materials. In both cases, constructing GB property diagrams as functions of temperature and bulk composition can be highly useful.

However, a GB has five macroscopic (crystallographic) degrees of freedom (DOFs) [13, 14], in addition to several thermodynamic DOFs, including temperature and the chemical potential(s) set by the bulk composition. Thus, it becomes virtually a “mission impossible” to construct bulk composition- and temperature-dependent property diagrams for GBs as functions of five crystallographic DOFs by either experiments or modeling. Advanced electron microscopy [15-17] and atom probe tomography [18] have been used to characterize GB structures at the atomic level, but the sample preparation and experimental procedures are time-consuming even for studying a small number of GBs at one given thermodynamic condition. Prior works of computing GB diagrams as functions of temperature and bulk composition mostly used highly simplified phenomenological or lattice models [3, 9-11]. A WC-Co interfacial diagram was constructed via a DFT-based cluster-expansion method that only surveyed a limited number of given interfacial structures [19]. Only a couple of recent studies computed GB diagrams as functions of the bulk composition (that sets/represents the chemical potential) and temperature via atomistic simulations, but only for one special tilt or twist GB [7, 8]. Recently, various advanced computational methods,

such as the evolutionary algorithm [20], genetic algorithm (GA) [7, 21], Bayesian optimization [22], and machine learning (ML) [23-25], combined with high-throughput calculations [26], data mining [27], and virtual screening [28], have been used to model GBs; however, most of these studies focused on either symmetric-tilt or twist GBs. More general and asymmetric GBs [15], which are ubiquitous in polycrystals and often the weak links chemically and mechanically, are hitherto scarcely investigated by virtually any modeling method. Understanding the GB properties as functions of seven DOFs (five crystallographic DOFs plus bulk composition and temperature) remains a grand challenge, which motivated this study.

Herein, we demonstrate a GA-guided deep learning approach to predict GB properties as a function of seven DOFs (or construct bulk composition- and temperature-dependent GB diagrams as function of five DOFs) accurately and rapidly by combining isobaric semi-grand-canonical ensemble hybrid Monte Carlo and molecular dynamics (hybrid MC/MD) simulations, GA-based variable selection, and deep neural networks (DNN) prediction. Notably, our final DNN model is capable of predicting properties of not only simpler symmetric-tilt and twist GBs, but also more complex and general GBs.

3.2. Computational Methods

3.2.1. High-Throughput MC/MD Simulation

For each GB, the initial structure was first annealed at 1000 K for 500 ps with a time step of 0.1 fs via the classical MD simulation in constant *NPT* ensembles to relax the GB structure at a high temperature. Subsequently, the hybrid Monte Carlo and molecular dynamics (hybrid MC/MD) simulations in constant-*N*$\Delta\mu$*PT* ensembles were performed to dope Ag atoms in Cu at the given temperature and constant chemical potential difference $\Delta\mu = \mu_{\mathrm{Cu}} - \mu_{\mathrm{Ag}}$, where $\mu_{\mathrm{Cu(Ag)}}$ is the chemical potential of Cu(Ag). Similar to prior works [7, 8], five MC trial moves were performed between each MD step with a 0.1 fs MD time step, and ~1 million hybrid MC/MD steps were typically performed for each simulation to achieve convergence (to achieve an equilibrium).

To construct a GB diagram as a function of temperature and Ag composition, the hybrid MC/MD simulations were carried out from 700 K to 1250 K with a step 50 K. At each temperature *T*, a series of simulations with increasing $\Delta\mu$ were preformed to represent different bulk Ag compositions until the amount of Ag reached the maximal bulk solid solubility. Then, the GB properties diagrams were constructed from interpolation of ~30-120 simulations conducted at different *T* and $\Delta\mu$ for each of the 100 GBs selected.

The above-discussed isobaric semi-grand canonical (constant-*N*$\Delta\mu$*PT*) ensemble atomistic simulations (via MD relaxation followed by hybrid MC/MD

simulations) were systematically performed for 100 selected GBs of all four (ST, TW, AT, and MX) types. Due to the limited computational resource and time, ~30% of the 30 ST and 30 TW GBs and ~50% of 20 AT and 20 MX GBs were chosen to compute GB property diagrams with dense grids (~120 simulations at different T and $\Delta\mu$ for each GB). The other GBs were calculated and interpolated with less data points (~30-40 simulations per GB).

All together, we performed 6581 individual constant-$N\Delta\mu PT$ ensemble atomistic (MD relaxation followed by hybrid MC/MD) simulations for 100 selected GBs of four types (~1872 for ST, ~1787 for TW, ~1145 for AT, and ~1777 for MX GBs, respectively).

3.2.2. Genetic Algorithm for Variable Selection

A genetic algorithm (GA) was used to rank and select GB descriptors via using the PLS Toolbox (version 8.2.1; Eigenvector Research Inc., Wenatchee, WA, USA) interfaced with MATLAB2018[a] (MathWorks Inc., Natick, MA, USA). The GA is used to identify the subset or combination of GB descriptors that are most useful for predicting GB diagrams. Specifically, the partial-least-square (PLS) regression method was used to determine the root-mean-square error of cross validation (RMSECV) for each GB descriptor associated with T and $\Delta\mu$. The maximal latent variables (LVs) for the PLS regression was set to be 8. To avoid variable overfitting, a small generation size was set to be 50, a large population size for each generation was adopted to be 256 (upper limit of software), and a low convergence

sensitivity of 25% criteria was utilized. In addition, the random and double cross-validation (CV) settings were applied.

To screen the important GB descriptors for each GB type, we repeated GA 10 times for three different GB property diagrams. After each GA run, the selected GB descriptors can obtain one GA point. We define the descriptors with total score $\geq$ 20 (out of 3×10) are important GB descriptors. If two interdependent descriptors have high GA score at same time (> 20), such as Σ and Σ^{-1} in TW GBs, we consider only the one with the higher score as important descriptor.

Finally, the important GB descriptors identified by the GA for each GB type were used to train, test, and validate deep neural networks (DNN) models.

3.2.3. Deep Neural Networks

The data set of each GB type was divided into training, validation, and test subsets. We selected 20% of total GBs as the test set, and randomly split the remaining GBs into training and validation sets with a 4:1 ratio. By repeating the random sub-sampling CV process 50 times, we found the optimized network architectures for the two-layer single-task DNN (n^i-$n^{[1]}$-$n^{[2]}$-1, where n^i is the number of input parameter, $n^{[1]}$ and $n^{[2]}$ are the number of neurons in the 1st and 2nd layers) were found to be 13-10-4-1 for ST, 6-16-6-1 for TW, 10-18-16-1 for AT, and 12-18-4-1 for MX GBs, respectively. The optimized network architecture for the unified all-included DNN model was found to be 15-18-10-1. Training of the DNN models were carried out using the Adam optimizer at a learning rate of 0.01 by adopting

the RMSE as the loss metric and a rectified-linear unit (RELU) as the activation function. All data processing and DNN development were performed in Python3.6.1 using the Sklearn and Tensorflow packages.

3.3. Results and Discussion

3.3.1. Benchmark Simulations of Cu-Ag Binary System

To ensure the quality of our data generated by large-scale atomistic simulations, we performed comprehensive benchmark tests of both *NPT* MD simulations of pure Cu and *N*$\Delta\mu$*PT* hybrid MC/MD simulations of Ag-doped Cu. Overall, our simulations are consistent with prior experimental [18, 29] and modeling [20, 30, 31] results. First, the GB energy (E_{GB}) and free volume (V_{Free}) obtained from the *NPT* simulations agree with the first-principles DFT calculations; in particular, the V_{Free} values obtained from the *NPT* simulations agree better with DFT results than those from the *NVT* simulations [30] (Fig. 3.1(a)). Second, the *N*$\Delta\mu$*PT* simulated bulk phase diagram agrees well with the experimentally-measured phase diagram [32]. Third, temperature-induced GB structural transformations from normal to split and filled kites are evident (Fig. 3.2), being qualitatively consistent with prior *NVT* simulations [31]; moreover, *NPT* simulated GB structures *vs.* misorientation angles are also consistent with prior *NVT* simulations with open surfaces [20, 30] (Fig. 3.3). Fourth, both *NPT* and *N*$\Delta\mu$*PT* simulated GB structures and properties are robust with respect to perturbations of adding vacancies and interstitials (Fig. 3.4 and 3.5), thereby demonstrating that the GB free volume (local density) can be effectively adjusted in our constant-

pressure simulations to achieve equilibria. Fifth, our $N\Delta\mu PT$ simulations of GB adsorption *vs.* bulk X_{Ag} agree with prior MC simulations for a Σ5 GB [18, 31] (Fig. 3.6) within our simulation errors. Noting that the $N\Delta\mu PT$ hybrid MC/MD simulations show continuous transformations of GB adsorption, disordering, and free volume with temperature or bulk composition. Sixth (and notably), our $N\Delta\mu PT$ hybrid MC/MD simulations successfully reproduced the segregation-induced GB nano-faceting in an asymmetric GB observed in a prior experiment [29] (Fig. 3.7). Therefore, this agreement provided a further test and validation of our $N\Delta\mu PT$-ensemble hybrid MC/MD simulation with the experiment.

3.3.2. Workflow of Machine-Learning Prediction of GB Diagrams

The workflow of the GA-guided DNN prediction for GB diagrams is displayed in Fig. 3.8. First, large-scale isobaric semi-grand-canonical (*i.e.*, constant-$N\Delta\mu PT$) ensemble hybrid MC/MD simulations were performed to compute three GB properties (*i.e.*, GB adsorption Γ_{Ag}, GB excess disorder $\Gamma_{\mathrm{Disorder}}$, and GB free volume V_{Free}) for 30 symmetric-tilt (ST), 30 twist (TW), 18 asymmetric-tilt (AT), and 22 mixed tilt-twist (MX) GBs as a function of chemical potential difference $\Delta\mu$ (= $\mu_{\mathrm{Ag}} - \mu_{\mathrm{Cu}}$) and temperature T (Fig. 3.8(a)). All together, we performed 6,581 individual constant-$N\Delta\mu PT$ atomistic simulations (each with ~16,000-50,000 atoms for ~1 million hybrid MC/MD steps at constant $N\Delta\mu PT$ until reaching convergence). To the best of our knowledge, the simulations here have generated the largest and most systematic dataset of binary GBs to date, which

are used for the subsequent data-driven prediction of GB diagrams as a function of five macroscopic DOFs. Second, the dataset generated by hybrid MC/MD simulations was used to perform GA-based variable selection to identify the most significant GB descriptors for each property and each GB type, and subsequently for all GBs together (Figs. 3.8(b, c)). Third, the GA-selected descriptors were used to train, validate, and test DNN models. Finally, the DNN models were used to predict GB diagrams as functions of five DOFs plus two thermodynamic DOFs (Fig. 3.8(e)).

3.3.3. Genetic-Algorithm Selection for Most Important GB Descriptors

GBs can be characterized by five macroscopic DOFs based on coincident-site-lattice (CSL) misorientation scheme or interface-plane scheme [13, 14, 33]. We primarily adopt the latter, where GBs are classified into four groups: ST, TW, AT, and MX GBs (Fig. 3.9(a)). Moreover, we identified and summarized 38 commonly used GB descriptors in Table 3.2, including both structural and geometrical parameters.

Subsequently, we used GA-based variable selection (Fig. 3.8(b)) to identify the significant GB descriptors that control each GB property of each group, as well as all GBs together. The GA inspired by Darwinian evolution is a metaheuristic optimization method that can be used to select optimal parameters [34, 35]. One GA process can include variable evaluation, selection, crossover, and mutation to identify the significant descriptors that control the targeted property (Fig. 3.8(b)). For ST, TW, and AT GBs, we only consider the first 32 descriptors because these

GBs only require either a tilt or a twist rotation to transform Grain 1 to Grain 2. For MX and all-included GBs, all 38 descriptors, including the last six descriptors related to the overall (combined tilt-twist) rotation axis and plane, are considered. We plot the GA scores of significances for these GB descriptors in Fig. 3.9(b) and use red pentagrams to label the significant GB descriptors.

The GA-selected significant GB descriptors for ST, TW, AT, TW, and all-included GBs are shown in Table 3.1. Selected interesting findings are outlined here. First, the GA identified Σ, the inverse of degree of coincidence, as a significant descriptor for ST, TW, and AT GBs. An important result is that Σ was not selected as a significant descriptor for the most general MX GBs. This result challenges the class wisdom [13] by suggesting that Σ is not an important parameter to characterize the properties of general GBs; however, this maverick finding is supported by a series of recent studies by Rohrer, Randle, and their co-workers [36-39]. Second, the GA found the orientations of the terminal GB planes to be important in general, which is consistent with recent theoretical [13, 40, 41] and experimental studies [13, 15, 16, 42]. Third, the GA found that denser (lower Miller index) terminating grain plane is more important to control adsorption and structures of asymmetric AT and MX GBs, as well as all-included GBs. Notably, this finding is again consistent with recent advanced microscopy observations that lower-index grain surface dictates faceting and segregation behaviors [15, 42].

Interestingly, the GA also reproduced some common knowledge and conventions. For ST GBs, the GA-identified significant descriptors are all in the

CSL-misorientation notation φ_{tlt} [u_{tlt} v_{tlt} w_{tlt}] (*h k l*) commonly-used to denote ST GBs, where φ_{tlt} and [u_{tlt} v_{tlt} w_{tlt}] are the tilt angle and axis, and (*h k l*) is the boundary plane [13]. Twist GBs only have five GA-selected significant descriptors, which are all in their characteristic structural relation of $\Sigma = \gamma(\Phi_{twst})\delta r^2$, where Φ_{twst} is the twist angle (noting that $\Phi_{twst} = \theta_{mis}$ for TW GBs), γ is the inverse planar coincident-site density [13], and δ = 1 or 0.5 to ensure Σ to be odd.

For the most comprehensive case of all-included GBs, a large number of fifteen significant GB descriptors were chosen by the GA. Several interesting findings are discussed as follows. First, the GA selection indicates that Σ^{-1} is a significant GB descriptor, and it is better than Σ itself that is not a significant descriptor. Second, the orientations of terminating grain planes are still important. Third, misorientation angle θ_{mis} was not selected by the GA, but decomposed tilt angle φ_{tlt} was chosen. Fourth, the interplanar distance d_1 (for the lower Miller index grain surface) was selected (and is more important than d_2), which again suggests that the lower-index plane is important overall. Fifth, the overall (combined tilt and twist) rotation axis and plane are also important for all-included GBs. This overall rotation is reduced to the tilt or twist rotation for simpler ST, TW, and AT GBs so they are not present there. It is interesting to note that the inclusion of the overall rotation axis/plane has significantly improved the prediction accuracies for all-included GBs. Finally, we summarized the significant descriptors for each GB property for different GB types in Table 3.3. Moreover, we plotted the GA scores of the first 32 descriptors *vs*. GB type in Fig. 3.10.

3.3.4. Deep Learning Prediction of GB Diagrams and Performance

Using GA-selected descriptors, two-layer single-task DNN models were developed for four groups of (ST, TW, AT, and MX) GBs, as well as for all four types together (referred to as “all-included GBs” and labeled as “All” for brevity). The detailed DNN architecture is shown in Fig. 3.8(d). To compare the performance of these five DNN models, we plot the weighted average root-mean-square error (RMSE) based on training, validation, and test sets of them for three GB properties (Γ_{Ag}, $\Gamma_{\mathrm{Disorder}}$, and V_{Free}) in Fig. 3.11. The RMSEs of five DNN models not only have small and comparable RMSEs (see Fig. 3.11), but also only vary in a small range of about 3~6% of the maximal GB property, thereby suggesting the robust performance for all five DNN models.

Notably, the three GB properties predicted by the all-included DNN model are sufficiently accurate. Specifically, the weighted average RMSEs of all-included DNN model always lie in the maximal and minimal RMSEs among four individual DNN models (see Fig. 3.11). For example, the all-included DNN model in fact works better than the individual DNN models for predicting ST and AT GBs (except $\Gamma_{\mathrm{Disorder}}$), while slightly lower performance for TW and MX GBs, see Fig. 3.11. Thus, we do not need to make separate predictions for each group of GBs (albeit that the GA selection of significant descriptors for each GB type has provided useful physical insights). Our subsequent analysis and discussion are focused on the all-included DNN model.

For the all-included DNN model, the parity plots between DNN-predicted

and MC/MD-computed values of Γ_{Ag}, $\Gamma_{\mathrm{Disorder}}$, and V_{Free}, respectively, are shown in Figs. 3.12(a-b), respectively. The linear relations between training, validation, and test datasets demonstrate the robustness of this DNN model. We note that there are more deviations between the DNN predictions and MC/MD simulations at high values, which can be ascribed to high levels of thermal noises in the MC/MD simulations at high temperatures or near solidus lines.

Moreover, we compare the image similarity between DNN-predicted and MC/MD-simulated GB diagrams by calculating the structural similarity index (SSIM; 0 = different and 1 = same) The SSIM histogram plots of three property diagrams (Γ_{Ag}, $\Gamma_{\mathrm{Disorder}}$, and V_{Free}) for four groups of ST, TW, AT, and MX GBs, as well as all-included GBs, are shown in Figs. 3.12(d-f). Relatively high SSIM values of ~0.84-0.93 have been achieved for three GB property diagrams for all-included DNN model, as well as for each of four individual groups of GBs (Figs. 3.12(d-f)).

As an example, a comparison plot of MC/MD-simulated *vs*. DNN-predicted diagrams for a Σ81 MX GB with boundary planes $(1\bar{1}0)//(7\bar{8}7)$ is shown in Figs. 3.12(g-i), where high SSIM values of 0.99, 0.98, and 0.94 are obtained for the Γ_{Ag}, $\Gamma_{\mathrm{Disorder}}$, and V_{Free} diagrams, respectively. The high similarities between MC/MD-calculated and DNN-predicted diagrams further verify the accuracy and robustness of this DNN model. It is worth noting that the relatively lower SSIM values for the $\Gamma_{\mathrm{Disorder}}$ and V_{Free} diagrams can be ascribed to their more complex quantification procedures that introduce more noises in the DNN training and test sets.

Using this all-included DNN model, we further plotted and documented the MC/MD-calculated *vs*. DNN-predicted the GB diagrams of three properties (Γ_{Ag}, $\Gamma_{\mathrm{Disorder}}$, and V_{Free}) for 103 different GBs (*i.e.* 618 GB diagrams), including three additional GBs with $\Sigma > 100$ discussed subsequently.

Finally, we tested and compared the speed performance of the DNN predictions *vs*. MC/MD simulations. We tabulated simulation time for one MC/MD simulation with one-million steps by using two Intel microprocessors. On the one hand, the needed CPU hours increase linearly from ~200 to 550 with the increasing size of the simulation cell from ~16,000 to 47,000 atoms. On the other hand, the all-included DNN model only takes ~0.001 CPU seconds for one prediction, which is about 10^8 faster than the typical MC/MD simulation.

3.3.5. The Effective Range of the Current DNN Model

The DNN model adopted here makes predictions under a certain range of GB descriptors. For example, we selected the Σ value to be between 5 and 99. Here, we excluded Σ = 3 GBs because they are too special with distinctly different behaviors [43]; thus they should be treated separately. Similarly, we did not consider small-angle (<10^o) GBs that also behave differently from more general GBs and are better to be treated separately using dislocation-based models [44]. In other words, the current work focuses on more general GBs. We have listed the effective ranges of all 38 GB descriptors used in this study in Table 3.2.

Finally, we have to admit that the transferability of all DNN models are

somewhat limited to other alloy systems due to the complex GB segregation behavior. However, the large dataset generated in this work enables potential studies on the optimization of classical thermodynamic models. Such an optimized models with explicit analytical expression make it possible to be extended to other systems by using a small set of simulations.

3.3.6. Further Extensibility of the DNN Model

We can further extend the upper bound of the Σ value to represent even more general GBs, *e.g.*, those GBs with Σ > 500 [15]. Such a large Σ value renders MC/MD simulation infeasible to provide a training set for the DNN model. Thus, we need a method for extrapolation. The GA selection of all-included GBs shows that Σ itself is not important, but the descriptor Σ^{-1} becomes significant (Fig. 3.10). Since Σ^{-1} only varies in a small range beyond Σ > 100, we can use the DNN model to predict more general GBs via extrapolation.

To test this extensibility, we computed the Γ_{Ag}, $\Gamma_{\mathrm{Disorder}}$, and V_{Free} diagrams for a few GBs with Σ > 100, including Σ113, Σ171 and Σ599 GBs, as well as an asymmetric (110)//(610) GB characterized in a prior experiment [29]. Since the asymmetric (110)//(610) GB is not a CSL GB (Σ→∞), we conducted a MC/MD simulation on a large cell (with a small strain to allow periodic boundary condition; see Fig. 3.7). We used two large Σ values (99 and 599) in the DNN predictions to extrapolate (noting that Σ > 500 represents sufficiently general GBs) to Σ→∞.

First, we found that RMSEs of the three GB properties (Γ_{Ag}, $\Gamma_{\mathrm{Disorder}}$, and

V_{Free}) predicted by DNN for these four GBs (Σ99, Σ113, Σ171, and Σ599) still follow the linear trends in the parity plots of three diagrams, as shown in Figs. 3.12(a-c). Second, the direct comparisons of MC/MD-simulated *vs*. DNN-predicted GB diagrams shown also suggest similar similarities and acceptable SSIM values between DNN predictions and MC/MD simulations for these four cases of Σ ≥ 99.

Furthermore, we plotted the GB Γ_{Ag}, Γ_{Disorder}, and V_{Free} diagrams predicted from the DNN model using Σ = 99 and Σ = 599, along with MC/MD-simulated asymmetric (110)//(610) GB (Σ → ∞), in Fig. 3.13 for comparison. Notably, the three GB diagrams predicted by the DNN model using Σ = 99 and Σ = 599, respectively, are essentially identical (SSIM = 1.0 for all comparisons; see Fig. 3.13). Moreover, these DNN-predicted GB diagrams are similar to the MC/MD-simulated GB diagrams with high SSIM values of 0.96, 0.86, and 0.83, respectively, for the GB Γ_{Ag}, Γ_{Disorder}, and V_{Free} diagrams, respectively.

Thus, we conclude that this all-included DNN model can also predict properties for GBs with Σ > 100 from extrapolation by adopting Σ^{-1} as an input parameter.

The prior experiment [29] found Ag segregation induced nano-faceting at this (110)//(610) GB, which has also been successfully reproduced by our MC/MD simulations (Fig. 3.7). This suggests that the DNN prediction is also valid for nano-faceted GBs. It is worth noting that other significant GB descriptors (as the input of the DNN model) also have effective ranges (given in Table 3.2). Especially, some

descriptors (*e.g.*, h_1 and k_2) may go beyond the bound when Σ is set to a too large value. Nonetheless, GBs with Σ ~100 (or Σ^{-1} ~ 0.01) are typically sufficiently good to represent general GBs, *e.g.*, the case shown in Fig. 3.7.

3.3.7. Analysis of GB Diagrams for 100 GBs

We further explore the similarity of 100 GBs' diagrams between DNN prediction and MC/MD simulation by analyzing the SSIM distribution as a function of GB types and symmetry. Figs. 3.14(a-c) are the SSIM distribution of 100 GBs *vs*. GB types categorized by θ_{mis} and Φ_{twst}. It shows that ST and AT GBs (Φ_{twst} = 0) always have low SSIM values when tilt-rotation angles are small (see blue arrows). This is because small-angle tilt GBs behave more like dislocations. Meanwhile, some TW GBs ($\theta_{\text{mis}} = \Phi_{\text{twst}}$), especially for (111)-twist GBs, have low SSIM values owing to very small Γ_{Ag}, Γ_{Disorder}, and V_{Free}. Hence, they are like twin GBs and may be more efficient to be treated by other simple models. However, the MX GBs ($\theta_{\text{mis}} \neq \Phi_{\text{twst}}$) always have higher SSIM values (see purple ellipses) because these GBs are more like general GBs and behave similarly.

Moreover, Figs. 3.14(d-f) shows the SSIM distribution of 100 GBs' diagram *vs*. GB symmetry categorized by interplanar distances. It clearly shows that some GBs with high symmetry ($d_1 = d_2$) may have lower SSIM values (see blue arrows) because they may have either dislocation-like (e.g., small rotation angle) or twin-GB (e.g., terminating with two low-energy surfaces) behaviors, but the asymmetric GBs ($d_1 \neq d_2$) are more like general GBs and thus they may have similar GB properties. Note that all the analysis here are in fact consistent with the SSIM

histogram distribution as shown in Fig. 3.12.

In summary, this current all-included DNN model can predict the temperature- and bulk composition-dependent Γ_{Ag}, $\Gamma_{\mathrm{Disorder}}$, and V_{Free} diagrams for an extremely large number of distinct ST, TW, AT, and MX GBs in the space of five macroscopic DOFs. In other words, this DNN model can map out the Γ_{Ag}, $\Gamma_{\mathrm{Disorder}}$, and V_{Free} values in a 7-D space!

3.4. Conclusions

We developed a data-driven approach that combined large-scale atomistic simulations, GA-based variable selection, and DNN to accurately and rapidly predict the temperature- and bulk composition-dependent GB Γ_{Ag}, $\Gamma_{\mathrm{Disorder}}$, and V_{Free} diagrams as functions of five GB crystallographic DOFs. These include not only the well-studied symmetric (ST and TW) GBs, but also the more general asymmetric (AT and MX) GBs that had been less studied before.

To our best knowledge, this work has also generated the largest and most systematic (>6500 hybrid MC/MD) atomistic simulations dataset for binary GBs to date, thereby enabling the DNN model to predict the GB properties as functions of seven (five crystallographic plus two thermodynamic) DOFs. The GA-based variable selection discovered interesting characters for each of four GB groups, as well as for all GBs combined together. Finally, a unified all-included DNN model has been developed to predict the GB Γ_{Ag}, $\Gamma_{\mathrm{Disorder}}$, and V_{Free} diagrams, which are ~10^8 faster than the atomistic simulations.

Chapter 3, in part, is a reprint of the material “Genetic Algorithm-Guided Deep Learning of Grain Boundary Diagrams: Addressing the Challenge of Five Degrees of Freedom”, C. Hu, Y. Zuo, C. Chen, S. Ong, and J. Luo, as it appears in Materials Today, 2020, 38, 49-57. The deep learning models were developed by Y. Zuo, C. Chen, and S. Ong. The dissertation author was the primary investigator and first author of this paper.

Table 3.1 GA-selected significant GB descriptors based on three GB properties for four individual groups of GBs, as well as all-included GBs. Σ is the GB coincidence number, and Σ^{-1} is its reciprocal. d_1 and d_2 are the interplanar distances of Plane 1 and 2, and the effective interplanar distance for an asymmetric GB is defined as: $d_{\text{eff}} = (d_1 + d_1)/2$. $(r, \theta_{\text{sph}}, \varphi_{\text{sph}})$ is the the sphereical coodination of Miller index (h k l). (n, m, o) is the normal vector of Plane 1 or 2 (denoted as subscript). Tilt (decomposed tilt-rotation) or twist (decomposed twist-rotation) axis is represented by $[u_{\text{tlt}}\ v_{\text{tlt}}\ w_{\text{tlt}}]$ or $[u_{\text{twst}}\ v_{\text{twst}}\ w_{\text{twst}}]$, with the corresponding tilt or twist angle (φ_{tlt} or Φ_{twst}). The misorientation angle is θ_{mis}. The overall (undecomposed) rotation axis is represented $[u_{\text{rot}}\ v_{\text{rot}}\ w_{\text{rot}}]$ with the rotation plane ($h_{\text{rot}}\ k_{\text{rot}}\ l_{\text{rot}}$). The empty space denotes that no significant GB descriptor was elected by the GA in this sub-group.

GB Descriptors	Symmetric-tilt (ST)	Twist (TW)	Asymmetric-tilt (AT)	Mixed (MX)	All-included (All)
GB coincidence parameter	Σ	Σ	Σ		Σ^{-1}
Interplanar distances			d_1		d_1
Miller index of Plane 1 ($h_1\ k_1\ l_1$)	h_1, l_1		h_1	h_1	k_1, l_2
Miller index of Plane 2 ($h_2\ k_2\ l_2$)	l_2			k_2	l_2
Sphereical Plane 1 ($r_1, \varphi^1_{\text{sph}}, \theta^1_{sph}$)		r_1		θ^1_{sph}	$\theta^1_{\text{sph}}, \varphi^1_{\text{sph}}$
Sphereical Plane 2 ($r_2, \varphi^2_{\text{sph}}, \theta^2_{sph}$)	θ^2_{sph}	r_2			φ^2_{sph}
Normal of Plane 1 ($n_1\ m_1\ o_1$)	n_1				
Normal of Plane 2 ($n_2\ m_2\ o_2$)	m_2, o_2		n_2	n_2	n_2, o_2
Tilt-rotation axis $[u_{\text{tlt}}\ v_{\text{tlt}}\ w_{\text{tlt}}]$	u_{tlt}, v_{tlt}, w_{tlt}		u_{tlt}, v_{tlt}, w_{tlt}	u_{tlt}, w_{tlt}	
Twist-rotation axis $[u_{\text{twst}}\ v_{\text{twst}}\ w_{\text{twst}}]$					
Angles: φ_{tlt}, Φ_{twst}, θ_{mis}	φ_{tlt}, θ_{mis}	Φ_{twst},θ_{mis}	θ_{mis}	φ_{tlt}	φ_{tlt}
Rotation axis $[u_{\text{rot}}\ v_{\text{rot}}\ w_{\text{rot}}]^*$					u_{rot}, v_{rot}
Rotation plane ($h_{\text{rot}}\ k_{\text{rot}}\ l_{\text{rot}}$)*				h_{rot}, k_{rot}, l_{rot}	k_{rot}, l_{rot}

Table 3.2 Summary of 32 GB descriptors used to perform genetic algorithm (GA)-based variable selection. The range (min-max) of each descriptor that covers in five DNN models is given for each case. For the significant GB descriptors (colored in red), the given parameter ranges also represent the effective input ranges for the DNN models to predict GB diagrams.

No.	Character	Description	ST	TW	AT	MX	ALL
1	Σ	Inverse of degree of coincidence	5-97	5-99	5-95	5-99	5-99
2	d_1[a] (Å)	Interplanar distance of Crystal 1	0.13-1.09	1.27-2.08	0.17-1.86	0.18-2.15	0.13-2.15
3	d_2 (Å)	Interplanar distance of Crystal 2	0.13-1.09	1.27-2.08	0.13-0.56	0.14-0.72	0.13-2.15
4	d_{eff} (Å)	Effective Interplanar distance	0.13-1.09	1.27-2.08	0.17-1.12	0.16-1.43	0.13-2.15
5	h_1	Miller index (*hkl*) of Plane 1	0-11	1-1	0-5	1-8	0-11
6	k_1	Miller index (*hkl*) of Plane 1	-8-7	0-1	-7-7	-8-7	-8-7
7	l_1	Miller index (*hkl*) of Plane 1	-7-11	0-1	-5-6	-4-5	-7-11
8	h_2	Miller index (*hkl*) of Plane 2	-7-11	1-1	-4-8	-2-9	-8-11
9	k_2	Miller index (*hkl*) of Plane 2	-8-11	0-1	-8-9	-8-8	-8-11
10	l_2	Miller index (*hkl*) of Plane 2	-4-11	0-1	-10-9	-5-7	-10-11
11	r_1	Spherical coordination (r,θ_{sph}, φ_{shp}) of Plane 1	2.24-13.93	1-1.73	1-10.49	1.41-9.90	1-13.93
12	θ^1_{sph} (°)	Spherical coordination (r,θ_{sph}, φ_{shp}) of Plane 1	-90-90	0-45	-71.57-90	-82.88-81.87	-90-90
13	φ^1_{sph} (°)	Spherical coordination (r,θ_{sph}, φ_{shp}) of Plane 1	8.93-120.2	54.74-90	26.57-156	15.79-117	8.93-156
14	r_2	Spherical coordination (r,θ_{sph}, φ_{shp}) of Plane 2	2.24-13.93	1-1.73	5-14.07	1-12.73	1-14.07
15	θ^2_{sph} (°)	Spherical coordination (r,θ_{sph}, φ_{shp}) of Plane 2	-104-172	0-45	-74.05-180	-108-90	-108-180
16	φ^2_{sph} (°)	Spherical coordination (r,θ_{sph}, φ_{shp}) of Plane 2	8.93-153	54.74-90	11.31-156	36-125	8.93-162
17	Σ^{-1}	Degree of coincidence	0.011-0.2	0.010-0.2	0.10-0.2	0.010-0.2	0.010-0.2
18	n_1	Normal vector [*nmo*] of Plane 1	0-0.91	0.58-1	0-0.71	0.12-0.95	0-1
19	m_1	Normal vector [*nmo*] of Plane 1	-0.86-0.97	0-0.71	-0.83-1	-0.99-0.96	-0.99-1
20	o_1	Normal vector [*nmo*] of Plane 1	-0.50-0.99	0-0.58	-0.91-1	-0.63-0.96	-0.91-1
21	n_2	Normal vector [*nmo*] of Plane 2	-0.86-0.88	0.58-1	-0.44-0.70	-0.25-0.97	-0.86-1
22	m_2	Normal vector [*nmo*] of Plane 2	-0.78-0.97	0-0.71	-0.70-0.99	-0.98-0.98	-0.98-0.99
23	o_2	Normal vector [*nmo*] of Plane 2	-0.89-0.99	0-0.58	-0.91-0.98	-0.75-1.0	-0.95-1
24	u_{tlt}	Decomposed tilt rotation axis [*uvw*]	-1-2	/	-2-7	-9-25	-9-25
25	v_{tlt}	Decomposed tilt rotation axis [*uvw*]	-2-2	/	0-5	-3-8	-3-8
26	w_{tlt}	Decomposed tilt rotation axis [*uvw*]	-2-1	/	-1-1	-9-13	-9-13
27	u_{twst}	Decomposed twist rotation axis [*uvw*]	/	0-1	/	0-9	0-9
28	v_{wst}	Decomposed twist rotation axis [*uvw*]	/	0-1	/	-8-8	-8-8
29	w_{twst}	Decomposed twist rotation axis [*uvw*]	/	0-1	/	-3-8	-3-8
30	φ_{tlt} (°)	Decomposed tilt rotation angle	10.38-168	/	22.6-64.62	16.26-48.19	10.38-168
31	Φ_{twst} (°)	Decomposed twist rotation angle	/	8.80-87.79	/	6.73-52.17	8.80-162
32	θ_{mis} (°)	Misorientation angle	10.38-168	8.80-87.79	22.6-64.62	21.80-61.93	8.80-168
33	u_{rot}[b]	Rotation axis [*uvw*]	/	/	/	1-7	-1-7
34	v_{rot}[b]	Rotation axis [*uvw*]	/	/	/	0-5	-2-5
35	w_{rot}[b]	Rotation axis [*uvw*]	/	/	/	0-5	-2-5
36	h_{rot}[b]	Rotation plane (*hkl*)	/	/	/	1-8	0-8
37	k_{rot}[b]	Rotation plane (*hkl*)	/	/	/	-8-7	-8-7
38	l_{rot}[b]	Rotation plane (*hkl*)	/	/	/	-4-7	-7-10

a. For asymmetric GBs ($d_1 \neq d_2$), we choose the boundary plane with the lower index number as Plane 1 while another plane as Plane 2. Hence, the corresponding d_1 is always greater than d_2. The interplanar distances here are at 0K.

b. Rotation axis and plane are only considered for mixed GBs and all-included (All) GBs. For other GB types, only one rotation (either twist or tilt) is needed to transform grain 1 to grain 2.

Table 3.3 Ranking of GA-Selected Important Descriptors for Three GB Properties of Each GB type. The “sum” is the overall score of three GB properties. For each GB property (Γ_{Ag}, $\Gamma_{Disorder}$, and V_{Free}), the descriptors with GA score ≥ 7 (out of 10) are identified as significant descriptors. For overall score (Sum.), the descriptors with GA score ≥ 20 are identified as significant descriptors. The ranking of GA-selected important descriptors is based on decreasing of GA score. Note that many GA-selected descriptors may have same score, this ranking list can only provide general trend for descriptor importance.

	Symmetric-Tilt (ST)					Twist (TW)					Asymmetric-Tilt (AT)					Mixed (MX)					All-Type				
	Γ_{Ag}	$\Gamma_{Disorder}$	V_{Free}	Sum.		Γ_{Ag}	$\Gamma_{Disorder}$	V_{Free}	Sum.		Γ_{Ag}	$\Gamma_{Disorder}$	V_{Free}	Sum.		Γ_{Ag}	$\Gamma_{Disorder}$	V_{Free}	Sum.		Γ_{Ag}	$\Gamma_{Disorder}$	V_{Free}	Sum.	
1	l_1	h_1	Σ	l_1	1	Σ^{-1}	Σ	Σ	Σ^{-1}	1	Σ	Σ	d_1	v_{tilt}	1	k_2	k_2	Σ	h_1	1	d_2	d_1	d_1	l_2
2	k_2	l_1	k_1	θ^2_{sph}	2	r_1	Σ^{-1}	Σ^{-1}	θ_{mis}	2	φ^2_{sph}	d_1	h_2	n_2	2	θ^1_{sph}	θ^1_{sph}	d_1	h_{rot}	2	l_1	h_1	l_1	φ^2_{sph}
3	θ^2_{sph}	h_2	l_1	m_2	3	θ_{mis}	φ^1_{sph}	n_1	r_1	3	Σ^{-1}	h_1	l_2	u_{tilt}	3	φ_{tilt}	n_1	h_1	k_{rot}	3	h_2	h_2	k_2	Σ^{-1}
4	m_2	θ^2_{sph}	θ^2_{sph}	o_2	4	d_1	r_2	v_{tilt}	r_2	4	θ_{mis}	n_2	n_1	θ_{mis}	4	k_{rot}	n_2	k_1	l_{rot}	4	l_2	l_2	l_2	u_{rot}
5	o_2	n_1	n_1	u_{tilt}	5	r_2	o_1		Φ_{twst}	5	n_2	u_{tilt}	v_{tilt}	v_{tilt}	5	u_{tilt}	k_{rot}	r_1	n_2	5	φ^2_{sph}	φ^1_{sph}	θ^1_{sph}	v_{rot}
6	u_{tilt}	m_2	m_2	v_{tilt}	6		Φ_{twst}			6	o_2	v_{tilt}	w_{tilt}	Σ	6	w_{twst}	h_1	φ^1_{sph}	k_2	6	Σ^{-1}	φ^2_{sph}	φ^1_{sph}	k_{rot}
7	v_{tilt}	o_2	o_2	m_1	7		θ_{mis}			7	u_{tilt}	w_{tilt}	d_2	d_1	7	l_{rot}	h_2	Σ^{-1}	θ^1_{sph}	7	o_1	Σ^{-1}	φ^2_{sph}	d_1
8	k_2	u_{tilt}	u_{tilt}	l_2	8					8	v_{tilt}	h_2	d_{eff}	h_1	8	w_{tilt}	u_{twst}	u_{tilt}	φ_{tilt}	8	n_2	m_1	Σ^{-1}	φ^1_{sph}
9	o_1	v_{tilt}	v_{tilt}	Σ	9					9	h_1	w_{twst}	r_1		9		v_{twst}	θ_{mis}	u_{tilt}	9	m_2	v_{tilt}	n_1	k_1
10	φ_{tilt}	w_{tilt}	w_{tilt}	w_{tilt}	10					10	m_2		n_2		10		φ_{tilt}	l_1	w_{tilt}	10	φ_{tilt}	w_{twst}	u_{twst}	l_1
11			θ_{mis}	h_1	11					11	φ_{tilt}		m_2		11		h_{rot}	r_2		11	u_{rot}	u_{rot}	v_{wst}	θ^1_{sph}
12			l_1	φ_{tilt}	12					12			φ_{tilt}		12			θ^2_{sph}		12	v_{rot}	v_{rot}	w_{twst}	n_2
13			h_2	θ_{mis}	13					13			θ_{mis}		13			o_1		13	k_{rot}	h_{rot}	φ_{tilt}	m_2
14			k_2		14					14					14			n_2		14	d_2	k_{rot}	u_{rot}	φ_{tilt}
15					15					15					15			m_2		15	h_1	l_{rot}	v_{rot}	l_{rot}
16					16					16					16			w_{tilt}		16	φ^1_{sph}	θ^1_{sph}	k_{rot}	
17					17					17					17			w_{rot}		17	u_{tilt}	k_1	l_{rot}	
18					18					18					18			l_{rot}		18	k_1	m_2	k_1	
19					19					19					19					19	h_{rot}	v_{wst}	n_2	
20					20					20					20					20			m_2	
21					21					21					21					21			w_{rot}	

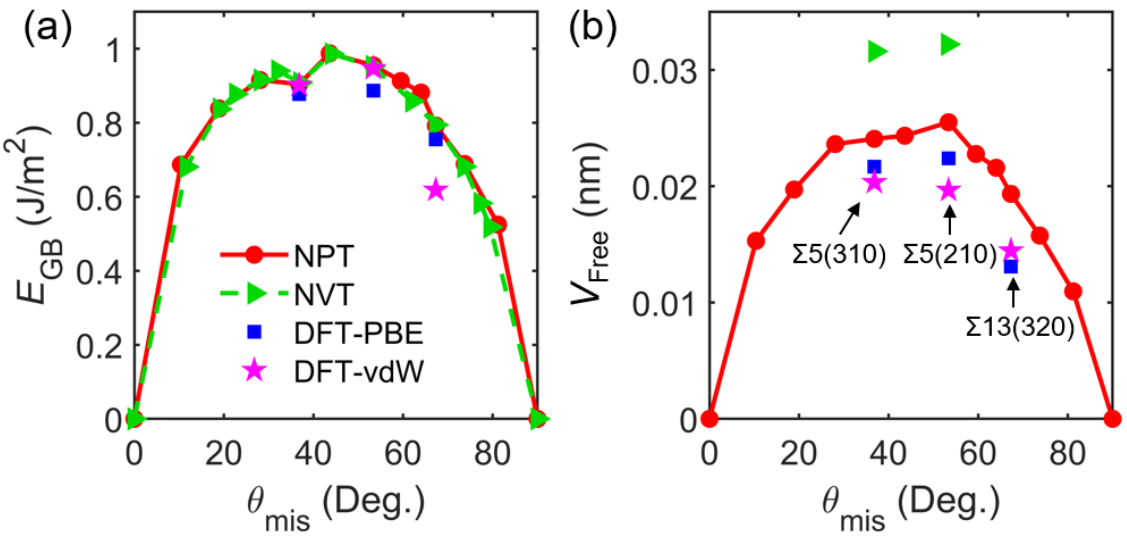

Figure 3.1 Hybrid MC/MD simulations *vs.* DFT calculations for (a) GB energies (E_{GB}) and (b) GB free volume (V_{Free}) as a function of misorientation angle (tilt angle) for 13 symmetric-tilt (ST) GBs. *NPT* simulations were carried out at a low temperature 10 K, where the energies and volumes were averaged based on the structures at last 50 ps (out of total 500 ps). Two DFT functionals, PBE and optB86b-vdW (without and with vdW-corrections), were used to calculate E_{GB} and V_{Free} for Σ5(310), Σ5(210), and Σ13(320) GBs for comparison with *NPT* and *NVT* simulations.

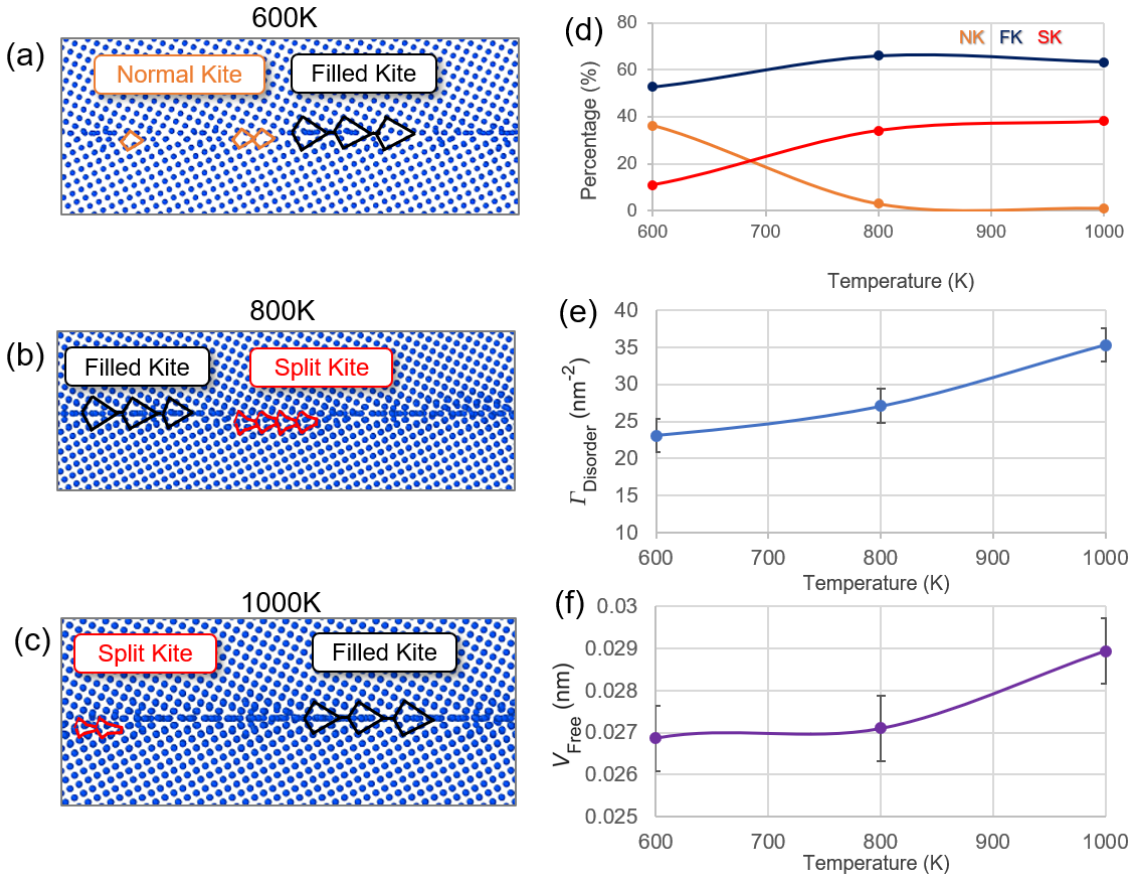

Figure 3.2 MD-based *NPT* simulations for temperature-induced GB structural transformations at the Σ5 (210) ST Cu GB at (a) 600 K, (b) 800K, and (c) 1000 K. (d) The percentage of normal kite (NK), filled kite (FK), and split kite (SK) *vs*. temperature curves.

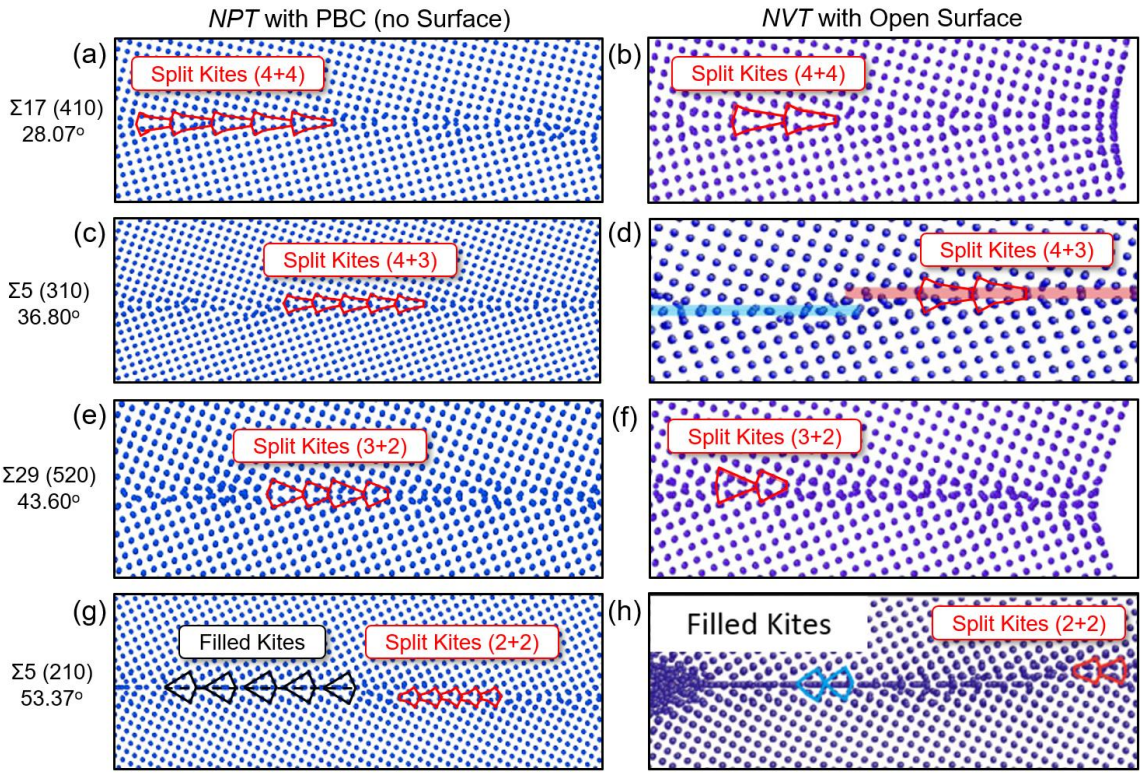

Figure 3.3 Comparison of MD *NPT* simulation with periodic boundary conditions *vs.* MD *NVT* simulation with open surfaces for representative symmetric-tilt GBs. (a) The screenshots of Σ17(410) GB simulated by *NPT* simulation at 1000 K and (b) *NVT* simulation at 900 K, both showing a split kite (4 + 4) structure. (c) The screenshots of Σ5 (310) GB simulated by *NPT* simulation at 1000 K and (d) *NVT* simulation at 800K, both showing split kite (4 + 3) structures. (e) The screenshots of Σ29 (520) GB simulated by NPT simulation at 1000 K and (f) *NVT* simulation at 900 K, both showing split kite (3 + 2) structures. (g) The screenshots of Σ5 (210) GB simulated by *NPT* simulation at 1000 K and (h) *NVT* simulation at 800 K, both showing coexisting filled kite and split kite (2 + 2) structures. Panels (b), (d), and (f) are extracted from K from Ref. [20], and Panel (h) is extracted from Ref. [30], with permission,. The total simulation time for our *NPT* simulation shown in Panel (a, c, e, g) was set to be 1 ns with a time step 1fs. Then, a 2-fs fast MD quench at 10K was performed in each case to remove the thermal noises.

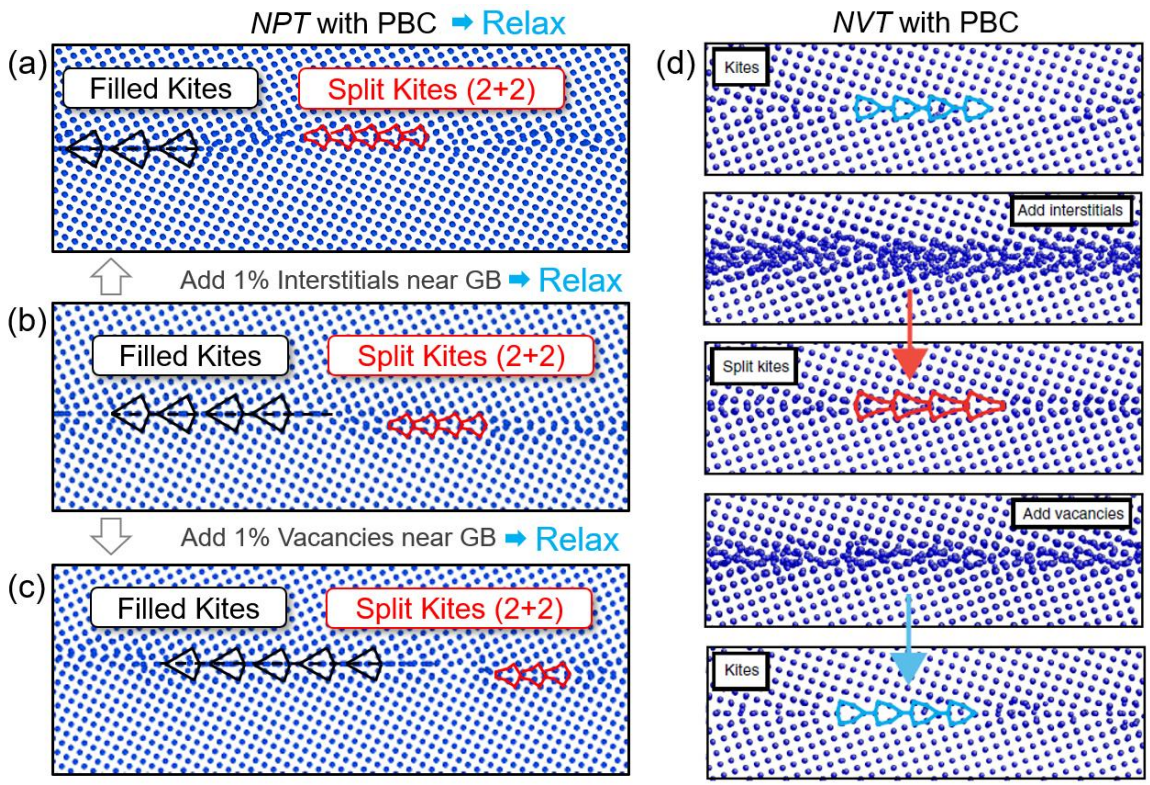

Figure 3.4 MD *NPT* simulation with periodic boundary conditions *vs.* MD *NVT* simulation with open surfaces for GB structural transformations induced by introducing point defects. MD *NPT*-ensemble simulated Σ5(210) GB structures with periodic boundary conditions at 900 K for three cases: (a) with 1% interstitial atoms added into GB region, (b) without adding any point defect and (c) with 1% vacancy atoms added. (d) MD *NVT*-ensemble simulated Σ5(210) GB structures at 800 K under the effects of interstitials and vacancies. Panel (d) was extracted from Ref. [30] with permission to compare with our *NPT* simulations). Noting that we found similar GB configurations at 800 K and 900 K.

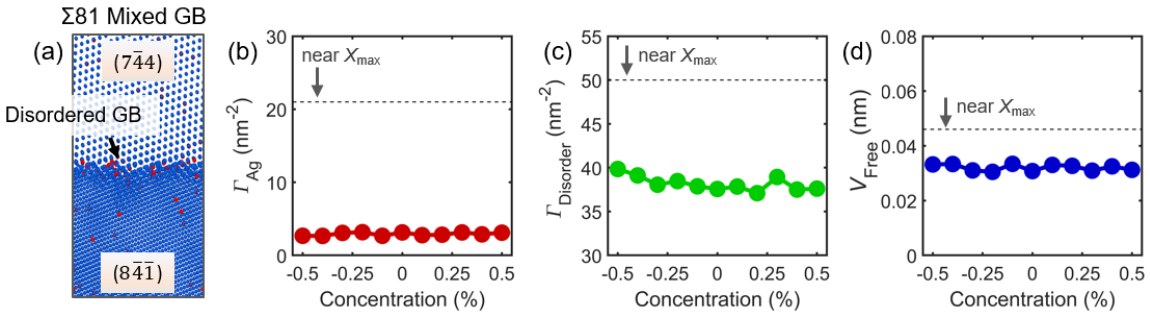

Figure 3.5 The stability of the hybrid MC/MD simulated GBs with respect to adding extra interstitials or vacancies. Using an asymmetric Σ81(7$\bar{4}$4)//(8$\bar{4}\bar{1}$) GB as an example, we tested the stability of the equilibrium interfacial structures obtained in our *N*Δμ*PT*-ensemble hybrid MC/MD simulations. Specifically, extra vacancies and interstitial atoms were introduced as perturbations to probe the convergence and stability of the equilibrium interfacial structure obtained in our *N*Δμ*PT* simulations. (a) Screenshot of a mixed Σ81 GB after 1 million steps of MC/MD simulations at 1000 K and $\Delta\mu = -0.5$ eV. The effects of point defects were considered by adding interstitials or vacancies at the GB region. (b) Calculated GB excess of adsorption (Γ_{Ag}), (c) GB excess of disorder ($\Gamma_{Disorder}$), and (d) GB free volume (V_{Free}) as a function of point defect concentration at $\Delta\mu = -0.5$ eV. A negative value represents the addition of vacancies defect while a positive value means the addition of interstitial atoms. The grey dashed lines indicate the maximum value near the Ag solubility limit (X_{max}) at 1000 K. This test illustrated that the equilibrium state obtained by hybrid MC/MD simulations, including adsorption, disorder, and GB free volume, are stable against the perturbations of adding and removing atoms in the GB region. Thus, the equilibrium state is likely achieved by our *N*Δμ*PT*-ensemble hybrid MC/MD simulation.

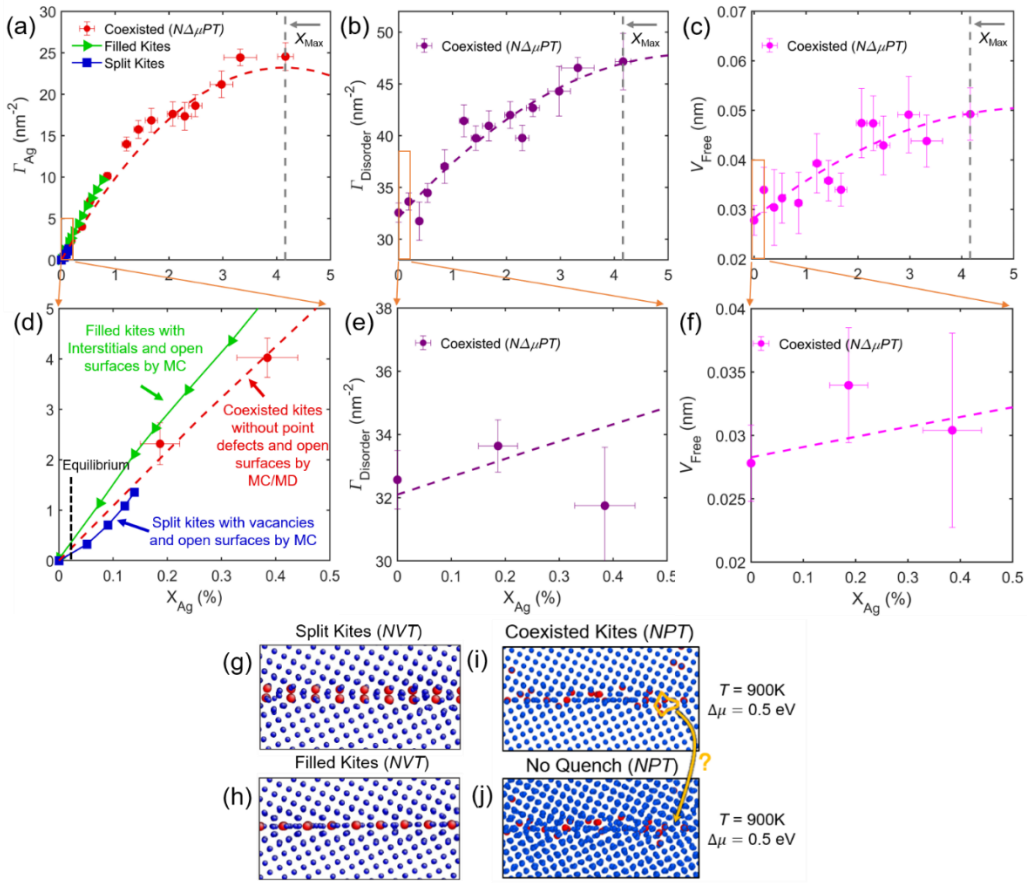

Figure 3.6 Comparison of prior *NVT* simulation [31] and *NΔμPT* simulations for ST Σ5(210) GB. (a) GB excess of solute (Γ_{Ag}), (b) GB excess disorder ($\Gamma_{\mathrm{Disorder}}$), and (c) free volume ($V_{\mathrm{Free}}$) as a function of the bulk Ag composition (X_{Ag}) at 900 K. The grey dotted line indicates the maximal Ag solubility (X_{max}) at 900 K. (d), (e), and (f) are enlarged plot of (a), (b), and (c). The black dashed line in (d) at 0.02% indicates an equilibrium between filled kites and split kites that was simulated by prior *NΔμVT*-ensemble MC simulations by using two different simulation blocks (see more detail in Ref. [31]). The atomic structure of these two simulation blocks are shown in (g, h), extracted from Ref. [31] with permission. (i-j) Coexistence of filled and split kites simulated by *NΔμPT* (this work) at 900 K and $\Delta\mu$ of 0.5 eV with and without fast quench (to remove thermal noises). The non-quenched structures with thermal noises always give more disordered GB structures, rendering it more difficult to identify split kite (yellow lines) and filled kite structures. The prior MC simulations with fixed atomic positions in two separate blocks reduced thermal noises, albeit some possible artifacts. Noting that in the prior NVT simulations, the filled kites and split kites are stabilized by injecting extra interstitials and vacancies (as the GB free volume was forced to increase or decrease with a constant volume), while in the *NΔμPT* used in this work, the GB free volume is allowed to adjusted at a constant pressure, so an equilibrium is more likely to be achieved.

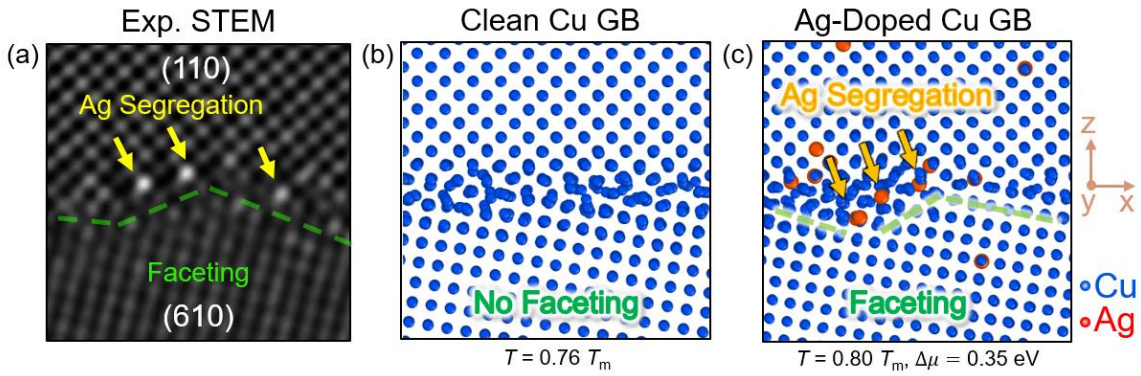

Figure 3.7 Ag segregation-induced GB faceting: validating simulations with an experiment. (a) Experimental STEM image of a Ag-doped Cu (110)//(610) GB at 1050K (~0.80 T_m) (adapted from Ref. [29] with permission). The yellow arrows indicate Ag segregation and the green dashed lines represent GB faceting. (b) MD simulated clean Cu GB structure at 0.76 T_m (1000K) with no faceting *vs.* (c) hybrid MC/MD simulated Ag-doped Cu GB structure at 0.80 T_m and $\Delta\mu = 0.35$ eV with a nano-faceted structure similar to that observed in the experiment shown in panel (a). Noting that the simulation model based on experimental STEM exhibits 1% strain along the *x* direction (to allow periodic boundary conditions), 0% strain along *y* direction, the *z* direction was fully optimized during the constant-pressure MD isothermal annealing.

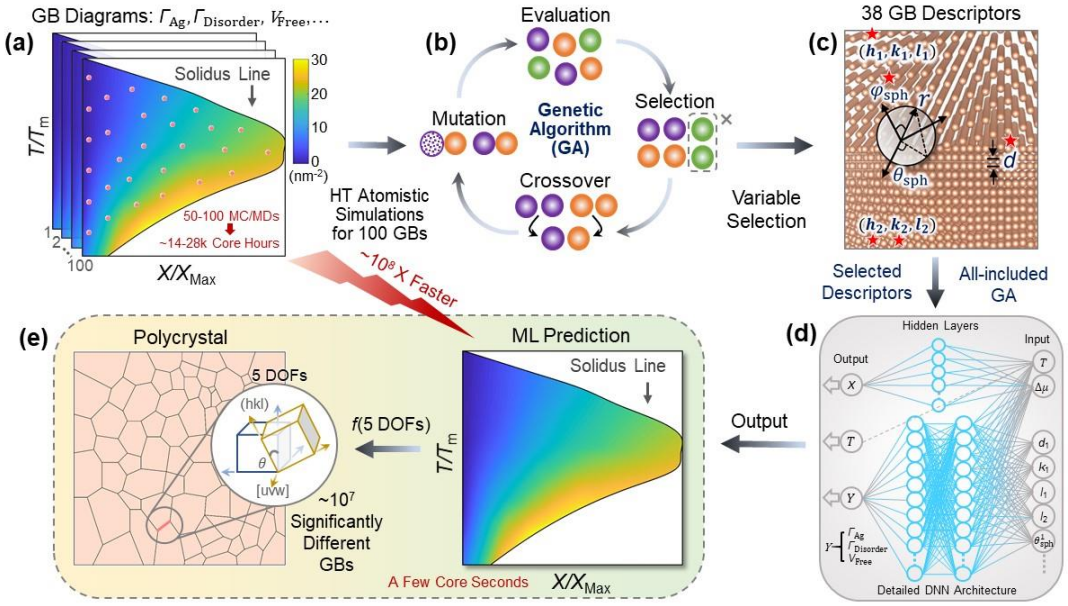

Figure 3.8 Workflow of machine learning prediction of bulk composition- and temperature-dependent grain boundary (GB) diagrams as a function of five macroscopic degrees of freedom (5 DOFs). (a) 6,581 individual isobaric semi-grand-canonical (constant-$N\Delta\mu PT$) ensemble atomistic simulations were performed for 100 representative GBs to calculate three types of GB diagrams of adsorption (Γ_{Ag}), excess disorder ($\Gamma_{Disorder}$), and free volume (V_{Free}). ~50-100 atomistic simulations (schematically represented by the red dots) are generally required to interpolate one set of three GB diagrams, which takes around 14,000-28,000 core hours of the simulation time per GB. (b) Schematic illustration of genetic algorithm (GA) based selection of significant GB descriptors. (c) The selected significant GB descriptors (indicated by red pentagram stars) were used as the input parameters to train, evaluate, and test deep neural network (DNN) models. (d) Schematic diagram of a two-layer single-task DNN with a 15-18-10-1 architecture for predicting GB properties ($Y = \Gamma_{Ag}$, $\Gamma_{Disorder}$, and V_{Free}) combined with a simplified single-layer artificial neural network (ANN) for predicting the bulk (grain) atomic fraction of Ag (X_{Ag}, which is normalized to the maximum solubility and represented by X/X_{Max}). The input parameters for the all-included DNN mode are the significant GB descriptors selected by GA plus two thermodynamic DOFs ($\Delta\mu$ and T). Here, the ANN predicted bulk (grain) composition at given $\Delta\mu$ and T is a bulk property, independent of the GB structure. (e) The established DNN model can predict GB diagrams in a few core seconds per GB (i.e. ~10^8 faster than the atomistic simulation). This DNN-based machine learning model enables the forecast of the Γ_{Ag}, $\Gamma_{Disorder}$, and V_{Free} diagrams of millions of distinctly different GBs as a function of five macroscopic DOFs, which is otherwise a “mission impossible” to construct by either experiments or modeling.

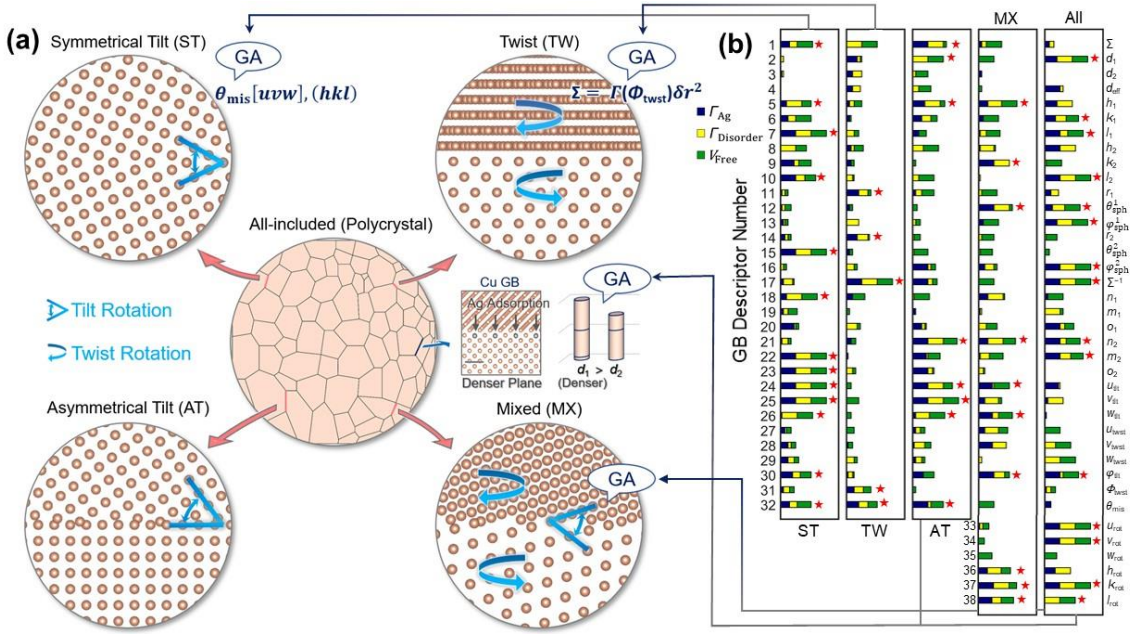

Figure 3.9 The classification of grain boundaries (GBs) and genetic algorithm (GA) based variable selection for GB descriptors. (a) GBs in a polycrystal can be classified into four types: symmetric-tilt (ST), twist (TW), asymmetric-tilt (AT), and mixed tilt-twist (MX) GBs. (b) Plots of the GA scores for 32 GB descriptors for ST, TW, and AT GBs, and 38 GB descriptors for MX and all four type GBs together (denoted as "all-included" or "All"). See the detailed descriptions for the 38 descriptors in Table 3.2. The red pentagram stars are used to label GA selected significant descriptors. The most significant GB descriptors selected by the GA include the parameters in the common notation $\theta_{\mathrm{mis}}[uvw](hkl)$ for ST GBs and the those in the characteristic relation $\Sigma = \gamma(\Phi_{\mathrm{twst}})\delta r^2$ for twist GBs. Moreover, the GA finds d_1 (of the lower-index plane) and d_2 to be the most and second most significant descriptors for AT GBs, as well as all-included GBs, which suggest that GB properties are dominated by the (denser) lower-index plane.

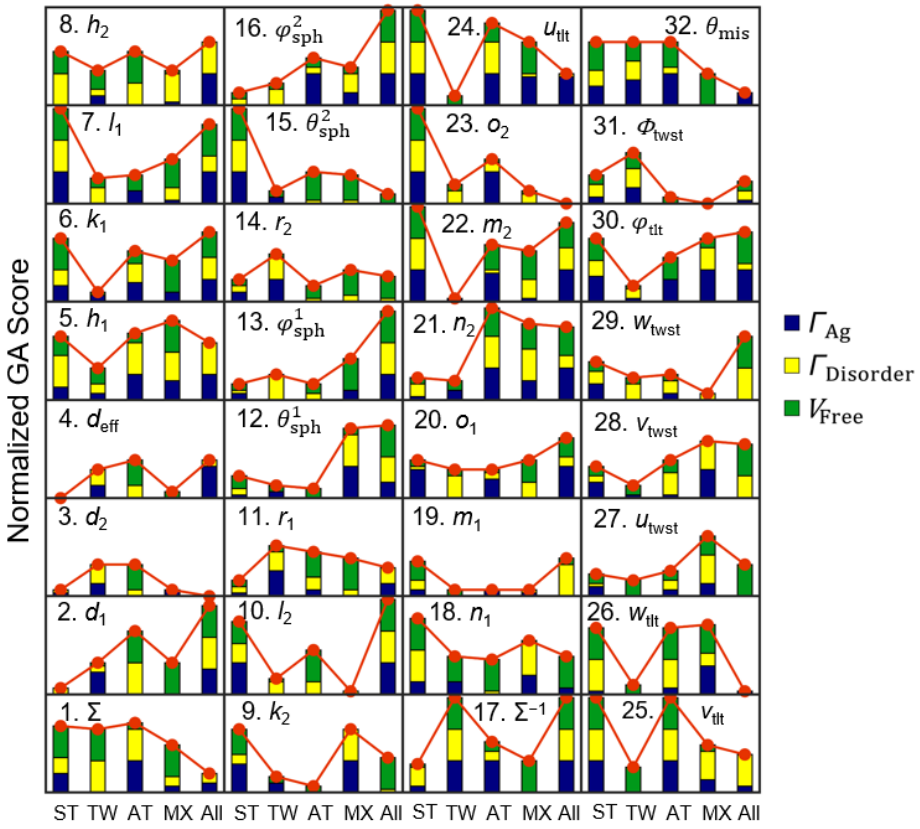

Figure 3.10 The GA scores for the GB descriptors from No.1-32 *vs*. GB types: symmetric-tilt (ST), twist (TW), asymmetric-tilt (AT), mixed (MX), and all-included (All) GBs. The red solid lines were labeled as trend line. See a list of these GB descriptors and explanations in Table 3.2. The GB Descriptor No. 1, 2, 3, 4, and 17 are GB geometrical parameters; others are variables that can be used to describe the GB degrees of freedom (DOF). Noting that GA score of descriptors No. 33-38 are not considered for ST, TW, and AT GBs.

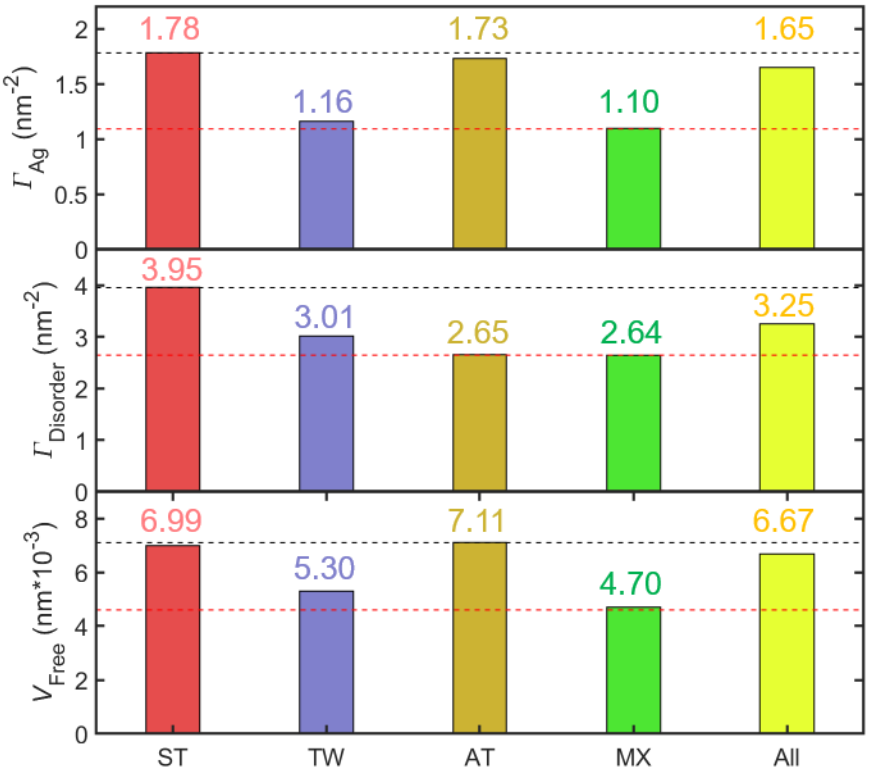

Figure 3.11 Comparison of weighted average root-mean-square error (RMSE) of Γ_{Ag}, $\Gamma_{\mathrm{Disorder}}$, and V_{Free} diagrams for four individual DNN models (ST, TW, AT, and MX) and an unified all-included (All) DNN model. For each DNN model, the weighted average RMSEs were calculated based on the RMSEs of training, validation, and test sets. The black and red dashed lines respectively represent the maximal and minimal values of RMSEs.

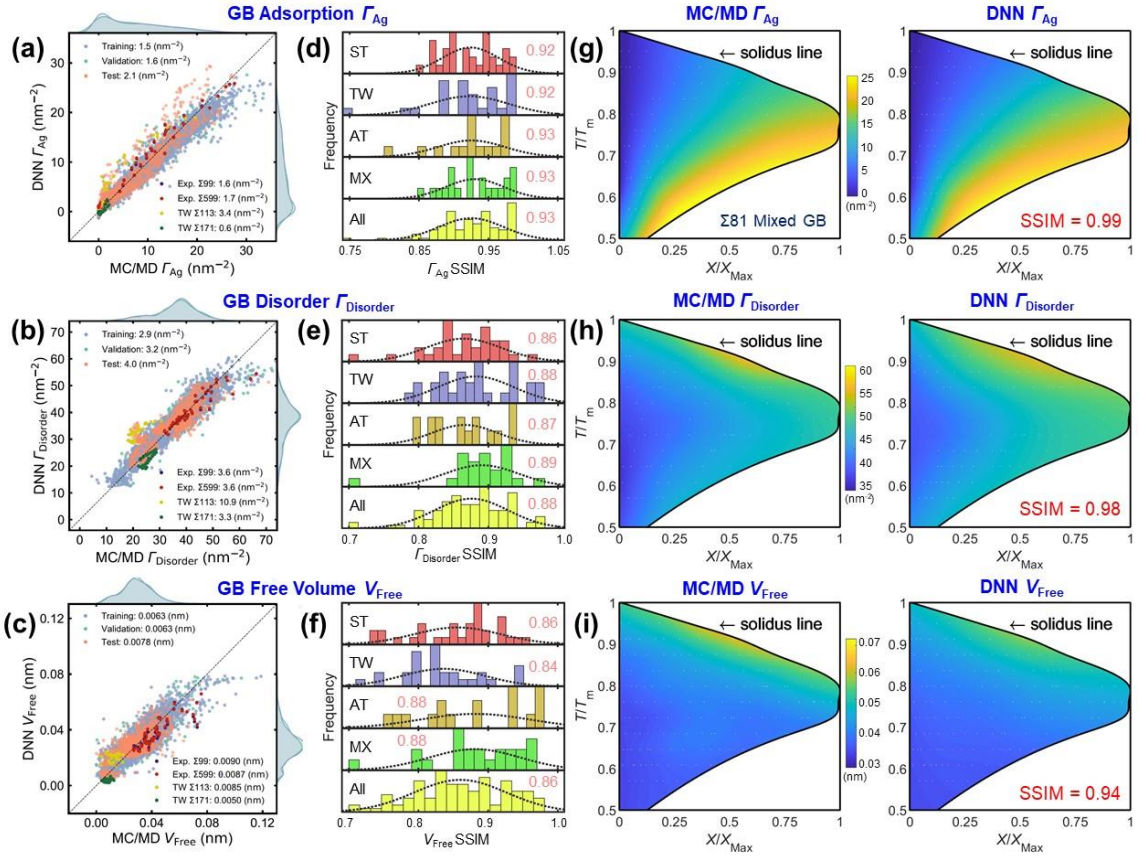

Figure 3.12 Performance of deep neural network (DNN) models. (a-c) Parity plots of DNN-predicted values of Γ_{Ag}, $\Gamma_{\mathrm{Disorder}}$, and V_{Free} using the all-included DNN model with an optimized network architecture 15-18-10-1 vs. hybrid MC/MD-simulated values (via $N\Delta\mu PT$ atomistic simulations). (d-f) Histogram plots with distribution line (black dotted line) of structural similarity index (SSIM) for characterizing the similarities between MC/MD-simulated GB diagrams and DNN-predicted GB diagrams of Γ_{Ag}, $\Gamma_{\mathrm{Disorder}}$, and V_{Free}. The pink numbers labelled are mean SSIMs for each GB type. (g-i) Comparison of the MC/MD-simulated vs. DNN-predicted GB Γ_{Ag}, $\Gamma_{\mathrm{Disorder}}$, and V_{Free} diagrams using all-included DNN model for a Σ81 mixed GB with boundary planes $(1\bar{1}0)//(7\bar{8}7)$. The structural similarity indices (SSIMs) for characterizing the similarities between MC/MD-simulated and DNN-predicted GB diagrams are labeled.

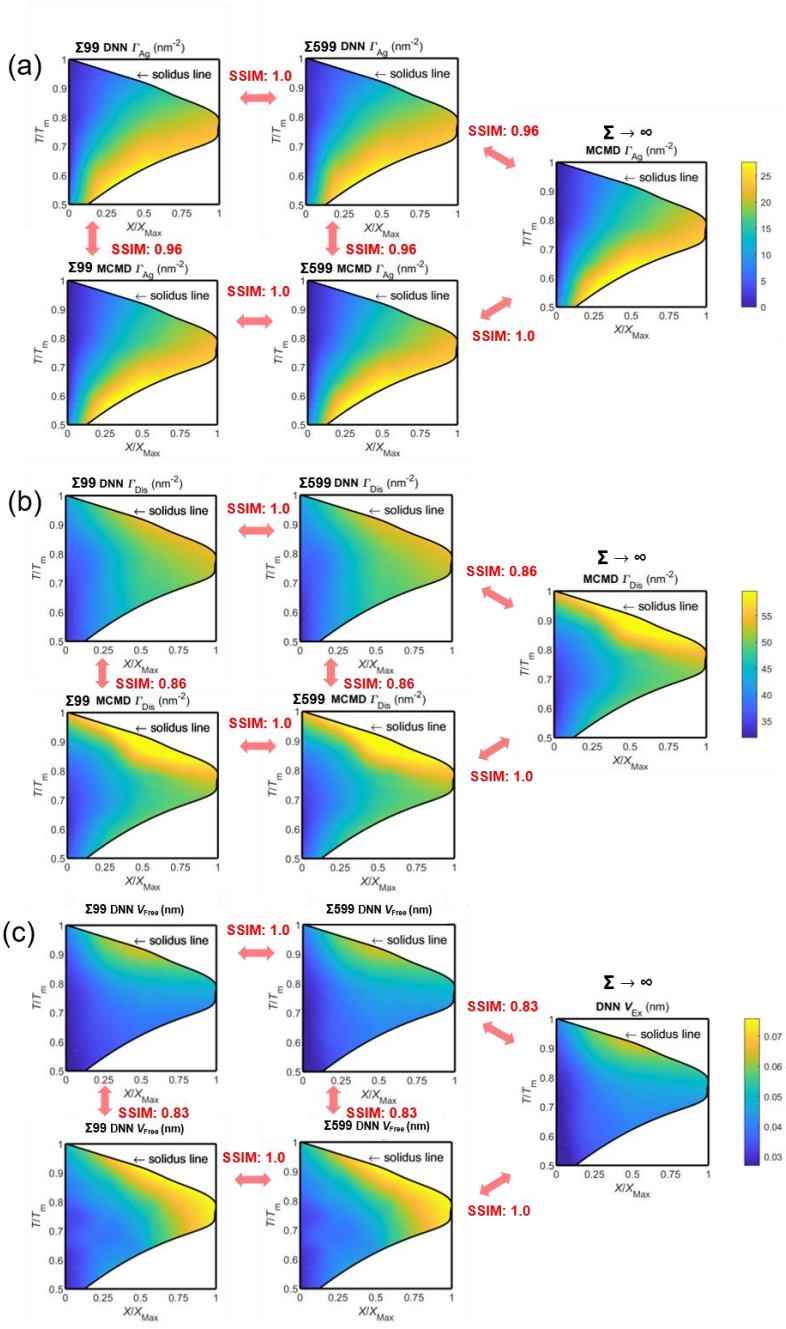

Figure 3.13 The extensibility of DNN predicted GB diagrams to general GBs with $\Sigma \rightarrow +\infty$. Comparison of GB (a) Γ_{Ag}, (b) $\Gamma_{\mathrm{Disorder}}$, and (c) V_{Free} diagrams predicted by the DNN model using $\Sigma = 99$ and $\Sigma = 599$, respectively, in comparison with those calculated by atomistic simulations using hybrid MC/MD simulation, and a $\Sigma \rightarrow +\infty$ GB model with minimum strains (1% strain along the *x* direction and 0% strain along *y* direction, see Fig. 3.7). The structural similarity index (SSIM) values were calculated to compare the similarity between DNN-predicted GB diagrams with different Σ values and DNN *vs*. MC/MD simulations.

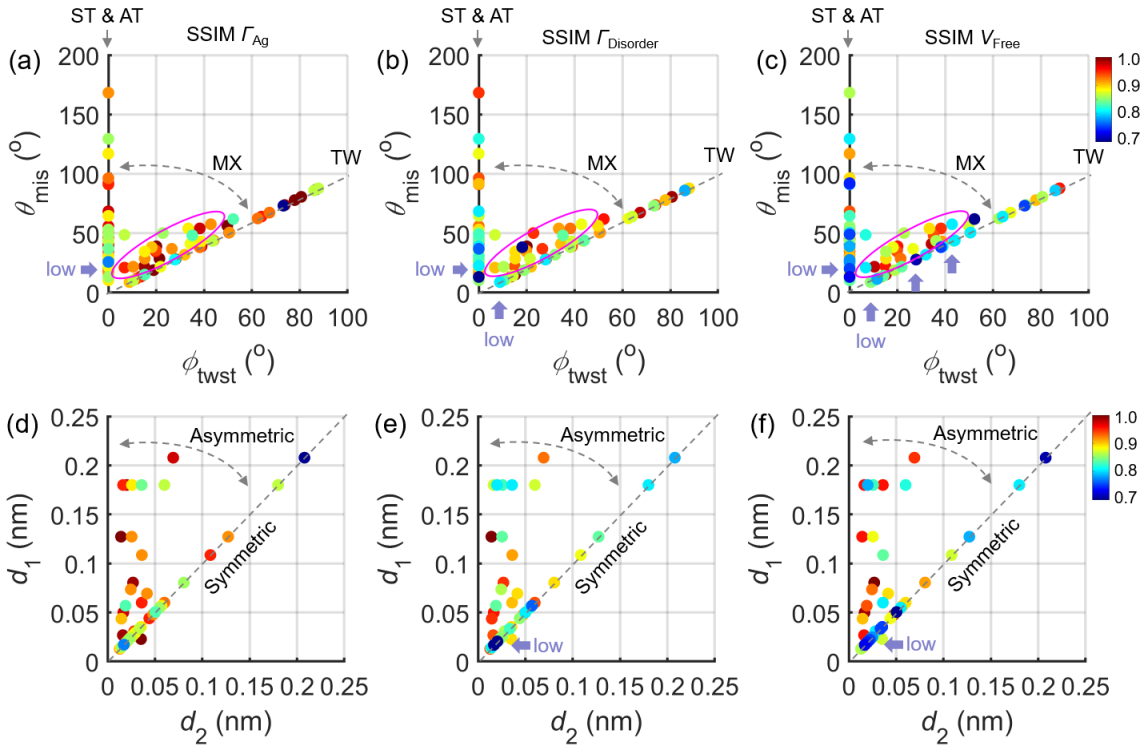

Figure 3.14 The SSIM distribution of 100 GBs for (a) Γ_{Ag}, (b) $\Gamma_{\mathrm{Disorder}}$, and (c) V_{Free} diagrams based on four GB types categorized by misorientation angle θ_{mis} and twist rotation angle Φ_{twst}. The dashed lines represent TW GBs due to $\theta_{\mathrm{mis}} = \Phi_{\mathrm{twst}}$. The ST and AT GBs always have $\Phi_{\mathrm{twst}} = 0$, see grey arrows, and the GBs are often MX type when $\theta_{\mathrm{mis}} \neq \Phi_{\mathrm{twst}}$, see dashed curves with arrows. The purple ellipses were used to label the high SSIM values for MX GBs. The blue arrows indicate low SSIM values for some tilt and twist GBs with low rotation angles. The SSIM distribution of 100 GBs for (a) Γ_{Ag}, (b) $\Gamma_{\mathrm{Disorder}}$, and (c) V_{Free} diagrams based on the GB symmetry categorized by interplanar distance d_1 and d_2. The ST and TW GBs always have high symmetry due to $d_1 = d_2$, see dashed lines (albeit a little AT and MX GBs may also have $d_1 = d_2$). The AT and MX GBs are often asymmetric due to $d_1 \neq d_2$, see dashed curves with arrows. The blue arrows are used to label the low SSIM values. All color bars were presented for SSIM value from 0.7 to 1.

References

[1] S.J. Dillon, M. Tang, W.C. Carter, M.P. Harmer, Complexion: A new concept for kinetic engineering in materials science, Acta Materialia, 55 (2007) 6208-6218.

[2] P.R. Cantwell, M. Tang, S.J. Dillon, J. Luo, G.S. Rohrer, M.P. Harmer, Grain boundary complexions, Acta Materialia, 62 (2014) 1-48.

[3] M. Tang, W.C. Carter, R.M. Cannon, Grain Boundary Transitions in Binary Alloys, Physical Review Letters, 97 (2006) 075502.

[4] J. Luo, H. Cheng, K.M. Asl, C.J. Kiely, M.P. Harmer, The Role of a Bilayer Interfacial Phase on Liquid Metal Embrittlement, Science, 333 (2011) 1730-1733.

[5] T. Hu, S. Yang, N. Zhou, Y. Zhang, J. Luo, Role of disordered bipolar complexions on the sulfur embrittlement of nickel general grain boundaries, Nature Communications, 9 (2018) 2764.

[6] P.R. Cantwell, T. Frolov, T.J. Rupert, A.R. Krause, C.J. Marvel, G.S. Rohrer, J.M. Rickman, M.P. Harmer, Grain Boundary Complexion Transitions, Annual Review of Materials Research, (2020).

[7] S. Yang, N. Zhou, H. Zheng, S.P. Ong, J. Luo, First-Order Interfacial Transformations with a Critical Point: Breaking the Symmetry at a Symmetric Tilt Grain Boundary, Physical Review Letters, 120 (2018) 085702.

[8] C. Hu, J. Luo, First-order grain boundary transformations in Au-doped Si: Hybrid Monte Carlo and molecular dynamics simulations verified by first-principles calculations, Scripta Materialia, 158 (2019) 11-15.

[9] J. Luo, Developing Interfacial Phase Diagrams for Applications in Activated Sintering and Beyond: Current Status and Future Directions, Journal of the American Ceramic Society, 95 (2012) 2358-2371.

[10] N. Zhou, Z. Yu, Y. Zhang, M.P. Harmer, J. Luo, Calculation and validation of a grain boundary complexion diagram for Bi-doped Ni, Scripta Materialia, 130 (2017) 165-169.

[11] P. Wynblatt, D. Chatain, Solid-state wetting transitions at grain boundaries, Materials Science and Engineering: A, 495 (2008) 119-125.

[12] Y. Mishin, W.J. Boettinger, J.A. Warren, G.B. McFadden, Thermodynamics of grain boundary premelting in alloys. I. Phase-field modeling, Acta Materialia, 57 (2009) 3771-3785.

[13] D. Wolf, J.F. Lutsko, On the geometrical relationship between tilt and twist grain boundaries, Zeitschrift für Kristallographie - Crystalline Materials, 189 (1989) 239-262.

[14] H. Grimmer, W. Bollmann, D.H. Warrington, Coincidence-site lattices and complete pattern-shift in cubic crystals, Acta Crystallographica Section A, 30 (1974) 197-207.

[15] Z. Yu, P.R. Cantwell, Q. Gao, D. Yin, Y. Zhang, N. Zhou, G.S. Rohrer, M. Widom, J. Luo, M.P. Harmer, Segregation-induced ordered superstructures at general grain boundaries in a nickel-bismuth alloy, Science, 358 (2017) 97.

[16] Z. Luo, C. Hu, L. Xie, H. Nie, C. Xiang, X. Gu, J. He, W. Zhang, Z. Yu, J. Luo, A highly asymmetric interfacial superstructure in WC: expanding the classic grain boundary segregation and new complexion theories, Materials Horizons, 7 (2020) 173-180.

[17] Z. Wang, M. Saito, K.P. McKenna, L. Gu, S. Tsukimoto, A.L. Shluger, Y. Ikuhara, Atom-resolved imaging of ordered defect superstructures at individual grain boundaries, Nature, 479 (2011) 380-383.

[18] N.J. Peter, T. Frolov, M.J. Duarte, R. Hadian, C. Ophus, C. Kirchlechner, C.H. Liebscher, G. Dehm, Segregation-Induced Nanofaceting Transition at an Asymmetric Tilt Grain Boundary in Copper, Physical Review Letters, 121 (2018) 255502.

[19] S.A.E. Johansson, G. Wahnström, First-principles study of an interfacial phase diagram in the V-doped WC-Co system, Physical Review B, 86 (2012) 035403.

[20] Q. Zhu, A. Samanta, B. Li, R.E. Rudd, T. Frolov, Predicting phase behavior of grain boundaries with evolutionary search and machine learning, Nature Communications, 9 (2018) 467.

[21] A.L.S. Chua, N.A. Benedek, L. Chen, M.W. Finnis, A.P. Sutton, A genetic algorithm for predicting the structures of interfaces in multicomponent systems, Nature Materials, 9 (2010) 418-422.

[22] S. Kikuchi, H. Oda, S. Kiyohara, T. Mizoguchi, Bayesian optimization for efficient determination of metal oxide grain boundary structures, Physica B: Condensed Matter, 532 (2018) 24-28.

[23] L. Huber, R. Hadian, B. Grabowski, J. Neugebauer, A machine learning approach to model solute grain boundary segregation, npj Computational Materials, 4 (2018) 64.

[24] J.A. Gomberg, A.J. Medford, S.R. Kalidindi, Extracting knowledge from molecular mechanics simulations of grain boundaries using machine learning, Acta Materialia, 133 (2017) 100-108.

[25] C.W. Rosenbrock, E.R. Homer, G. Csányi, G.L.W. Hart, Discovering the building blocks of atomic systems using machine learning: application to grain boundaries, npj Computational Materials, 3 (2017) 29.

[26] H. Zheng, X.-G. Li, R. Tran, C. Chen, M. Horton, D. Winston, K.A. Persson, S.P. Ong, Grain boundary properties of elemental metals, Acta Materialia, 186 (2020) 40-49.

[27] S. Kiyohara, T. Mizoguchi, Effective search for stable segregation configurations at grain boundaries with data-mining techniques, Physica B: Condensed Matter, 532 (2018) 9-14.

[28] S. Kiyohara, H. Oda, T. Miyata, T. Mizoguchi, Prediction of interface structures and energies via virtual screening, Science Advances, 2 (2016) e1600746.

[29] N.J. Peter, C.H. Liebscher, C. Kirchlechner, G. Dehm, Beam-induced atomic migration at Ag-containing nanofacets at an asymmetric Cu grain boundary, Journal of Materials Research, 32 (2016) 968-982.

[30] T. Frolov, D.L. Olmsted, M. Asta, Y. Mishin, Structural phase transformations in metallic grain boundaries, Nature Communications, 4 (2013) 1899.

[31] T. Frolov, M. Asta, Y. Mishin, Segregation-induced phase transformations in grain boundaries, Physical Review B, 92 (2015) 020103.

[32] P.R. Subramanian, J.H. Perepezko, The ag-cu (silver-copper) system, Journal of Phase Equilibria, 14 (1993) 62-75.

[33] H. Ogawa, GBstudio: A Builder Software on Periodic Models of CSL Boundaries for Molecular Simulation, MATERIALS TRANSACTIONS, 47 (2006) 2706-2710.

[34] A. Mansouri Tehrani, A.O. Oliynyk, M. Parry, Z. Rizvi, S. Couper, F. Lin, L. Miyagi, T.D. Sparks, J. Brgoch, Machine Learning Directed Search for Ultraincompressible, Superhard Materials, Journal of the American Chemical Society, 140 (2018) 9844-9853.

[35] P.C. Jennings, S. Lysgaard, J.S. Hummelshøj, T. Vegge, T. Bligaard, Genetic algorithms for computational materials discovery accelerated by machine learning, npj Computational Materials, 5 (2019) 46.

[36] G.S. Rohrer, V. Randle, C.-S. Kim, Y. Hu, Changes in the five-parameter grain boundary character distribution in α-brass brought about by iterative thermomechanical processing, Acta Materialia, 54 (2006) 4489-4502.

[37] G.S. Rohrer, Grain boundary energy anisotropy: a review, Journal of Materials Science, 46 (2011) 5881-5895.

[38] V. Randle, The coincidence site lattice and the ‘sigma enigma’, Materials Characterization, 47 (2001) 411-416.

[39] C.-S. Kim, Y. Hu, G.S. Rohrer, V. Randle, Five-parameter grain boundary distribution in grain boundary engineered brass, Scripta Materialia, 52 (2005) 633-637.

[40] S. Ratanaphan, D.L. Olmsted, V.V. Bulatov, E.A. Holm, A.D. Rollett, G.S. Rohrer, Grain boundary energies in body-centered cubic metals, Acta Materialia, 88 (2015) 346-354.

[41] V. Randle, Role of grain boundary plane in grain boundary engineering, Materials Science and Technology, 26 (2010) 774-780.

[42] H.-I. Yoon, D.-K. Lee, H.B. Bae, G.-Y. Jo, H.-S. Chung, J.-G. Kim, S.-J.L. Kang, S.-Y. Chung, Probing dopant segregation in distinct cation sites at perovskite oxide polycrystal interfaces, Nature Communications, 8 (2017) 1417.

[43] R. Kirchheim, Reducing grain boundary, dislocation line and vacancy formation energies by solute segregation: II. Experimental evidence and consequences, Acta Materialia, 55 (2007) 5139-5148.

[44] D.L. Olmsted, D. Buta, A. Adland, S.M. Foiles, M. Asta, A. Karma, Dislocation-Pairing Transitions in Hot Grain Boundaries, Physical Review Letters, 106 (2011) 046101.

Chapter 4. Deciphering the GB Segregation in High-Entropy Alloy: Coupled Multicomponent Segregation and Disordering

4.1. Introduction

Since the Bronze and Steel Ages, the development of every major class of metallic alloys, such as the Cu, Fe, Al, Ti, and Ni-based alloys, have revolutionized technologies and changed our daily lives [1-4]. High-entropy alloys (HEAs), also known as multi-principal alloys (MPEAs) or complex concentrated alloys (CCA), represent the newest class of alloys that attract worldwide interest owing to their promising mechanical properties [1-4]. The vast composition spaces of HEAs offer immense opportunities for designing materials for various applications.

In every class of polycrystalline metallic alloys, grain boundaries (GBs) are the ubiquitous crystal imperfection [5, 6]. The elemental segregation (*a.k.a* adsorption) at GBs is a critical interfacial phenomenon because it can change microstructural evolution [7-9], induce chemical transitions [10, 11], and govern a broad range of materials properties [12-14]. Even though the GB segregation in metallic alloys have been extensively researched for more than 50 years [15-17], most of the studies are limited to conventional alloys with only one or two base elements [18-22]. The GB segregation in multicomponent systems, especially for the emerging HEAs containing five or more principle elements, are hitherto only investigated by few experiments [23, 24] and modeling [25, 26]. The underlying physical mechanisms and predictive model of GB segregation in HEAs still remain elusive, which motivates us to explore.

More broadly, GBs can be treated as 2D interfacial phases at thermodynamic equilibria. It has been proposed that constructing GB properties diagrams as a function of temperature and bulk composition [5, 6] is as potentially important as developing “bulk” phase diagrams. Recently, a spectrum of GB properties diagrams have been reported for binary or ternary systems [21, 22, 27, 28], but they are rarely developed for multicomponent systems [29, 30]. The challenge mainly comes from the large compositional space. For example, four independent compositional degrees of freedom (DOFs) of CrMnFeCoNi HEAs associated with temperature in 5D space make it impossible to develop GB diagrams by using any conventional methods. Furthermore, most of GB diagrams are based on either symmetric tilt or twist GBs that are relatively easy to image and model. The more general GBs (asymmetric GB with mixed twist and tilt feature), which are ubiquitous in polycrystalline materials and often the weak links chemically and mechanically [27, 31], are still scarcely studied for HEA.

Herein, by combining the high-throughput hybrid Monte Carlo/molecular dynamic (MC/MD) simulations and artificial neural networks (ANN), we can accurately predict the GB properties as functions of four compositional DOFs and temperature in 5D space for a representative general GB in CrMnFeCoNi HEAs. As an example to quest the new underlying physics, our MC/MD simulations from ternary to quinary alloys shows that site competition in more ordered GBs result in weak segregation in medium-entropy alloys, while the multicomponent segregation coupled with GB disordering can induce strong co-segregation in

HEAs. Furthermore, a physics-informed model was developed to address the relation between segregation and GB disordering that cannot be captured by classical thermodynamic isotherms.

4.2. Computational Methods

4.2.1. High-Entropy Alloy Selection and Principle Component Analysis

In this work, the composition of each element was fixed in a range from 5 at% to 35 at% with a step of 5 at% for $Cr_xMn_yFe_zCo_lNi_m$. Since $x + y + z + l + m = 1$, there are totally 1371 $Cr_xMn_yFe_zCo_lNi_m$ subsystems. Among them, we randomly selected 258 subsystems to perform high-throughput MC/MD simulations for data set generation. Principle component analysis (PCA) was used to analyze the composition distribution for these 258 subsystems, and singular value decomposition (SVD) algorithm was chosen. The PCA were performed by Matlab2019a.

4.2.2. High-Throughput MC/MD Simulation

The energy minimization for each GB was first performed at 0 K by conjugate gradient (CG) algorithm. Subsequently, the hybrid Monte Carlo and molecular dynamics (hybrid MC/MD) simulations in constant-*NPT* ensembles were carried out to swap atoms to find energetically favorable structure. Five MC trial moves were conducted between each MD step with a 0.1 fs MD time step, and 10^5 hybrid MC/MD steps performed for each simulation to achieve convergence. All MC/MD simulations were performed using LAMMPS code [32] and 2NN MEAM

potential [33] was adopted for CrMnFeCoNi alloy.

The methods used to calculate GB excess of adsorption (Γ_{Cr}, Γ_{Mn}, Γ_{Fe}, Γ_{Co}, Γ_{Ni}) and disorder ($\Gamma_{Disorder}$) diagrams were same as our prior works, see detailed procedures in refs. [22, 27]. For calculating GB free volume (V_{Free}) for HEA GB, we used the relation of $V_{Free} = V_{Total} \cdot \sum \Gamma_i$, where V_{Total} is the total volume of GB structure and i = Cr, Mn, Fe, Co, Ni.

4.2.3. Artificial Neural Networks

The data set was divided into training, validation, and test subsets in a ratio of 0.7:0.15:0.15. The Levenberg-Marquardt backpropagation function was adopted to train ANN models. We found the optimized network architectures for the ANN (n^i-$n^{[i]}$-1, where n^i is the number of input parameter, $n^{[i]}$ (the number of neurons in the single layers) is set to be 6-20-1. All data processing and ANN development were performed by Deep Learning Toolbox in Matlab2019a.

4.2.4. First-Principles Calculations

The first-principles DFT calculations were performed by using the Vienna *ab initio* Simulations Package (VASP) [34, 35]. The Kohn-Sham equations were used to solve the projected-augmented wave (PAW) method [36, 37] along with standard PAW potentials. All GB structures were fully relaxed until the Hellmann-Feynman forces were smaller than 0.02 eV/Å. The Brillouin-zone integrations were sampled on a Γ-centered 2×2×1 k-point grids. The kinetic energy cutoff for plane waves was set to 368 eV. The convergence criterion for the electronic self-

consistency was set to 10^{-4} eV. The “high” precision setting was adopted to avoid wrap around errors. The spin-polarization was not considered due to weak effect on atomic arrangement [38]. The SBO was calculated by using DDEC06 method [39] following the all-electron static calculations.

4.3. Results and Discussion

4.3.1. Workflow of Machine Learning Prediction of GB Diagrams in HEA

The workflow of ANN prediction for HEA GB diagrams is displayed in Fig. 4.1. First, we selected a Σ81 mixed GB as the model to represent general GBs in polycrystal and randomly generated 258 different HEA compositions out of 1371 total subsystems by varying the amount of each element from 5-35% with a step of 5%. Second, principle components analysis (PCA) was used to ensure the 258 HEA compositions are randomly selected. Third, the high-throughput isobaric *NPT*-based MC/MD simulations were carried out to calculate bulk composition of each element and GB excess of adsorption (Γ_{Cr}, Γ_{Mn}, Γ_{Fe}, Γ_{Co}, Γ_{Ni}), GB excess of disorder ($\Gamma_{\mathrm{Disorder}}$), and GB free volume ($V_{\mathrm{Free}}$) from 1000 K to 1300 K with a temperature step of 100 K. Fourth, the MC/MD-simulated dataset was used to train, evaluate, and test ANN models to predict six GB properties (except V_{Free} due to weak correlation). Here, the five bulk compositions and temperature are used as input parameters (Fig. 4.1(d)). Next, the well-trained ANN models can be used to predict GB property diagrams with multiple variables. For example, we can generate isothermal surfaces of Γ_{Cr} for $Cr_xMn_yFe_zCo_{0.2}Ni_{0.2}$ subsystem, where $x + y + z = 0.6$, from 1000 to 1200 K (Fig. 4.1(e)). It is worth noting that we performed

strict benchmark simulations to validate our *NPT*-based MC/MD method by comparing it with prior *NVT*-based MC simulations [26] as well as experiments [23, 24, 40] (Fig. 4.2). Finally, we analyzed MC/MD-simulated GB structures to decipher the coupling effect of segregation and disordering on GB segregation in HEA and developed a physics-informed surrogate model to predict GB properties (Fig. 4.1(f)).

4.3.2. ANN Prediction of GB Diagrams

The dataset generated by 1032 MC/MD simulations were used to train, evaluate, and test one-layer single-task ANN models to predict six GB properties (except V_{Free} due to weak correlation). The histogram of root-mean-square errors (RMSEs) was used to justify ANN performances. Notably, the ANN models are sufficiently accurate to predict the values of Γ_{Co}, Γ_{Fe}, Γ_{Cr}, and Γ_{Mn} owing to small RMSEs, but slightly less accurate for predicting Γ_{Ni} and $\Gamma_{\mathrm{Disorder}}$ (Fig. 4.3). This can be further supported by the parity plots between ANN prediction and MC/MD simulation, where the promising linear relation can be achieved for Γ_{Cr}, Γ_{Mn}, Γ_{Fe}, and Γ_{Co} (Fig. 4.4) but relatively large deviation was found for Γ_{Ni} and $\Gamma_{\mathrm{Disorder}}$. Such a less performance can be ascribed to the weak segregation of Ni and large uncertainty of MC/MD calculation on $\Gamma_{\mathrm{Disorder}}$. Finally, we believe the ANN models are robust enough to predict most GB properties, especially for strong segregation (e.g., Cr and Mn) and de-segregation elements (e.g., Fe and Co).

To further validate our ANN models, we use structural similarity index (SSIM; 1 = same and 0 = different) to compare the similarity of ANN-predicted GB binary

diagrams *vs*. MC/MD simulations (see representative GB diagrams in Figs. 4.5(b-c)). The SSIM histogram (Fig. 4.6) shows that the high values of ~0.88-0.89 can be obtained for most GB property diagrams, such as Γ_{Cr}, Γ_{Mn}, Γ_{Fe}, and Γ_{Co}, but relatively low SSIM values (~0.63-0.66) for Γ_{Ni} and $\Gamma_{\mathrm{Disorder}}$ diagrams. Note that the low SSIM can be also attributed to the relatively large RMSEs of ANN prediction.

By comparing the ANN models *vs*. MD/MD simulations, ANN prediction outperforms than MC/MD simulations in two aspects. First, ANN models can significantly minimize the MC/MD errors due to the large thermal noises at high temperatures (Fig. 4.7). Second, the ANN models are more efficient than MC/MD simulations to predict GB diagrams with multiple variables, such as GB ternary diagrams. For example, Fig. 4.5(d-i) shows the ANN-predicted Γ_{Cr} diagram as a function of three compositions in $Cr_xMn_{0.2}Fe_yCo_{0.2}Ni_z$ subsystem, where $x + y + z = 0.6$, at 1000 K. Finally, the efficient ANN models make it possible to map out GB states as a function of four compositional DOFs and temperature in 5-D space for HEA.

4.3.3. Coupling Effect on GB Segregation in HEA

Although ANN models can successfully predict the GB properties of HEA, the underlying physical mechanisms of segregation remain elusive. Here, by performing MC/MD simulations from ternary (medium-entropy) to quinary (high-entropy) systems using nine representative alloys, we found that the site competition associated with ordered GB can lead to weak segregation in ternary

systems, but multicomponent segregation coupled with large GB disordering can induce strong co-segregation in quinary system (Fig. 4.8). For example, the MC/MD-simulated GB structure of CrMnNi ternary alloy at 1000 K (Fig. 4.8(c)) shows that the relatively ordered GB structure ($\Gamma_{\mathrm{Disorder}}$ of ~39 nm^{-2}) has weak segregation of Cr and tiny(almost no) segregation of Mn (Γ_{Cr} = 5.3 nm^{-2} and Γ_{Mn} = 0.8 nm^{-2}). However, CrMnFeCoNi HEA with more disordered GB structure ($\Gamma_{\mathrm{Disorder}}$ of ~43 nm^{-2}) exhibit strong co-segregation of Cr and Mn (Γ_{Cr} = 18.6 nm^{-2} and Γ_{Mn} = 7.0 nm^{-2}). The compositional profile (Fig. 4.8(c-d)) further confirms the strong accumulation of both Cr and Mn atoms at CrMnFeCoNi HEA GB, but weak segregation at CrMnNi GB. Meanwhile, the disorder profile also verifies the large disordering at CrMnFeCoNi HEA GB with ~0.88 nm thickness, but less disordering at CrMnNi GB with ~0.75 nm thickness.

It is interesting to note that, on one hand, for the systems without Mn element (e.g., CrCoFe and CrFeCoNi), Cr atoms always de-segregate at relatively ordered GBs owing to strong agglomeration at bulk phases. On the other hands, the structural analysis based on polyhedral template matching (PTM) approach [41] shows that Mn segregation can always induce large GB disordering. Since disordered GB can prompt segregation, this unambiguously indicate that the Cr segregation at HEA GB is strongly controlled by the coupled interaction between Mn segregation and Mn-induced GB disordering. Finally, it is worthy to note that all abovementioned phenomena can be also found in other ternary, quaternary, and quinary systems, thereby suggesting the generality of this coupling effect.

4.3.4. Correlation Analysis for GB Properties

We further analyzed the correlation between GB adsorption (i.e., Γ_{Cr}, Γ_{Mn}, Γ_{Fe}, Γ_{Co}, Γ_{Ni}) and structural properties ($\Gamma_{\mathrm{Disorder}}$ and V_{Free}) by calculating the Pearson correlation coefficient (PCC) using the MC/MD-simulated dataset. Notably, the heat map of PCC shows that GB disordering has strong correlations with GB adsorption properties (Fig. 4.9(a)). However, there is almost no correlation between GB free volume (V_{Free}) with others. Especially, the segregation of Mn (Γ_{Mn}) has the strongest correlation with GB disorder ($\Gamma_{\mathrm{Disorder}}$) among all elements, which agree with the MC/MD simulations showing that Mn segregation can induce large GB disordering. In addition, by calculating the PCC at different temperatures, we found that the correlations between GB disordering and adsorption properties decrease as increasing the temperature, while the correlations between other GB properties almost remain unchanged (Fig. 4.9(b)). Therefore, the correlation analysis further verifies the importance of interfacial disordering on GB segregation.

Next, we examined the correlation of Γ_i *vs.* $\Gamma_{\mathrm{Disorder}}$ at different temperatures to further understand their quantitative relations. Taking Cr as one example, Fig. 4.9(c) shows that the MC/MD-simulated Γ_{Cr} has strong linear relation with $\Gamma_{\mathrm{Disorder}}$ at certain temperatures. Specifically, the regression lines of Γ_{Cr} *vs.* $\Gamma_{\mathrm{Disorder}}$ have positive slope ($\beta_{\mathrm{Disorder}}^{\mathrm{Cr}}$), which are steep at relatively low temperatures (Fig. 4.9(c)). Such a variation results in a linear decay of $\beta_{\mathrm{Disorder}}^{\mathrm{Cr}}$ with increasing temperature, and a similar behavior can be also found for $\beta_{\mathrm{Disorder}}^{\mathrm{Mn}}$ (Fig. 4.10). In contrast, The slope of $\Gamma_{\mathrm{Fe(Co)}}$ *vs.* $\Gamma_{\mathrm{Disorder}}$ regression lines is

negative ($\beta_{\mathrm{Disorder}}^{\mathrm{Fe(Co)}}$ < 0), and $\beta_{\mathrm{Disorder}}^{\mathrm{Fe(Co)}}$ linearly increases as increasing the temperature (Fig. 4.9(d)). By plotting the regression lines of $\beta_{\mathrm{Disorder}}^{i}$ *vs*. temperature for all five elements (Fig. 4.9(d)), we found that they all cross over at nearly one point on the *x* axis with $\beta_{\mathrm{Disorder}}^{i}$ ~ 0. Here, we denote this corresponding temperature as the critical temperature ($T_c \approx 1350$ K).

4.3.5. Physics-Informed Model for GB Segregation in HEA

Expanding the Brunauer, Emmett, and Teller (BET) type isotherm of GB segregation [17] and basing on the linear correlation between Γ_i *vs.* $\Gamma_{\mathrm{Disorder}}$, we further developed a physics-informed model to predict GB adsorption Γ_i (*i* = Cr, Mn, Fe, Co, Ni) as a function of temperature (*T*) and bulk composition x_b^i. First, we express the GB excess disorder as:

$$\Gamma_{\mathrm{Disorder}} = \Sigma(\varepsilon_{\mathrm{Disorder}}^{i} \cdot x_{\mathrm{b}}^{i}) \cdot \exp(-\frac{E_{\mathrm{a}}}{RT}) \quad (1)$$

where $\varepsilon_{\mathrm{Disorder}}^{i}$ is a coefficient ($i = \mathrm{Cr, Mn, Fe, Co, or\ Ni}$), E_{a} is the activation energy of disordering, and *R* is the Boltzmann constant. By using the fitted parameters listed in Table 4.1, the small RMSE value of ~2.3 nm^{-2} can be achieved, suggesting the good performance for prediction of $\Gamma_{\mathrm{Disorder}}$. Second, we express the GB excess of solute *i* (adsorption) as:

$$\Gamma_i(T, x_i, \Gamma_{\mathrm{Disorder}}) = (\Gamma_{\mathrm{Disorder}} - \Gamma'_{\mathrm{Disorder}}) \cdot \beta_{\mathrm{Disorder}} \cdot (T_{\mathrm{c}} - T) + \Sigma(\varepsilon_{\mathrm{Seg}}^{i} \cdot x_b^i) \quad (2)$$

where $\Delta\Gamma_{Disorder} = \Gamma_{\mathrm{Disorder}} - \Gamma_{Disorder}^{min}$, $\Gamma_{Disorder}^{min}$ is the minimal $\Gamma_{\mathrm{Disorder}}$ among all possible HEA compositions, $\beta_{\mathrm{Disorder}}$ is a temperature coefficient , $\varepsilon_{\mathrm{Seg}}^{i}$

is a GB segregation coefficient, and T_c is the critical temperature. Notably, we can predict the Γ_i with relatively small RMSEs (albeit a bit larger than ANN) for each element using a simple analytic form based in Eqs. (1) and (2). Further, the parity plots show that good linear relations between model prediction *vs*. MC/MD simulations can be achieved for Cr and other four elements, thereby suggesting promising performance of this model.

Several interesting observations with physical insights can be found for this model. By plotting the values of first (pink dots) and second (blue dots) terms for Γ_{Cr} on the right-hand side of Eq. (2), along with total Γ_{Cr}, in the parity plot (Fig. 4.11(a)), we found that first term plays the dominated role. Since these two terms represent the disordering and chemical compositional contributions to GB adsorption, respectively, this again suggests the importance of disordering effect on GB segregation in HEA.

Moreover, it is interesting to compare the compositional coefficients of the second term in Eq. (2) with the segregation enthalpies in binary systems. Here, we plotted the four compositional coefficients for Cr segregation ($\Sigma\varepsilon_{\mathrm{Seg}}^{i-\mathrm{Cr}}, i = \mathrm{Mn, Fe, Co, Ni}$) and corresponding Cr segregation enthalpies ($\Delta H_{\mathrm{seg}}^{i-\mathrm{Cr}}$) [42] together in Fig. 4.11(b). Interestingly, $\Sigma\varepsilon_{\mathrm{Seg}}^{i-\mathrm{Cr}}$ has similar distribution as $\Delta H_{\mathrm{seg}}^{i-\mathrm{Cr}}$. For example, both $\Sigma\varepsilon_{\mathrm{Seg}}^{\mathrm{Fe(Co)-Cr}}$ and $\Delta H_{\mathrm{Seg}}^{\mathrm{Fe(Co)-Cr}}$ are positive, suggesting that Cr atoms prefer to segregate at Fe(or Co) GBs. However, the negative values of $\Sigma\varepsilon_{\mathrm{Seg}}^{\mathrm{Mn(Ni)-Cr}}$ and $\Delta H_{\mathrm{Seg}}^{\mathrm{Mn(Fe)-Cr}}$ indicate Cr atoms are unfavorable to segregate at Mn(or Ni) GBs. The

similar behavior of $\Sigma\varepsilon_{\mathrm{Seg}}^{i-\mathrm{Cr}}$ and $\Delta H_{\mathrm{seg}}^{i-\mathrm{Cr}}$ not only indicate they have strong correlation, but also supports the assumption of our model that the chemical compositional effect on GB segregation can be treated as a linear combination of individual elements.

To further understand the physical meaning of critical temperature T_{c}, we derived an approximated relation of $T_{\mathrm{c}} = \frac{\Delta H_{\mathrm{Seg}}^{\mathrm{All}}}{1.6R}$ based on a revised ideal-solution model, where segregation enthalpy is written as $\Delta H_{\mathrm{Seg}}^{\mathrm{All}} = \Delta H_{\mathrm{Seg}}^{\mathrm{o}} + \Delta H_{\mathrm{Seg}}^{\mathrm{Dis}}(\eta)$. The similar T_{c} of all elements (Table 4.2) indicates they have comparable $\Delta H'^{\mathrm{Dis}}_{\mathrm{Seg}}$ and similar segregation ability. Therefore, the vanishing of disordering effect can be considered as the segregation compensation effect due to strong site competition at T_{c}

Notably, the calculated $\Delta H_{\mathrm{Seg}}^{\mathrm{All}}$ at T_{c} is about -0.186 eV/atom. Next, we performed DFT calculations to compute Cr segregation energy ($E_{\mathrm{Seg}}^{\mathrm{Cr}}$) at 0 K to compare with $\Delta H_{\mathrm{Seg}}^{\mathrm{All}}$. Here, a representative Σ15 asymmetric GB with 288 atoms was adopted for calculation, and three non-equimolar HEA compositions (HEA1-3) with strong Cr segregation selected from MC/MD simulation were considered. The calculated $E_{\mathrm{Seg}}^{\mathrm{Cr}}$ is around -0.026 eV/atom (green circles in Fig. 4.11(b)), which is significantly higher than $\Delta H_{\mathrm{Seg}}^{\mathrm{All}}$ (red star). This suggest that GB disordering can lower the segregation enthalpies of Cr and thus confirms the importance of disordering effect on GB segregation in HEA.

4.3.6. GB Segregation in Classical Thermodynamic Models *vs*. HEA

It is also interesting to compare the GB segregation predicted by regular-solution models with MC/MD-simulated segregation in HEA to illustrate the unique behaviors in HEAs. First, by using the Wynblatt-Ku model [43] (a modified regular solution model by considering both chemical and elastic contribution to GB), we computed GB concentration (x_{GB}) of Cr as a function of bulk composition (x) for four $Cr_xMn(Fe, Co, Ni)_{1-x}$ binary systems at 1000 K (see Fig. 4.11(c)). Meanwhile, we selected four similar $Cr_xMn(Fe, Co, Ni)_{0.4-x}$ HEA subsystems ($0.05 \leq x \leq 0.35$; the fractions only change between Cr and another one element while the composition of rest three are fixed at 0.2) and plotted MC/MD-simulated Γ_{Cr} as a function of x in Fig. 4.11(d). Interestingly, the segregation ability of Cr in binary systems has a tendency of Fe > Co > Ni > Mn (Fig. 4.11(c)), while it turns to Mn ≈ Ni > Co ≈ Fe in HEAs (Fig. 4.11(d)). Such a different behavior indicates GB segregation behavior of HEA is beyond regular-solution model.

Recently, Li et al., applied a density-based thermodynamic model to explain the GB misorientation and energy effects on GB segregation in CrMnFeCoNi HEA [25]. This phenomenological model was under the assumption that GB energy can be written a function of GB density (ρ_{GB}), which alternatively indicates the importance of GB free volume (V_{Free}). However, the PCC heat map (Fig. 4a) shows that V_{Free} almost has no correlations with GB adsorption properties (Γ_i). Instead, $\Gamma_{\mathrm{Disorder}}$ exhibits strong correlation with Γ_i (Fig. 4.9(a)). Thus, GB disordering

should be treated as a key parameter for developing novel phenomenological models in the future

4.3.7. Generality of MC/MD-Simulated GB Behavior

To test generality of GB behavior in the selected Σ81 mixed GB, we performed MC/MD simulations for other three types GBs including Σ15 asymmetric GB, Σ41 tilt GB, and Σ13 twist GB. For each of them, four non-equimolar HEAs identified from Σ81 GB diagrams, where first three (named as HEA1-3) exhibit strong Cr segregation while last one (HEA4) has weak Cr segregation, were considered. Notably, MC/MD simulations show that HEA1-3 always have large Γ_{Cr} but HEA4 has small value of Γ_{Cr} for all other GBs (Table 4.3). Meanwhile, MC/MD-simulated GB structures with Cr compositional profile further verify the strong Cr segregation in HEA1-3 but tiny segregation in HEA4 (Fig. 4.12). Further, DFT calculation also confirms that $E_{\mathrm{Seg}}^{\mathrm{Cr}}$ (around -0.026 eV/atom) of HEA1-3 is significantly lower than HEA4 with a $E_{\mathrm{Seg}}^{\mathrm{Cr}}$ value of ~ 0.0001 eV/atom (Table 4.3). Therefore, the segregation behavior in Σ81 mixed GB is highly general and MC/MD-simulated dataset based on this GB is representative.

4.3.8. DFT Calculation for Sum of Bond Ordering in HEA

A recent work shows that sum of bond ordering (SBO) can be considered as a descriptor to predict GB segregation [27]. Herein, we also calculated SBO for four non-equimolar HEA1-4. Interestingly, Fe, Cr, and Co atoms always share similar SBO which are ~4.04, ~3.95, and ~3.78 respectively, but Mn and Ni exhibits

two distinct SBO which are respectively ~4.20 and ~3.49. Since SBO represents the total number of electrons that form bonds, the similar SBO always indicates similar bonding environments. Therefore, Fe and Co atoms may provide more favorable segregation sites for Cr, which successfully explains that Cr is highly favorable to segregate at Fe/Co-rich GBs (e.g., HEA1-3). However, Mn and Ni atoms, with dissimilar SBO, may inhibit (or compete) Cr segregation due to different chemical environment (e.g., HEA4).

Moreover, SBO can be used as a descriptor design GB segregation in HEAs. For example, if we want to promote segregation of certain element (e.g., Cr), we may increase the fraction of elements with similar SBO (e.g., Fe and Co) and reduce the elements with different SBO (e.g., Mn and Ni).

4.4. Conclusion

In summary, using hybrid MC/MD simulations, PCA, correlation analysis, we reveal the multicomponent segregation, GB disordering, and their couplings can control the GB segregation in HEA. A physics-informed analytical model was developed to predict GB adsorption properties as a function of temperature and bulk compositions. The ANN model is more accurate and efficient to predict GB property diagrams as a function of four independent compositional DOFs and temperature in 5-D space. This work not only opens a new paradigm to explore the vast compositional space of high-entropy materials, but also expands our fundamental knowledge on segregation theory.

Chapter 4, in part, is a reprint of the material “Deciphering the Grain-Boundary Properties in High-Entropy Alloys in a 5D Space: Coupled Segregation and Disordering”, C. Hu and J. Luo, in preparation. The dissertation author was the primary investigator and first author of this paper.

Table 4.1 Fitted coefficient for Eq. (1). The E_a is the activation energy and $\varepsilon^{i}_{\mathrm{Disorder}}$ is the compositional coefficient on GB disorder, where i = Cr, Mn, Fe, Co, Ni. The root-mean-square errors (RMSEs) of fitted statistical model and ANN model are also tabulated. The RMSEs of ANN models are averaged value of training, evaluation, and test sets.

$\varepsilon^{\mathrm{Cr}}_{\mathrm{Disorder}}$ (atom/nm^2)	$\varepsilon^{\mathrm{Mn}}_{\mathrm{Disorder}}$ (atom/nm^2)	$\varepsilon^{\mathrm{Fe}}_{\mathrm{Disorder}}$ (atom/nm^2)	$\varepsilon^{\mathrm{Co}}_{\mathrm{Disorder}}$ (atom/nm^2)	$\varepsilon^{\mathrm{Ni}}_{\mathrm{Disorder}}$ (atom/nm^2)	E_a (meV)	Model RMSE (nm^{-2})	ANN RMSE (nm^{-2})
52	49	46	44	23	-15.4	2.4	1.8

Table 4.2 Fitted coefficient of physical-informed model using 1032 hybrid MC/MD data points. The T_c is the critical temperature, $\omega_{\mathrm{Disorder}}$ is the coupling coefficient of GB disordering and temperature, $\varepsilon_{\mathrm{Seg}}^{i}$ is the compositional coefficient on GB segregation, where i = Cr, Mn, Fe, Co, Ni. The root-mean-square errors (RMSEs) of fitted statistical model and ANN model are also tabulated. The RMSEs of ANN models are averaged value of training, evaluation, and test sets.

	T_c (K)	$\omega_{\mathrm{Disorder}}$ (K^{-1})	$\varepsilon_{\mathrm{Seg}}^{\mathrm{Cr}}$ (atom/nm^2)	$\varepsilon_{\mathrm{Seg}}^{\mathrm{Mn}}$ (atom/nm^2)	$\varepsilon_{\mathrm{Seg}}^{\mathrm{Fe}}$ (atom/nm^2)	$\varepsilon_{\mathrm{Seg}}^{\mathrm{Co}}$ (atom/nm^2)	$\varepsilon_{\mathrm{Seg}}^{\mathrm{Ni}}$ (atom/nm^2)	Fitted RMSE (nm^{-2})	ANN RMSE (nm^{-2})
Γ_{Cr}	1347	0.0109	32	-47	13	1	-17	7.4	3.0
Γ_{Mn}	1464	0.0014	1	-5	8	3	1	1.2	0.6
Γ_{Fe}	1370	-0.0046	-13	26	-26	14	14	5.3	1.9
Γ_{Co}	1371	-0.0075	-15	27	4	-17	12	3.8	1.6
Γ_{Ni}	/	~0	-0.5	-7.1	-6.4	-1.2	3.7	0.88	0.7

Table 4.3. Comparison of MC/MD-simulated asymmetric Σ81GB with other types of GBs. HEA1-3 are non-equimolar HEAs with large GB excess of Cr adsorption (Γ_{Cr}) and disorder ($\Gamma_{\mathrm{Disorder}}$) in Σ81 asymmetric GB based on ANN-predicted GB diagrams, and HEA4 has weak Cr segregation and small disorder. The segregation structures of HEA1-4 share similarity for other asymmetric Σ15 GB, tilt Σ41GB, and Σ13 twist GB, where HEA1-3 have larger Γ_{Cr} and $\Gamma_{\mathrm{Disorder}}$ than HEA4. The Γ_{Cr} and $\Gamma_{\mathrm{Disorder}}$ were calculated from MC/MD-simulated GB structures at 1000 K. A detailed comparison of GB structures was shown in Fig. 4.12.

	Composition	Σ81 Mixed. GB[a]		Σ15 Asym. GB		Σ41 Tilt GB		Σ13 Twist GB		DFT[b] E_{Seg}^{Cr} (meV/atom)
		Γ_{Cr} (nm^{-2})	$\Gamma_{\mathrm{Disorder}}$ (nm^{-2})	Γ_{Cr} (nm^{-2})	$\Gamma_{\mathrm{Disorder}}$ (nm^{-2})	Γ_{Cr} (nm^{-2})	$\Gamma_{\mathrm{Disorder}}$ (nm^{-2})	Γ_{Cr} (nm^{-2})	$\Gamma_{\mathrm{Disorder}}$ (nm^{-2})	
HEA1	$Cr_{0.2}Mn_{0.05}Fe_{0.35}Co_{0.2}Ni_{0.2}$	31	41	69	64	107	42	44	32	-28.3
HEA2	$Cr_{0.2}Mn_{0.2}Fe_{0.35}Co_{0.2}Ni_{0.05}$	44	49	60	68	108	58	23	30	-23.6
HEA3	$Cr_{0.25}Mn_{0.2}Fe_{0.25}Co_{0.2}Ni_{0.10}$	45	47	42	61	101	37	26	32	-24.7
HEA4	$Cr_{0.20}Mn_{0.05}Fe_{0.2}Co_{0.2}Ni_{0.35}$	4	37	15	58	14	31	12	31	0.1

a. ANN models were developed from Σ81 asymmetric GB.

b. DFT calculations were based on ten random configurations for Cr segregated and non-segregated structures using a small Σ15 asymmetric GB with 288 atoms.

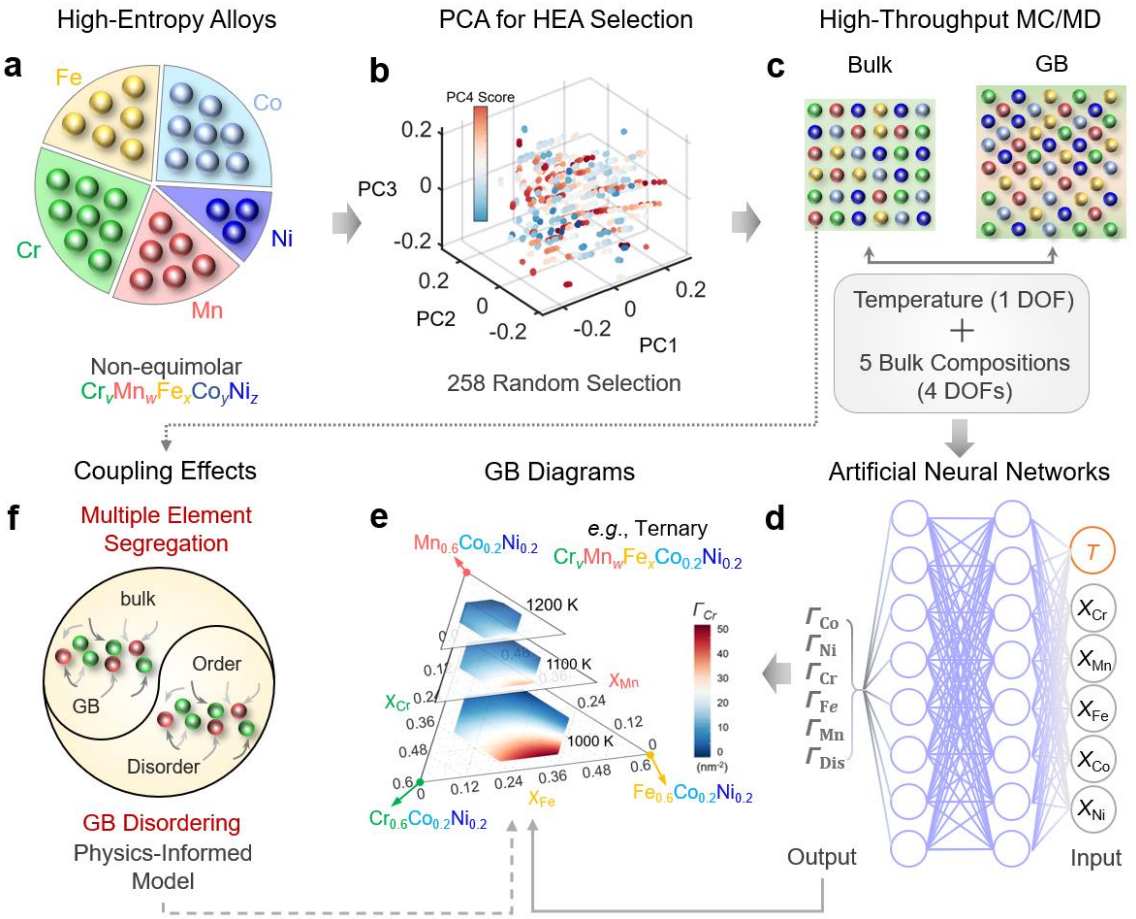

Figure 4.1 Workflow of machine learning prediction of grain boundary (GB) properties for high-entropy alloys (HEAs). (a) Schematic diagram of non-equimolar five-element $Cr_xMn_yFe_zCo_lMn_m$ alloys. (b) Principle component analysis (PCA) for the random selection of 258 HEAs. (c) 1032 individual isothermal-isobaric (constant-*NPT*) ensemble hybrid Monte Carlo and molecular dynamics (MC/MD) simulations were performed for 258 HEAs to calculate GB excesses of solutes (i.e., $\Gamma_{\mathrm{Cr}}, \Gamma_{\mathrm{Mn}}, \Gamma_{\mathrm{Fe}}, \Gamma_{\mathrm{Co}}, \Gamma_{\mathrm{Ni}}$), disorder ($\Gamma_{\mathrm{Disorder}}$), and free volume ($V_{\mathrm{Free}}$). This dataset was used to develop the artificial neural networks (ANN) models. (d) Schematic diagram of an ANN with a 6-20-1 architecture for predicting six GB properties, with the bulk compositions and temperature as the input parameters. (e) The ANN model can predict GB properties in the 5D space to help design HEAs; *e.g.*, here, we plot isothermal sections of the Γ_{Cr} diagram of the $Cr_xMn_yFe_zCo_{0.2}Ni_{0.2}$ subsystem, where $x + y + z = 0.6$, from 1000 to 1200 K. Meanwhile, we also developed a physics-informed model to predict GB diagrams. (f) MC/MD simulations can also help us to reveal new physical insights, *e.g.*, the couplings of the segregation of multiple elements and interfacial disordering in HEAs, and a novel physics-informed model was develop to predict GB segregation of HEAs that cannot be captured by classical thermodynamic models.

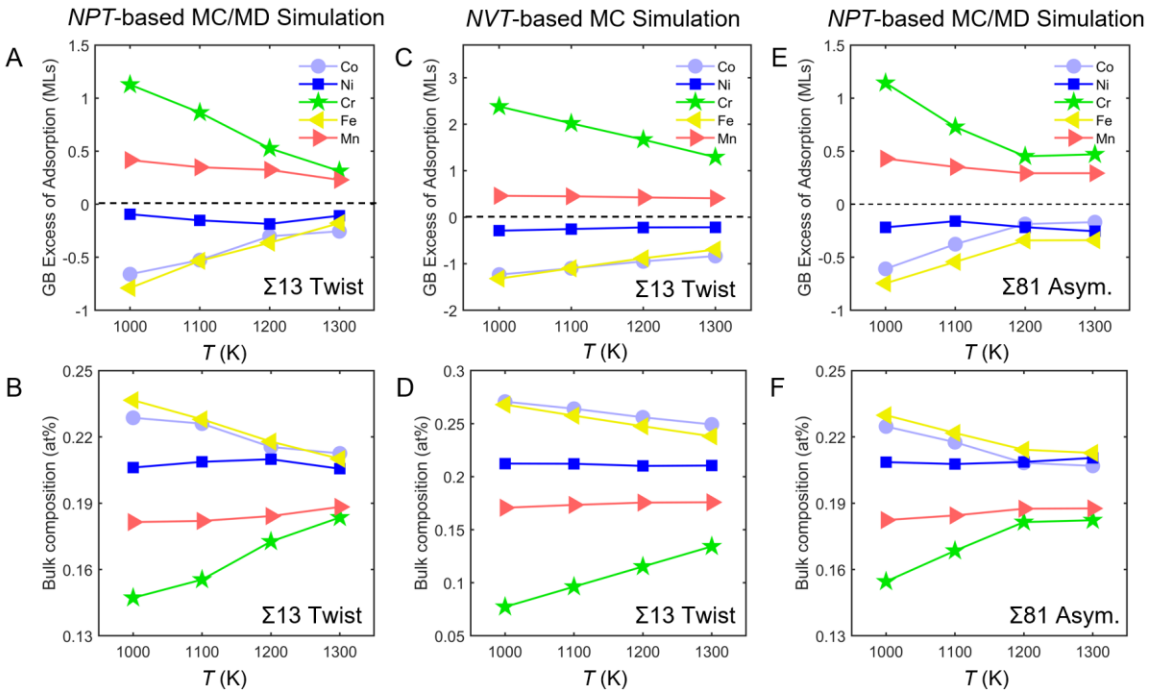

Figure 4.2 Benchmark of *NPT*-based MC/MD simulations *vs*. *NVT*-based MC simulation for a Σ13 twist GB of the equimolar HEA. (a) The GB excess of segregation of each element from 1000 K to 1300 K calculated by *NPT*-based MC/MD simulations. (b) The elemental bulk composition from 1000 K to 1300 K by our *NPT* simulations. (c) The GB excess of segregation and (d) the bulk composition of each element from 1000 K to 1300 K based on prior *NVT* simulations. (e) The calculated GB excess of segregation and f, bulk compositions by *NPT*-based MC/MD simulations for another Σ81 asymmetric GB.

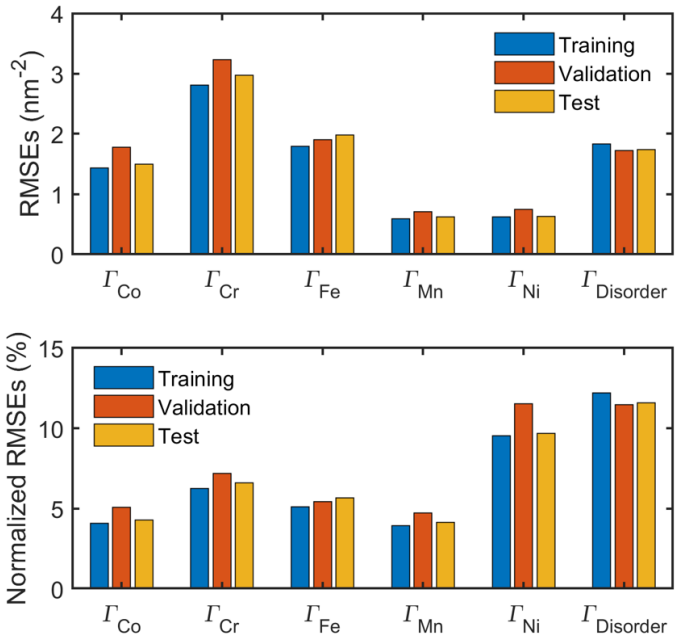

Figure 4.3 Root-mean-square errors (RMSEs) of ANN model. Histogram of RMSEs of the ANN training, evaluation, and test data sets (upper panel) for six GB properties (i.e., Γ_{Cr}, Γ_{Mn},Γ_{Fe},Γ_{Co},Γ_{Ni}, and $\Gamma_{\mathrm{Disorder}}$). Histogram of normalized RMSEs (divided by maximal value or maximal variation range) of the ANN training, evaluation, and test data sets (bottom panel) for six GB properties.

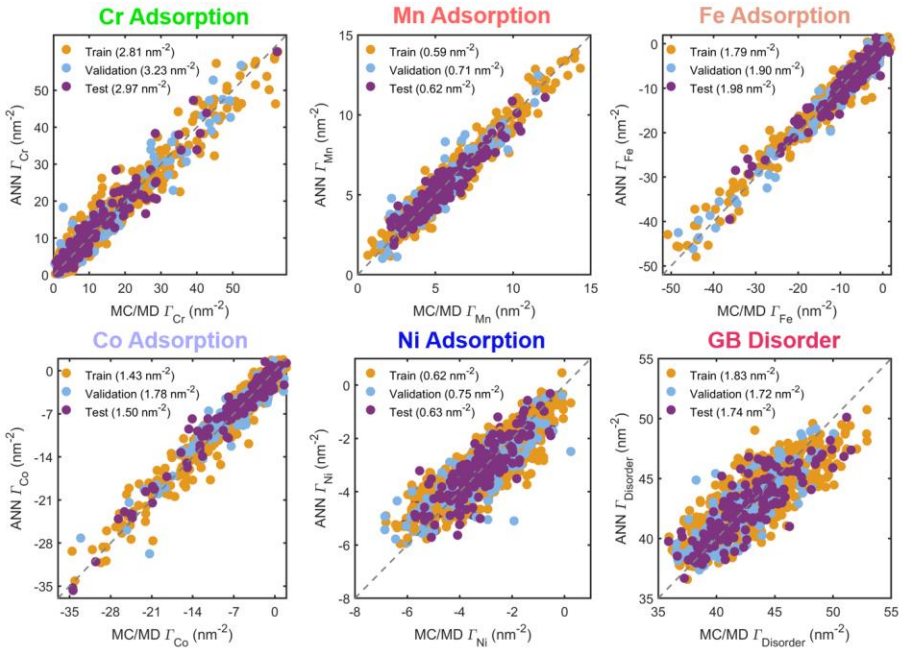

Figure 4.4 Performance of ANN model for predicting GB properties in HEA. Parity plots for ANN-predicted GB adsorption properties (i.e., Γ_{Cr}, Γ_{Mn}, Γ_{Fe}, Γ_{Co}, Γ_{Ni}) and disorder ($\Gamma_{\mathrm{Disorder}}$) *vs.* MC/MD simulations. The root-mean-square errors (RMSE) of training, validation, and test sets are labelled. Note that the ANN models always outperform than statistical model for predicting GB properties.

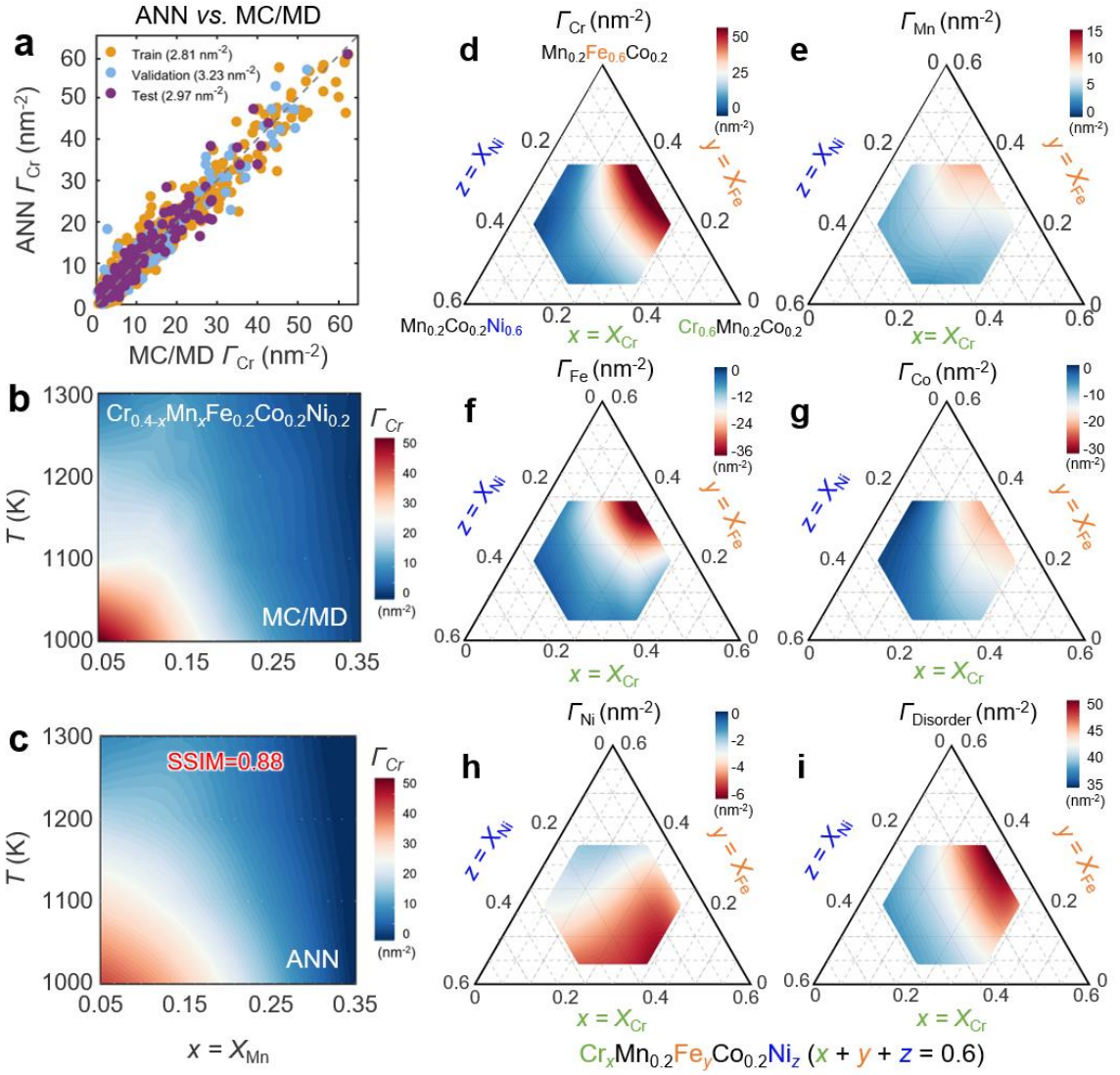

Figure 4.5 ANN performance for predicting GB properties. (a) Parity plot of ANN predictions *vs*. MC/MD simulations for the GB excess of Cr adsorption (Γ_{Cr}). (b-c) MC/MD-simulated *vs.* ANN-predicted isopleths of Γ_{Cr} diagrams as a function of temperature and Mn bulk composition (x_{Mn}) for the $Cr_{0.4-x}Mn_xFe_{0.2}Co_{0.2}Ni_{0.2}$ system. (d-i) Representative ternary isothermal sections of ANN-predicted GB diagrams of Γ_{Cr}, Γ_{Mn}, Γ_{Fe}, Γ_{Co}, Γ_{Ni}, and $\Gamma_{\mathrm{Disorder}}$ for the $Cr_xMn_{0.2}Fe_yCo_{0.2}Ni_z$ ($x + y + z = 0.6$; $x = X_{\mathrm{Cr}}$, $y = X_{\mathrm{Fe}}$, $z = X_{\mathrm{Ni}}$) subsystem at 1000 K.

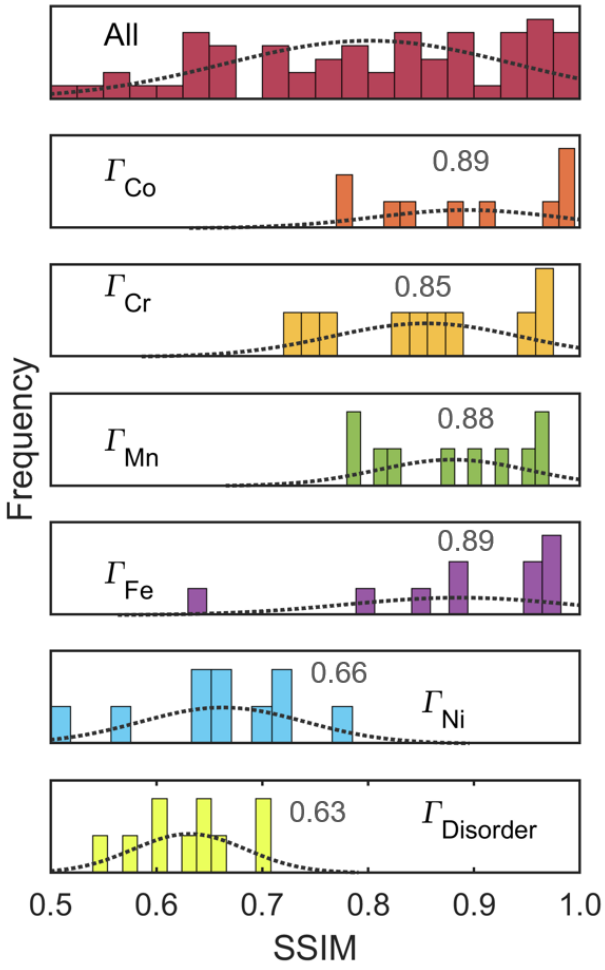

Figure 4.6 Histogram of structural similarity index (SSIM) of ANN-predicted *vs*. MC/MD-simulated binary GB diagrams for six GB properties. The relatively low SSIM values for Γ_{Ni} and $\Gamma_{\mathrm{Disorder}}$ diagrams can be ascribed to the small variation range. Since we mainly focus on the strong segregation elements (e.g., Cr and Mn) or strong de-segregation elements (e.g., Fe and Co), the promising ANN performance are good enough for current study.

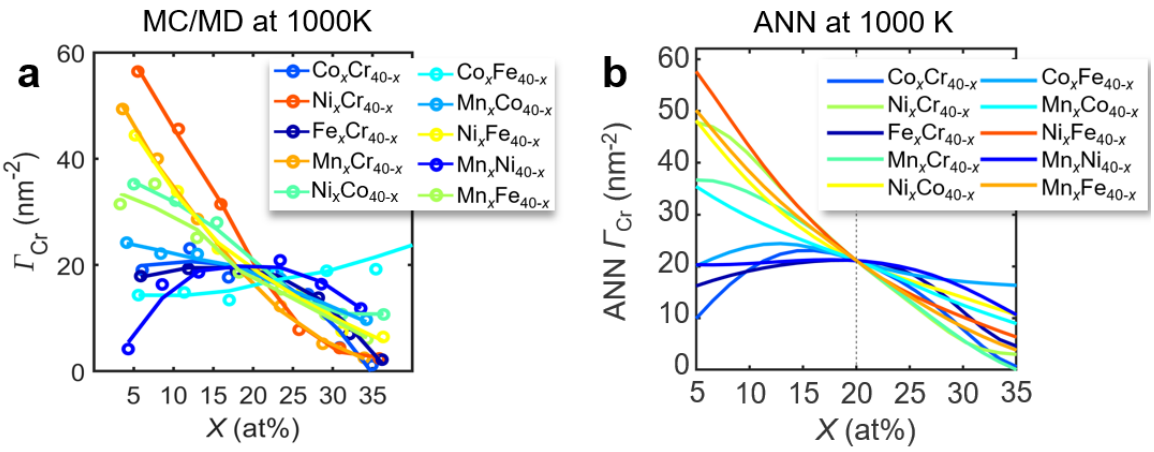

Figure 4.7 MC/MD simulation *vs*. ANN prediction for ten subsystems. (a) MC/MD-simulated Γ_{Cr} curves *vs.* one compositional variable *x* for 10 different cases at 1000 K; in each case, we select two (out of five elements) and vary its relative fractions while keeping the fractions of the three other elements (not noted in the figure) constant at 0.2. For example, the notation Co_xCr_{40-x} represents $Cr_{40-x}Mn_{0.2}Fe_{0.2}Co_xNi_{0.2}$ as a function of the Co bulk composition *x*, balanced by Cr. (b) ANN-predicted Γ_{Cr} curves for 10 different cases at 1000 K.

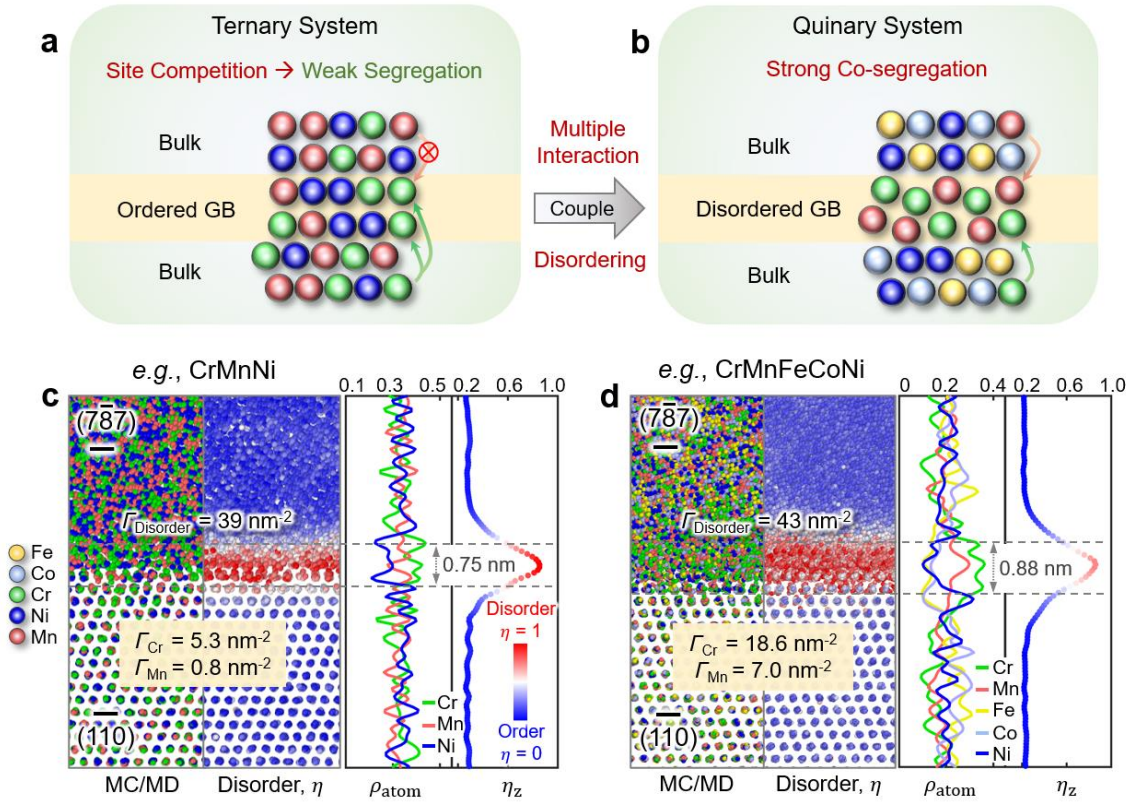

Figure 4.8 Coupling effects on GB segregation in HEA. (a) Schematic of weak segregation in ternary system, which can be ascribed to the site competition and relatively ordered (less-disordered) GB. (b) Schematic of strong segregation in quinary system. The coupling effect of multiple interaction and GB disordering result in strong co-segregation. (c) MC/MD-simulated GB structure of Σ81 asymmetric GB for equimolar CrMnNi alloy at 1000 K. The disorder parameter (η) and atomic density profiles show GB exhibits smaller $\Gamma_{\mathrm{Disorder}}$ (~39 nm^{-2}) and weak segregation of Cr and Mn (~5.3 and 0.8 nm^{-2}). (d) MC/MD-simulated GB structure of Σ81 asymmetric GB for Cantor alloy (equimolar CrMnFeCoNi) at 1000 K. The disorder parameter (η) and atomic density profiles show GB exhibits relatively larger $\Gamma_{\mathrm{Disorder}}$ (~43 nm^{-2}) and strong co-segregation of Cr and Mn (~18.6 nm^{-2} and 7.0 nm^{-2}).

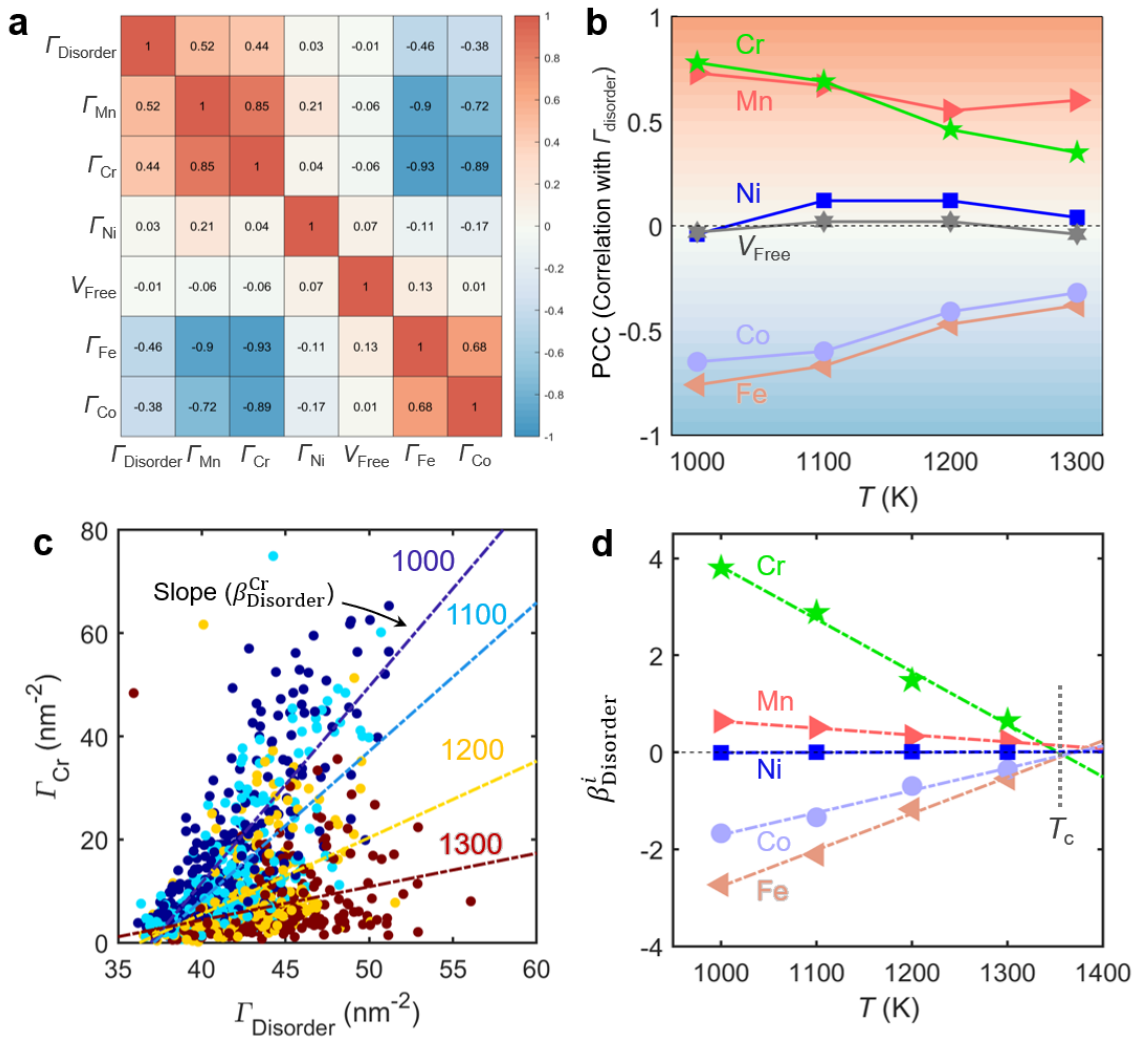

Figure 4.9 Correlation analysis for GB properties. (a) Heat map of Pearson correlation coefficients between all seven GB properties. The red/blue/white color represents positive/negative/no correlation. (b) Calculated correlation coefficients between $\Gamma_{\mathrm{Disorder}}$ and other GB properties at different temperatures. (c) Plot of GB excess of Cr (Γ_{Cr}) *vs*. $\Gamma_{\mathrm{Disorder}}$ under from 1000 K to 1300 K. The dashed lines are regression lines of Γ_{Cr} *vs*. $\Gamma_{\mathrm{Disorder}}$ at different temperatures based on 258 HEA compositions. (d) Fitted slope ($\beta^{i}_{\mathrm{Disorder}}$, *i* = Cr, Mn, Fe, Co, Ni) of five elements as a function of temperature. The five trends lines of $\beta^{i}_{\mathrm{Disorder}}$ *vs. T* almost cross over at nearly one point, where GB segregation and de-segregation vanished (Γ_i = 0). The corresponding temperature was named as critical temperature T_c.

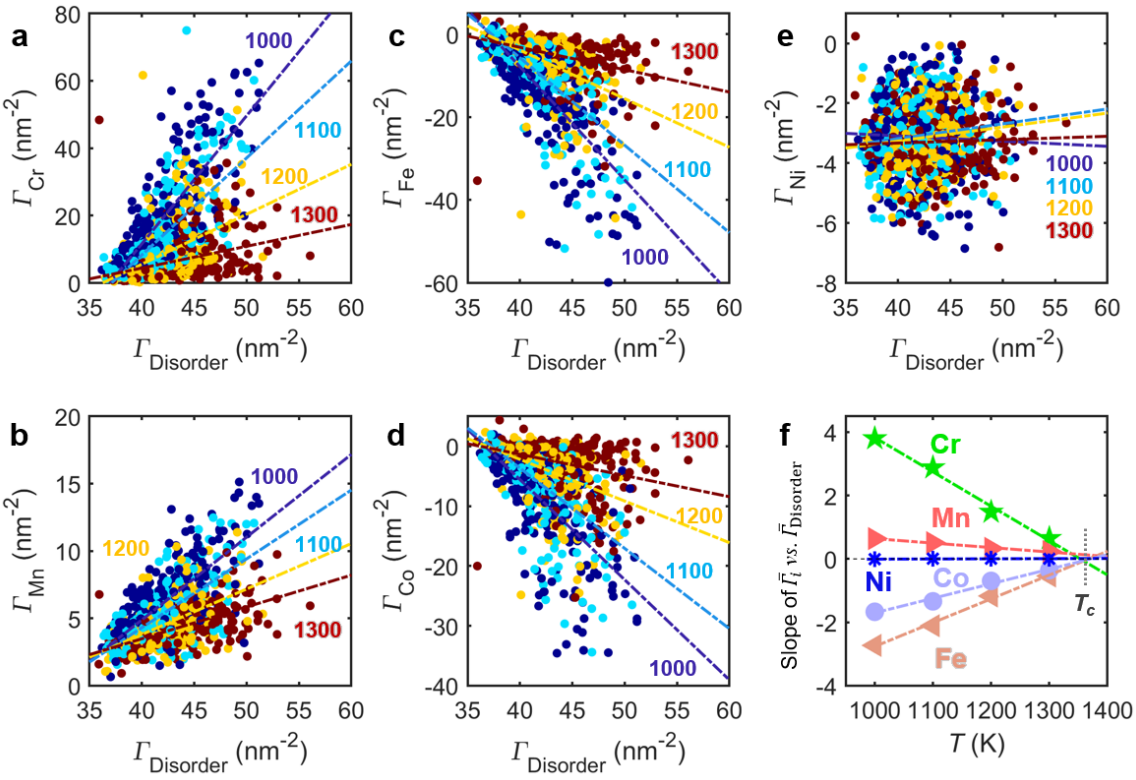

Figure 4.10 The relation between GB excess of solutes and disorder. (a-e) The relation between Γ_i *vs.* $\Gamma_{\mathrm{Disorder}}$ (i = Cr, Mn, Fe, Co, Ni) from 1000 K to 1300 K. The dashed lines are trend lines of $\bar{\Gamma}_i$ *vs.* $\bar{\Gamma}_{\mathrm{Disorder}}$ at four different temperature. Here, $\bar{\Gamma}_i$ and $\bar{\Gamma}_{\mathrm{Disorder}}$ are the average GB excess adsorption of solutes and GB disorder based on 258 different HEAs. (f) Slope of $\bar{\Gamma}_i$ *vs.* $\bar{\Gamma}_{\mathrm{Disorder}}$ trendlines as a function of temperature for five elements. The five slope trends lines almost cross over at same temperature, where GB segregation and de-segregation vanished, and we named it as critical temperature T_c.

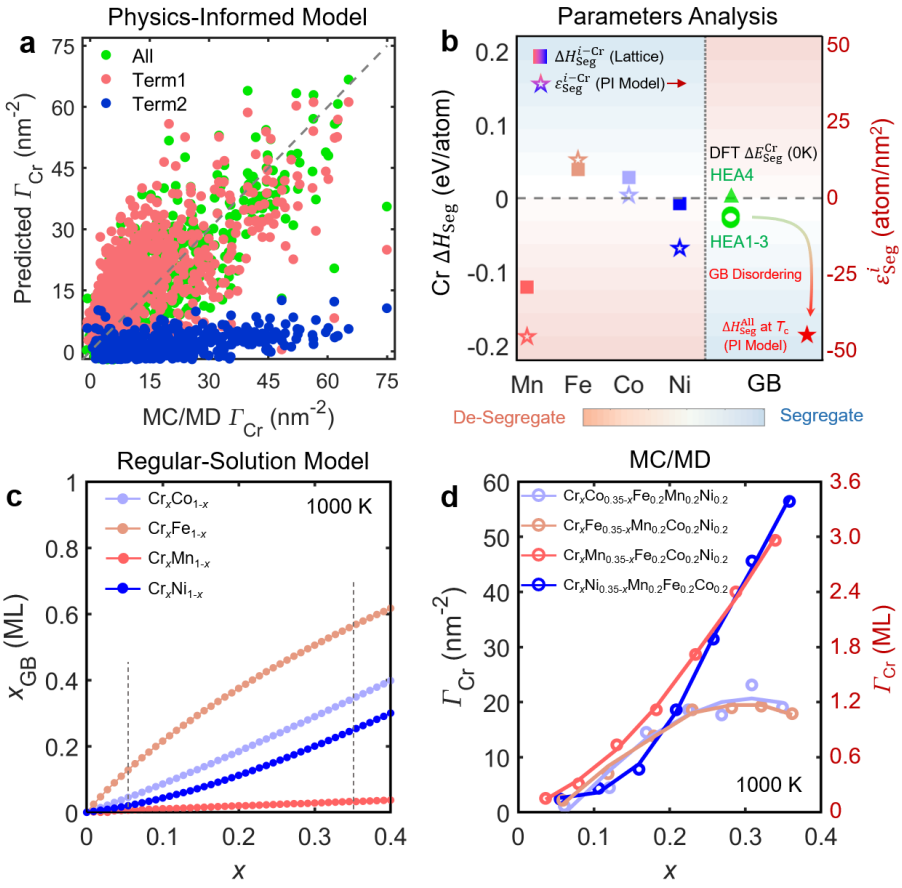

Figure 4.11 Physics-informed model for GB segregation in HEA and comparison of classical segregation model *vs*. MC/MD simulations. (a) Parity plots of model-predicted Γ_{Cr} *vs.* MC/MD simulations (green dots). The pink and blue dots represent the contribution from term1 and term2, respectively. (b) Comparison of Cr segregation in different models. The ΔH_{Seg}^{i-Cr} is the segregation enthalpy of Cr in binary system based on a lattice-type model. The $\Delta\varepsilon_{Seg}^{i-Cr}$ are the fitted parameters based on Eq. (2), which are the compositional coefficients on Cr segregation in HEA. The ΔE_{Seg}^{Cr} is the DFT-calculated segregation energy for four non-equimolar HEAs (HEA1-4, see composition in Table 4.3) at 0 K. The ΔH_{Seg}^{All} is the disorder-corrected segregation enthalpies at critical temperature T_c. Since the sign of ΔH_{Seg} has different meaning of segregation according to different definitions, we used blue and red color to represent segregation and de-segregation, respectively. (c) Calculated GB segregation *vs*. bulk composition of Cr for four $Cr_xCo(Fe, Mn, Ni)_{1-x}$ binary systems at 1000 K using regular-solution-based Wynblatt-Ku model [43]. The dashed lines represent the range of elemental composition used in HEA system. (d) MC/MD-simulated Γ_{Cr} curves *vs.* Cr bulk composition for four HEA subsystems at 1000 K; in each case, the fraction varies between Cr and another one (out of four elements) while keeping the fractions of the three other elements as constant at 0.2 (noted in the figure).

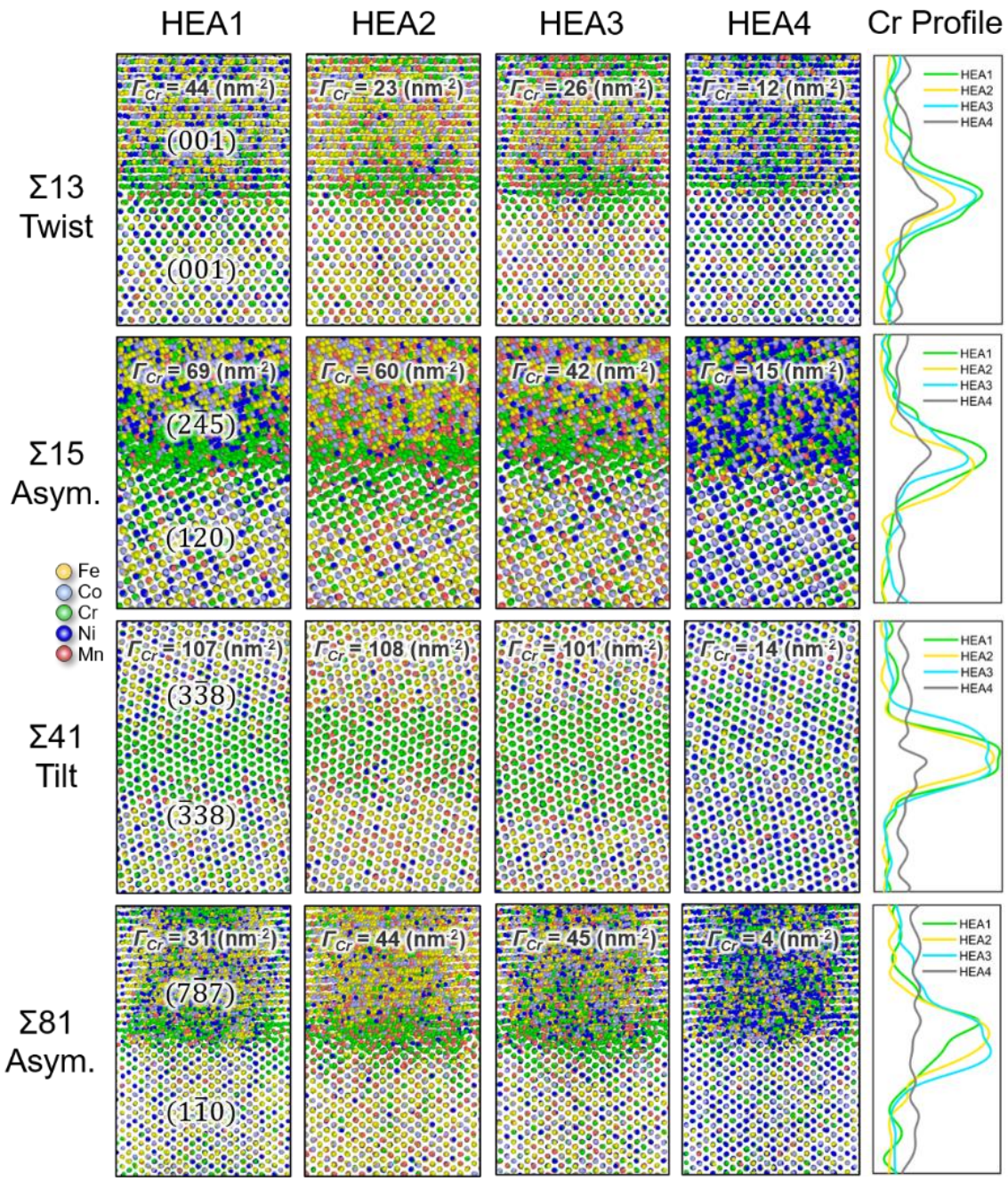

Figure 4.12 Screenshot of MC/MD-simulated GB structures at 1000 K for four non-equimolar HEAs of four different GBs. The right panels are Cr distribution profiles perpendicular to the GB direction. For all four types of GB, HEA1-HEA3 always have larger GB excess of Cr adsorption (Γ_{Cr}) than HEA4 (see detailed compositions in Table 4.3), and corresponding Cr profiles further confirmed the stronger Cr segregation at HEA1-3 GBs than HEA4.

References

[1] Y.F. Ye, Q. Wang, J. Lu, C.T. Liu, Y. Yang, High-entropy alloy: challenges and prospects, Materials Today, 19 (2016) 349-362.

[2] M.-H. Tsai, J.-W. Yeh, High-Entropy Alloys: A Critical Review, Materials Research Letters, 2 (2014) 107-123.

[3] D.B. Miracle, O.N. Senkov, A critical review of high entropy alloys and related concepts, Acta Materialia, 122 (2017) 448-511.

[4] E.P. George, D. Raabe, R.O. Ritchie, High-entropy alloys, Nature Reviews Materials, 4 (2019) 515-534.

[5] S.J. Dillon, M. Tang, W.C. Carter, M.P. Harmer, Complexion: A new concept for kinetic engineering in materials science, Acta Materialia, 55 (2007) 6208-6218.

[6] P.R. Cantwell, M. Tang, S.J. Dillon, J. Luo, G.S. Rohrer, M.P. Harmer, Grain boundary complexions, Acta Materialia, 62 (2014) 1-48.

[7] D. Dey, R.C. Bradt, Grain Growth of ZnO during Bi2O3 Liquid-Phase Sintering, Journal of the American Ceramic Society, 75 (1992) 2529-2534.

[8] J. Nie, J.M. Chan, M. Qin, N. Zhou, J. Luo, Liquid-like grain boundary complexion and sub-eutectic activated sintering in CuO-doped TiO2, Acta Materialia, 130 (2017) 329-338.

[9] J. Luo, H. Wang, Y.-M. Chiang, Origin of Solid-State Activated Sintering in Bi2O3-Doped ZnO, Journal of the American Ceramic Society, 82 (1999) 916-920.

[10] M. Kuzmina, M. Herbig, D. Ponge, S. Sandlöbes, D. Raabe, Linear complexions: Confined chemical and structural states at dislocations, Science, 349 (2015) 1080.

[11] A. Kwiatkowski da Silva, R.D. Kamachali, D. Ponge, B. Gault, J. Neugebauer, D. Raabe, Thermodynamics of grain boundary segregation, interfacial spinodal and their relevance for nucleation during solid-solid phase transitions, Acta Materialia, 168 (2019) 109-120.

[12] S.J. Dillon, K. Tai, S. Chen, The importance of grain boundary complexions in affecting physical properties of polycrystals, Current Opinion in Solid State and Materials Science, 20 (2016) 324-335.

[13] A.R. Krause, P.R. Cantwell, C.J. Marvel, C. Compson, J.M. Rickman, M.P. Harmer, Review of grain boundary complexion engineering: Know your boundaries, Journal of the American Ceramic Society, 102 (2019) 778-800.

[14] T. Hu, S. Yang, N. Zhou, Y. Zhang, J. Luo, Role of disordered bipolar complexions on the sulfur embrittlement of nickel general grain boundaries, Nature Communications, 9 (2018) 2764.

[15] J.H. Westbrook, SEGREGATION AT GRAIN BOUNDARIES, Metallurgical Reviews, 9 (1964) 415-471.

[16] D. McLean, Grain Boundaries in Metals, Oxford, Clarendon Press, (1957).

[17] E.D. Hondros, M.P. Seah, The theory of grain boundary segregation in terms of surface adsorption analogues, Metallurgical Transactions A, 8 (1977) 1363-1371.

[18] Z. Pan, T.J. Rupert, Effect of grain boundary character on segregation-induced structural transitions, Physical Review B, 93 (2016) 134113.

[19] T. Frolov, S.V. Divinski, M. Asta, Y. Mishin, Effect of Interface Phase Transformations on Diffusion and Segregation in High-Angle Grain Boundaries, Physical Review Letters, 110 (2013) 255502.

[20] T. Frolov, M. Asta, Y. Mishin, Segregation-induced phase transformations in grain boundaries, Physical Review B, 92 (2015) 020103.

[21] C. Hu, J. Luo, First-order grain boundary transformations in Au-doped Si: Hybrid Monte Carlo and molecular dynamics simulations verified by first-principles calculations, Scripta Materialia, 158 (2019) 11-15.

[22] S. Yang, N. Zhou, H. Zheng, S.P. Ong, J. Luo, First-Order Interfacial Transformations with a Critical Point: Breaking the Symmetry at a Symmetric Tilt Grain Boundary, Physical Review Letters, 120 (2018) 085702.

[23] K. Ming, L. Li, Z. Li, X. Bi, J. Wang, Grain boundary decohesion by nanoclustering Ni and Cr separately in CrMnFeCoNi high-entropy alloys, Science Advances, 5 (2019) eaay0639.

[24] Y.J. Li, A. Savan, A. Kostka, H.S. Stein, A. Ludwig, Accelerated atomic-scale exploration of phase evolution in compositionally complex materials, Materials Horizons, 5 (2018) 86-92.

[25] L. Li, R.D. Kamachali, Z. Li, Z. Zhang, Grain boundary energy effect on grain boundary segregation in an equiatomic high-entropy alloy, Physical Review Materials, 4 (2020) 053603.

[26] P. Wynblatt, D. Chatain, Modeling grain boundary and surface segregation in multicomponent high-entropy alloys, Physical Review Materials, 3 (2019) 054004.

[27] C. Hu, Y. Zuo, C. Chen, S. Ping Ong, J. Luo, Genetic algorithm-guided deep learning of grain boundary diagrams: Addressing the challenge of five degrees of freedom, Materials Today, (2020).

[28] M. Tang, W.C. Carter, R.M. Cannon, Grain Boundary Transitions in Binary Alloys, Physical Review Letters, 97 (2006) 075502.

[29] N. Zhou, T. Hu, J. Luo, Grain boundary complexions in multicomponent alloys: Challenges and opportunities, Current Opinion in Solid State and Materials Science, 20 (2016) 268-277.

[30] S.A.E. Johansson, G. Wahnström, First-principles study of an interfacial phase diagram in the V-doped WC-Co system, Physical Review B, 86 (2012) 035403.

[31] A. Morawiec, K. Glowinski, On “macroscopic” characterization of mixed grain boundaries, Acta Materialia, 61 (2013) 5756-5767.

[32] S. Plimpton, Fast Parallel Algorithms for Short-Range Molecular Dynamics, Journal of Computational Physics, 117 (1995) 1-19.

[33] W.-M. Choi, Y.H. Jo, S.S. Sohn, S. Lee, B.-J. Lee, Understanding the physical metallurgy of the CoCrFeMnNi high-entropy alloy: an atomistic simulation study, npj Computational Materials, 4 (2018) 1.

[34] G. Kresse, J. Hafner, Ab Initio Molecular Dynamics for Liquid Metals, Phys. Rev. B, 47 (1993).

[35] G. Kresse, G. Furthmüller, Efficient Iterative Schemes for Ab Initio Total-Energy Calculations Using a Plane-Wave Basis Set, Phys. Rev. B, 54 (1996) 11169-11186.

[36] P.E. Blöchl, Projector Augmented-Wave Method, Phys. Rev. B 50 (1994) 17953-17979.

[37] G. Kresse, D. Joubert, From Ultrasoft Pseudopotentials to the Projector Augmented-Wave Method, Phys. Rev. B 59 (1999).

[38] Z. Leong, J.S. Wróbel, S.L. Dudarev, R. Goodall, I. Todd, D. Nguyen-Manh, The Effect of Electronic Structure on the Phases Present in High Entropy Alloys, Scientific Reports, 7 (2017) 39803.

[39] T.A. Manz, Introducing DDEC6 atomic population analysis: part 3. Comprehensive method to compute bond orders, RSC Advances, 7 (2017) 45552-45581.

[40] L. Li, Z. Li, A. Kwiatkowski da Silva, Z. Peng, H. Zhao, B. Gault, D. Raabe, Segregation-driven grain boundary spinodal decomposition as a pathway for phase nucleation in a high-entropy alloy, Acta Materialia, 178 (2019) 1-9.

[41] P.M. Larsen, S. Schmidt, J. Schiøtz, Robust structural identification via polyhedral template matching, Modelling and Simulation in Materials Science and Engineering, 24 (2016) 055007.

[42] H.A. Murdoch, C.A. Schuh, Estimation of grain boundary segregation enthalpy and its role in stable nanocrystalline alloy design, Journal of Materials Research, 28 (2013) 2154-2163.

[43] P. Wynblatt, R.C. Ku, Surface energy and solute strain energy effects in surface segregation, Surface Science, 65 (1977) 511-531.

Chapter 5. Grain Boundary Mechanical Property Diagrams of Ga-Doped Al Binary System

5.1. Introduction

Grain boundary (GB) property diagram has been considered as an important materials science tool on par with phase diagrams [1-5]. Most of GB diagrams are hitherto only developed for GB structural properties [1-5], e.g., GB excess of adsorption and disorder, but scarcely for functional properties. Here, using a mixed Σ81 Al GB that exhibits similar Ga segregation behavior with electron microscopy experiment, we developed two types of GB mechanical properties diagrams, i.e., fracture toughness and ultimate tensile strength diagrams, as a function of temperature and bulk composition of Ga via hybrid Monte Carlo and molecular dynamic (MD) simulation and MD tensile tests. In addition, a modified Langmuir-Mclean (L-M) model can be used to directly predict the GB excess of adsorption with high accuracy and GB ductile-to-brittle transition line. This study opens a new paradigm to design novel metallic alloys with optical mechanical performance using GB diagrams.

5.2. Computational Methods

5.2.1. Hybrid MC/MD Simulation

The initial GB structure was first relaxed at high temperature 700 K for 500 ps with a time step of 0.1 fs by classical MD simulation in constant-*NPT* ensembles. Next, the hybrid Monte Carlo and molecular dynamics (hybrid MC/MD) simulations

in constant-*NPT* ensembles were carried out to dope Ga atoms into Al GBs at the given temperature by setting the chemical potential difference $\Delta\mu = \mu_{\mathrm{Al}} - \mu_{\mathrm{Ga}}$, where $\mu_{\mathrm{Al(Ga)}}$ is the chemical potential of Al(Ga). Five MC trial moves were conducted between each MD step with a 0.1 fs MD time step, and 1 million hybrid MC/MD steps performed for each simulation to achieve convergence [2, 4]. All MC/MD simulations were performed using LAMMPS code [6] and Al-Ga EAM potential [7, 8] was adopted.

The methods used to calculate GB excess of Ga adsorption (Γ_{Ga}) and disorder ($\Gamma_{\mathrm{Disorder}}$) diagrams were same as our prior works, see detailed procedures in refs. [2, 3]. The GB thickness (δ_{GB}) were calculated based on the 2-D averaged disorder (η) profile along the direction perpendicular to GB, and we define the half-width of maximal η as the GB thickness. To construct GB diagrams as a function of temperature and Ga composition, the hybrid MC/MD simulations were performed from 300 K to 860 K with a temperature step 100 K. At each temperature, a series of MC/MD simulations with increasing $\Delta\mu$ were conducted until the bulk composition of Ga (x_{Ga}) reaches the solubility limits.

5.2.2. STEM Simulation

STEM images were simulated by using the QSTEM program. The MC/MD-simulated Ga-doped Al Σ81 asymmetric GB structure at 300 K and $\Delta\mu = -0.4415$ eV was used for imaging simulation. The thickness of the simulated sample was set to 3.5 nm. The scattering semi-angle for HAADF imaging was set

to 70 mrad, the convergence angle was adopted to 15 mrad, and the spherical aberration coefficient was set to 0 μm.

5.2.3. MD Tensile test

Using the MC/MD-simulated GB structures, a series of tensile tests of GBs were carried out by constant-*NPT* MD simulations at different temperatures and $\Delta\mu$. The strain rate was set to ~$5.4 \cdot 10^8$/s and tensile tests were performed until the final strain reaches ~0.2. The fracture toughness (K_C) was calculated by integrating the stress-strain curve based on MC/MD simulations. The maximal tensile stress based on the MC/MD simulations was considered as the ultimate strength (σ_{UTS}).

5.3. Results and Discussion

5.3.1. Ga Segregation in Al General GBs

Fig. 5.1(a) shows the experimental HAADF image of Ga-doped Al GB annealed at room temperature 300 K. The line-by-line intensity profile clearly shows GB has large peak compared to bulk phases. Since the intensity of HAADF signal is proportional to the square of atomic number (Z) [9, 10], where Z_{Al}= 13 and Z_{Ga} = 31, this suggests the large brightness at GB is caused by the Ga segregation. Further, the line-by-line intensity exhibits partially ordered pattern at GB, suggesting the partially ordered Ga segregation structure. This can be further confirmed by fast Fourier transformation (FFT) analysis. To mimic this experimental GB structure, we first selected a Σ81 $(1\bar{1}0)//(7\bar{8}7)$ mixed GB and

performed hybrid MC/MD simulation at 300 K and $\Delta\mu$ = -0.4415, where $\Delta\mu$ is the chemical potential different between Al and Ga. The MC/MD-simulated GB structure was shown in Fig. 5.1(c), where the atomic density of Ga distribution perpendicular to GB (*z* direction) clearly shows strong Ga segregation at GB region. Based on MC/MD-simulated structure, we perform STEM image simulation (Fig. 5.1(b)). By plotting the line-by-line intensity profile (cyan line), we can observe strong intensity peak at GB, which suggests the strong Ga segregation. The partially ordered intensity peak and FFT analysis further confirmed the partially ordered Ga segregation at Al GB. Meanwhile, we also calculated disorder (η_{Dis}) parameter for MC/MD-simulated GB structure (Fig. 5.1(d)). The 2D averaged η_{Dis} profile shows that most Ga atoms segregated at GB are highly disordered, but Ga atoms close to bulk phases are more ordered. This indicates that Ga segregation exhibits an order-to-disorder structures. It is also worthy to note that by calculating the half width of Ga composition and η_{Dis} profile, we found that the GB width of η_{Dis} profile is ~0.70 nm, which is smaller than Ga composition profile with a value of ~0.80 nm. This further suggests that the Ga atoms near bulk regions are very ordered. Finally, by comparing the GB width with experiments, we found that GB widths calculated by disorder profile and intensity profiles (for both experiment and simulation) have good agreement, which is ~0.70 nm. Therefore, we believe our MC/MD simulation of Ga segregation in Σ81 Al GB is very robust, and we adopted this GB to calculate GB diagrams.

5.3.2. GB Diagrams of Structural Diagrams

Next, we performed a series of MC/MD simulations under different T and $\Delta\mu$ to interpolate the GB diagrams (see method), and three types of structural properties including GB excess of Ga adsorption Γ_{Ga}, GB excess of disorder $\Gamma_{\mathrm{Disorder}}$, and GB thickness δ_{GB} are computed based on MC/MD-simulated structures (Fig. 5.2(a-c)). First, Γ_{Ga} diagram shows that GB adsorption is high at low temperature, but it becomes weak at higher temperature. By plotting the Γ_{Ga} as a function of normalized bulk composition (X/X_{Max}) at different temperatures in Fig. 5.2(d), all the transition lines are actually continuous, indicating no first-order adsorption transition existed in Ga-doped Al GB. Second, $\Gamma_{\mathrm{Disorder}}$ and δ_{GB} diagrams show that they exhibit similar distribution (Fig. 5.2(b-c)). For example, they always have low values at lower temperature, and turn to high value at higher temperature and near solidus line region from $0.5T_{\mathrm{m}}$ -$0.9T_{\mathrm{m}}$. The plots of $\Gamma_{\mathrm{Disorder}}$ (δ_{GB}) *vs.* X/X_{Max} further confirms the similarity of these two diagrams, which also means that GB disordering and GB thickness are highly correlated.

5.3.3. GB Diagrams of Mechanical Properties

Following with MC/MD-simulated GB structures, we subsequently performed MD tensile test of each GB to compute fracture toughness (K_{C}) and ultimate tensile strength (σ_{UTS}) diagrams (see Fig. 5.3(a-b)). The K_{C} diagram shows that GB can easily turn to brittle behavior even with tiny Ga segregation at low temperature. For example, GB becomes brittle when normalized bulk composition (X/X_{Max}) of Ga reaches a small value of ~0.6 at% at 300 K, see the

plot of K_C *vs*. X/X_{Max} in Fig. 5.3(c). However, the segregation effect on GB embrittlement becomes weak when temperature increases (Fig. 5.3(c)). Here, a ductile-to-brittle transition line can be identified in Fig. 5.3(a), where it shows that GB embrittlement vanished when temperature is above ~0.65 T_m. The σ_{UTS} diagram shows that both Ga segregation and temperature can lower the σ_{UTS} (Fig. 5.3(b)). For example, σ_{UTS} is ~2.95 GPa for "clean GB" and reduced to ~ 1.06 GPa when X/X_{Max} is ~0.70 at% at 300 K (near solubility at 300 K), see Fig. 5.3(d). In addition, the σ_{UTS} of "clean" GB can reduce to ~1.03 GPa when temperature reaches 0.93 T_m (Fig. 5.3(d)). By examining the relation between K_C (or σ_{UTS}) and Γ_{Ga} at different temperatures, it is interesting to note that GB fracture always occurred at nearly same segregation level with a Γ_{Ga} of ~11 nm^{-2} even at different temperatures (Fig. 5.3(e)). This indicates that GB embrittlement behavior is dominated by GB segregation, and we can denote corresponding Γ_{Ga} as fracture GB excess of adsorption ($\Gamma_{Ga}^{Fracture}$). Meanwhile, Fig. 5.3(f) shows that σ_{UTS} almost linearly decays with Γ_{Ga} at different temperatures, which also suggests that σ_{UTS} has strong relation with GB adsorption.

5.3.4. Revised Thermodynamic Model for GB Segregation

The classical Langmuir-Mclean model was used to address the relation of GB segregation in ideal solution [11-13]:

$$\frac{x_{GB}}{x_{GB}^{o}-x_{GB}} = \frac{x_b}{1-x_b} exp(-\frac{\Delta H_{Seg}}{RT}) \quad (1)$$

where x_{GB} and x_{b} are solute composition at GB and bulk phases, x_{GB}^{o} is the solute saturation level at GB and bulk, and ΔH_{Seg} is the segregation enthalpy. However, this model is under the one monolayer assumption [11-13], meaning that $0 < x_{\mathrm{GB}} < 1\mathrm{ML}$. Based on Eq. (1), we further revised the Langmuir-Mclean model by using the more strictly defined parameter Γ_{Ga} and also introducing the interaction effect between solute and solvent (i.e., regular solution):

$$\frac{\Gamma_{\mathrm{Ga}}}{\Gamma_{Ga}^{o}-\Gamma_{Ga}} = \frac{x_{bulk}}{1-x_{bulk}} \exp\left[-\frac{\left(\Delta H_{\mathrm{Seg}}^{\mathrm{o}}+\omega\frac{\Gamma_{\mathrm{Ga}}}{\Gamma_{\mathrm{Ga}}^{o}}\right)}{RT}\right] \quad (2)$$

where Γ_{Ga}^{o} is the saturation level of GB excess of Ga, $\Delta H_{\mathrm{Seg}}^{\mathrm{o}}$ is the intrinsic segregation enthalpy, and ω is the interaction parameter between solute and solvent atoms. Using Eq. (2), we can fit the above parameters by using the MC/MD-simulated GB adsorption diagram as shown in Fig. 5.2(a). The fitted values are 48.030 nm^{-2} for Γ_{Ga}^{o}, -0.113 eV/atom for $\Delta H_{\mathrm{Seg}}^{\mathrm{o}}$, and -0.025 eV/atom for ω. It is interesting to note that the sign of these parameters gives reasonable explanation for Eq. (2). For example, Γ_{Ga}^{o} is the saturation-level of Ga segregation at GB, which also means this parameter can be considered as the maximal value of GB segregation. Besides, based on our definition, the negative value of fitted $\Delta H_{\mathrm{Seg}}^{\mathrm{o}}$ indicates the positive segregation at GB [14]. This is consistent with our MC/MD simulations and experiments that Ga atoms strongly segregate at Al GBs. Furthermore, the negative value of ω means that interaction between can lower the segregation enthalpy of solute (i.e., Ga). Therefore, the fitted parameters have

perfect physical meaning, suggesting that our revised model is highly solid and robust.

To further validate our fitting results, we use above parameters to predict Γ_{Ga} and compare it with MC/MD simulations. Fig. 5.4(a) shows that the parity plot of model-predicted Γ_{Ga} *vs*. MC/MD values have promising linear relation, which suggests the robust model. This can be further confirmed by the small root-mean-square error (RMSE) with value ~ 3.8 nm^{-2}, which only varies in 7.6% out of Γ_{Ga}. The model-predicted GB diagram of Γ_{Ga} (Fig. 5.4(b)) exhibits high similarity compared to the MC/MD-simualted diagram (Fig. 5.2(a)). Meanwhile, by adopting the GB excess of Ga at $\Gamma_{\mathrm{Ga}}^{\mathrm{Fracture}}$ ~11 nm^{-2} in Eq. (2), we can predict the GB ductile-to-brittle line of Al-Ga system, see red dashed line in Fig. 5.4(c). It shows our prediction has good agreement with MC/MD-simulated fracture line (purple). Meanwhile, if we solve Eq. (2) based on the assumption of monolayer segregation on lower-index $(1\bar{1}0)$ plane with a Γ_{Ga} value of ~8.6 nm^{-2} (green dot line), we can find the all three fracture lines can match well with each other. This indicates that the GB embrittlement behavior can be roughly estimated by monolayer assumption. It is also worthy to note that our fitted $\Gamma_{\mathrm{Ga}}^{\mathrm{o}}$ with a value of 48.030 nm^{-2} is about 5.6 $(1\bar{1}0)$ monolayers of Ga at Al GB, which furthers indicates the classical Langmuir-Mclean model is insufficient to predict such behavior.

5.4. Conclusions

Two types of GB mechanical properties diagrams, i.e., K_{C} and σ_{UTS}, have been developed of Al-Ga binary system for the first time. MC/MD simulations show that mechanical properties of GB are closely related to the segregation behavior. For example, the GB embrittlement can occur for Al GB with a small amount Ga segregation at low temperature but disappear at relatively high temperature. This phenomenon can be ascribed to occurrence of large interfacial disordering that softens the GB. Moreover, even at different temperature, the GB embrittlement always happens at nearly same segregation level with a $\Gamma_{\mathrm{Ga}}^{\mathrm{Fracture}}$ value ~11 nm^{-2}. Notably, this value is very closed to the assumption of one monolayer segregation at lower-index $(1\bar{1}0)$ plane with a Γ_{Ga} value of ~8.6 nm^{-2}. This implies that one monolayer segregation may be considered as a critical segregation value that can induce GB decohesion.

The classical Langmuir-Mclean model is based on assumption of homogeneous segregation at each layer, and thus it cannot predict multiple layer segregation in Al-Ga system. Instead, we proposed a modified Langmuir-Mclean model by introducing interaction parameter. The parameter analysis demonstrates this model is robust and solid. Further, by combining this model and one monolayer fracture, we can directly predict the GB ductile-to-brittle transition line. We believe this method can be also used to other binary or ternary systems to forecast the ductile-to-brittle transition. This study offers new routine to design novel polycrystalline materials with optimal mechanical performance.

Chapter 5, in part, is a reprint of the material “Grain-Boundary Diagram of Mechanical Properties for Al-Ga Binary System”, C. Hu, Y. Li, Z. Yu, and J. Luo, in preparation. The electron microscopy characterization was carried out by Y. Li and Z. Yu. The dissertation author was the primary investigator to perform MD simulations and first author of this paper.

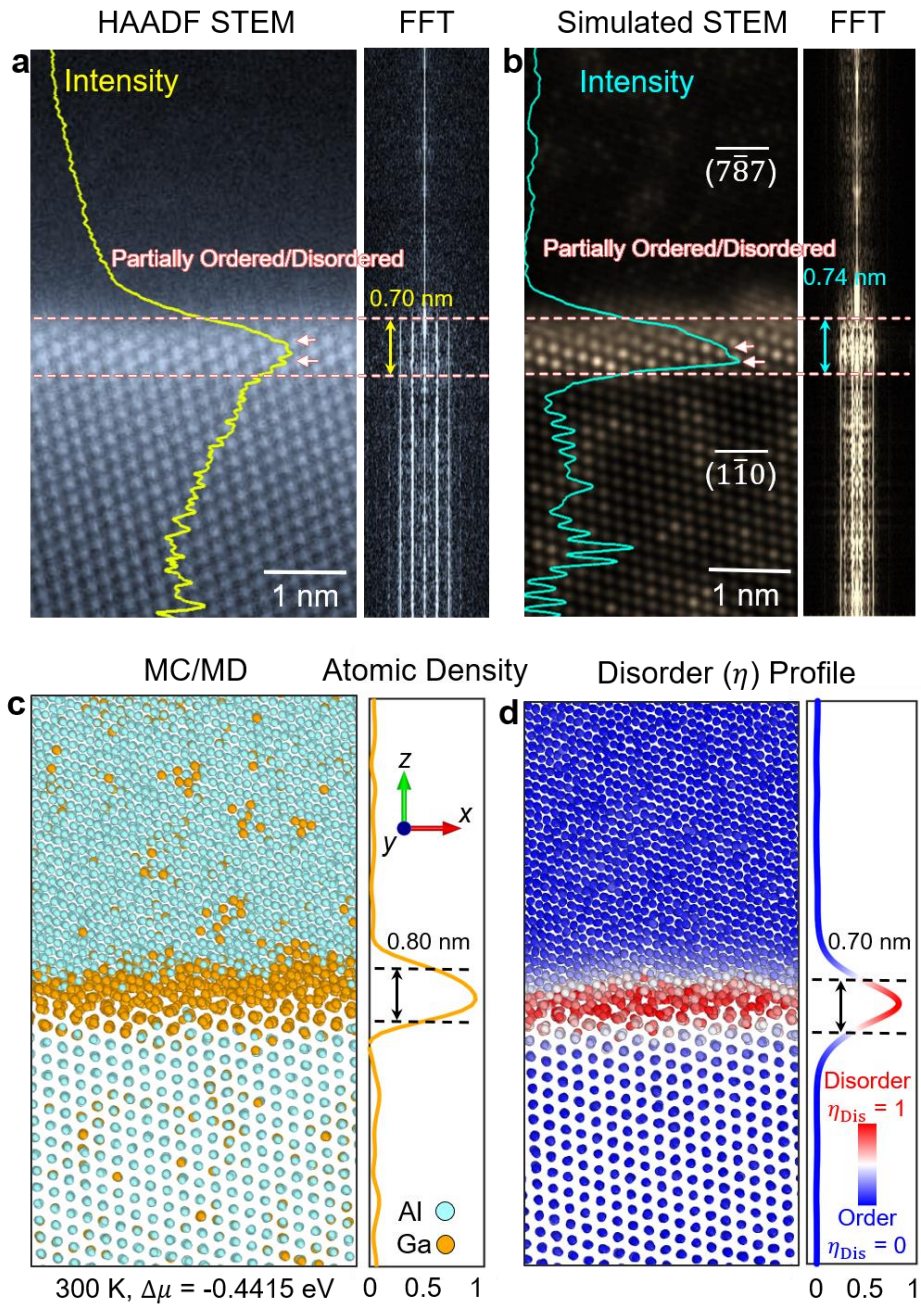

Figure 5.1 Ga segregation at Al general GB. (a) HAADF STEM of Ga-doped Al GB at asymmetric GB. (b) Simulated HAADF STEM based on MC/MD-simulated Ga-doped Al Σ81 asymmetric GB at 300 K, $\Delta\mu$ = -0.4415 eV (c). (d) calculated disorder parameter (η_{Dis}) profile of MC/MD-simulated GB. The η_{Dis} = 1 indicates disordered structure and η_{Dis} = 0 means ordered crystal.

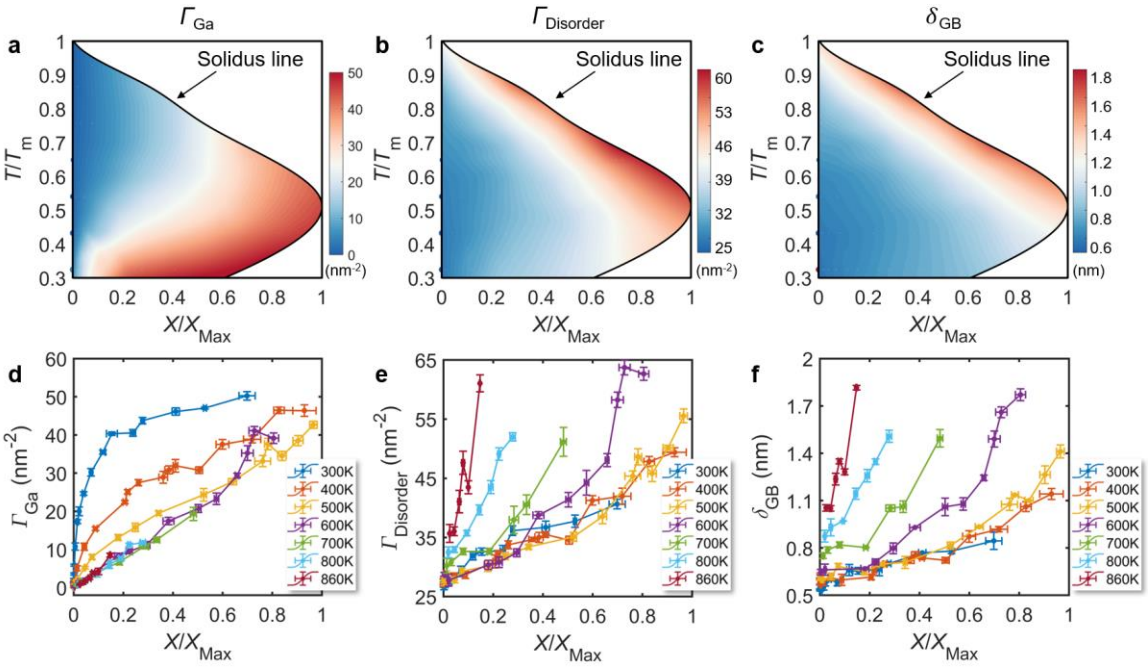

Figure 5.2 GB diagrams of structural properties. (a) MC/MD-simulated GB excess of Ga adsorption (Γ_{Ga}) diagram of Ga-doped Al Σ81 asymmetric GB. (b) GB excess of disorder ($\Gamma_{\mathrm{Disorder}}$) diagram. (c) GB thickness (δ_{GB}) diagram. (d) Calculated Γ_{Ga} *vs*. normalized bulk composition (X/X_{Max}) at different temperature. (e) Calculated $\Gamma_{\mathrm{Disorder}}$ *vs*. X/X_{Max} at different temperature. (f) Calculated δ_{GB} *vs*. X/X_{Max} at different temperature.

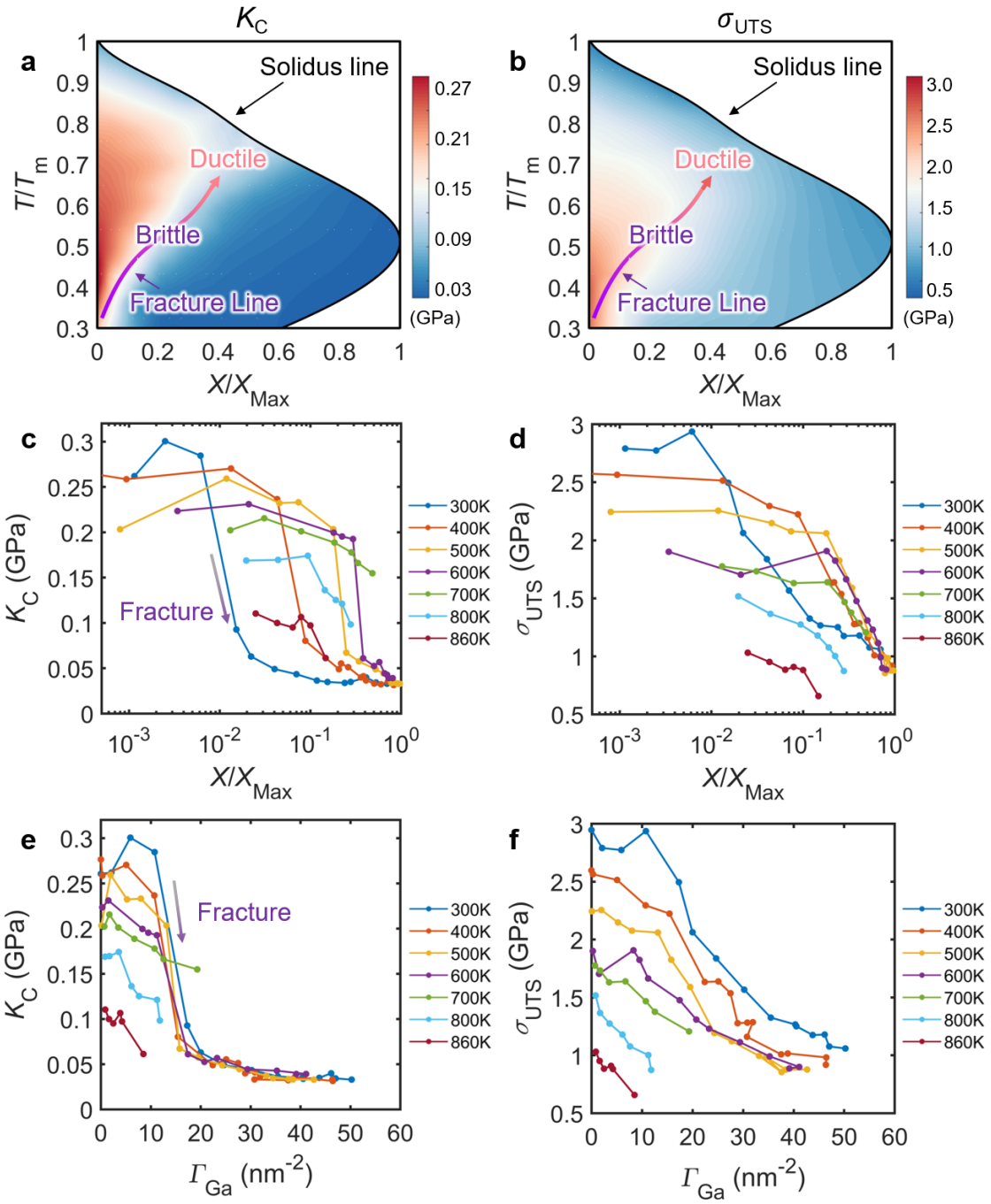

Figure 5.3 GB diagrams of mechanical properties. (a) MC/MD-simulated GB toughness (K_C) diagram of Ga-doped Al Σ81 asymmetric GB. (b) GB diagram of ultimate strength (σ_{UTS}). (c) Calculated K_C *vs*. normalized bulk composition (X/X_{Max}) at different temperature. (d) Calculated σ_{UTS} *vs*. X/X_{Max} at different temperature. (e) Calculated K_C *vs*. GB excess of Ga adsorption (Γ_{Ga}) at different temperatures. (f) Calculated σ_{UTS} *vs*. Γ_{Ga} at different temperatures.

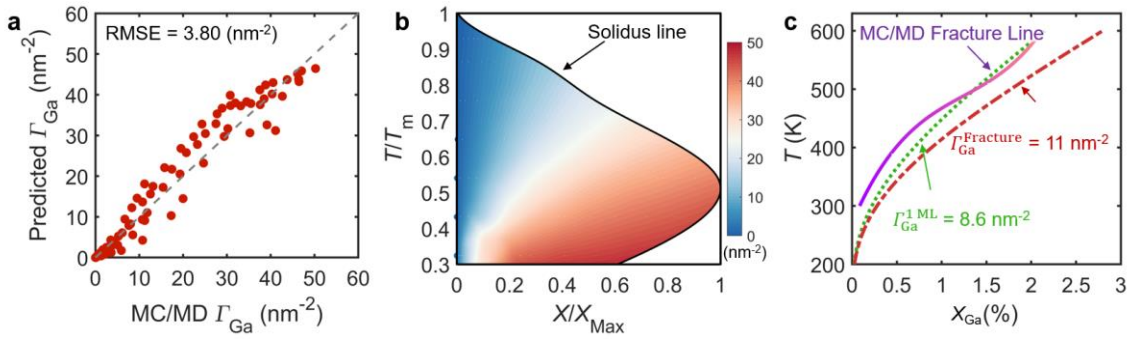

Figure 5.4 Thermodynamic model for predicting GB adsorption and fracture line. (a) parity plot of model-predicted GB excess adsorption of Ga (Γ_{Ga}) *vs*. MC/MD simulation. (b) model-predicted Γ_{Ga} diagram. (c) MC/MD-simulated GB fraction line under different temperature and bulk composition *vs*. model prediction.

References

[1] J. Luo, Developing Interfacial Phase Diagrams for Applications in Activated Sintering and Beyond: Current Status and Future Directions, Journal of the American Ceramic Society, 95 (2012) 2358-2371.

[2] S. Yang, N. Zhou, H. Zheng, S.P. Ong, J. Luo, First-Order Interfacial Transformations with a Critical Point: Breaking the Symmetry at a Symmetric Tilt Grain Boundary, Physical Review Letters, 120 (2018) 085702.

[3] C. Hu, Y. Zuo, C. Chen, S. Ping Ong, J. Luo, Genetic algorithm-guided deep learning of grain boundary diagrams: Addressing the challenge of five degrees of freedom, Materials Today, (2020).

[4] C. Hu, J. Luo, First-order grain boundary transformations in Au-doped Si: Hybrid Monte Carlo and molecular dynamics simulations verified by first-principles calculations, Scripta Materialia, 158 (2019) 11-15.

[5] X. Shi, J. Luo, Developing grain boundary diagrams as a materials science tool: A case study of nickel-doped molybdenum, Physical Review B, 84 (2011) 014105.

[6] S. Plimpton, Fast Parallel Algorithms for Short-Range Molecular Dynamics, Journal of Computational Physics, 117 (1995) 1-19.

[7] M. Rajagopalan, M.A. Bhatia, M.A. Tschopp, D.J. Srolovitz, K.N. Solanki, Atomic-scale analysis of liquid-gallium embrittlement of aluminum grain boundaries, Acta Materialia, 73 (2014) 312-325.

[8] H.-S. Nam, D.J. Srolovitz, Molecular dynamics simulation of Ga penetration along $\ensuremath{\Sigma}5$ symmetric tilt grain boundaries in an Al bicrystal, Physical Review B, 76 (2007) 184114.

[9] Z. Yu, P.R. Cantwell, Q. Gao, D. Yin, Y. Zhang, N. Zhou, G.S. Rohrer, M. Widom, J. Luo, M.P. Harmer, Segregation-induced ordered superstructures at general grain boundaries in a nickel-bismuth alloy, Science, 358 (2017) 97.

[10] Z. Luo, C. Hu, L. Xie, H. Nie, C. Xiang, X. Gu, J. He, W. Zhang, Z. Yu, J. Luo, A highly asymmetric interfacial superstructure in WC: expanding the classic grain boundary segregation and new complexion theories, Materials Horizons, 7 (2020) 173-180.

[11] P. Wynblatt, D. Chatain, Anisotropy of segregation at grain boundaries and surfaces, Metallurgical and Materials Transactions A, 37 (2006) 2595-2620.

[12] E.W. Hart, Two-dimensional phase transformation in grain boundaries, Scripta Metallurgica, 2 (1968) 179-182.

[13] J.W. Cahn, Thermodynamics of Solid and Fluid Surfaces, in: The Selected Works of John W. Cahn, 1998, pp. 377-378.

[14] P. Lejček, S. Hofmann, Thermodynamics and structural aspects of grain boundary segregation, Critical Reviews in Solid State and Materials Sciences, 20 (1995) 1-85.

Chapter 6. A Highly Asymmetric Interfacial Structure in WC: Expanding Classical Grain Boundary Segregation and New Complexion Theory

6.1. Introduction

The enrichment and redistribution of solute atoms at the boundaries between two crystalline grains, known as “grain boundary (GB) segregation (a.k.a. adsorption),” [1] could drastically alter the microstructural evolution and various materials properties of virtually all engineered polycrystalline materials [2, 3]. Hence, understanding GB segregation is a key avenue to demystifying the complicated structure-processing-property relationship, thereby being a key interest of materials scientists. Classic thermodynamic adsorption models, including the well-known Langmuir-Mclean model and its various extensions [1, 4] were adopted to describe the equilibrium segregation behaviors. Those models typically treated GB as thermodynamic entities without much structural detail. More recently, diffuse-interface [5, 6] and multilayer adsorption [7-9] models were developed to describe spatially-varying GB segregation, but they are limited in predicting GB structural transitions (other than GB disordering in the diffuse-interface models [5, 6]), e.g., interfacial symmetry change and/or reconstruction. Furthermore, atomistic simulations using density functional theory (DFT) or hybrid Monte Carlo and molecular dynamics (hybrid MC/MD) methods enable more realistic modeling of GB segregation. However, most prior atomistic simulations are limited to the symmetric tilt or twist GBs (albeit a recent report suggested segregation can induce symmetry breaking at an otherwise symmetric GB [10]).

Yet, asymmetric GBs of mixed twist and tilt character, which are ubiquitous in real polycrystalline materials and can often be the weaker link chemically and mechanically, have not been studied thoroughly.

With the rapid development of advanced electron microscopy, interesting solute segregation patterns have been revealed at the atomic scale. Aside from the well-known monolayer and submonolayer segregation at symmetric tilt GBs [11], nanoscale, equilibrium-thickness, intergranular films (IGFs) with compositional and structural gradients were widely observed at GBs in Si_3N_4 and various other ceramic materials [12-14], as well as some metallic alloys [15, 16]. Notably, Dillon and Harmer further discovered a series of discrete “complexions,” a.k.a. interfacial phases that are thermodynamically two-dimensional (2-D). This series of six Dillon-Harmer complexions include: intrinsic (“clean”) GB, (Langmuir-McLean type) monolayer, bilayer, trilayer, nanolayer (nanoscale, equilibrium-thickness IGF), and wetting layer (complete wetting); they can be understood as segregated adsorbates with nominal thickness of 0, 1, 2, 3, *x* (nanoscale), and $+\infty$ (arbitrary) of atomic layers, respectively [17, 18]. More recently, several so-called interfacial “superstructures” have also been revealed, showing further complexity of the possible GB segregation structures. These GB superstructures include an ordered defect superstructure at the Σ5 symmetric tilt GB of MgO [19], the symmetric Y/Zr/Y adsorption structure at the Σ3 tilt GB of yttria-stabilized zirconia (YSZ) [20], the “sub-surface” segregation of La and Ta at perovskite GBs [21], and interfacial reconstruction within the adsorbed Bi bilayers at Ni general GBs [22].

In this study, we have discovered, characterized, and modeled a highly asymmetric GB superstructure in Ti doped WC-Co cermet; it combines features of asymmetric and off-the-center (subsurface) segregation that induces asymmetric GB structural transitions of interfacial symmetry alteration (reconstruction) and disordering in the opposite sides. This GB superstructure is not only significantly more complex than the Dillon-Harmer complexions and/or other interfacial superstructures reported previously, but also beyond the predictions of all existing interfacial thermodynamic models. Thus, this discovery knowingly extends our fundamental knowledge of atomic level GB segregation structures; particularly, it demonstrates the possible existence of complex asymmetric interfacial superstructures beyond the current understanding and theories, with potentially broad technological implications.

6.2. Methods

6.2.1. Experiments

The tungsten carbide (WC) hard metal containing ~0.29 wt% of TiC (as a grain growth inhibitor) and ~10.0 wt% of Co was prepared by a powder metallurgical (PM) process. Specifically, WC, TiC, and Co powders of Fisher particle sizes of 4.0, 1.5, and 0.8 μm, respectively, were used as starting materials. After mixing and milling, these powders were vacuum dried to produce granulated powders. The granulated powders were pressed in a mould under 150 MPa pressure, dewaxed, and subsequently sintered in vacuum at 1450 ˚C for 1 hour. Finally, the sintered WC hard metal samples were carefully grinded and polished.

We used a focus ion beam (FIB) to prepare transmission electron microscopy (TEM) samples. To guarantee high-resolution STEM imaging, the sample thickness was finally thinned to 80 ± 5 nm. All high-angle annular dark field (HAADF) images and atomic-resolution energy dispersive X-ray spectroscopy (EDS) mapping were recorded on a Thermo Fisher Scientific TEM (Themis Z, 300 kV). The collection angle of HAADF imaging was set 60-200 mrad. The EBSD technique was employed to determine the grain boundary (GB) character in Ti-doped WC-Co. The GBs with orientation relationships close (<10°) to (0001) // $(01\bar{1}0)$ and $[2\bar{1}\bar{1}3]$ // $[2\bar{1}\bar{1}0]$, which represent 2-3% of the ~1000 GBs examined. All near (0001) // $(01\bar{1}0)$ GBs, which represent 8-9% of all GBs.

6.2.2. First-Principles Calculations

First-principles DFT calculations were performed by using Vienna *ab initio* Simulations Package (VASP) [23, 24]. The projected-augmented wave (PAW) [25, 26] method was used to solve Kohn-Sham equations, along with standard PAW potentials for the elements W, C, Ti, and Co. Based on the validations for a gamut of DFT functionals with and without vdW corrections, see Table 6.1, a nonlocal optB86b-vdW [27] functional was selected for structural optimization of WC GB structures. It has been previously shown that van der Waals (vdW) interactions can alter structural and cohesive properties not only for layered structure [28, 29], but also for three-dimensional (3D) bulk materials [30-32]. Due to the large crystal structure (592 atoms), the Brillouin-zone integrations were sampled on a Γ-centered 1×1×1 grid. The kinetic energy cutoff for plane waves was set to 400 eV,

the convergence criterion for electronic self-consistency was set to 5×10^{-4} eV, and the "medium" precision setting was used. The lattice parameters of the WC GB structure were kept unchanged and only atomic positions were fully relaxed until the force components on atoms were smaller than 0.02 eV/Å. To isolate the interaction between GBs, the WC slab was terminated with a vacuum region of ~ 12 Å. The GGA+U method with U = 3.0 and J = 1.0 eV [19] were considered for Ti *d* electrons. The spin-polarized effect was also considered for all calculations, and initial magnetic moments were assigned by 3 μ_B and 5 μ_B to Ti and Co elements respectively.

To assess the segregation tendency of Co and Ti, we calculated the segregation energy E_{seg} by using following equation [10, 33]:

$$E_{seg} = \left(E_{GB}^{doped} - E_{GB}^{undoped}\right) - \left(E_{Bulk}^{doped} - E_{Bulk}^{undoped}\right) \quad (1)$$

where E_{GB}^{doped} , $E_{GB}^{undoped}$, E_{Bulk}^{doped} and $E_{Bulk}^{undoped}$ are the energies of doped GB, clean GB, doped bulk phase and clean bulk phase. This is essentially the energy difference by moving a dopant atom from bulk to a grain boundary (GB) and Eq. (1) can be re-written as:

$$E_{seg} = \left(E_{Bulk}^{undoped} + E_{GB}^{doped}\right) - \left(E_{Bulk}^{doped} + E_{GB}^{undoped}\right) \quad (2)$$

Thus, the two terms in the above equation have the exact same total stoichiometry so that the calculated segregation energy does not depend on the chemical potentials. This represents the conventional definition of segregation

energy when the sizes of the calculation supercells approach infinity. Here, we use separate supercells for the (doped vs. undoped) bulk WC and the GB structure (with four separate DFT calculations in each case) so that the calculated segregation energy is less sensitive to the size effects. Specifically, a 4×4×4 supercell with 128 atoms in total was used as WC bulk structure. The GB model is discussed above, and 5-10 different segregation sites at each GB layer and bulk structures were taken into account. A stoichiometric substitution is ensured in each calculation of the segregation energy based on Eqs. (1) or (2).

With the fully-optimized WC GB structures, the static all-electron calculations were carried out based on Perdew-Burke-Ernzerhof (PBE) [34] exchange-correlation functional in order to calculate the charge density for both valence and core electrons. The default 96×168×294 FFT-grids were large enough to sample charge density based on the convergence test for a total number of electrons. The Bader charge analysis [35] was used to calculate charge transfer for dopant Ti and Co atoms with surrounding C atoms. The CHARGMOL code based on the DDEC6 atomic population analysis method was used to calculate the sum of bond ordering (SBO) [36, 37].

6.3. Results and Discussion

6.3.1. Asymmetric Segregation of Ti & Co Co-Doped WC GB

The two phases in the Ti-doped WC + 10 wt% Co cermet are the primary hexagonal WC and a secondary Co binder phase, where WC GBs are the

dominant interfaces in this composite. Via aberration-corrected scanning transmission electron microscopy (AC STEM) high-angle annular dark-field (HAADF) imaging, we identify a (0001) // $(0\bar{1}\bar{1}0)$ and $[2\bar{1}\bar{1}0]$ // $[2\bar{1}\bar{1}3]$ WC GB near a WC-Co interface and align this GB to an edge-on condition. A crystallography analysis based on Kikuchi patterns shows that this is a "near Σ 28" GB. Here, the Σ value is not exact, because the coincidental lattice exist only with substantial strains in this hexagonal WC system [38], which would likely be relaxed by the formation of GB disconnections and steps. We catalog this GB as an asymmetric "mixed twist and tilt GB" following Rohrer et al., [22, 38] which represents the most "general" group of GBs (vs. the more special symmetric twist, symmetric tilt, and asymmetric tilt GBs).

Interestingly, this GB is interrupted by multiple steps (Fig. 6.1(a)). But similar dark/bright/dark fringes persist at multiple, disconnected, straight terraces (that can be >30 nm long). Thus, the GB structure (Fig. 6.1) likely represents the stable configuration because it re-appears in several independent (disconnected) segments. An analysis of EBSD mapping suggests that this specific type of (0001) // $(01\bar{1}0)$ and $[2\bar{1}\bar{1}0]$ // $[2\bar{1}\bar{1}3]$ GB represents about 2~3% of ~1000 GBs analyzed. Its frequency is on a par with the top three most frequently-observed GBs in a WC-Co specimen reported by a prior EBSD study [38]. We should point out that similar interfacial structures also exist in other types of (0001) // $(01\bar{1}0)$ GBs that accounts for about 8-9% of all GBs. Thus, this interfacial structure is not rare. The generality of this observation will be discussed further subsequently.

Atomic-resolution HAADF images (Fig. 6.1(b) and (c)) shows a unique segregation superstructure with dark/bright/dark fringes that has never been reported before. The enlarged intensity profile on the right side of Fig. 6.1(c) verifies this dark/bright/dark intensity variation. For convenience, we define the center atomic plane with the brighter fringe as the layer L0. The layers in the WC-2 grain with the $(01\bar{1}0)$ terminal orientation are labeled as L1, L2, etc., and the layers in the WC-1 grain with the (0001) terminal orientation are labeled as $L\bar{1}$, $L\bar{2}$, etc.. Since W is the heaviest element in the system, the dark/bright/dark fringes from $L\bar{1}$ to L1 suggests that the segregation of lighter elements is stronger in the two off-the-center atomic planes ($L\bar{1}$ and L1), which is sometimes called "sub-surface segregation." This off-the-center or sub-surface segregation is further confirmed by an atomic-resolution compositional analysis (Figs. 6.2(a) and (b))

Atomic-resolution STEM-based EDS elemental maps of W, C, Ti, and Co are shown in Fig. 6.2(a). The center L0 layer consists of mostly W, while the $L\bar{1}$ layer is enriched in Ti and the L1 layer is enriched in Co, respectively. A quantitative analysis (Fig. 6.2(b)) shows that the segregation peak compositions of Co and Ti, respectively, both occur off the center asymmetrically in the opposite directions. Specifically, the maximum segregation occurs at the layer L1 with 23 at% Co and the layer $L\bar{1}$ with 24 at% Ti, respectively. The center atomic plane L0 is still largely WC with 35 at% W and ~49 at% C, but only 9 at% Co and 8 at% Ti. Since the HAADF signal intensity is approximately proportional to the square of the atomic number Z [39], where $Z_{Ti} = 22$, $Z_{Co} = 27$, and $Z_W = 74$, this explains the

brighter HAADF intensity at the center L0 layer with two darker layers at L1 and $\mathrm{L}\bar{1}$ on both sides (Fig. 6.1 and 6.2(a)). A prior atom probe tomography (APT) experiment revealed the co-segregation of Co and Ti at WC GBs [40], but the asymmetric distribution of Co and Ti solutes had not been recognized.

On the basis of atomic-resolution EDS analysis and HAADF images from this study, we can conclude that the L1 layer at the $(01\bar{1}0)$ side is enriched in Co and the $\mathrm{L}\bar{1}$ layer at the (0001) side is enriched in Ti, while the center L0 layer in between is W rich. Such a chemically asymmetric and off-the-center segregation profile has never been observed before, nor predicted by any existing model or theory.

More interestingly, the asymmetric segregation further induces asymmetric interfacial structural transitions at the both sides of this GB. On the one hand, the Ti segregation induced a symmetry change on the (0001) side of WC-1 grain from the hexagonal WC to a FCC-like interfacial layer that spans from the layer $\mathrm{L}\bar{2}$ to L0 (Fig. 6.1(c)); i.e., this interfacial layer is represented by one unit cell of the rocksalt TiC-like structure (centered at the $\mathrm{L}\bar{1}$ layer) that accounts two lattice spacings in its apparent thickness. On the other hand, the Co-rich segregation layer on the $(01\bar{1}0)$ side or WC-2 grain is partially disordered, as indicated by the yellow arrows in Fig. 6.1(c). The existence of structural disorder in this Co-enriched segregation layer at L1 is further confirmed by our theoretical calculations that will be discussed below.

While the detailed AC-STEM and atomic-resolution EDS analysis have revealed the highly asymmetric and off-the-center segregation, along with distinct interfacial structural transitions in the opposite sides, the formation mechanism of this complex GB superstructure is hitherto unclear. Hence, we carry out first-principles density functional theory (DFT) calculations to achieve a deeper understanding.

6.3.2. DFT Validation of Asymmetric Segregation

First, based on the DFT optimized undoped GB structures without and with the FCC-like interfacial layer (Fig. 6.2(c) *vs*. 2(d)), we have calculated segregation energies of Ti and Co solutes in different layers in the dilute limit (Fig. 6.2(e)). The GB with an FCC-like interfacial layer exhibits the most negative segregation energy E_{seg} of −3.08 eV/atom for Co at the L1 layer and the most negative E_{seg} of −3.04 eV/atom for Ti at the L$\bar{1}$ layer, as shown by the solid lines in Fig. 6.2(e). These results agree well with our HAADF and EDS observations (Fig. 6.2(a)). In comparison, without the formation of the FCC-like interfacial layer, the strongest segregation (most negative E_{seg}) occurs at the center L0 layer for both Co and Ti, as shown by the dashed lines in Fig. 6.2(d). Thus, the formation of the FCC-like interfacial layer is essential to induce the asymmetric and off-the-center segregation in this GB.

Second, we performed detailed structural analysis for two DFT optimized (relaxed) interfacial structures: the undoped WC GB without the FCC-like interfacial layer (Fig. 6.2(c)) vs. the doped GB (Fig. 6.2(d)) based on the

experimental compositions profiles with the FCC-like interfacial layer (Fig. 6.1(c)). On the one hand, Fig. 6.2(c) shows that undoped WC GB exhibits highly ordered W layers from L$\bar{1}$ to L1 layers although some C atoms near the L1 layer are slightly disordered. On the other hand, in the optimized structure of the doped GB, the Ti-rich L$\bar{1}$ layer maintains a highly ordered structure, but the Co-rich L1 layer becomes partially disordered. Specifically, Co segregation can induce structural disorder in not only the surrounding C atoms, but also the W atoms at the adjacent L1 layer (Fig. 6.2(d)). This predicted Co segregation induced partial disorder further validates our experimental observation (Fig. 6.1(c)).

Third, we further calculated a stability diagram as a function of Ti and Co segregation amounts by comparing relative energies of the GB structures with and without the formation of the FCC-like interfacial layer. This stability diagram (Fig. 6.4) indicates that the FCC-like interfacial layer is stable when the Ti fraction (of metals, excluding C) at the L$\bar{1}$ layer is above ~0.75 (virtually independent of the Co fraction at the L1 layer). Hence, we conclude that the Ti segregation induces an interfacial symmetry change to form the FCC-like interfacial layer. It should be noted that, the segregation induced FCC-like structural reconstruction can be also found in WC/Co phase boundary by both experimental [41] and theoretical studies [42, 43].

Fourth, we examined the changes of coordination environments at each layer in the dilute segregation structures to investigate the causes for the Co and Ti segregation. To illustrate bonding environments clearly, the GB structure are cut

along P1 and P2 planes for three cases if the segregation occurs at the layer L$\bar{1}$ (Fig. 6.5(a)), layer L0 (Fig. 6.5(b)), and layer L1 (Fig. 6.5(c)), respectively; the detailed coordination environments are shown in Fig. 6.5(d) for Ti and Fig. 6.5(e) for Co, respectively, where each has 3 (segregation at L$\bar{1}$, L0, and L1) $\times$ 2 (projected on P1 vs. P2) panels.

On the one hand, the Ti atom is mostly octahedrally coordinated with six carbon atoms at the L$\bar{1}$ layer (Fig. 6.5(d)), suggesting a TiC-based FCC-like rocksalt structure [44, 45] (Fig. 6.6). A similar coordination environment of Ti is also found in the L0 layer (as shown in middle panel of Fig. 6.5(d). On the other hand, if Ti segregated to the L1 layer (the right panel in Fig. 6.5(d)), the W atoms (in the L2 layer), which are not octahedrally coordinated with carbon atoms, would distort the preferred carbon coordination environment of Ti. For example, DFT optimization shows that the upper two carbon atoms would move away from the Ti atom, thereby distorting the Ti octahedron at the L1 layer and reducing the corresponding coordination number. Since octahedral coordination with six Ti-C bonds is the most stable for Ti [30, 46], this destabilizes the segregation of Ti at L1 layer. This analysis explains why the current GB form an FCC-like interfacial layer with the preferred segregation of Ti in the L$\bar{1}$ layer.

Furthermore, we find that Co also exhibits an FCC-like sublattice with six surrounding carbon atoms at L$\bar{1}$ and L0 layers (as shown in the right and middle columns of Fig. 6.5(e)). However, the adjacent carbon atoms can be easily repelled away from the Co atom segregated at the L1 layer, because the loosely-pack W

atoms at the L2 layer provide a large space for them to relax; see, e.g., the white circles with arrows in the right panel of Fig. 6.5(e). Since a tetrahedral coordination with three carbon atoms is more stable for Co (see Materials Project Website [46]); the Co segregation at the L1 layer is favorable.

Thus, DFT calculations discussed above suggest that the observed asymmetric segregation stems from the different coordination environments: the octahedral coordination with six carbons for Ti at the L$\bar{1}$ layer vs. the tetrahedral coordination with only approximately three carbons for Co at the L1 layer. Furthermore, a strong distortion in the carbon coordination at the L1 layer can lead to interfacial disordering (Fig. 6.2(d)), which explains the experimental observation of the partially disordered Co segregation layer (Fig. 6.1(c)).

6.3.3. Differential Charge Density Map

Fifth, we further calculated the differential charge density (DCD) to reveal the correlation between segregation and charge transfer. The projected DCD maps (Fig. 6.5(d)) show that strong charge accumulation occurred between Ti and six coordinated C atoms in the FCC-like interfacial layer (at the L$\bar{1}$ and L0 layers), while less accumulation is found at the L1 layer. Since large charge transfer can prompt the segregation of the solute atom [47, 48]. the formation of an FCC-like interfacial layer should favor the Ti segregation. A quantitative analysis of the excess charge transfer, Δq_{ex}, further confirms this suggestion (Fig. 6.7). In comparison, the strong charge transfer near Co at the L1 layer (right column of Fig. 6.5(e)) favor strong Co segregation at this L1 layer, whereas the much weak

charge transfer between Co and six individual C atoms at the L$\bar{1}$ and L0 layers (left and middle columns of Fig. 6.5(e)) accounts for weak segregation there. These predictions from charge transfers again agree well with experimental observations (Fig. 6.1).

6.3.4. Sum of Bond Ordering as a Novel GB Segregation Descriptor

The above discussions illustrate that both coordination environment and charge transfer are useful to understand solute segregation at the GB. However, neither of them can illustrate the true bonding environment and local chemical structure. Thus, we propose a new quantity, sum of bond ordering (SBO) [37], to uncover the relation between the solute segregation and the bonding environment.

On the one hand, Fig. 6.8(a) shows calculated SBO of Ti and Co segregated at each GB layer, in a comparison with all possible Ti- and Co-based carbides (Figs. 6.8(b-c)). Notably, the Ti SBO of 3.09 at the L$\bar{1}$ layer (represented by the red dot in Fig. 6.8(b)) is very close to that of the FCC TiC, the titanium carbide with the lowest formation energy E_f (Fig. 6.8(b)). The similarity of the SBO values also suggests the favorable formation of a Ti-based FCC-like interfacial layer at the L$\bar{1}$ layer, in an excellent agreement with our experiments and calculations.

On the other hand, Fig. 6.8(c) shows the a Co SBO value of 3.90 at the L1 layer (represented by the red dot) is towards to relatively stable Co_2C and Co_3C phases (with coordination of 3 and 2), whereas the segregated Co at all other layers have smaller SBO values (of ~3.4 - 3.6), towards to highly unstable FCC-

and WC-structured CoC phases (both with 6 coordination). Consequently, the most favorable SBO of the segregated Co occurs at the L1 layer and corresponds to a loosely bonding environment between Co-C, which promotes interfacial disordering.

Furthermore, there are two stable ternary phases (Co_6W_6C and Co_3W_3C with $E_f < 0$) in Fig. 6.8(c), where Co and C atoms do not form direct bonds but are separated by W atoms. This also implies that direct Co-C bond is less stable (Fig. S8C-D). Similarly, the intermediate W-rich L0 layer of the observed asymmetric segregation superstructure (Fig. 6.1 and Fig. 6.2(a)) can also allow an intermediate layer for a gradual transition from a highly stable, six-coordinated Ti-C to a relatively unstable and less-coordinated Co-C bonding environment. Thus, this SBO analysis explains the formation of off-the-center, asymmetric segregation structure (Fig. 6.1 and Fig. 6.2(a)).

The success of the proposed SBO theory to explain segregation behavior implies that SBO can be used as a new descriptor to predict segregation trend in complex interfacial structures, which can be applied to other systems beyond the WC.

6.3.5. Factors to Form Highly Asymmetric Interfacial Superstructure

Based on molecular-orbital theory, the bonding of transition-metal monocarbides includes a mixture of covalent, ionic, and metallic contributions [45, 49]. Such a complex bonding nature enables a variety of polymorphs. For instance,

a carbide with nine or less valence electrons per unit cell (i.e., four for Ti ($3d^2 4s^2$) and four for C ($2s^2 2p^2$)) is more likely to form the FCC structure that is more covalent. In contrast, ten or more valence electrons in WC hexagonal structure (i.e. six for W ($5d^4 6s^2$) and four for C) may lead to more metallic (mixed metallic-covalent) bonding, according to the crystal orbital overlap population (COOP) analysis by Wijeyesekera and Hoffman [50]. Co-based carbides do not follow the same valence electron rule due to complex metal lattices (Co_2C and Co_3C); however, it is likely that seven *d* valence electrons of Co ($3d^7 4s^2$) lead to more metallic bonding in Co-based carbides.

Thus, the asymmetric segregation observed in this study can be related to the transition from the strong covalent bonding in Ti-rich $L\bar{1}$ layer to the mixed metallic-covalent bonding in the W-rich L0 layer, and finally to the strong metallic bonding in Co-rich L1 layer.

Furthermore, Wijeyesekera and Hoffman [50] suggested that bonding in a closed-packed metal is generally isotropic while the bonding in non-closed-packed metal is more anisotropic. This may imply that the bonding in the FCC TiC is relatively isotropic, the bonding in hexagonal WC is intermediate, while the bonding in Co-based carbides is highly anisotropic. This may also contribute the formation of a highly asymmetric Ti/Co/W based interfacial superstructure observed in this study.

Therefore, we suggest that the highly asymmetric segregation and asymmetric interfacial superstructures may exist in other carbides, as well as

borides, nitrides, sulfides, and other materials systems, with similar bonding characters (e.g., different preferred coordination numbers, metallic vs. covalent, the degree of close packing, and isotropic vs. anisotropy bonding environment of the two co-dopants and hosting metals). As we have discussed in the main text, we also expect similar highly asymmetric segregation to occur more frequently at mixed GBs with two low-index grain surface terminal planes (e.g., the three (0001) // $(01\bar{1}0)$ GBs observed in this study), but with little (or less) lattice matching between the two abutting grains. Further experiments and modeling studies are needed to confirm these hypotheses.

6.4. Conclusions

We observed highly asymmetric and off-the-center segregation of Ti and Co in mixed GBs in WC, along with different interfacial structural transitions of symmetry change (reconstruction) and interfacial disordering in the two sides, via detailed AC-STEM characterization and atomic resolution EDX mapping. Large-scale (592-atom) first-principles calculations further verified the energetic stability of this highly asymmetric interfacial superstructure and further reveal the important roles of the coordination and bonding environments of the solute atoms on determining the segregation pattern and interfacial structure.

Our results not only shed light on the complex GB segregation structures in Ti-doped WC-Co, but also demonstrate the possible existence of asymmetric complex interfacial superstructures that differ significantly from all prior experimental observations and are beyond the predictions of any existing models.

Thus, this discovery greatly expands our knowledge of atomic level segregation structures in real polycrystalline materials, with potentially broad impacts.

Chapter 6, in part, is a reprint of manuscript “A highly asymmetric interfacial structure in WC: expanding classical grain boundary segregation and new complexion theory”, Z. Luo, C. Hu, L. Xie, H. Nie, C. Xiang, X. Gu, J. He, W. Zhang, Z. Yu, and J. Luo, Materials Horizon, 2020, 7, 173-180. The experiments were carried out by Z. Luo et al. The dissertation author was the primary investigator to perform theoretical calculation and the first co-author of this paper.

Table 6.1. Calculated lattice parameters (***a***, ***c***), ground-state energies (*E*), and enthalpy of formation ($-\Delta H$), for the hexagonal WC (space group: $P\bar{6}m2$, No. 187), graphite C (space group: $P6_3/mmc$, No. 194), and BCC-W (space group: $Im\bar{3}m$, No. 229) using various DFT methods, and comparison with experimental data from the Inorganic Crystal Structure Database (ICSD).

	WC				C (Graphite)			W	
DFT functionals	***a*** (Å)	***c*** (Å)	*E* (eV/Unit)	$-\Delta H$ (KJ/mol)	***a*** (Å)	***c*** (Å)	*E* (eV/atom)	***a*** (Å)	*E* (eV/atom)
PBE	2.924	2.849	-22.457	26.002	2.468	8.685	-9.227	3.185	-12.961
PBE-D2	2.870	2.794	-24.567	68.530	2.464	6.421	-9.336	3.122	-14.521
PBE-D3	2.910	2.843	-23.173	27.813	2.467	6.932	-9.308	3.158	-13.577
TS	2.900	2.840	-23.788	30.616	2.462	6.679	-9.354	3.131	-14.117
TS+SCS	2.916	2.840	-23.305	8.231	2.464	6.706	-9.338	3.163	-13.882
revPBE	2.951	2.874	-16.809	20.578	2.478	7.109	-7.521	3.213	-9.074
optPBE	2.934	2.859	-17.956	30.578	2.472	6.826	-7.874	3.193	-9.765
optB88	2.930	2.854	-18.322	34.263	2.466	6.673	-8.020	3.186	-9.947
optB86b	2.916	2.846	-19.007	41.835	2.468	6.631	-8.138	3.171	-10.436
rPW86	2.982	2.896	-16.343	-3.874	2.477	7.037	-7.620	3.246	-8.764
PBEsol	2.902	2.830	-23.908	43.594	2.462	8.602	-9.643	3.155	-13.813
	2.902	2.849[a]	/	41.83[f]	2.462	3.354[g]	/	3.142[h]	
	2.889	2.841[b]						3.165[i]	
Experiment	2.895	2.858[c]						3.164[j]	
	2.894	2.827[d]						3.168[k]	
	2.885	2.821[e]						3.165[l]	

a. ICSD 246149
b. ICSD 246150
c. ICSD 246151
d. ICSD 260168
e. ICSD 260171
f. Experimental free standard formation enthalpy $\Delta G = -10000 + 1.17T \pm 100$ cal/mol, see ref. [51]. When $T = 0$, $\Delta G = -10$ kcal/mol = -41.83 kJ/mol.
g. X-ray diffraction data for graphite to 20 GPa.
h. ICSD 167904
i. ICSD 653430
j. ICSD 653431
k. ICSD 653432
l. ICSD 43421

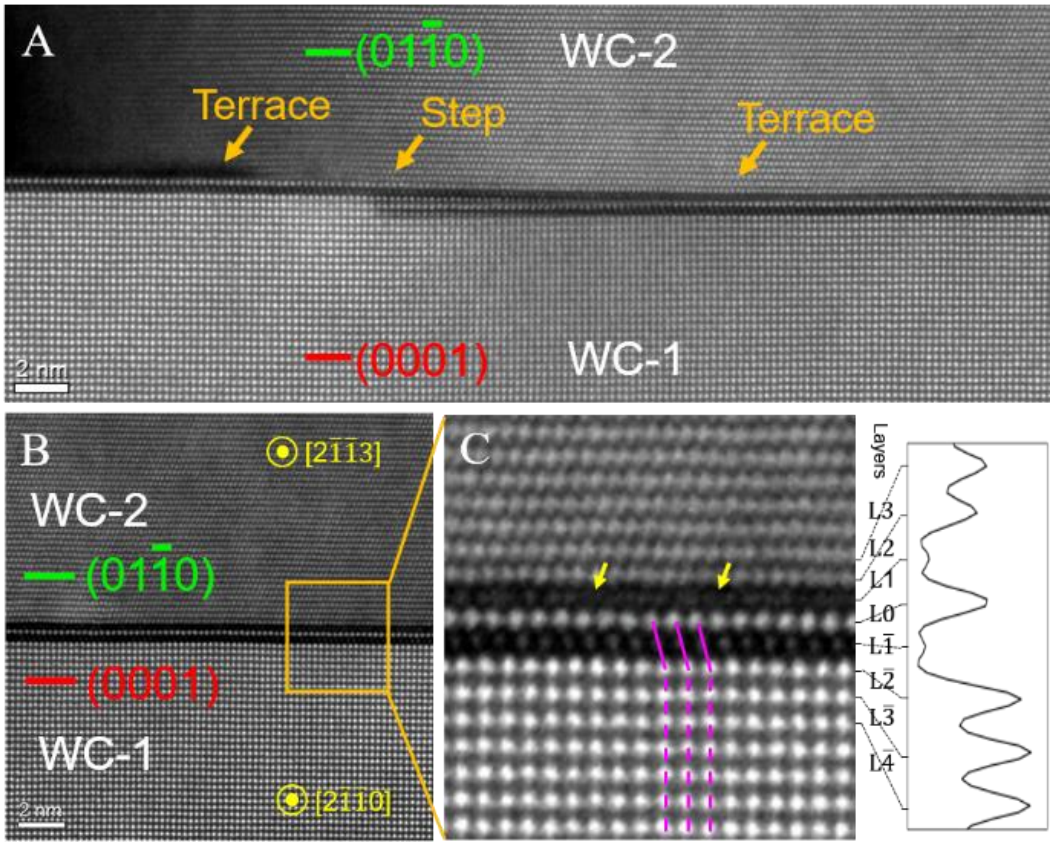

Figure 6.1 (a) Lower-magnification AC STEM HAADF image of a WC grain boundary (GB) with a step. The two terraces exhibit similar dark/bright/dark fringes despite they are disconnected, showing the persistence of this unique interfacial superstructure. (b) Higher-magnification HAADF micrograph of the edge-on GB. (c) Enlarged view of the orange box with an enlarged intensity profile shown in the right panel. For convenience, we labeled the brightest column in the center of the GB core as the layer L0. The yellow arrows indicate some segregation-induced interfacial structural (partial) disorder in layer L1. The parallel pink lines show an FCC-like interfacial layer (i.e., a segregation-induced interfacial symmetry change) on the other side.

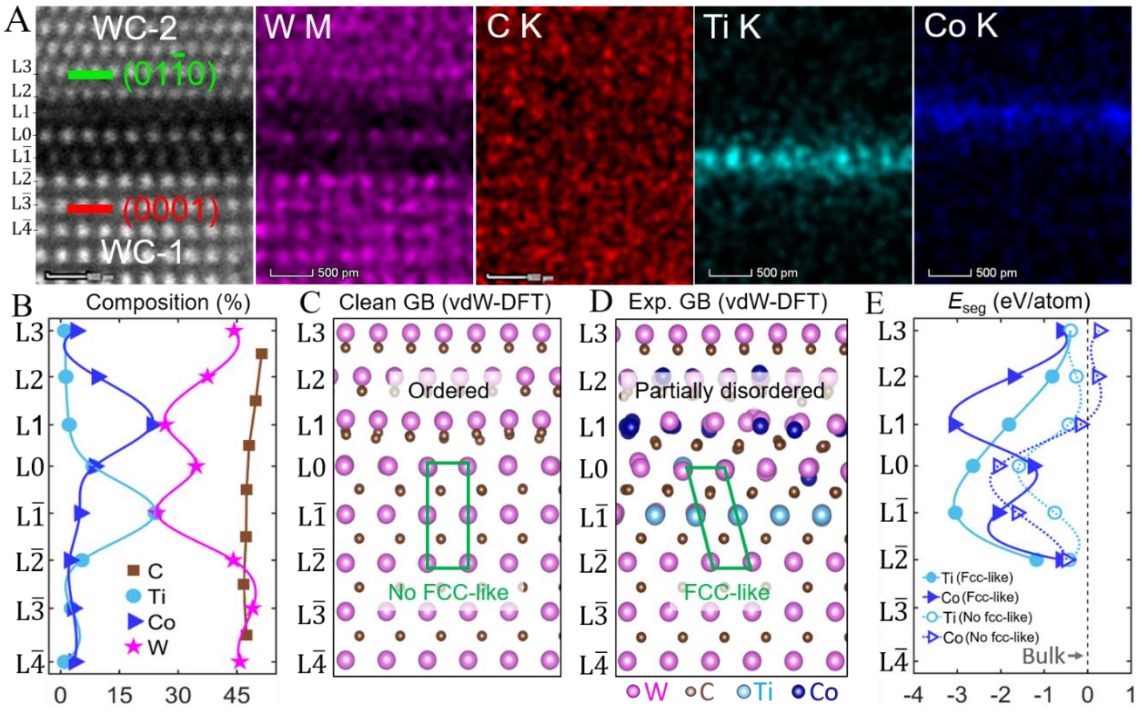

Figure 6.2 (a) Experimental HAADF and corresponding energy dispersive X-ray spectroscopy (EDS) elemental maps of W, C, Ti, and Co. (b) Measured chemical compositions for each layer. (c) Density functional theory (DFT) optimized undoped WC GB structure. The green rectangular indicates no formation of face-centered cubic (FCC)-like interfacial layer. Note that the L1 layer in the undoped WC GB is highly ordered. (d) DFT optimized doped WC GB structure based on experimentally measured compositional profiles, where the green parallelogram shows the formation of an FCC-like interfacial layer (from L$\bar{2}$ to L0) at the (0001) side. Note that the Co-rich L1 layer is partially disordered. (e) DFT calculated segregation energies (E_{seg}) of Ti and Co at different layers; the dashed lines represent the segregation energies without the formation of the FCC-like interfacial layer.

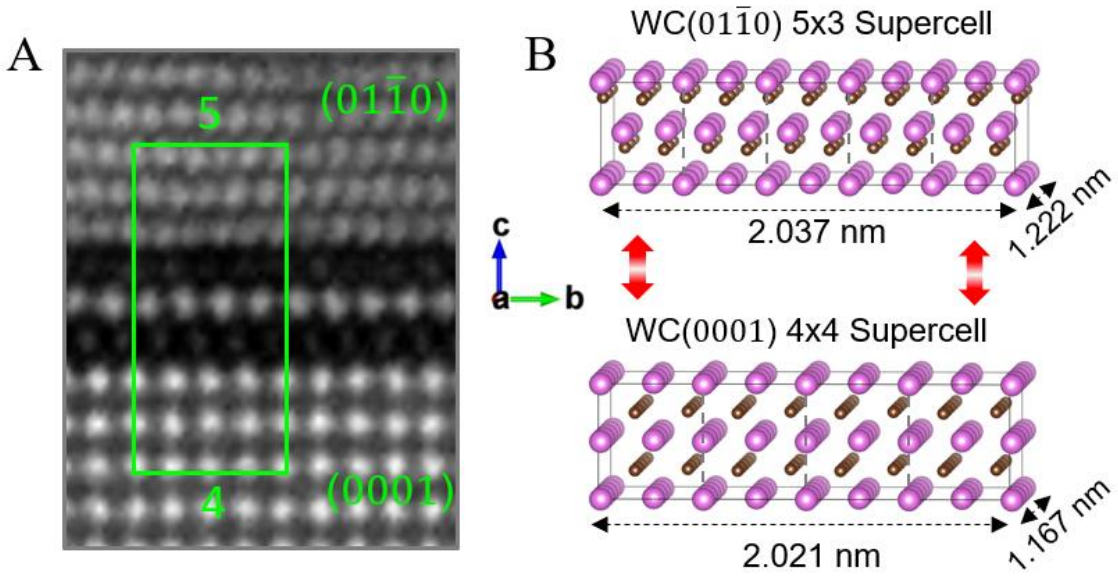

Figure 6.3 (a) STEM HAADF image of the WC $(01\bar{1}0)$ // (0001) and $[2\bar{1}\bar{1}3]$ // $[2\bar{1}\bar{1}0]$ GB. The green box highlights a coherent match between $5\times(01\bar{1}0)$ grains and $4\times(0001)$ grains along the direction parallel to GB. (b) The computation model of this WC GB jointed by a 5×3 WC $(01\bar{1}0)$ orthogonal supercell and a 4×4 WC (0001) orthogonal supercell.

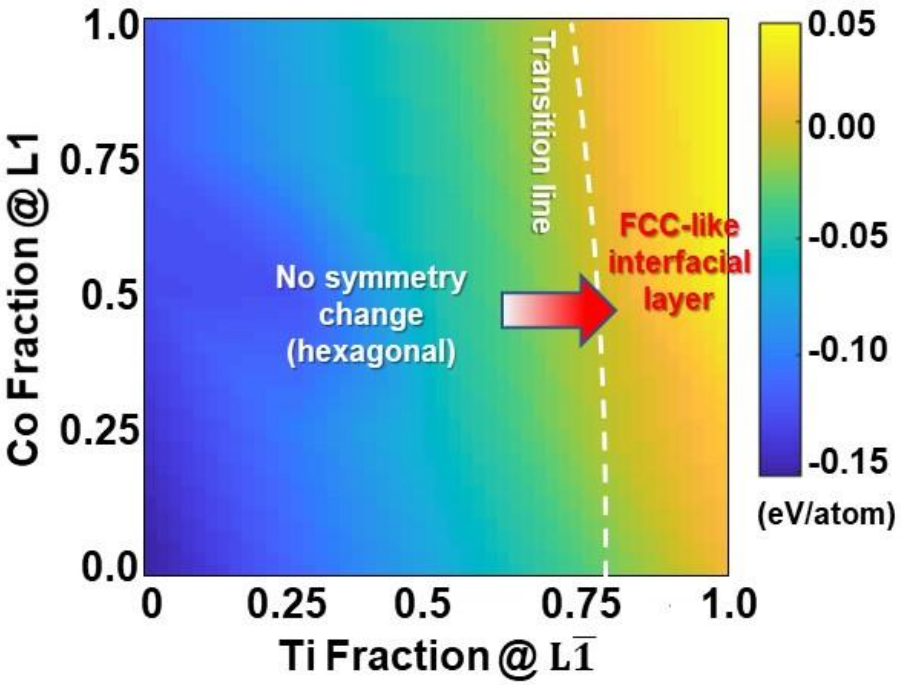

Figure 6.4 The GB structure (complexion) stability map as a function of Ti doping fraction at the L$\bar{1}$ layer and Co doping fraction at the L1 layer. The color map represents the calculated the energy difference, $\Delta E = (E_{\mathrm{FCC-like}} - E_{\mathrm{no\ FCC-like}})/N_{\mathrm{atom}}$, where $E_{\mathrm{Fcc-like}}$ is the energy of a GB with the formation FCC-like layer, $E_{\mathrm{no\ FCC-like}}$ is the energy of GB without the symmetry change (i.e., remaining the hexagonal symmetry without the formation of the FCC-like interfacial layer), and N_{atom} is the total number of atoms. The white dashed line indicates the occurrence of an interfacial structural transition to form an FCC-like interfacial layer with a local (interfacial) symmetry change.

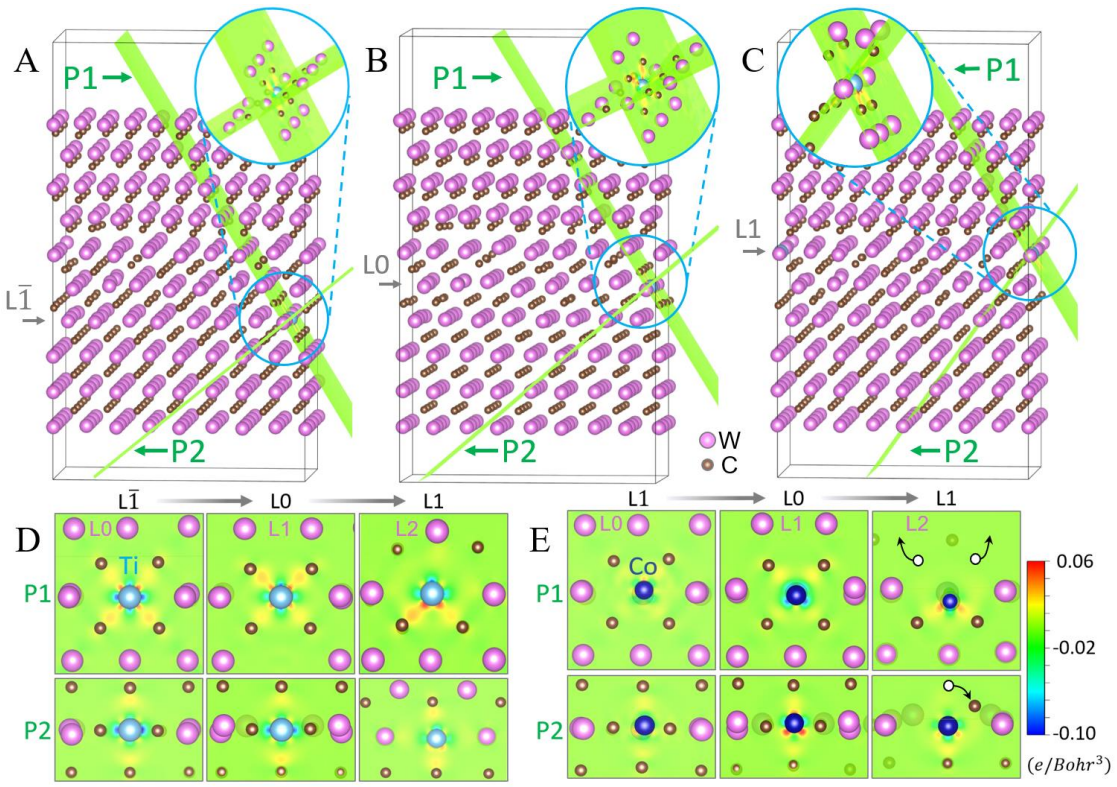

Figure 6.5 3-D structures showing the coordination environments, if the segregation occurs at the (a) layer L$\bar{1}$, (b) layer L0, and (c) layer L1, respectively. P1 and P2 planes were plotted to illustrate the chemical bonding environments. 2-D differential charge density maps projected on the P1 and P2 planes for (d) Ti and (e) Co solute atoms, where each has 3×2 panels to represent three segregation positions (L$\bar{1}$, L0, and L1) and two projected planes (P1 and P2). The white circles in (e) were the carbon atoms before structural optimizing. The arrows indicated that the carbon atoms are driven away in that direction after the DFT structural optimization.

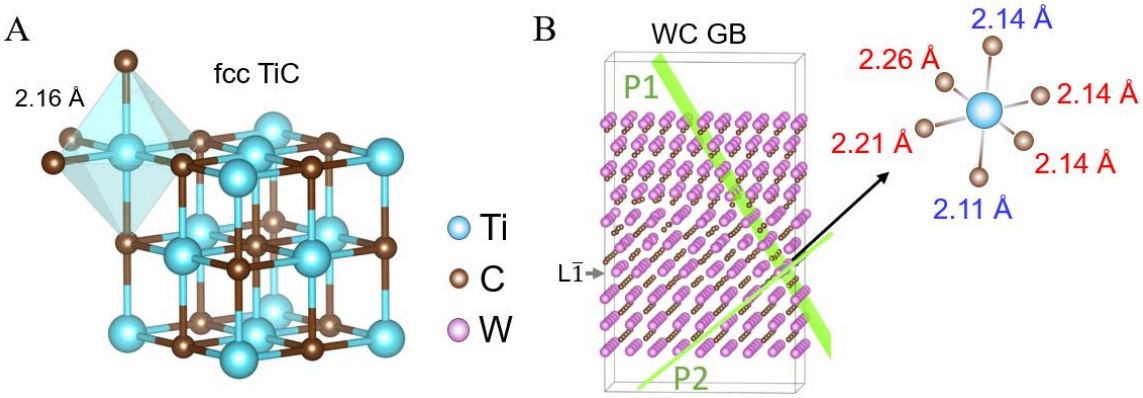

Figure 6.6 Crystal structure of (a) rocksalt (FCC) TiC. The Ti atom is octahedrally coordinated with six C atoms, as illustrated by the blue octahedron. The Ti-C bond length is 2.16 Å. (b) DFT-optimized TiC-based, FCC-like interfacial layer formed at the WC GB on the (0001) side (i.e., around the $L\bar{1}$). The four DFT-optimized bond lengths colored in red are on Plane 1 (P1), and the other two-colored blue are on Plane 2 (P2). The slightly different bond lengths show there are distortions in the FCC-like interfacial layer (so that it is not a perfect FCC or rocksalt structure).

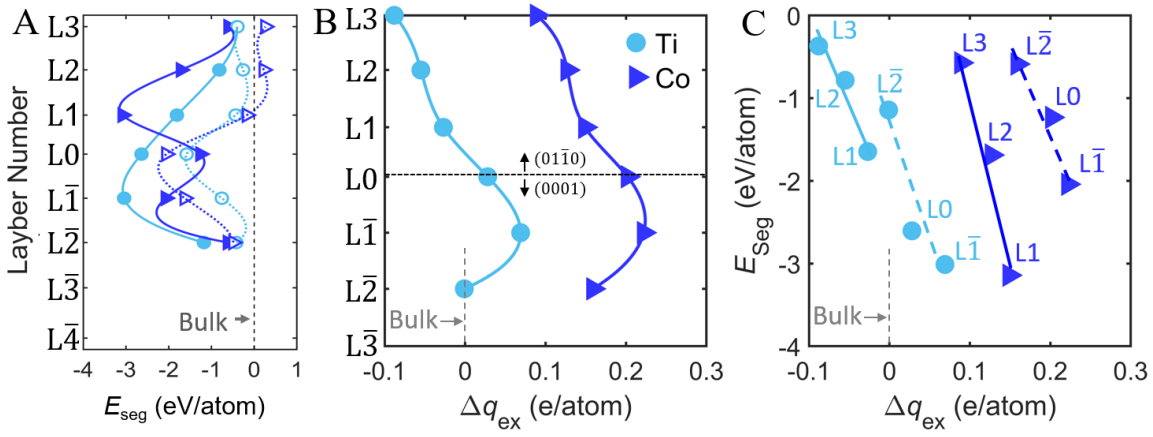

Figure 6.7 (a) DFT calculated segregation energies of Ti and Co at different layers, referenced to the bulk. The dashed lines represent the segregation energies without the formation of the FCC-like interfacial layer. (b) Computed excess charge transfer Δq_{ex} of dopant Ti or Co at the different layer position in the direction perpendicular to the WC GB. The black horizontal dot line separates GB into two regions: the upper (01$\bar{1}$0) side vs. the lower (0001) side. The grey vertical dashed line indicates the computed charge transfer insider the bulk WC grain. (c) Computed segregation energy of dopant atoms as a function of Δq_{ex}. The solid trend lines are drawn for the segregation of Ti and Co at the (01$\bar{1}$0) side, while the dashed trend lines are drawn for the segregation of Ti and Co at the (0001) side.

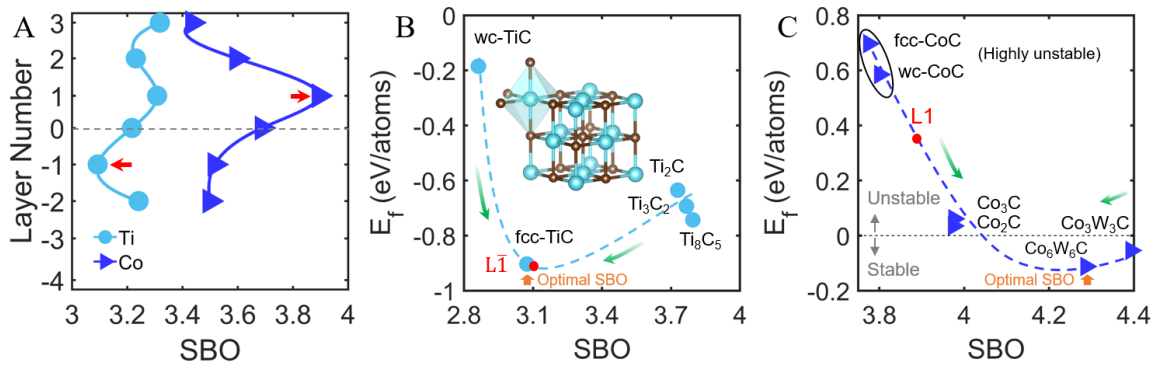

Figure 6.8 (a) Sum of bond ordering (SBO) of solute atoms at different layers near the GB. Red arrows indicate the layer position with the most negative segregation energy for each solute atom. (b) The formation energy (E_f) of all the possible Ti-based carbides as a function of Ti SBO, where the brown arrow indicates an optimal SBO of Ti that corresponds to the lowest E_f. The red dot represents Ti SBO at $L\bar{1}$, which is close to the optimal. The inset is the FCC (rocksalt) TiC crystal structure. (c) The E_f of all possible Co-based carbides as a function of Co SBO, where the brown arrow indicates optimal SBO that corresponds to the lowest E_f. The red dot represents the Co SBO at the L1 layer. The green arrows point to the directions to achieve optimal SBO with the lower E_f.

References

[1] D. McLean, Grain Boundaries in Metals, Oxford, Clarendon Press, (1957).

[2] J. Luo, H. Cheng, K.M. Asl, C.J. Kiely, M.P. Harmer, The Role of a Bilayer Interfacial Phase on Liquid Metal Embrittlement, Science, 333 (2011) 1730-1733.

[3] R.F. Klie, J.P. Buban, M. Varela, A. Franceschetti, C. Jooss, Y. Zhu, N.D. Browning, S.T. Pantelides, S.J. Pennycook, Enhanced current transport at grain boundaries in high-Tc superconductors, Nature, 435 (2005) 475-478.

[4] E.D. Hondros, M.P. Seah, The theory of grain boundary segregation in terms of surface adsorption analogues, Metallurgical Transactions A, 8 (1977) 1363-1371.

[5] M. Tang, W.C. Carter, R.M. Cannon, Grain Boundary Transitions in Binary Alloys, Physical Review Letters, 97 (2006) 075502.

[6] Y. Mishin, W.J. Boettinger, J.A. Warren, G.B. McFadden, Thermodynamics of grain boundary premelting in alloys. I. Phase-field modeling, Acta Materialia, 57 (2009) 3771-3785.

[7] P. Wynblatt, D. Chatain, Solid-state wetting transitions at grain boundaries, Materials Science and Engineering: A, 495 (2008) 119-125.

[8] J.M. Rickman, J. Luo, Layering transitions at grain boundaries, Current Opinion in Solid State and Materials Science, 20 (2016) 225-230.

[9] J. Luo, Grain boundary complexions: The interplay of premelting, prewetting, and multilayer adsorption, Applied Physics Letters, 95 (2009) 071911.

[10] S. Yang, N. Zhou, H. Zheng, S.P. Ong, J. Luo, First-Order Interfacial Transformations with a Critical Point: Breaking the Symmetry at a Symmetric Tilt Grain Boundary, Physical Review Letters, 120 (2018) 085702.

[11] G. Duscher, M.F. Chisholm, U. Alber, M. Rühle, Bismuth-induced embrittlement of copper grain boundaries, Nature Materials, 3 (2004) 621-626.

[12] J. Luo, Stabilization of Nanoscale Quasi-Liquid Interfacial Films in Inorganic Materials: A Review and Critical Assessment, Critical Reviews in Solid State and Materials Sciences, 32 (2007) 67-109.

[13] D.R. Clarke, On the Equilibrium Thickness of Intergranular Glass Phases in Ceramic Materials, Journal of the American Ceramic Society, 70 (1987) 15-22.

[14] N. Shibata, S.J. Pennycook, T.R. Gosnell, G.S. Painter, W.A. Shelton, P.F. Becher, Observation of rare-earth segregation in silicon nitride ceramics at subnanometre dimensions, Nature, 428 (2004) 730-733.

[15] T. Hu, S. Yang, N. Zhou, Y. Zhang, J. Luo, Role of disordered bipolar complexions on the sulfur embrittlement of nickel general grain boundaries, Nature Communications, 9 (2018) 2764.

[16] J. Luo, V.K. Gupta, D.H. Yoon, H.M. Meyer, Segregation-induced grain boundary premelting in nickel-doped tungsten, Applied Physics Letters, 87 (2005) 231902.

[17] S.J. Dillon, M. Tang, W.C. Carter, M.P. Harmer, Complexion: A new concept for kinetic engineering in materials science, Acta Materialia, 55 (2007) 6208-6218.

[18] P.R. Cantwell, M. Tang, S.J. Dillon, J. Luo, G.S. Rohrer, M.P. Harmer, Grain boundary complexions, Acta Materialia, 62 (2014) 1-48.

[19] Z. Wang, M. Saito, K.P. McKenna, L. Gu, S. Tsukimoto, A.L. Shluger, Y. Ikuhara, Atom-resolved imaging of ordered defect superstructures at individual grain boundaries, Nature, 479 (2011) 380-383.

[20] B. Feng, T. Yokoi, A. Kumamoto, M. Yoshiya, Y. Ikuhara, N. Shibata, Atomically ordered solute segregation behaviour in an oxide grain boundary, Nature Communications, 7 (2016) 11079.

[21] H.-I. Yoon, D.-K. Lee, H.B. Bae, G.-Y. Jo, H.-S. Chung, J.-G. Kim, S.-J.L. Kang, S.-Y. Chung, Probing dopant segregation in distinct cation sites at perovskite oxide polycrystal interfaces, Nature Communications, 8 (2017) 1417.

[22] Z. Yu, P.R. Cantwell, Q. Gao, D. Yin, Y. Zhang, N. Zhou, G.S. Rohrer, M. Widom, J. Luo, M.P. Harmer, Segregation-induced ordered superstructures at general grain boundaries in a nickel-bismuth alloy, Science, 358 (2017) 97.

[23] G. Kresse, J. Furthmüller, Efficient iterative schemes for ab initio total-energy calculations using a plane-wave basis set, Physical Review B, 54 (1996) 11169-11186.

[24] G. Kresse, J. Hafner, Ab initio molecular dynamics for liquid metals, Physical Review B, 47 (1993) 558-561.

[25] P.E. Blöchl, Projector augmented-wave method, Physical Review B, 50 (1994) 17953-17979.

[26] G. Kresse, D. Joubert, From ultrasoft pseudopotentials to the projector augmented-wave method, Physical Review B, 59 (1999) 1758-1775.

[27] J. Klimeš, D.R. Bowler, A. Michaelides, Chemical accuracy for the van der Waals density functional, Journal of Physics: Condensed Matter, 22 (2009) 022201.

[28] Y.-H. Tian, J. Huang, X. Sheng, B.G. Sumpter, M. Yoon, M. Kertesz, Nitrogen Doping Enables Covalent-Like π–π Bonding between Graphenes, Nano Letters, 15 (2015) 5482-5491.

[29] S. Lebègue, J. Harl, T. Gould, J.G. Ángyán, G. Kresse, J.F. Dobson, Cohesive Properties and Asymptotics of the Dispersion Interaction in Graphite by the Random Phase Approximation, Physical Review Letters, 105 (2010) 196401.

[30] D. Connétable, First-principles study of transition metal carbides, Materials Research Express, 3 (2016) 126502.

[31] C. Hu, X. Zeng, Y. Liu, M. Zhou, H. Zhao, T.M. Tritt, J. He, J. Jakowski, P.R.C. Kent, J. Huang, B.G. Sumpter, Effects of partial La filling and Sb vacancy defects on $\mathrm{CoS}{\mathrm{b}}_{3}$ skutterudites, Physical Review B, 95 (2017) 165204.

[32] C. Hu, P. Ni, L. Zhan, H. Zhao, J. He, T.M. Tritt, J. Huang, B.G. Sumpter, Theoretical investigations of electrical transport properties in CoSb3 skutterudites under hydrostatic loadings, Rare Metals, 37 (2018) 316-325.

[33] R. Tran, Z. Xu, N. Zhou, B. Radhakrishnan, J. Luo, S.P. Ong, Computational study of metallic dopant segregation and embrittlement at molybdenum grain boundaries, Acta Materialia, 117 (2016) 91-99.

[34] J.P. Perdew, K. Burke, M. Ernzerhof, Generalized Gradient Approximation Made Simple, Physical Review Letters, 77 (1996) 3865-3868.

[35] G. Henkelman, A. Arnaldsson, H. Jónsson, A fast and robust algorithm for Bader decomposition of charge density, Computational Materials Science, 36 (2006) 354-360.

[36] T.A. Manz, N.G. Limas, Introducing DDEC6 atomic population analysis: part 1. Charge partitioning theory and methodology, RSC Advances, 6 (2016) 47771-47801.

[37] N.G. Limas, T.A. Manz, Introducing DDEC6 atomic population analysis: part 4. Efficient parallel computation of net atomic charges, atomic spin moments, bond orders, and more, RSC Advances, 8 (2018) 2678-2707.

[38] C.-S. Kim, G.S. Rohrer, Geometric and Crystallographic Characterization of WC Surfaces and Grain Boundaries in WC-Co Composites, Interface Science, 12 (2004) 19-27.

[39] Z. Yu, J. Luo, B. Shi, J. Zhao, M.P. Harmer, J. Zhu, Embedding Ba Monolayers and Bilayers in Boron Carbide Nanowires, Scientific Reports, 5 (2015) 16960.

[40] J. Weidow, H.-O. Andrén, Grain and phase boundary segregation in WC–Co with TiC, ZrC, NbC or TaC additions, International Journal of Refractory Metals and Hard Materials, 29 (2011) 38-43.

[41] X. Liu, X. Song, H. Wang, X. Liu, F. Tang, H. Lu, Complexions in WC-Co cemented carbides, Acta Materialia, 149 (2018) 164-178.

[42] S.A.E. Johansson, G. Wahnström, A computational study of thin cubic carbide films in WC/Co interfaces, Acta Materialia, 59 (2011) 171-181.

[43] S.A.E. Johansson, G. Wahnström, Theory of ultrathin films at metal–ceramic interfaces, Philosophical Magazine Letters, 90 (2010) 599-609.

[44] C. Hu, J. Huang, B.G. Sumpter, E. Meletis, T. Dumitrică, Ab Initio Predictions of Strong Interfaces in Transition-Metal Carbides and Nitrides for Superhard Nanocomposite Coating Applications, ACS Applied Nano Materials, 1 (2018) 2029-2035.

[45] C. Hu, J. Huang, B.G. Sumpter, E. Meletis, T. Dumitrică, Ab Initio Predictions of Hexagonal Zr(B,C,N) Polymorphs for Coherent Interface Design, The Journal of Physical Chemistry C, 121 (2017) 26007-26018.

[46] A. Jain, S.P. Ong, G. Hautier, W. Chen, W.D. Richards, S. Dacek, S. Cholia, D. Gunter, D. Skinner, G. Ceder, K.A. Persson, Commentary: The Materials Project: A materials genome approach to accelerating materials innovation, APL Materials, 1 (2013) 011002.

[47] C. Hu, J. Luo, First-order grain boundary transformations in Au-doped Si: Hybrid Monte Carlo and molecular dynamics simulations verified by first-principles calculations, Scripta Materialia, 158 (2019) 11-15.

[48] H. Zheng, R. Tran, X.-G. Li, B. Radhakrishnan, S.P. Ong, Role of Zr in strengthening MoSi2 from density functional theory calculations, Acta Materialia, 145 (2018) 470-476.

[49] Z. Wu, X.-J. Chen, V.V. Struzhkin, R.E. Cohen, Trends in elasticity and electronic structure of transition-metal nitrides and carbides from first principles, Physical Review B, 71 (2005) 214103.

[50] S.D. Wijeyesekera, R. Hoffmann, Transition metal carbides. A comparison of bonding in extended and molecular interstitial carbides, Organometallics, 3 (1984) 949-961.

[51] D.K. Gupta, L.L. Seigle, Free energies of formation of WC and W2C, and the thermodynamic properties of carbon in solid tungsten, Metallurgical Transactions A, 6 (1975) 1939.

Chapter 7. Uncovering Electrochemically Induced Grain Boundary Phase-Like Transition

7.1. Introduction

It has been long proposed that grain boundaries (GBs) can be considered as two-dimensional (2D) interfacial phases [1] (*a.k.a.* "complexions" [2-7]), which can undergo phase-like transitions to influence a variety of properties [2, 5, 8-11]. Notably, GB transitions can alter microstructural evolution abruptly, *e.g.*, triggering abnormal grain growth [3-5]. However, how an abnormal (excessively large) grain can initiate remains elusive defying scrutiny for over 50 years. Also, interestingly, electric fields and currents, which are used in various innovative materials processing [12-15] and electrochemical energy conversion [16, 17] and storage [18] devices, can often alter microstructures unexpectedly and abruptly. However, the underlying atomic-level mechanisms remain elusive. Using ZnO-Bi_2O_3 as a model system, we uncover how an applied electric current can drastically change the microstructural evolution through electrochemically induced GB transitions. By combining aberration-corrected electron microscopy, photoluminescence spectroscopy, first-principles calculations, a generalizable thermodynamic model, and *ab initio* molecular dynamics, we reveal that electrochemical reduction can cause GB disorder-to-order transitions to markedly increase GB diffusivities. Consequently, enhanced or abnormal grain growth takes place. This work builds a bridge between two important areas of GB phase-like transitions and electric field effects on microstructural evolution, while advancing our fundamental knowledge

in both areas and opening a new window of tailoring GB properties and microstructures electrochemically.

This study first aims at decoding how an electric field/current can alter microstructural evolution, an outstanding scientific problem of fundamental interest yet with broad technological implications. A spectrum of fascinating and intriguing observations of the "electric field effects" of suppressed [12, 19] *vs.* enhanced [19-24] (including abnormal [16, 22]) grain growth have been made in several oxides. Moreover, electric currents are used in various electrochemical devices for energy storage and conversion, such as solid oxide fuel cells [16, 17] and solid-state batteries [18], where they can cause unexpected (often undesirable) changes in microstructures or GB properties.

In a broader context, the formation and transition of 2D interfacial phases [1], which were also named as "complexions" [2-5, 7] to differentiate them from thin layers of precipitated 3D bulk phases at GBs, can often control various kinetic, mechanical, chemical, electronic, and other properties [2, 5, 8-11]. However, the majority of prior studies focused on symmetric tilt or twist GBs that are relatively easy to image and model. For example, a most recent study observed GB phase transitions at a symmetric tilt GB in pure copper [25]. General GBs (asymmetric GBs that are often of mixed tilt and twist characters [26]) are much less understood, but they are ubiquitous and can often be the weaker links mechanically and chemically in polycrystalline materials [8, 9, 27]. Moreover, Dillon and Harmer proposed that anisotropic complexion transitions at general GBs can cause

abnormal grain growth (AGG) [3-5], which shed light on one of the most long-standing mysteries in materials science but open questions remain. Specifically, how an abnormal grain can initiate remains under debate for decades, albeit the cause can vary for different cases. Herein, we unequivocally show that an applied electric current can abruptly increase GB diffusivity and mobility, thereby inducing AGG, via an electrochemically induced disorder-order transition at general GBs. Furthermore, the discovery opens up a new window to tailor a broad range of GB (*e.g.*, unique electronic) properties, as well as microstructures, electrochemically.

7.2. Methods

7.2.1. Sample Preparation and Characterization

0.5 mol. % Bi_2O_3-doped ZnO powders were prepared by mixing ZnO (99.98% purity, ~18 nm, US Nanomaterials) with bismuth acetate (≥99.99% purity, Sigma Aldrich). Mixed powders were ball-milled for 10 hours with a small amount of isopropyl alcohol. Powders were subsequently dried in an oven at 80 °C for 12 hours and annealed at 500 °C for 1 hour. ZnO $(11\bar{2}0)$ single crystals with both sides polished were purchased from MTI Corporation (Richmond, California, USA). Dense Bi_2O_3-doped ZnO polycrystal/single crystal/polycrystal (PC/SC/PC) sandwich specimens were fabricated by spark plasma sintering (SPS) or field assisted sintering technology (FAST) at 780 °C for 5 minutes under a pressure of 50 MPa using a Thermal Technologies 3000 series SPS (Chatsworth, California, USA), and subsequently de-carbonized by annealing at 700 °C for 9 hours in air. After sintering, sandwich specimens reached >99% relative densities. Each

sandwich specimen was ground to 5.0×5.0×~1.6 mm^3 cuboids with a 0.5-mm thick single crystal in between, which completely separated the two polycrystalline regions.

7.2.2. First-Principles Calculations

The GBGenerator [28] code in Python Materials Genomics [29]library was used to construct ZnO GB structure. The lattice parameters of the ZnO hexagonal structure (*a* = 3.29 Å and *c* = 5.31 Å) were taken from the Materials Project [30].

An asymmetric GB terminated by $(11\bar{2}0)$ plane always requires a large simulation cell. Thus, we select the other GB plane to be the non-polar $(10\bar{1}0)$ with a rotate angle of ~53° along the [100] axis to construct a feasible model to mimic the GBs observed in the experiments within the limitation of the DFT cell size. Since lattice matching conditions cannot be achieved in three directions to apply periodic boundary conditions, a 15 Å thick layer of vacuum was added to isolate the interaction between two free surfaces created. The final simulation cell is triclinic with parameters: *a* = 0.62 nm, *b* = 1.45 nm, *c* = 5.30 nm, α = 104.69°, β = 78.69°, and γ = 74.70°. This simulation cell contains 240 atoms in total, which is about the largest for effective DFT and AIMD simulations.

The first-principles DFT calculations were performed by using the Vienna *ab initio* Simulations Package (VASP) [31, 32]. The Kohn-Sham equations were used to solve the projected-augmented wave (PAW) method [31, 33] along with standard PAW potentials for the elements Zn, O, and Bi. The Perdew-Burke-

Ernzerhof (PBE) [34] exchange-correlation functional was utilized to perform the structural optimization for the GB structure. The lattice parameters of ZnO were kept unchanged during the relaxation and only atomic positions were subjected to relaxation. All atoms were fully relaxed until the Hellmann-Feynman forces were smaller than 0.02 eV/Å. The Brillouin-zone integrations were sampled on a *Γ*-centered 4×2×1 *k*-point grids. The kinetic energy cutoff for plane waves was set to 400 eV. The convergence criterion for electronic self-consistency was adopted to 10^{-4} eV.

Based on the optimized GB structures, we performed *ab initio* molecular dynamics (AIMD) simulations under the *NVT* ensemble with a Nose-Hoover thermostat [35, 36] to obtain GB diffusivities. The temperature was set to 1123 K (850 °C), close to the experimental annealing condition. The overall simulation time was set to 1500 fs with a time step of 1 fs. Although the overall simulation time is relatively short (due to the limitation of a very large simulation cell), we believe the GB structures can achieve equilibrium based on monitoring the potential energy *vs.* time. The *k*-point grids were adopted to 1×1×1 (*Γ* point only). To avoid the effects of vacuum, we fixed 2~3 monolayer atoms near the free surfaces and only allowed other atoms to move. The atoms' trajectories during AIMD simulation were used to calculate the mean square displacement (MSD) over time (*t*). Finally. the GB diffusivities for Zn, O and Bi, respectively, were obtained by linearly fitting the corresponding MSD *vs. t* curves for both stoichiometric and reduced GBs for comparison.

7.2.3. DFT Calculation of GB Energies

To further verify and model the reduction-induced GB disorder-order transition, we calculated the GB energy as a function of chemical potentials for both stoichiometric and reduced GBs. The GB energy (γ_{GB}) can be determined from DFT calculations using the following equation:

$$\gamma_{\mathrm{GB}} = \frac{E_{\mathrm{Total}}^{GB\ Bi@ZnO} - E_{\mathrm{Grain1}}^{ZnO} - E_{\mathrm{Grain2}}^{ZnO} - n_{\mathrm{O}}\mu_{\mathrm{O}} + n_{\mathrm{Bi/Zn}}\mu_{\mathrm{Zn}} - n_{\mathrm{Bi/Zn}}\mu_{\mathrm{Bi}}}{A}, \quad (1)$$

where $E_{\mathrm{Total}}^{GB\ Bi@ZnO}$ is the total energy of the Bi-doped ZnO DFT calculation cell with the GB (after the full relaxation), $E_{\mathrm{Grain1(2)}}^{ZnO}$ is the reference energy of Grain 1 (or 2), $n_{\mathrm{Bi/Zn}}$ is the number of Zn atoms substituted by Bi atoms, n_{O} is the number of excess oxygen atoms (*i.e.*, number of the oxygen atoms added at the GB to compensate the charge of aliovalent Bi doping minus the number of the oxygen atoms removed for creating reduction), μ_i (*i* = O, Zn, or Bi) is the chemical potential of O, Zn, or Bi, and *A* is the cross-sectional area of the GB. The oxygen chemical potential difference $\Delta\mu_{\mathrm{O}}$ can be defined as:

$$\Delta\mu_{\mathrm{O}} = \mu_{\mathrm{O}} - \frac{1}{2}E_{\mathrm{O_2}}, \quad (2)$$

where $E_{\mathrm{O_2}}$ is the energy of the oxygen gas molecule with a correction [37]. The boundaries of $\Delta\mu_{\mathrm{O}}$ are given by:

$$\Delta\mu_{\mathrm{O}} < 0, \quad (3)$$

and

$$\Delta\mu_{\mathrm{O}} + \Delta\mu_{\mathrm{Zn}} = \Delta H_f(\mathrm{ZnO}), \tag{4}$$

where $\Delta H_f(\mathrm{ZnO})$ is the formation enthalpy of ZnO. Similarly, we define the Bi chemical potential difference as:

$$\Delta\mu_{\mathrm{Bi}} = \mu_{\mathrm{Bi}} - E_{\mathrm{Bi}}, \tag{5}$$

where E_{Bi} is the DFT energy of the Bi element (in its stable solid form). The upper and lower boundaries of $\Delta\mu_{\mathrm{Bi}}$ can be specified by a similar method. Using Eqs. (1-5), we calculated GB energies for both stoichiometric and reduced GBs as a function of chemical potential difference of oxygen ($\Delta\mu_{\mathrm{O}}$) and bismuth ($\Delta\mu_{\mathrm{Bi}}$), where the intersection line between the $\gamma_{\mathrm{GB}}^{\mathrm{Reduced}}$ and $\gamma_{\mathrm{GB}}^{\mathrm{Stoichiometric}}$ planes defines a GB transition.

Subsequently, we define the GB energy difference, $\Delta\gamma_{\mathrm{GB}}$, as:

$$\Delta\gamma_{\mathrm{GB}} = \gamma_{\mathrm{GB}}^{\mathrm{Reduced}} - \gamma_{\mathrm{GB}}^{\mathrm{Stoichiometric}}, \tag{6}$$

where $\gamma_{\mathrm{GB}}^{\mathrm{Stoichiometric}}$ and $\gamma_{\mathrm{GB}}^{\mathrm{Reduced}}$, respectively, are the GB energies for stoichiometric (disordered) and reduced (ordered) GBs, respectively, calculated from DFT. Here, $\Delta\gamma_{\mathrm{GB}}$ = 0 defines a transition.

7.3. Results and Discussion

7.3.1. Electrochemically Induced Enhanced Grain Growth

We design and fabricate a Polycrystal 1/Single Crystal/Polycrystal 2

(PC1/SC/PC2) sandwich specimen to conduct a grain growth experiment with a constant current density of 6.4 mA/mm^2 (see schematic diagram in Fig. 7.1(a)). First, we observe AGG in the PC1- region (where "-" *vs.* "+" denotes the reduced *vs.* oxidized region) near the negative electrode (cathode). An applied electric current can also induce similar AGG near the cathode in a simple polycrystalline specimen. Second, we observe enhanced migration of the SC/PC2- interface *vs.* only moderate migration of the PC1+/SC interface (see schematic diagram in Fig. 1(b)). Quantitative measurements of the migration distances show abruptly enhanced migration at the (most reduced) middle section of the SC/PC2- interface, in comparison with the (oxidized) PC1+/SC interface and the both interfaces in a reference sandwich specimen annealed with no electric field.

Next, let us show that the PC1- and PC2- regions in our sandwich specimen, where we observe increased GB mobilities (either AGG or enhanced migration of the SC/PC interface), are oxygen reduced. Here, Bi_2O_3-enriched liquid-like IGFs in polycrystals are ion-conducting but the ZnO single crystal is electron-conducting but ion-blocking. Hence, PC1+ and PC2+ regions are oxidized (as the oxygen ions are blocked and accumulated near the interfaces), which is evident by the pore formation due to an oxidation reaction that produces O_2. On the other hand, the PC1- and PC2- regions must be reduced (due to the depletion of oxygen ions). Subsequently, we can sketch the profiles of electric (ϕ), chemical ($\mu_{O^{2-}}$), and electrochemical ($\eta_{O^{2-}}$) potentials *vs.* locations in Fig. 7.1(b) in according to a model presented in prior work [16]. The electrochemical reduction in the PC1- region near

the negative electrode is well expected. To prove the reduction in the PC2- region, we conduct spatially resolved photoluminescence spectroscopy to probe oxygen vacancies (Fig. 7.2(a-b)). The integrated photoluminescence intensities for the combined photoluminescence peak at ~400-700 nm (representing all defects at GBs) at different locations are shown in Fig. 7.2(c-d). We further decompose this combined peak into a “green” band that is known to represent the oxygen vacancies and an “orange” band that most likely represents Zn interstitials. The decomposed green-band peaks at selected locations shown in Fig. 7.2(e-f) reveal the enrichment of oxygen vacancies to prove reduction in the PC2- region (that leads to enhanced migration of the SC/PC2- interface).

7.3.2. DFT Validation of Reduction-Induced GB Transition

Density functional theory (DFT) calculations are critically compared with AC STEM images to further verify the reduction-induced GB disorder-to-order transition. Based on STEM images, we construct an asymmetric GB to represent a general GB for DFT calculations. We set one terminal GB plane be $(11\bar{2}0)$ to mimic both SC/PC interfaces in the STEM images (Fig. 7.3(a-b)) to build a large simulation cell of 240 atoms. We also select the Bi coverage (Γ_{Bi} = ~11.7 nm^{-2}) to match prior experimental measurements [38].

DFT structural optimization shows that the stoichiometric GB (representing oxidized conditions in experiments) exhibits a more disordered structure (Fig. 7.3(c)), while a reduced GB (after removing approximately one monolayer of oxygens) exhibits a more ordered bilayer-like structure (Fig. 7.3(d); matching the

STEM image in Fig. 7.3(a)). The bilayer-like Bi adsorption can be evident in the projected Bi distribution profile shown below Fig. 7.3(d), with the interlayer distance of ~0.3 nm matching the STEM measurement (Fig. 7.3(b)). Furthermore, we calculate a structural disorder parameter (η_{Dis}) for each atom in the DFT relaxed structures and plot the projected disorder profiles ($\eta_{\mathrm{Dis}}(x)$) in Fig. 7.3(e, f). For the disordered GB, the interfacial width is ~0.8 nm from the $\eta_{\mathrm{Dis}}(x)$ profile in Fig. 7.3(e) *vs.* ~0.9 nm from the STEM image shown in Fig. 7.3(a). Further quantifications show that the stoichiometric GB has larger GB excess of disorder ($\Gamma_{\mathrm{Disorder}} \approx 25\ \mathrm{nm}^{-2}$) than the reduced GB (~14 nm^{-2}); in other words, oxygen reduction makes the GB structure more ordered, which agrees with the experiments (Fig. 7.3(a) *vs.* 7.3(b)). DFT calculations have also been conducted for GBs of different levels of Bi adsorption and oxygen reduction, see Figs. 7.4 and 7.5.

Furthermore, we calculate GB energies using the procedure described in §7.2.3 (Fig. 7.6). Since both stoichiometric and reduced GBs have the same amount of GB excess of Bi, the difference in the GB energies $\Delta\gamma_{\mathrm{GB}}(\equiv \gamma_{\mathrm{GB}}^{\mathrm{Reduced}} - \gamma_{\mathrm{GB}}^{\mathrm{Stoichiometric}})$ is in fact independent of $\Delta\mu_{\mathrm{Bi}}$. Thus, we can simplify 7.6(b) and directly show $\Delta\gamma_{\mathrm{GB}}$ as a function of $\Delta\mu_{\mathrm{O}}$ (Fig. 7.6a). The DFT-computed GB energy difference $\Delta\gamma_{\mathrm{GB}}$ indicates a GB phase-like (complexion) transition from the disordered and stoichiometric GB to the ordered and reduced GB with decreasing oxygen chemical potential, which is consistent with our experimental observations.

7.3.3. AIMD of GB Diffusivity to Explain the Enhanced Grain Growth

We further perform large-scale *ab initio* molecular dynamics (AIMD) simulations to calculate and compare the GB diffusivities for the stoichiometric and reduced GBs. Fig. 7.7(a) shows the calculated GB diffusivities at 840 °C, which are increased markedly in the reduced and ordered GB in comparison with those in stoichiometric and disordered GB. Thus, the AIMD simulations suggest the increased diffusion kinetics of the reduced and ordered GBs to explain the observed increased GB mobilities.

7.3.4. Intuitive Understandings of the Mechanisms

The above thermodynamic modelling, DFT, and AIMD results can be understood intuitively. The presence of aliovalent Bi^{3+} adsorbates (substituting Zn^{2+} cations) in the stoichiometric GB likely promotes interfacial disordering. The oxygen reduction decreases the effective charge on Bi adsorbates to reduce interfacial disordering.

The differential charge density maps obtained from DFT calculations further suggest that the increased diffusivity in the reduced GB can be attributed to the weaker charge transfer and chemical bonding (see Fig. 7.7(c) and 7.7(e)). Furthermore, we calculate average Bader charges [39] to show that the effective charge on the Bi cations is decreased with the reduction (*i.e.*, one Bi atom losses ~1.4 *e* in the stoichiometric GB *vs.* ~0.69 *e* in the reduced GB).

Thus, we can envision the following mechanism. The aliovalent Bi adsorbates serve as charged “hot spots” to provide “pinning” effects at the stoichiometric GB with strong charge transfer (Fig. 7.7(b) and 7.7(d)) or chemical bonding. In contrast, the oxygen reduction can reduce the effective charge on Bi adsorbates to weaken the bonding and alleviate “pinning” effects), thereby increasing the kinetics (diffusivities and mobilities) of the reduced GB.

7.4. Conclusion

In summary, ZnO-Bi_2O_3 is used as a model system to uncover a new mechanism of electrochemically induced GB transitions with significantly increased GB diffusivities, which subsequently result in enhanced and abnormal grain growth. Similar mechanisms can exist in other systems with potentially broad technological impacts on a variety of innovative materials processing technologies and electrochemical (or electronic) devices using electric fields and currents. This study also further suggests a new method to tailor the GB structure and properties electrochemically, as well as microstructures (*e.g.*, to intentionally produce graded and far-from-equilibrium microstructures). These findings have enriched our fundamental understandings of both electric field effects on microstructural evolution and the potentially transformative GB complexion (interfacial phase-like transition) theory via building a bridge between these two areas of great scientific importance and broad technological relevance.

Chapter 7, in part, is a reprint of manuscript “Uncovering Electrochemically Induced Grain Boundary Phase-Like Transition” J. Nie, C. Hu, Q. Yan, and J. Luo,

manuscript submitted. The experiments were carried out by J. Nie with the help of Q. Yan. The dissertation author was the primary investigator to perform theoretical calculations and first co-author of this paper.

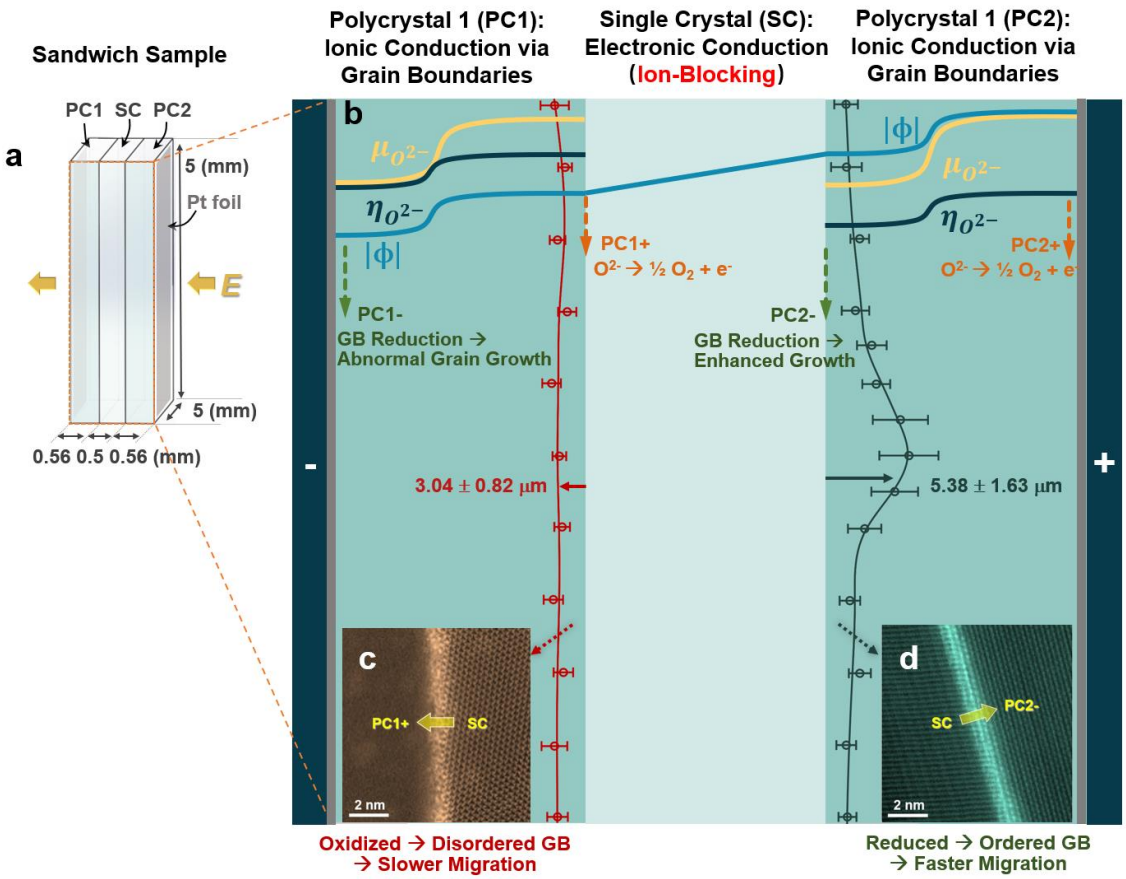

Figure 7.1 The schematic profiles of electric, chemical, and electrochemical potentials. (a) Schematic drawing of sandwich sample using the same ratio of actual specimen. (b) Schematic profiles of electric (ϕ), chemical ($\mu_{O^{2-}}$), and electrochemical ($\eta_{O^{2-}}$) potentials *vs.* locations. Grain boundaries (GBs) in the two polycrystals are mostly ion-conducting via the Bi_2O_3-enriched liquid-like IGFs, while the ZnO single crystal is electron-conducting but ion-blocking. The actual migration distance at PC1+/SC and SC/PC2- regions were plotted with error bars using red and green colors, respectively. The average migration distances are respectively $3.04 \pm 0.82\ \mu$m and $5.38 \pm 1.63\ \mu$m for PC1+/SC and SC/PC2- interfaces. (c) a slow-moving disordered GB at the oxidized PC1-/SC interface and (d) a fast-moving ordered GB at the reduced SC/PC2+ interface.

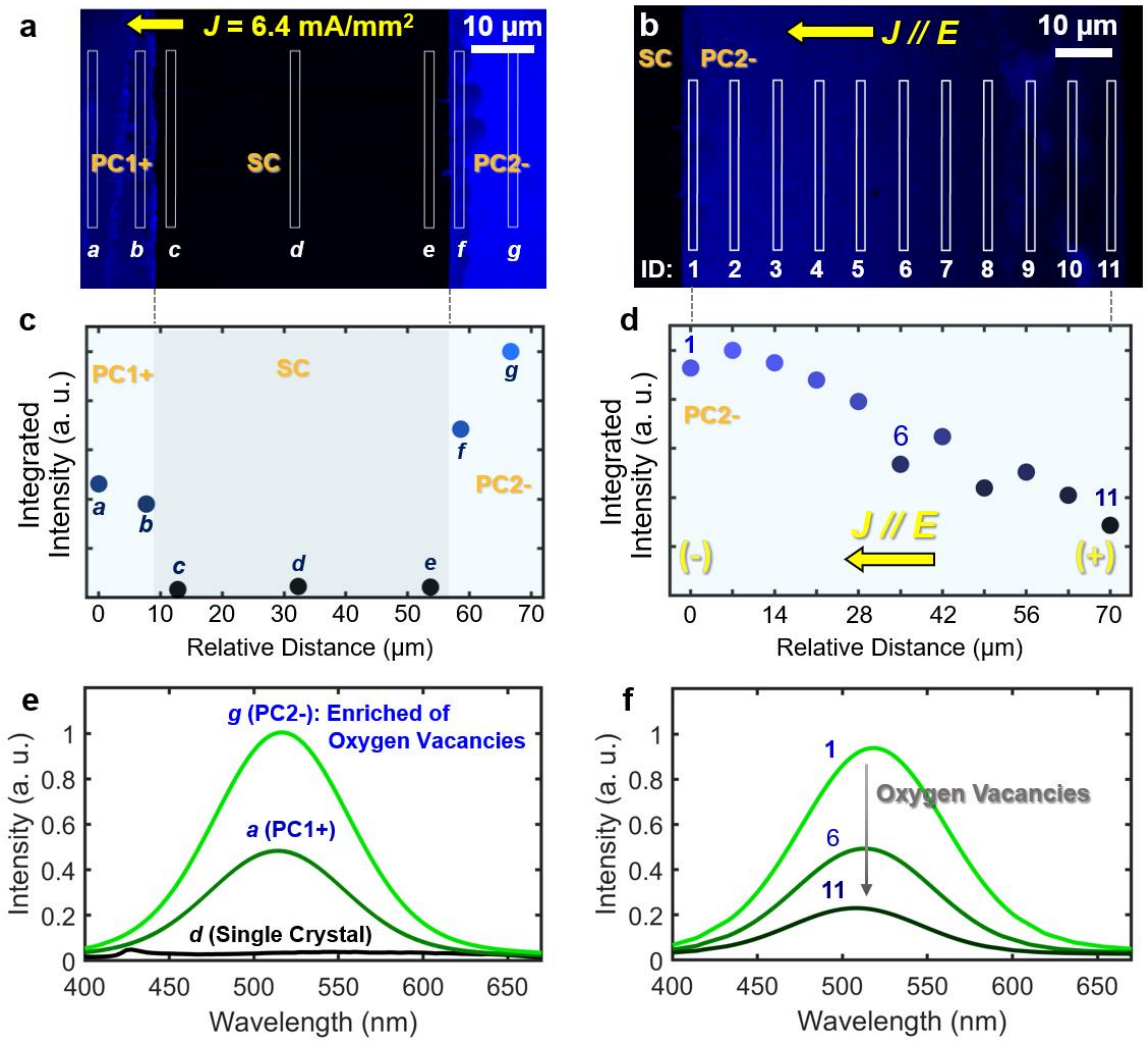

Figure 7.2 Photoluminescence spectroscopy of the sandwich specimen annealed with a constant applied electric current, suggesting the enrichment of oxygen vacancies in the reduced PC2- region. (a, b) Maps of the photoluminescence intensity at the 526 nm wavelength of the cross-sectional PC1/SC/PC2 sandwich specimen. (c, d) Integrated photoluminescence intensities for the combined photoluminescence peak at ~400-700 nm at different locations, representing all defects at GBs. Photoluminescence spectra are collected at Locations *a-g* labeled in Panel (a) and Locations 1-11 labeled in Panel (b), respectively. (e, f) The photoluminescence intensity *vs.* wavelength curves of decomposed green-emission band (representing the oxygen vacancy concentration) at selected locations.

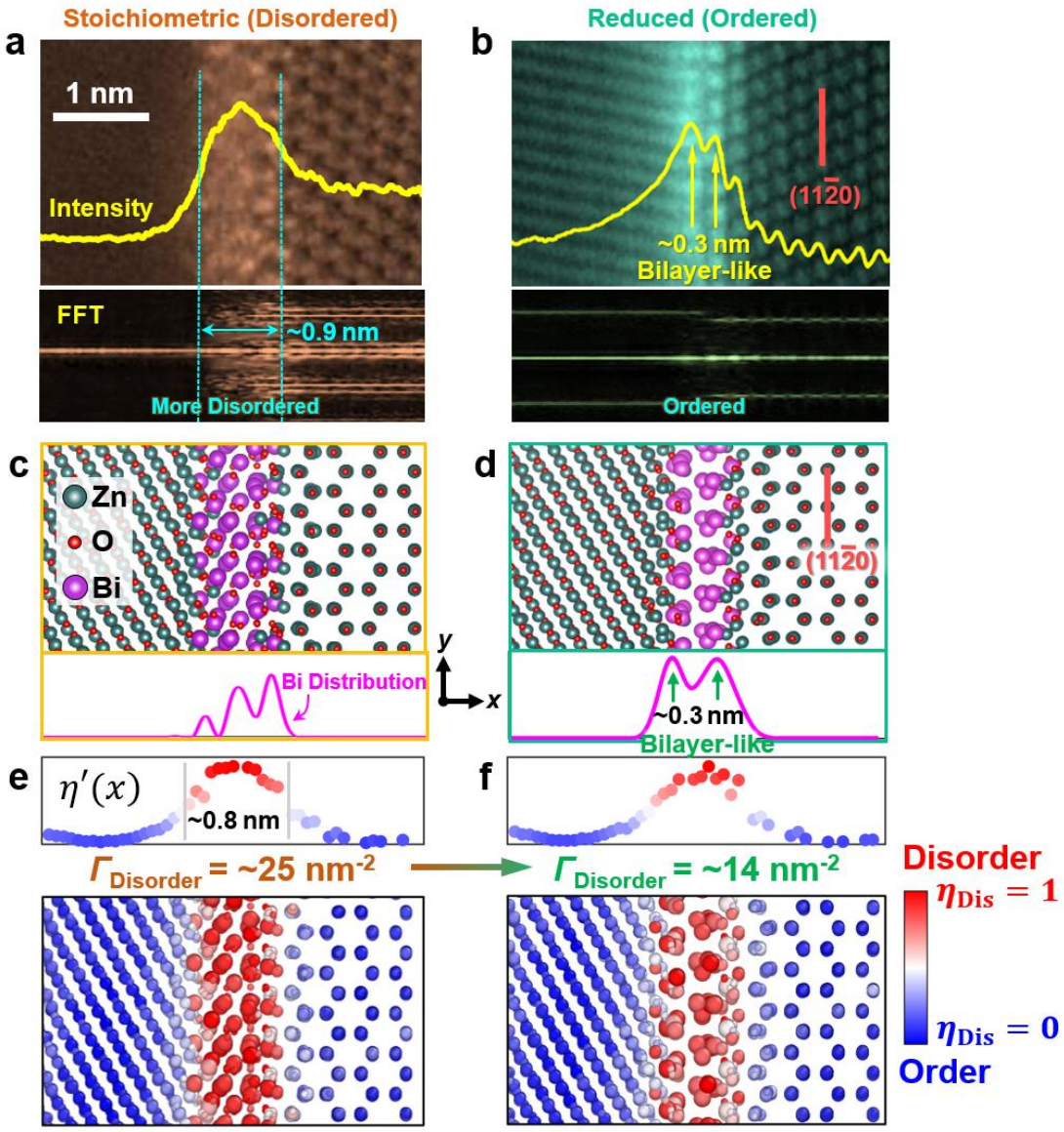

Figure 7.3 Comparison of experiments and DFT simulations of stoichiometric (disordered) *vs.* reduced (ordered) GB structures. (a-b) Expanded experimental STEM HAADF images for a disordered stoichiometric GB *vs.* an ordered (bilayer-like) reduced GB; here, we plot the averaged HAADF intensity and line-by-line FFT patterns to illustrate the layering and periodic orders. (c-d) DFT-optimized structures of the stoichiometric *vs.* reduced GBs, where the projected Bi concentration profiles are plotted beneath. (e-f) The calculated disorder parameters for all atoms for DFT-optimized stoichiometric *vs.* reduced GB structures. The projected disorder parameter profiles ($\eta_{\mathrm{Dis}}(x)$) are shown above. The GB excess of disorder (computed by integrating $\eta_{\mathrm{Dis}}(x)$) decreases from $\Gamma_{\mathrm{Disorder}}$ = ~25 nm^{-1} for the stoichiometric GB to $\Gamma_{\mathrm{Disorder}}$ = ~14 nm^{-1} for the reducing GB, thereby showing that the oxygen reduction induces GB ordering.

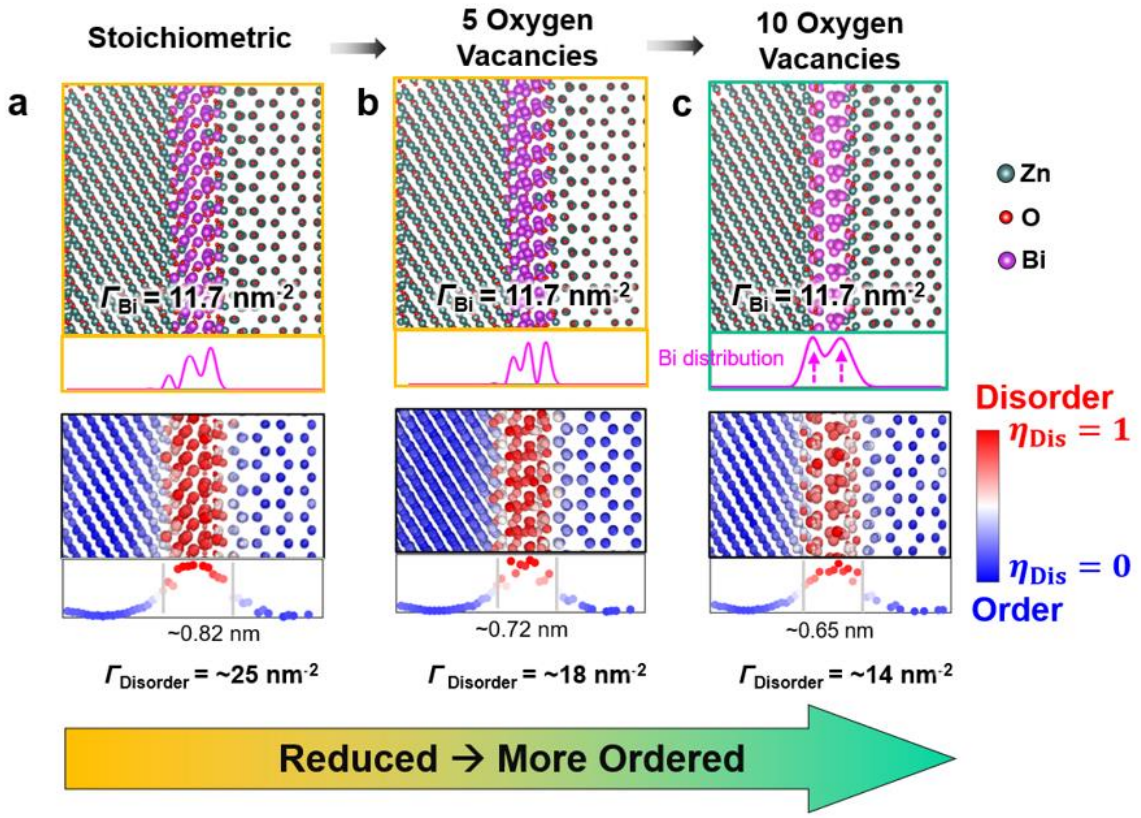

Figure 7.4 Variation of GB structures with increasing levels of reduction predicted by DFT. (a) The DFT-relaxed stoichiometric GB (mimic the oxidized condition in experiments). The DFT-relaxed reduced GB structures by (b) removing ~5.8 oxygen atoms per nm^2 (about half monolayer) and (c) ~11.7 oxygen atoms per nm^2 (about one monolayer), respectively. The computed Bi distribution and disorder profiles indicate that oxygen reduction leads to the formation of more ordered GB structures.

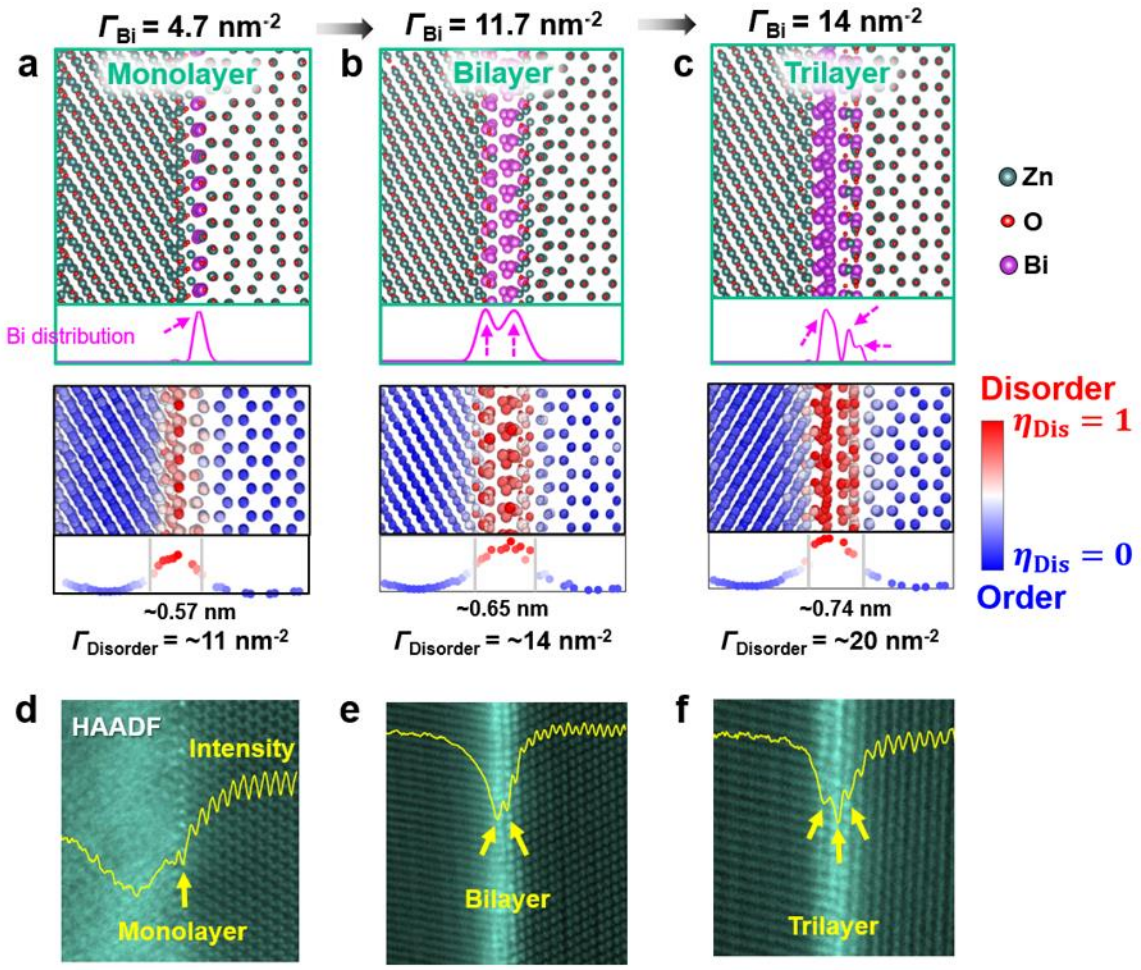

Figure 7.5 A series of ordered complexions (Bi adsorption structures) formed at electrochemically reduced GBs. (a-c) DFT-optimized reduced GB structures with increasing Bi adsorption (Γ_{Bi}), showing the formation of monolayer-, bilayer-, and trilayer-like complexions. (d-f) STEM HAADF images of ordered GBs observed in the reduced regions of our specimen that resemble these layered adsorption structures predicted from DFT (albeit different GB characters).

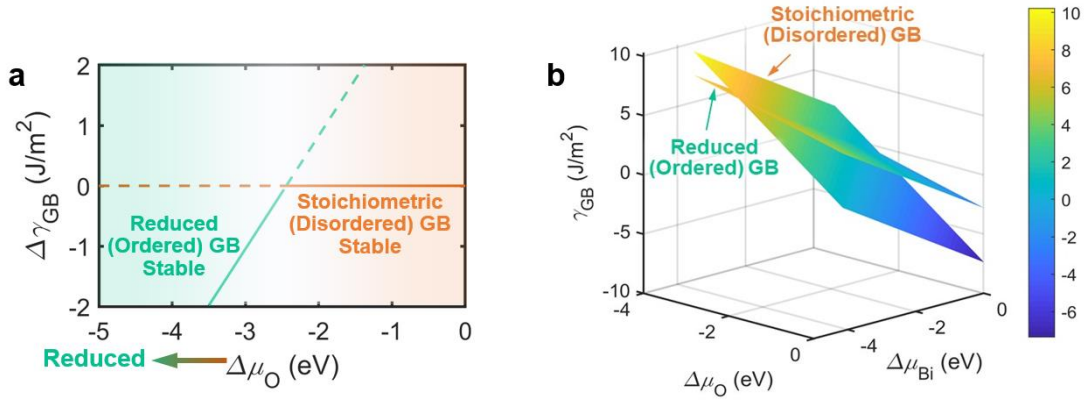

Figure 7.6 (a) Computed GB energy difference $\Delta\gamma_{\mathrm{GB}}$ ($\equiv \gamma_{\mathrm{GB}}^{\mathrm{Reduced}} - \gamma_{\mathrm{GB}}^{\mathrm{Stoichiometric}}$) *vs.* oxygen chemical potential difference $\Delta\mu_{\mathrm{O}}$ ($\equiv \mu_{\mathrm{O}} - \frac{1}{2}E_{\mathrm{O}_2}$), showing a transformation from the stoichiometric (disordered) GB to the reduced (ordered) GB with decreasing oxygen chemical potential. (b) DFT calculated GB energies γ_{GB} of stoichiometric (disordered) and reduced (ordered) GBs as a function of chemical potential difference of oxygen ($\Delta\mu_{\mathrm{O}}$) and bismuth ($\Delta\mu_{\mathrm{Bi}}$). Note that this calculation adopted same GB excess of Bi adsorption for both GBs, so that the difference in the GB energies $\Delta\gamma_{\mathrm{GB}}$ is independent of $\Delta\mu_{\mathrm{Bi}}$. Consequently, a simplified plot of $\Delta\gamma_{\mathrm{GB}}$ as a function of $\Delta\mu_{\mathrm{O}}$ can be plotted in (a)

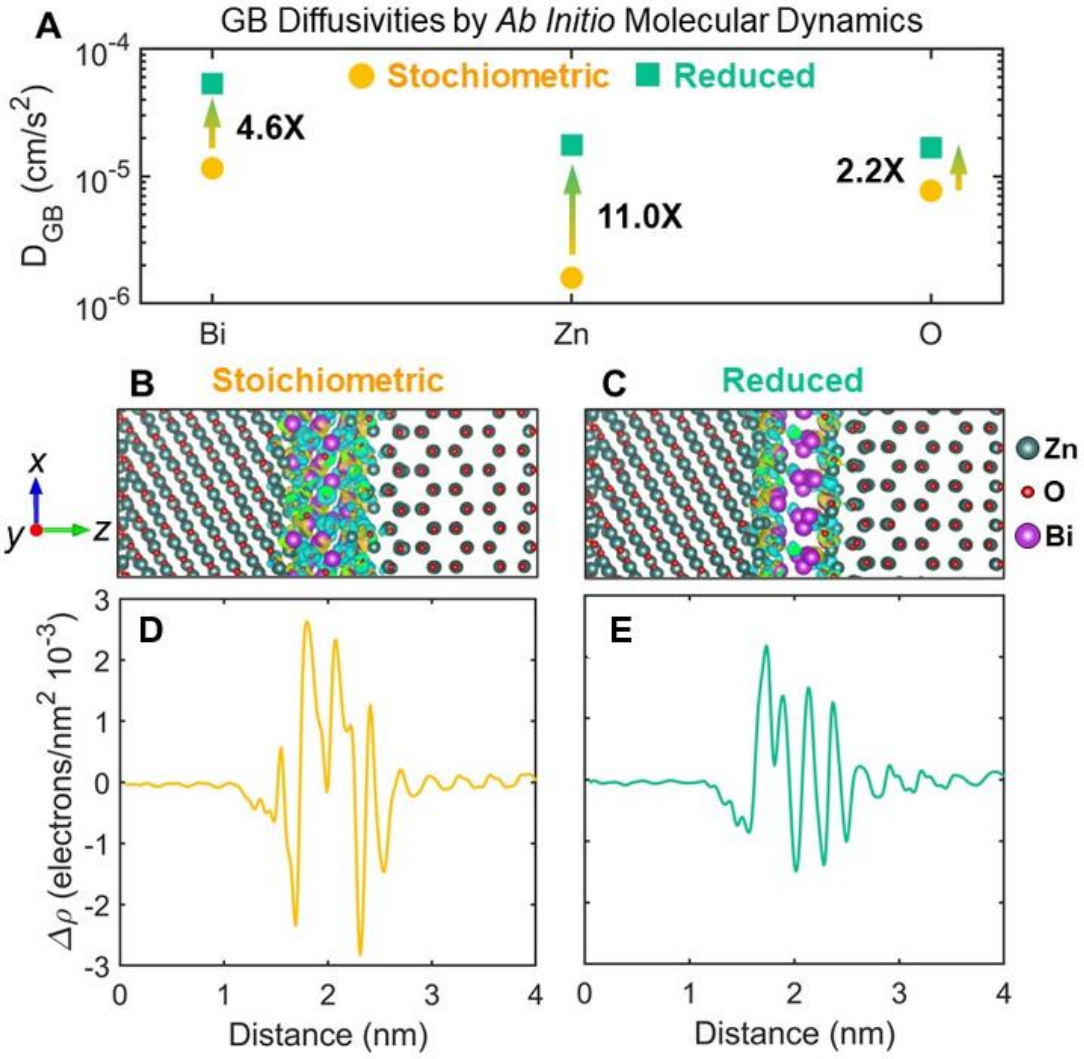

Figure 7.7 GB diffusivities calculated by *ab initio* molecular dynamics (AIMD) simulations and the differential charge densities calculated from DFT. (a) GB diffusivities calculated by AIMD simulations. The GB diffusivities in the reduced (ordered) GB are increased by ~4.6× for Bi, ~11.0× for Zn, and ~2.2× for O, respectively, in comparison with those in the stoichiometric (disordered) GB. (b-c) Isosurfaces of the differential charge densities of the stoichiometric GB and reduced GB. The isovalue is set to 0.01 e/Å^3 for the plots. The yellow and cyan isosurfaces, respectively, represent charge accumulation and depletion, respectively. (d-e) The differential charge density profiles projected along the *z* direction of (b) the stoichiometric GB and (c) the reduced GB, suggesting weaker bonding in the reduced (ordered) GB that leads to enhanced diffusivities.

References

[1] E.W. Hart, Two-dimensional phase transformation in grain boundaries, Scripta Metallurgica, 2 (1968) 179-182.

[2] W.D. Kaplan, D. Chatain, P. Wynblatt, W.C. Carter, A review of wetting versus adsorption, complexions, and related phenomena: the rosetta stone of wetting, Journal of Materials Science, 48 (2013) 5681-5717.

[3] S.J. Dillon, M. Tang, W.C. Carter, M.P. Harmer, Complexion: A new concept for kinetic engineering in materials science, Acta Materialia, 55 (2007) 6208-6218.

[4] P.R. Cantwell, M. Tang, S.J. Dillon, J. Luo, G.S. Rohrer, M.P. Harmer, Grain boundary complexions, Acta Materialia, 62 (2014) 1-48.

[5] P.R. Cantwell, T. Frolov, T.J. Rupert, A.R. Krause, C.J. Marvel, G.S. Rohrer, J.M. Rickman, M.P. Harmer, Grain Boundary Complexion Transitions, Annual Review of Materials Research, (2020).

[6] M. Baram, D. Chatain, W.D. Kaplan, Nanometer-Thick Equilibrium Films: The Interface Between Thermodynamics and Atomistics, Science, 332 (2011) 206-209.

[7] M. Tang, W.C. Carter, R.M. Cannon, Grain Boundary Transitions in Binary Alloys, Physical Review Letters, 97 (2006) 075502.

[8] T. Hu, S. Yang, N. Zhou, Y. Zhang, J. Luo, Role of disordered bipolar complexions on the sulfur embrittlement of nickel general grain boundaries, Nature Communications, 9 (2018) 2764.

[9] Z. Yu, P.R. Cantwell, Q. Gao, D. Yin, Y. Zhang, N. Zhou, G.S. Rohrer, M. Widom, J. Luo, M.P. Harmer, Segregation-induced ordered superstructures at general grain boundaries in a nickel-bismuth alloy, Science, 358 (2017) 97.

[10] J. Luo, Let thermodynamics do the interfacial engineering of batteries and solid electrolytes, Energy Storage Materials, 21 (2019) 50-60.

[11] J. Luo, Stabilization of Nanoscale Quasi-Liquid Interfacial Films in Inorganic Materials: A Review and Critical Assessment, Critical Reviews in Solid State and Materials Sciences, 32 (2007) 67-109.

[12] M. Cologna, B. Rashkova, R. Raj, Flash Sintering of Nanograin Zirconia in <5 s at 850°C, Journal of the American Ceramic Society, 93 (2010) 3556-3559.

[13] S.-W. Kim, S.-J.L. Kang, I.W. Chen, Electro-Sintering of Yttria-Stabilized Cubic Zirconia, Journal of the American Ceramic Society, 96 (2013) 1398-1406.

[14] Z.A. Munir, U. Anselmi-Tamburini, M. Ohyanagi, The effect of electric field and pressure on the synthesis and consolidation of materials: A review of the spark plasma sintering method, Journal of Materials Science, 41 (2006) 763-777.

[15] C. Wang, W. Ping, Q. Bai, H. Cui, R. Hensleigh, R. Wang, A.H. Brozena, Z. Xu, J. Dai, Y. Pei, C. Zheng, G. Pastel, J. Gao, X. Wang, H. Wang, J.-C. Zhao, B. Yang, X. Zheng, J. Luo, Y. Mo, B. Dunn, L. Hu, A general method to synthesize and sinter bulk ceramics in seconds, Science, 368 (2020) 521-526.

[16] Y. Dong, I.W. Chen, Oxygen potential transition in mixed conducting oxide electrolyte, Acta Materialia, 156 (2018) 399-410.

[17] J.X. Sierra, H.F. Poulsen, P.S. Jørgensen, C. Detlefs, P. Cook, H. Simons, A.C. Jakobsen, J.R. Bowen, In-operando observation of microstructural evolution in a solid oxide cell electrolyte operating at high polarization, Journal of Power Sources, 413 (2019) 351-359.

[18] H.-K. Tian, Z. Liu, Y. Ji, L.-Q. Chen, Y. Qi, Interfacial Electronic Properties Dictate Li Dendrite Growth in Solid Electrolytes, Chemistry of Materials, 31 (2019) 7351-7359.

[19] D. Yang, R. Raj, H. Conrad, Enhanced Sintering Rate of Zirconia (3Y-TZP) Through the Effect of a Weak dc Electric Field on Grain Growth, Journal of the American Ceramic Society, 93 (2010) 2935-2937.

[20] Y. Dong, H. Wang, I.W. Chen, Electrical and hydrogen reduction enhances kinetics in doped zirconia and ceria: I. grain growth study, Journal of the American Ceramic Society, 100 (2017) 876-886.

[21] Y. Zhang, J.-I. Jung, J. Luo, Thermal runaway, flash sintering and asymmetrical microstructural development of ZnO and ZnO–Bi2O3 under direct currents, Acta Materialia, 94 (2015) 87-100.

[22] Z. Wang, M. Saito, K.P. McKenna, L. Gu, S. Tsukimoto, A.L. Shluger, Y. Ikuhara, Atom-resolved imaging of ordered defect superstructures at individual grain boundaries, Nature, 479 (2011) 380-383.

[23] W. Rheinheimer, M. Fülling, M.J. Hoffmann, Grain growth in weak electric fields in strontium titanate: Grain growth acceleration by defect redistribution, Journal of the European Ceramic Society, 36 (2016) 2773-2780.

[24] Y. Zhang, J. Nie, J. Luo, Flash sintering activated by bulk phase and grain boundary complexion transformations, Acta Materialia, 181 (2019) 544-554.

[25] T. Meiners, T. Frolov, R.E. Rudd, G. Dehm, C.H. Liebscher, Observations of grain-boundary phase transformations in an elemental metal, Nature, 579 (2020) 375-378.

[26] A. Morawiec, K. Glowinski, On “macroscopic” characterization of mixed grain boundaries, Acta Materialia, 61 (2013) 5756-5767.

[27] J. Luo, H. Cheng, K.M. Asl, C.J. Kiely, M.P. Harmer, The Role of a Bilayer Interfacial Phase on Liquid Metal Embrittlement, Science, 333 (2011) 1730-1733.

[28] H. Zheng, X.-G. Li, R. Tran, C. Chen, M. Horton, D. Winston, K.A. Persson, S.P. Ong, Grain boundary properties of elemental metals, Acta Materialia, 186 (2020) 40-49.

[29] S.P. Ong, W.D. Richards, A. Jain, G. Hautier, M. Kocher, S. Cholia, D. Gunter, V.L. Chevrier, K.A. Persson, G. Ceder, Python Materials Genomics (pymatgen): A robust, open-source python library for materials analysis, Computational Materials Science, 68 (2013) 314-319.

[30] A. Jain, S.P. Ong, G. Hautier, W. Chen, W.D. Richards, S. Dacek, S. Cholia, D. Gunter, D. Skinner, G. Ceder, K.A. Persson, Commentary: The Materials Project: A materials genome approach to accelerating materials innovation, APL Materials, 1 (2013) 011002.

[31] G. Kresse, J. Furthmüller, Efficient iterative schemes for ab initio total-energy calculations using a plane-wave basis set, Physical Review B, 54 (1996) 11169-11186.

[32] G. Kresse, J. Hafner, Ab initio molecular dynamics for liquid metals, Physical Review B, 47 (1993) 558-561.

[33] P.E. Blöchl, Projector augmented-wave method, Physical Review B, 50 (1994) 17953-17979.

[34] J.P. Perdew, K. Burke, M. Ernzerhof, Generalized Gradient Approximation Made Simple, Physical Review Letters, 77 (1996) 3865-3868.

[35] D.J. Evans, B.L. Holian, The Nose–Hoover thermostat, The Journal of Chemical Physics, 83 (1985) 4069-4074.

[36] Z. Deng, Z. Zhu, I.-H. Chu, S.P. Ong, Data-Driven First-Principles Methods for the Study and Design of Alkali Superionic Conductors, Chemistry of Materials, 29 (2017) 281-288.

[37] L. Wang, T. Maxisch, G. Ceder, Oxidation energies of transition metal oxides within the $\mathrm{GGA}+\mathrm{U}$ framework, Physical Review B, 73 (2006) 195107.

[38] J.R. Lee, Y.M. Chiang, G. Ceder, Pressure-thermodynamic study of grain boundaries: Bi segregation in ZnO, Acta Materialia, 45 (1997) 1247-1257.

[39] G. Henkelman, A. Arnaldsson, H. Jónsson, A fast and robust algorithm for Bader decomposition of charge density, Computational Materials Science, 36 (2006) 354-360.

Chapter 8. Dissertation Summary and Research Prospects

In this dissertation, a variety of GB properties diagrams, such as GB excess of adsorption, disorder, free volume, as well as fracture toughness and ultimate tensile strength, have been developed. On one hand, some of the computed GB diagrams (e.g., Au adsorption at Si twist GB) show first-order transition with critical line, which suggests a phase-like “complexion” behavior of GB. On the other hands, the GB diagrams can also have continuous transitions for many other systems, such as Cu-Ag and Al-Ga binary systems. In both cases, developing GB property diagrams as a function of temperature and bulk composition can be highly important and useful.

Second, this dissertation not only developed GB diagrams for symmetric tilt and twist GBs, but also asymmetric and general GBs; the latter are more ubiquitous in polycrystalline materials but are hitherto scarcely studied by virtually any modeling methods. The five DOFs for defining one GBs (especially for those general GBs) make it a “mission impossible” to map out all GB states as a function of DOFs, temperature, and composition in 7D space. To address this challenge, a data-driven method by combining high-throughput simulations, genetic algorithm, and deep neural networks have been developed. In addition, the artificial neural work associated with high-throughput modeling and principle component analysis have been used to predict GB diagrams of high-entropy alloy as a function of four independent DOFs and temperature in 5D space. Note that all abovementioned methods can be easily used to develop GB diagrams for any other materials, which

suggests immense opportunities for future GB research. More interestingly, predicting GB diagrams of HEA as a function of five crystallographic DOFs and 4 compositional DOFs as well as temperature in 10D space remain another grand challenge for materials science, and developing such GB diagrams in 10D space represents a paradigm shift.

Third, GB can be considered as 2D interfacial phases, which were also named as “complexions” (see Chapter 1), to differentiate them from thin layers of precipitated 3D bulk phases at GBs. Solute or impurity segregation at GB can dramatically alter microstructural evolution, GB embrittlement, and a broad range of materials properties. Thus, understanding the fundamental mechanism of GB segregation is of both scientific and practical interest. This dissertation deciphers the (*i*) the coupling effect of GB disordering and multicomponent segregation on GB segregation in HEA, (*ii*) the highly asymmetric GB segregation in Ti & Co co-doped WC GB, and (*iii*) reduction-induced GB disorder-order transition. These studies not only expand our fundamental knowledge of GB segregation, but also enrich the segregation theories.

Finally, the large datasets generated in this dissertation, such as 6300+ MC/MD simulations for Cu-Ag binary system and 1030+ MC/MD simulations for CrMnFeCoNi HEA, enables substantial future works to develop new and better phenomenological segregation models with a few parameters.